Mapping the Intracellular Temperature Dynamics with Organelle-Targeted Upconversion Nanoparticles

by Xiangjun Di

Thesis submitted in fulfilment of the requirements for

the degree of

Doctor of Philosophy

under the supervision of Prof. Dayong Jin, A/Prof. Jiajia Zhou, Dr. Qian Peter Su,

University of Technology Sydney

Faculty of Science

10/11/2022

Certificate of Original Authorship

I, Xiangjun Di declare that this thesis is submitted in fulfilment of the requirements for the award of Doctor of Philosophy, in the School of Mathematical and Physical Sciences, Faculty of Science, at the University of Technology Sydney.

This thesis is wholly my own work unless otherwise reference or acknowledged. In addition, I certify that all information sources and literature used are indicated in the thesis.

This document has not been submitted for qualifications at any other academic institution.

This research is supported by the Australian Government Research Training Program and the China Scholarship Council Scholarship.

Signature: Production Note:
Signature removed prior to publication.

Date: 10/11/2022

Acknowledgements

I would like to express my deep and sincere gratitude to my principal supervisor, Prof. Dayong Jin, for supporting me in research training and academic writing. He taught me how to solve problems logically.

I would like to thank my co-supervisor Dr. Qian Su for his patience and guidance. He provided technical support in the microscope and data analysis. I would like to thank my co-supervisor A/Prof. Jiajia Zhou for the help with the materials. They have been the source of inspiration and a safe port to reach for help.

I would like to address special thanks to the help from Dr. Hao He and Dr. Chaohao Chen in the surface functionalization of nanoparticles, Dr. Jiayan Liao, Dr. Sheng Mei and Dr. Yunfei Shang in nanoparticles synthesis, Mr. Dejiang Wang in cell experiments, Mr. Milad Nonahal, Mr. Javad Safaei, Miss Ziqing Du and Mr. Lei Ding in nanoparticles characterization, Ms. Mahnaz Mddahfar, Ms. Lin Zhang and Prof. Martina Stenzel for providing the polymers.

I would like to thank all the members of the IBMD (past and present) who has provided technical support and suggestions. I enjoy working with these lovely people.

Last but never least, I would like to thank my supportive family. To my parents for being immensely supportive in my choices. To my husband, Mr. Dejiang Wang, for encouraging me all the time.

Finally, I would like to acknowledge the UTS and the China Scholarship Council (CSC) for providing the scholarship and research opportunities.

Format of Thesis

This thesis consists of five chapters.

Chapter 1 is the introduction, including the basic knowledge of mitochondria, intracellular luminescence thermometry, and surface functionalization of upconversion nanoparticles ($NaYF_4$: 20%Yb^{3+}, 2%Er^{3+}).

Chapter 2 is the result of surface modification to determine the stability and dispersity of UCNPs ($NaYF_4$: 20%Yb^{3+}, 2%Er^{3+}) capped with different ligands in the water. Chapters 3 and 4 focus on the intracellular temperature dynamics studied by organelle-targeted UCNPs ($NaYF_4$: 20%Yb^{3+}, 2%Er^{3+}).

Chapter 5 summarizes the key results of this thesis and further discusses the perspective of UCNPs-based thermometry in intracellular temperature mapping. This thesis flowchart is illustrated below.

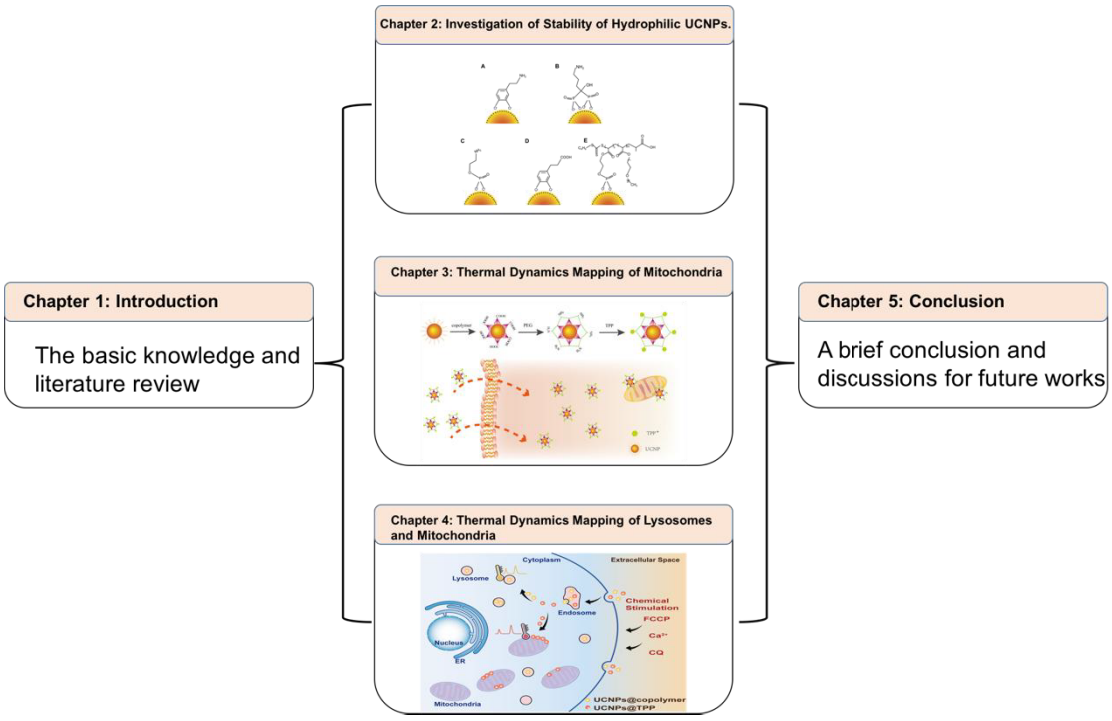

List of Publications

Articles

- **Xiangjun Di**, Dejiang Wang, Jiajia Zhou, Yongtao Liu, Qian Peter Su*, Dayong Jin*, Cascade Targeting Upconversion Nanoparticles to map Spatiotemporal Thermodynamics of Mitochondria and Lysosomes. (***In preparation***).
- **Xiangjun Di**, Dejiang Wang, Jiajia Zhou, Lin Zhang, Martina Stenzel, Qian Peter Su*, Dayong Jin*, Quantitatively Monitoring in situ Mitochondrial Thermal Dynamics by Upconversion Nanoparticles. ***Nano Letters***. 2021, 21, 4, 1651–1658.
- Baolei Liu, Chaohao Chen, **Xiangjun Di**, Jiayan Liao, Shihui Wen, Qian Peter Su, Xuchen Shan, Zai-Quan Xu, Lining Arnold Ju, Chao Mi, Fan Wang*, and Dayong Jin*, Upconversion Nonlinear Structured Illumination Microscopy, ***Nano Letters*** 20(7):4775-4781.
- Xuchen Shan, Fan Wang*, Dejiang Wang, Shihui Wen, Chaohao Chen, **Xiangjun Di**, Peng Nie, Jiayan Liao, Yongtao Liu, Lei Ding, Peter J. Reece* & Dayong Jin*, Optical tweezers beyond refractive index mismatch using highly doped upconversion nanoparticles, ***Nature Nanotechnology*** 16(5):1-7.
- Yuan Liu, Gungun Lin*, Guochen Bao, Ming Guan, Liu Yang, Yongtao Liu, Dejiang Wang, Xun Zhang, Jiayan Liao, Guocheng Fang, **Xiangjun Di**, Guan Huang, Jiajia Zhou, Yuen Yee Cheng, and Dayong Jin*, Stratified Disk Microrobots with Dynamic Maneuverability and Proton-Activatable Luminescence for in Vivo Imaging, ***Acs Nano***, 2021, 15, 12, 19924–19937.

Book Chapter

- **Xiangjun Di**†, Jinshan Qin†, Yujie Sun*, Qian Peter Su*, Visualize the Distribution and Dynamics of Mitochondrial DNA (mtDNA) nucleoids with Multiple Labelling Strategies. (***Book Chapter, in press***).
- Wanqing Du, **Xiangjun Di**, Qian Peter Su*, Studying Mitochondrial Network Formation by In Vivo and In Vitro Reconstitution Assay, ***Methods in molecular biology (Clifton, N.J.)*** 2276:333-341.

([1,2,6] are closely related to my PhD program)

Statement of Contribution of Authors

Xiangjun Di, Dejiang Wang, Jiajia Zhou, Lin Zhang, Martina Stenzel, Qian Peter Su*, Dayong Jin*, Quantitatively Monitoring in situ Mitochondrial Thermal Dynamics by Upconversion Nanoparticles. **Nano Letters**. 2021, 21, 4, 1651−1658.

	X.D	D.W	J.Z	L.Z	M.S	Q.S	D.J
Experiment Design	■	■	■			■	■
Sample Preparation	■	■		■	■		
Data Collection	■						
Analysis	■	■	■			■	■
Manuscript	■	■	■			■	■

The concept of this paper was developed by my supervisor Prof. Dayong Jin and Dr. Qian Peter Su. I designed the experiments and conducted the experimental work, including synthesis and modification of UCNPs ($NaYF_4$: 20%Yb^{3+}, 2%Er^{3+}), characterization of UCNPs ($NaYF_4$: 20%Yb^{3+}, 2%Er^{3+}), cell labelling, data collection, data analysis, and manuscript writing.

Table of Symbols

S_R	relative temperature sensing sensitivity
δT	temperature uncertainty
C	constant
ΔE	energy gap
k	Boltzmann constant
T	Absolute temperature
κ	Thermal conductivity
L	size of a heat source
P	Power
ΔD	the shift in the transition frequency
α	temperature susceptibility

Abbreviations

Abbreviations

ACR	accumulation rate
AEP	2-aminoethyl dihydrogen phosphate
AIE	aggregation-induced emission
ATP	adenosine 5'-triphosphate
ATPase	adenosine 5'-triphosphatase
BAK	Bcl-2 homologous antagonist/killer
BAX	Bcl-2-associated X protein
BrdU	bromodeoxyuridine
BSA	bovine serum albumin
C2C12 cells	mouse myoblast cell
Ca^{2+}	calcium ion
CCCP	carbonyl cyanide 3-chlorophenylhydrazone
CDs	carbon dots
cGAS	DNA sensor cyclic GMP-AMP synthase
CL	cardiolipin
copolymer	$PEGMEMA_{80}$-*b*-$EGMP_3$ di-block copolymer
CQ	chloroquine
CTAB	cationic cetyltrimethylammonium bromide
cyt c	cytochrome complex
3,4-DHCA	3,4-Dihydroxyhydrocinnamic acid
DLS	dynamic light scattering
DMEM	Dulbecco's Modified Eagle Medium
DMF	N, N-Dimethylformamide
DMSO	dimethyl sulfoxide
DNA	deoxyribonucleic acid

Abbreviations

Drp1	dynamin-related protein 1
EDC	1-Ethyl-3-(3-dimethylamino-propyl)-carbodiimide
EdU	5-ethynyl-2'-deoxyuridine
EMCCD	Electron-multiplying CCD camera
ER	endoplasmic reticulum
Er	erbium
$ErCl_3 \bullet 6H_2O$	erbium chloride hexahydrate
F	floride
FBS	fetal bovine serum
FCCP	carbonyl cyanide 4-(trifluoromethoxy)phenylhydrazone
FNDs	fluorescent nanodiamonds
FPs	fluorescent proteins
G1 phase	Gap 1 phase during the cell cycle
G2 phase	Gap 2 phase during the cell cycle
Gd	Gadolinium
GQDs	graphene quantum dots
GFP	green fluorescent proteins
GTPase	guanosine triphosphatase
H strand	heavy strand in mtDNA
HCl	Hydrochloric acid
HeLa	cervical cancer cells
HEPES	N-(2-Hydroxyethyl)piperazine-N′-(2-ethanesulfonic acid)
Ho	holmium
INF2	inverted-formin 2
IO_4^-	periodate

L strand	light strand in mtDNA
LD	lipid droplets
Ln	Lanthanide
Lu	lutetium
M phase	mitosis phase during the cell cycle
MCF-7	Michigan Cancer Foundation-7
MES	2-(*N*-morpholino)ethanesulfonic acid
MFF	tail-anchored proteins mitochondrial fission factor
Mfn1	mitofusin 1
Mfn2	mitofusin 2
MiDs	mitochondrial dynamics proteins
MnO_2	Manganese(IV) oxide
MnO_4^-	permanganate
MTT	3-(4,5-Dimethylthiazol-2-yl)-2,5-Diphenyltetrazolium Bromide
mtDNA	mitochondrial DNA
mtSSB	mitochondrial single-stranded DNA-binding protein
n	refractive index
Na	sodium
NADH	nicotinamide adenine dinucleotide (reduced)
Nd	neodymium
N-GQDs	nitrogen-doped graphene quantum dots
NHS	N-Hydroxysuccinimide
NIR	near-infrared
$NOBF_4$	nitrosonium tetrafluoroborate

NV^-	negatively charged nitrogen-vacancy
OA	oleic acid
ODMR	optically detected magnetic resonance
O_H and O_L	origin sites for replication in each strand of mtDNA
Opa1	optic atrophy 1
PAA	Poly (acrylic acid)
PBS	phosphate-buffered saline
PDA	poly(dopamine)
PEG	4Arm-PEG-NH_2
PFA	Paraformaldehyde
PLL	poly-l-lysine
PMA	phorbol 12-myristate-13-acetate
PMHC18	poly (maleic anhydride-alt-1-octadecene)
PMT	photomultiplier tube
POLRMT	mitochondrial RNA polymerase
POLγ	DNA polymerase γ
POLγA	DNA polymerase γ catalytic subunit A
POLγB	DNA polymerase γ catalytic subunit B
PS	penicillin-streptomycin
QDs	quantum dots
RAFT	reversible addition fragmentation chain transfer
RGQDs	reduced graphene quantum dots
RMSD	root-mean-square deviation
RNA	ribonucleic acid
ROS	reactive oxygen species

Abbreviations

rRNAs	Ribosomal RNA
RSS	Residual Sum of Squares
S phase	DNA synthesis during the cell cycle
SA	streptavidin
sacro/ER	sarcoplasmic reticulum
SDS	anionic sodium dodecyl sulfate
SEM	scanning electron microscopy
siRNA	Small interfering RNA
STED	stimulated emission depletion
STING	stimulator of interferon genes
TEM	transmission electron microscopy
TEOS	tetraethyl orthosilicates
TFAM	mitochondrial transcription factor A
TFEB	transcription factor EB
THF	tetrahydrofuran
TIRF	total internal reflection fluorescence
TPP	triphenylphosphonium/(3-carboxypropyl)triphenylphosphonium bromide
tRNAs	Transfer RNA
TWINKLE	DNA helicase
UCNPs	upconversion nanoparticles
UCNPs@AEP	UCNPs coated with AEP
UCNPs@Alendronate	UCNPs coated with alendronate
UCNPs@copolymer (LysoDots)	UCNPs coated with $PEGMEMA_{80}$-*b*-$EGMP_3$ di-block copolymer

UCNPs@3,4-DHCA	UCNPs coated with 3,4-DHCA
UCNPs@SA	UCNPs@copolymer conjugated with SA
UCNPs@SiO_2	UCNPs coated with silica shell
UCNPs@dSiO_2	UCNPs coated with dense silica shell
UCNPs@mSiO_2	UCNPs coated with mesoporous silica shell
UCNPs@OA	UCNPs coated with OA
UCNPs@PEG	UCNPs@copolymer linked with 4Arm-PEG-NH_2
UCNPs@PDA	UCNPs coated with polydopamine
UCNPs@PEG@TPP	UCNPs@PEG conjugated with TPP
UCNPs@PLL	UCNPs coated with PLL
UCNPs@PLL@TPP (MitoDots)	UCNPs@PLL conjugated with TPP
UCNPs@SiO_2	UCNPs coated with silica shell
UV	Ultraviolet
WT-1 cells	mouse brown preadipocyte cell line
Y	yttrium
Yb	ytterbium
$YbCl_3$•$6H_2O$	ytterbium chloride hexahydrate
YCl_3•$6H_2O$	yttrium(III) chloride hexahydrate

Table of Contents

List of Figures

List of Figures

List of Tables

Abstract

Temperature plays a key role in regulating intracellular activities. Accurate measurements of temperature inside living cells at the nanoscale can tell if the cells are under their healthy physiological status or in dysfunctional diseases. As the energy factory and metabolism center, mitochondria constantly release heat during ATP production, which greatly impacts the intracellular organelles' temperature. A direct visualization platform with probes that can sense the *in situ* temperature dynamics of mitochondria, and map the temperature-related interactions among intercellular organelles, will facilitate our understanding of mitochondria-related diseases towards better therapy.

Upconversion nanoparticles (UCNPs), being excited by near-infrared (NIR) light to generate visible light, have been widely applied in the fields of single-molecule bioassays, super-resolution microscopy, and recently non-contact thermometers, due to their unique optical properties, including their exceptional photo-stability against photo-bleaching or photo-blinking, tunable multi-wavelength emissions for multiplexing assays, anti-Stokes' emissions to suppress autofluorescence background, near infrared excitation and emissions allowing deep-tissue penetration depth, and most importantly, temperature-dependent ratiometric luminescence for thermometry application. However, the chemical stability of hydrophilic UCNPs has limited their developments in biomedical applications.

To obtain the hydrophilic UCNPs ($NaYF_4$: 20%Yb^{3+}, 2%Er^{3+}) with excellent stability and dispersibility in aqueous physiological buffers, five different functionalization strategies have been systematically evaluated (chapter 2). To study the temperature dynamics of mitochondria, I developed a mitochondria-targeting UCNPs-based thermometer with a sensing sensitivity of 3.2% K^{-1} to monitor the temperature variations through the chemical stimulations. The cells displayed distinct response time and temperature dynamic profiles (chapter 3).

To further study the interaction between lysosomes and mitochondria, I updated the design of UCNPs-based thermometer by optimizing the surface functionalization of UCNPs, which resulted in an enhanced reliability with the relative temperature sensing sensitivity of 2.7% K^{-1} and temperature uncertainty of 0.8 K in HeLa cells. The new

probes can cascade target lysosomes and mitochondria, respectively (chapter 4).

Chapter 5 concludes this thesis by providing a thermometry platform to study the temperature dynamics of mitochondria and organelles' functional interactions under the physiological or pathological status. Combined with other state-of-the-art technologies, such as sequential labelling of mtDNA, super-resolution imaging, UCNPs-based thermometer will become a powerful multimodal probe for imaging, sensing, and therapy.

Chapter 1 **Introduction**

Temperature is one of the crucial biophysical parameters in most chemical reactions and biological processes within live cells. The variations of temperature reflect that the cell is under the physiological status or in diseases [1, 2]. Mitochondria, the powerhouse of mammalian cells, transform carbohydrates to ATP, releasing the heat simultaneously [3]. Moreover, it coordinates with other organelles, such as lysosomes, endoplasmic reticulum (ER) to maintain the homeostasis of the cell. At present, the roles of mitochondria and other organelles are usually investigated from the direct physical membrane contacts by super-resolution microscopy or signaling pathways by molecular biology tools [4]. It is not clear how the temperature change of mitochondria and other organelles during the pathological process. Therefore, studying intracellular temperature dynamics is necessary to understand how they maintain homeostasis within a live cell.

Nowadays, a series of nano- or micro- thermometers have been reported in the field of temperature sensing [2, 5]. Among these thermometers, luminescence-based thermometers that worked as non-contact probes have attracted great attentions in the field of nanomedicine and diagnosis. Non-contact thermometers provide the information of imaging and local temperature at a spatial and temporal resolution simultaneously. Due to the excellent luminescence properties of upconversion nanoparticles (UCNPs), this thesis put efforts on the development of UCNPs ($NaYF_4$: 20%Yb^{3+}, 2%Er^{3+})-based thermometers in the intracellular temperature mapping within a single cell. The thesis aims to build a UCNPs ($NaYF_4$: 20%Yb^{3+}, 2%Er^{3+})-based mitochondrial thermometry platform for multi-functional imaging, sensing, and even tracking the pace of life. Therefore, Chapter 1 first introduces the basic structure and function of mitochondria, and then provides a detailed review of the progress and advancement of luminescence-based thermometers and their applications. The method of surface functionalization of UCNPs ($NaYF_4$: 20%Yb^{3+}, 2%Er^{3+}) and how to obtain a mitochondria-targeted probe are illustrated at last.

1.1 Mitochondrial Form and Function

Mitochondria play an essential role in the eukaryotic organisms, which are tubular, highly dynamic organelles surrounded by two membranes. They produce ATP by digesting fat, carbohydrates, and protein. And they participate in numerous cellular activities, such as metabolites, differentiation, and apoptosis [6]. The dysfunction of mitochondria will lead to a range of diseases, including diabetes, neurodegenerative disease, cancer, and aging [6].

1.1.1 Basic Background of Mitochondria

Mitochondria evolved from bacterial endosymbiosis [7, 8]. Two billion years ago, a larger primitive, heterotrophic, eukaryotic cell engulfed an α-proteobacterium [7]. The eukaryotic cell developed a mutually beneficial relationship with the bacteria instead of digesting it [7]. Then the bacteria became mitochondria of the host cell. During the evolution, mitochondria still have the double membrane structure and respiratory cellular machinery as their ancestors, but their form and composition have changed. Most genes bacteria used for independent life are lost or transferred to the nuclear genome [9]. There are ~16-kilobase genomes remaining in the human mitochondria, encoding 13 respiratory complexes, two ribosomal RNAs, and 22 transfer RNAs [10]. The respiratory complexes are involved in the ATP synthesis and form an electrochemical gradient between the matrix and the inner membrane space of mitochondria. The electrochemical potential is crucial to reflect the functional status of mitochondria, sending the signal to activate pathways of repairing or eliminating defective mitochondria. The two ribosomal RNAs and 22 transfer RNAs in the matrix are crucial to mitochondrial translation, which is relatively complex and highly regulated [11]. They are involved in RNA coding and mature and the translation of ribosomal proteins. However, only some mitochondrial ribosomal proteins are homologs with bacteria [12]. The function of most ribosomal proteins is not clear.

The genome of the nucleus also encodes some mitochondrial proteins. The nucleus-encoded mitochondrial proteins are translated into the cytoplasm and imported to the mitochondria [13, 14]. The nuclear and mitochondrial DNA (mtDNA) coordinate to maintain mitochondrial function [15]. The mutations of mitochondrial protein-related genes in the nucleus and mitochondria will lead to mitochondrial dysfunction, causing

human diseases [16]. However, the relationship between the mitochondria and the disorder is not understood well currently. Therefore, a better understanding of mitochondria organization, mtDNA, mitochondria-related nuclear gene, mitochondrial proteins, and the intercoms of mitochondria with other cellular organelles is necessary.

1.1.2 Mitochondrial architecture and function

Mitochondria are commonly between 0.75 and 3 μm in diameter with a double membrane composed of phospholipids and proteins. It has five distinct compartments, including the outer membrane, intermembrane space, inner membrane, cristae, and the matrix (**Figure 1-1**). The structure of mitochondria closely links to mitochondrial function.

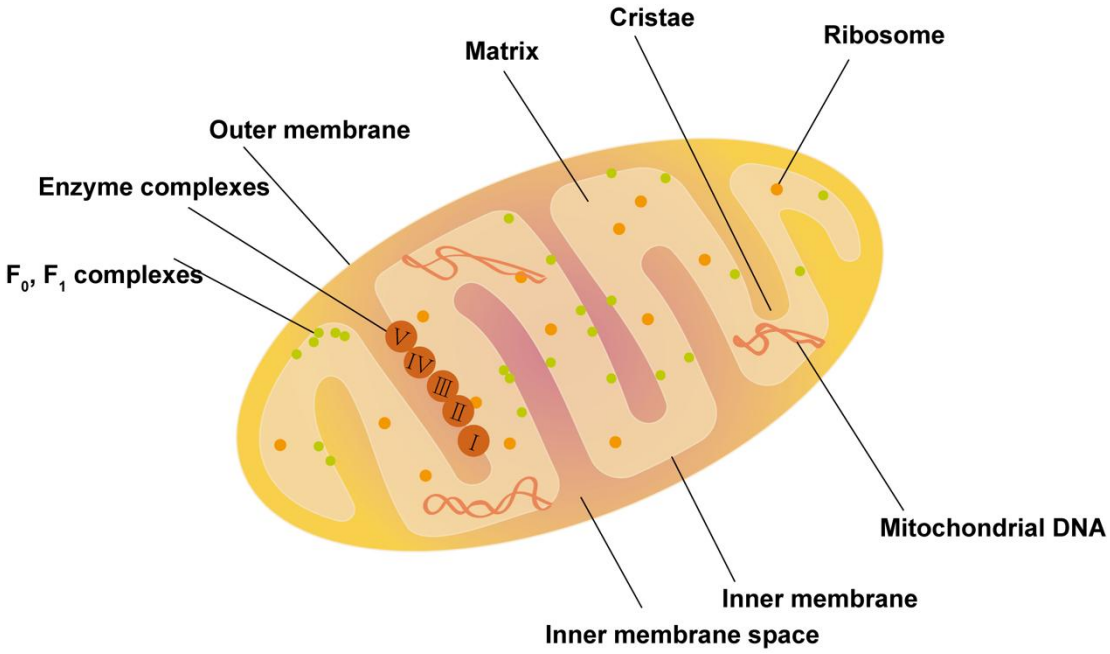

Figure 1-1 The architecture of mitochondria. *Complex I, II, III, IV, and V are located in the inner mitochondrial membrane and are responsible for ATP production. The matrix contains DNA, ribosomes, RNA, and proteins.*

The outer mitochondrial membrane has similar components to the cell membrane, separating the organelle from the cytosol [17]. The materials exchanged between mitochondria and cytosol are achieved by the proteins in the outer membrane. Voltage-dependent anion channels, also called mitochondria porins, are transporting smaller molecules, such as nucleotides, ions, and metabolites in the mitochondria and cytosol [18]. For the larger molecules (>5000 Daltons), the translocase in the mitochondrial

membrane actively moves the larger nucleus-encoding proteins into the mitochondria [19]. There is also a wide range of enzymes in the outer membrane involved in metabolism [17]. The permeabilization of the mitochondrial outer membrane will lead to the proteins enclosed in the mitochondria leaking to the cytosol, causing cell death [20].

The intermembrane space is the space between the outer and inner membranes. The most vital protein localized in the intermembrane space is the cytochrome complex (cyt c), which is the sign of apoptosis [21]. At the early stage of apoptosis, the oxidation of cardiolipin (CL) triggers the leaking of mitochondrial cyt c from mitochondria. Then the released cyt c will interact with the other organelles and start apoptosis [22]. Therefore, cyt c in the cytosol can work as a biomarker to evaluate the anti-tumor efficiency of the drug [23, 24].

The composition of the mitochondrial inner membrane is a bit different from the mitochondrial outer membrane, which is full of CL [25]. And the ratio of protein-to-phospholipid is higher than that of the outer membrane [26]. Moreover, there are no porins in the mitochondrial inner membrane [17]. Therefore, the mitochondrial inner membrane is highly impermeable. All molecules must be transported by the translocase to exchange between the mitochondrial matrix and cytosol [19]. In addition, there is an electrochemical potential across the inner membrane formed by the electron transport chain [17]. The electron transport chain contains five important proteins, including complex I [27], complex II [28], complex III [29], complex IV [30], and Complex V [31]. As an electron donor, NADH passes the electron to complex I. Then, coenzyme Q receives the electrons from complexes I and II and passes the electron to complex III. The cyt c in the intermembrane space receives the electron from complex III and further transfer it to complex IV, which reacts with molecular oxygen and produce H_2O [17]. During this process, protons released into the intermembrane space will be ferried to the matrix and react with ADP to synthesize ATP by ATP synthase.

The mitochondrial inner membrane folding inside forms cristae **(Figure 1-1)**. The cristae increase the area of the mitochondrial inner membrane, enhancing the ability to produce ATP [17]. Therefore, the liver and muscle cells requiring large amounts of energy for cellular activities usually have more cristae.

The space enclosed by the inner membrane is called the matrix. The mitochondrial matrix contains many biomolecules, such as DNA, RNA, enzymes, and ribosomes. Therefore, the matrix provides a space for many important reactions, including the production of ATP, citric acid cycle, oxidative phosphorylation [32].

1.1.3 Mitochondrial dynamics

Mitochondria are highly dynamic organelles [33]. They form complex and tubular networks in the live cell (**Figure 1-2 centre**). The mitochondria networks respond to the cellular function by changing the shape, size, number, and distribution of mitochondria and be identified as mitochondrial dynamics [34].

1.1.3.1 Fission and Fusion

Mitochondrial dynamics are dependent on the fusion, fission, shape transitions, and transportation along the cytoskeleton (**Figure 1-2**) [34, 35]. The mitochondrial shape changes with time and locations in a single cell [36, 37]. For example, the shape of mitochondria prefers to be tubular in the G1-phase and then elongates in the S-phase [33] (As shown in **Figure 1-3**, the cell cycle of a cell contains four stages: Gap 1 (G1), synthesis (S), Gap 2 (G2) and mitosis (M). The cell size increases in the G1 phase. The DNA replicates in the S phase. Then the cell prepares to divide in the G2 phase and divides in the M phase. After a cell cycle, the cell divides into two daughter cells.). When the cell cycle goes into the G2 and M-phase, mitochondria divide into granules or short rods [38]. In addition, mitochondria with different shapes will face different fates [36]. As reported by Suliana Manley group in 2021, they found that for the fission site in the mid-zone of mitochondria, then the large and tubule daughter mitochondria prefer to go to proliferation while the fission site in the peripheral, then the smll and rounded daughter mitochondria prefer to go to degradation [36]. In addition, the mitochondrial shape transforms by increasing the concentration of intracellular calcium and mitochondrial depolarization [39]. As a result, these two stimulations induce the production of small and rounded mitochondria.

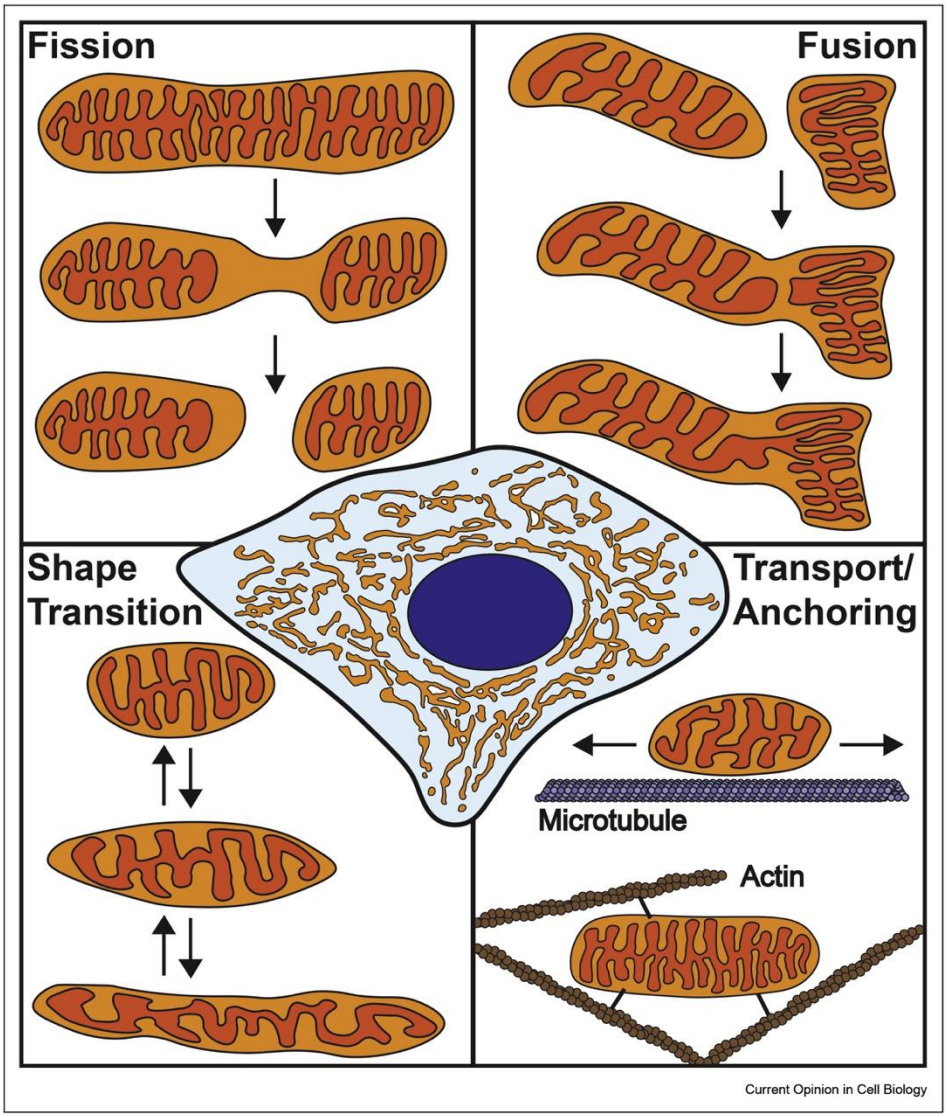

Figure 1-2 Overview of mitochondrial dynamics. *Mitochondria form a complex, interconnected network within the cell (centre). The morphology of this network is determined by fission, fusion, mitochondrial shape transition, and positioning along the cytoskeleton. Adapted with permission from reference [34].*

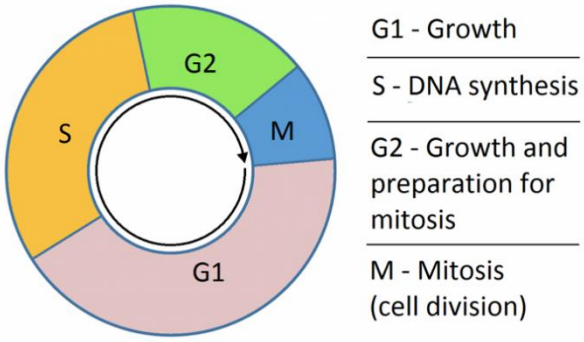

Figure 1-3 Schematic representation of the cell cycle in the eukaryotic cell. *The pink color represents the G1-phase. The yellow color represents the S-phase. The green color represents the G2- phase. The blue color represents the M-phase [https://teachmephysiology.com/biochemistry/cell-growth-death/cell-cycle/].*

Mitochondrial fission and fusion are two opposite processes [34]. The balance between these two dynamic transitions is required to maintain mitochondrial function and respond to the cellular environment, such as nutrients and stress [40]. Mitochondrial fission includes two stages, constriction and scission (**Figure 1-4**). Dynamin-related protein 1 (Drp 1) plays a crucial role in the constriction stage [41]. Drp 1 is recruited in the fission site to facilitate constriction [41-43]. At first, replicated mtDNA and contacts between the endoplasmic reticulum (ER) and mitochondria mark the fission site (**Figure 1-4A-B**). Then Drp 1 is recruited from the cytoplasm to the outer membrane of mitochondria, inducing the constriction of the membrane (**Figure 1-4C-D**). As for the mitochondria scission, Dnm2 is recruited to the constriction sites to finalize the last step of the mitochondrial division (**Figure 1-4E-G**)[44]. Dnm 2 is the downstream protein of Drp 1. It is recruited to the constriction site induced by the ER-mitochondria contacts and Drp 1, forming a collar-like structure around the constriction site [45]. Silencing RNA of Dnm 2 will cause the appearance of myriads elongated super narrow mitochondrial constriction sites [45].

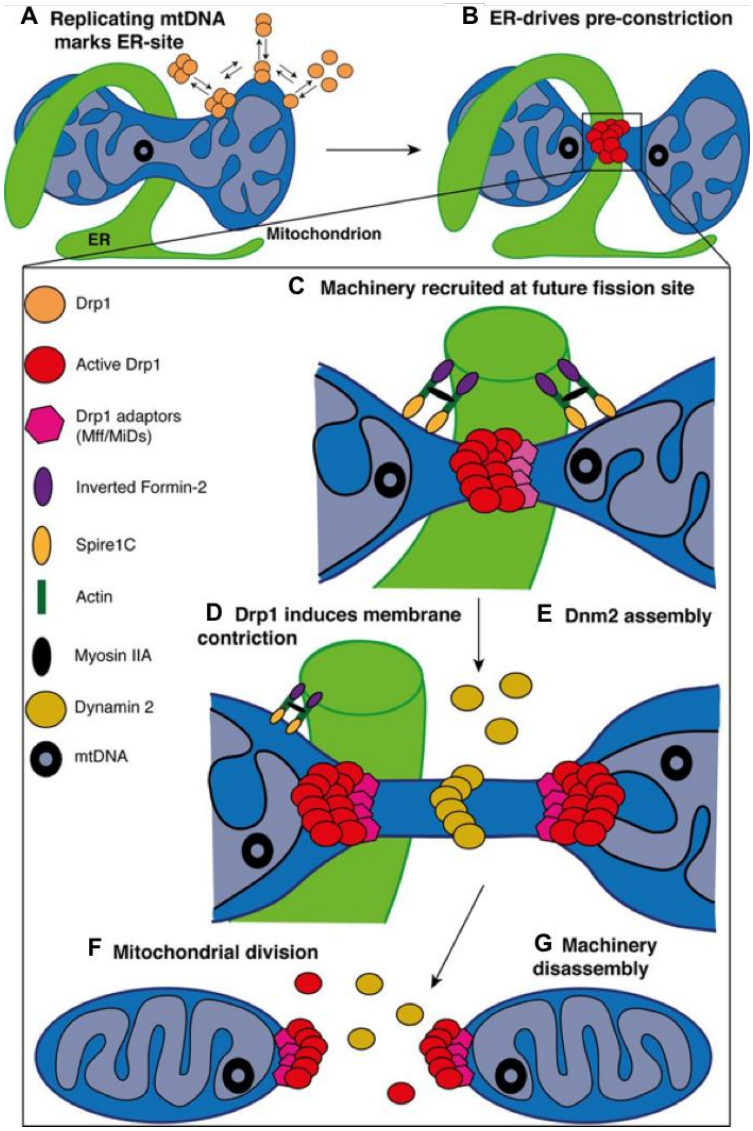

Figure 1-4 Schematic representation of the multi-step processes required for mitochondria division. *A. In the matrix, replicated mtDNA marks the site for ER recruitment. B. The active Drp1 accumulate at ER sites to initiate the pre-constriction of the membrane. C. The zoomed area highlights the factors regulating mitochondrial division. The ER-bound inverted-formin 2 (INF2) and mitochondrial anchored formin-binding Spire1C induce actin nucleation and polymerization at mitochondria–ER contact sites. The Myosin IIA may provide the mechanical force to drive mitochondria pre-constriction. At these sites, tail-anchored proteins mitochondrial fission factor (MFF) and mitochondrial dynamics proteins (MiDs) recruit Drp1 and D. GTP-hydrolysis leads to a conformational change, enhancing pre-existing mitochondrial constriction. E. Then, Dnm2 is recruited to Drp1-mediated mitochondrial constriction neck where it assembles and terminates membrane scission, F. leading to two daughter mitochondria. G. The mechanisms of disassembly of the fission machinery following division remain unclear but both adaptors and Drp1 are found at both mitochondrial tips after division. Adapted with permission from reference [46].*

Mitochondria fusion is regulated by mitofusin 1 (Mfn1), mitofusin 2 (Mfn2), and optic atrophy 1 (Opa1) [47, 48]. Opa1 has two different isoforms L-OPa1 and S-OPa1, which are responsible for the various function in the fusion [49]. At the start of mitochondria fusion, Mfn1 and Mfn2 regulate the tethering of mitochondria and promote the fusion of mitochondrial outer membrane (**Figure 1-5A(1)**). Once the outer membrane fuse with each other, the position of the inner membrane will face each other and prepare to fuse (**Figure 1-5A(2)**)[47, 50]. Then the L-OPa1 and CL located in the mitochondrial inner membrane bring the mitochondria closer, and S-OPa1 works together with L-OPa1 and CL to finalize fusion activity (**Figure 1-5A(3)-(4)**). The molar ratio of L-OPa1 and S-OPa1 determines the fate of fusion. When the ratio of L-OPa1/ S-OPa1 is 1, the fusion efficiency will be highest (**Figure 1-5B**)[34]. The ratio of L-OPa1/ S-OPa1 is lower or higher than one, leading to the inhibition of fusion [34].

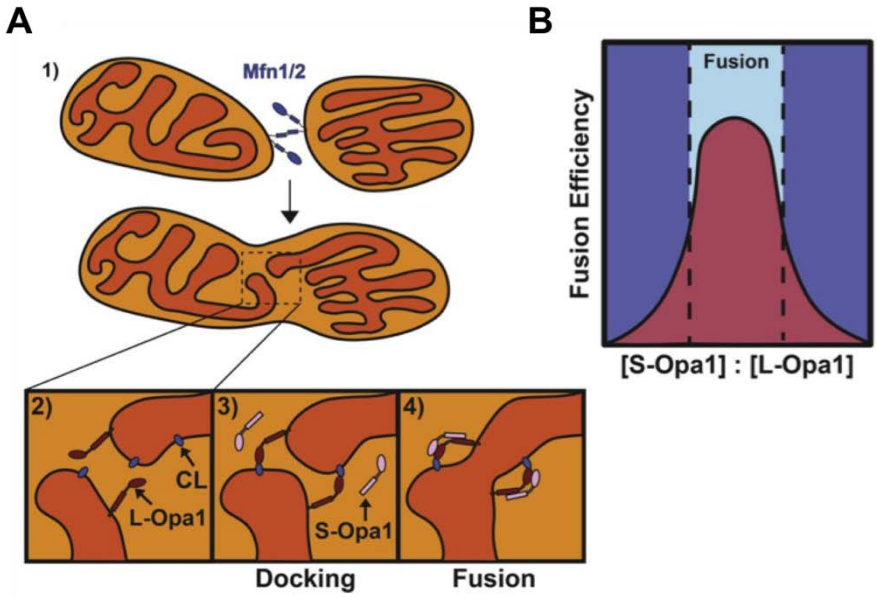

Figure 1- 5 Schematic representation of the multi-step processes required for mitochondria fusion. *A. The proposed model of mitochondrial fusion. 1) Mitochondrial fusion begins with Mfn1/2-mediated tethering of two mitochondrial outer membranes. 2) The inner membranes are positioned for fusion upon outer membrane fusion. 3) Interactions between L-Opa1 and CL dock the inner membranes, bringing them closer together. 4) S-Opa1 functions with L-Opa1 and CL to promote efficient inner membrane fusion. B. Fusion efficiency at different S-Opa1: L-Opa1 ratios. Fusion efficiency peaks at an equimolar ratio of S-Opa1 to L-Opa1, with higher and lower ratios inhibiting fusion. Adapted with permission from reference [34].*

In addition, mitochondrial networks have interacted with the cytoskeleton [51]. Mitochondria driven by motor proteins move to the plus-end microtubules or the minus-end microtubules [52]. Cytoskeleton-controlled mitochondria transportation plays a crucial role in neurons. In mammalian neurons, the stability of mitochondrial networks is regulated by actins [53]. The actins tether the mitochondria at presynaptic sites in axons to provide energy for neurotransmission [54, 55].

1.1.3.2 Contacts with other organelles

Mitochondria play a critical role in cellular activities, such as ATP production, metabolism, and signalling. It also communicates with other organelles through membrane contacts to maintain the homeostasis of cells. Mitochondria coordinate with ER, lysosomes, lipid droplets (LD), nucleus to regulate cellular processes, including energy metabolism, biosynthesis, immune response, and cell turnover (**Figure 1-6**) [56, 57].

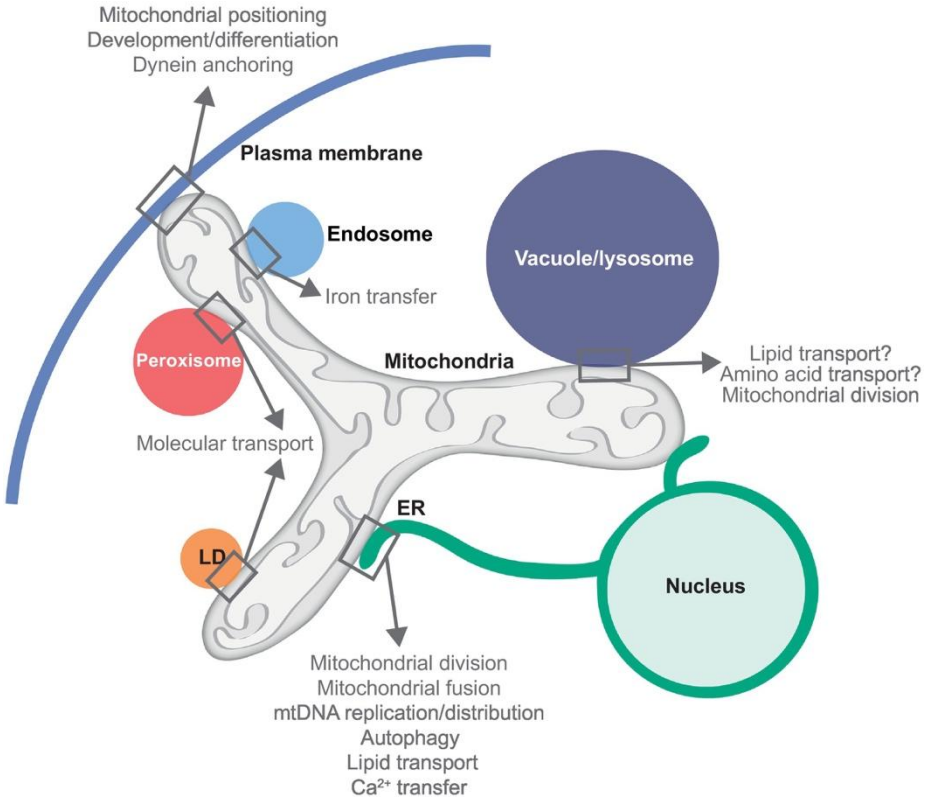

Figure 1-6 Schematic of mitochondria–organelle contacts and functions. *Mitochondria make functionally relevant contact with many organelles in the cell. A subset of mitochondria–organelle contacts and the functions ascribed to these contacts are shown. Adapted with permission from reference [57].*

1.1.3.2.1 Contacts with endoplasmic reticulum

Among the organelles, mitochondria have a closed interaction with ER. Because of the distinct membrane structure, mitochondria and ER contact frequently but do not fuse. The ER-mitochondria contact sites have been found by researchers using fluorescent microscopy and electricity microscopes [56]. Nunnari and her colleagues found that ER-mitochondria contact sites decided the fission sites during the mitochondrial fission process by fluorescent microscope [58]. Moreover, the contacts between ER and mitochondria are very stable, even when they move along the cytoskeleton [59]. These frequent ER-mitochondria contact sites make ER and mitochondria coordinate in a wide range of cellular functions, including Ca^{2+} signalling, phospholipids synthesis, and cellular stress [60]. The homeostasis of Ca^{2+} plays a crucial role in many biological processes. Mitochondria obtain Ca^{2+} from the cytoplasm by the mitochondrial membrane protein. However, the efficiency of Ca^{2+} transportation by mitochondrial membrane protein is very low. Thus, mitochondria also get Ca^{2+} from ER-mitochondria contacts. The disturbance of Ca^{2+} concentration will lead to cell death [61, 62]. Besides, the phospholipids are mainly synthesized in the ER and transported by the vesicles. The transportation of phospholipids from ER to mitochondria is controlled by the ER-membrane contacts [63]. There are many enzymes in the ER-membrane contact sites, which regulate lipid metabolism [61]. In addition, the process of ER response to the cellular stress by unfolded protein response also needs the coordination of mitochondria. The unfolded protein response recognizes misleading proteins and helps the cell restore from disorders to physiological states [60].

1.1.3.2.2 Contacts with lysosomes

The abnormal mitochondria will lead to the dysfunction of lysosomes [64, 65]. Mitochondrial transcription factor A (TFAM) is a crucial protein to participate the mtDNA replication and maintain the stability of mtDNA [10, 66]. The deficiency of TFAM leads to the loss of mtDNA and further affects the respiratory chain reaction [45]. Baixauli *et al.* deleted the gene of TFAM in the lymphocytes and found the behaviour of lysosomes changed simultaneously [67]. There were many autophagy intermediates accumulated in the cytoplasm, indicating the dysfunction of lysosomes [67]. The dysfunctional mitochondria will go to the degradation by lysosomes through mitophagy. Mitophagy signalling induces the biogenesis of lysosomes, which are regulated by

the transcription factor EB (TFEB). To explore if the mitophagy will lead to the biogenesis of lysosomes, Catherine L. Nezich and the colleagues treated the HeLa cells with ATP synthase inhibitor oligomycin and the complex III inhibitor antimycin A for 10 hours to induce the dysfunction of mitochondria, and they found most TFEB translocated to the nucleus, which was an essential feature for the lysosomal biogenesis [68]. Moreover, the lysosomal function and the morphology changed when the gene of mitochondrial protein apoptosis-inducing factor was deleted [69]. Julie Demers-Lamarche and colleagues found that lysosomal malfunction relied on reactive oxygen species [69]. In addition, the defects in the lysosome will contribute to mitochondrial dysfunction. In the lysosomal storage disease, the mitochondrial function is abnormal. This is because the abnormal mitochondria cannot be cleared by lysosomes, leading to pathological signalling [70].

Moreover, both mitochondria and lysosomes participate in Ca^{2+} regulation. Ca^{2+} is transported by mitochondrial transmembrane protein from the cytoplasm into mitochondria [71]. The Ca^{2+} in the mitochondria are involved in the respiration chain reaction and the production of ATP [72]. This is because four kinds of mitochondrial dehydrogenases are activated by Ca^{2+} [72, 73]. Moreover, Ca^{2+} plays a crucial role in the regulation of cell death by inducing apoptosis or necrosis in the mitochondria [74]. Ca^{2+} in the lysosome participates in many cellular signalling processes, such as autophagy [75], membrane fusion [76], and cell death [77]. Most importantly, protein TFEB can be activated by the Ca^{2+}, and then the activated TFEB controls the expression of mitochondrial fatty acid β [78, 79] and further regulate ATP production in the mitochondria [80].

In mammalian cells, lysosomes work as a degradation centre, digesting macromolecules into free amino acids, sugar, and lipids for biosynthesis and energy production [4]. However, mitochondria, work as a metabolism centre, making use of small molecules to produce energy. From the metabolic view, mitochondria and lysosome crosstalk with each other in the function as they coordinate the metabolites degradation, transportation, and production.

1.1.3.2.3 Contacts with peroxisomes

Peroxisomes are small and dynamic organelles with a single membrane in the live cells. The number, morphology, and function of peroxisomes respond to the different status of cells [81]. The dynamic characteristic of peroxisomes provides the basis to cooperate with other organelles to participate in many crucial biological processes, such as biosynthesis and signalling induction. Peroxisomes have a closed interaction with mitochondria in the process of lipids metabolism, ROS (reactive oxygen species) balance, and invasion resistance by membrane contact sites, vesicle transportation, and signalling [82]. The dysfunction of peroxisomes will lead to mitochondrial diseases [81].

1.1.4 Mitochondrial DNA (mtDNA) and dysfunction

Mitochondrial DNA (mtDNA) is a small circular double-stranded DNA containing 16.6 kb. One is a heavy strand (H), and the other one is a light strand (L). The difference between these two strands is their base composition [83]. The H strand is being rich in guanines [83]. The protein required in the mtDNA replication is distinct from nuclear DNA replication. DNA polymerase γ (POLγ) is the replicative polymerase responsible for DNA replication in the mitochondria [84]. POLγ is a highly accurate DNA polymerase with a frequency of misincorporation lower than 1×10^{-6} [85]. Another crucial protein in mtDNA replication is DNA helicase TWINKLE. During the replication, TWINKLE unwinds the double-stranded DNA into single-stranded DNA [86]. Therefore, POLγ can start replication with single-strand DNA as a template. Thus, mitochondrial single-stranded DNA-binding protein (mtSSB) binds to the newly formed single-strand DNA and protects mtDNA from nucleases digestion or secondary structure formation [87]. As an intermediate, mtSSB enhances the activity of TWINKLE and increases the processivity of POLγ [86].

How mtDNA replicates in mammalian cells? The strand-displacement model was first proposed in 1972 by Vinograd [88]. There is an origin for replication in each strand, O_H and O_L. The replication starts from O_H and synthesizes a new strand H. mtSSB binds to the parental H-strand to avoid RNA synthesis on the displaced strand by mitochondrial RNA polymerase (POLRMT) [89]. When the replication passes through the origin of L-strand (O_L), parental L-strand forms a stem-loop structure, blocking the mtSSB binding and providing accessibility for POLRMT to initiate RNA synthesis [90-92]. POLγ enables to replace POLRMT and start the L-strand synthesis [91]. The two strands synthesis are continuous and linked to each other as the initiation of H-strand DNA

synthesis is required for the start of L-strand synthesis (**Figure 1-7**) [93].

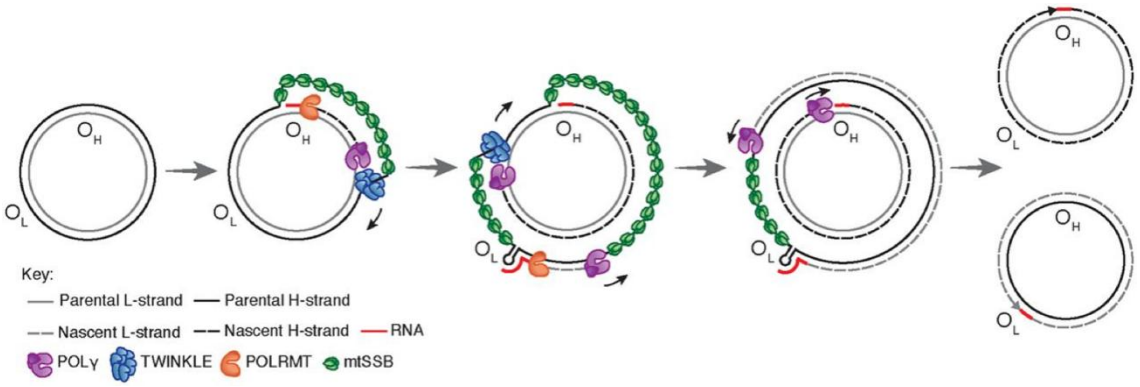

Figure 1-7 Replication of the human mitochondrial genome [83].

The newly synthesized mtDNA are packaged into nucleoids by TFAM in mitochondria. TFAM is an essential protein in the mtDNA nucleoids. It binds to mtDNA without sequence specificity and packages mtDNA into nucleoids [10]. Simply mixing TFAM and mtDNA in vitro can form nucleoid-like particles [94]. In addition, TFAM participates in the mitochondrial transcription machinery [95]. Researchers usually study the mtDNA integrity by imaging the activity of TFAM in the living cell or fixed cell by fluorescent microscopes [96]. Compared with the nucleus genome, mtDNA is less protective and easier to be mutant as there is no histone binding to the mtDNA. And the studies show the replication mode of mtDNA provides more chances for mutation [97]. Moreover, the mtDNA replicate all the time while the nucleus genome replicate across the cell cycle, which means higher replication frequency makes mtDNA easy to mutant. In addition, the DNA repair mechanism of efficacy is lower than that of the nuclear DNA repair systems [98]. Dysfunctions of mtDNA integrity are related to a wide range of diseases, such as neurodegenerative and senescence-linked disorders, cancer, diabetes, and cardiovascular diseases [6, 7]. One of the possible results is the increase of ROS levels. The excess of ROS impairs mitochondrial function and further influences cellular activities, such as signalling, ATP generation, and apoptosis. Edward R. Sauter and his colleagues found there were large-scale mtDNA deletion mutations in human breast cancer [99]. Judd M.Aiken's group illustrated that mtDNA mutation accumulated in aged human skeletal muscle fibers [100]. Bielas *et al.* analyzed the total deletion load in the brain tissue with a new tool termed 'Digital Deletion Detection' and found that the total mtDNA deletion load increased with the age [101]. That's why older people easily get neurodegenerative diseases, such as Alzheimer's disease [102].

1.2 Intracellular Luminescence Thermometers

Luminescence thermometry is a technique that can measure the local temperature by monitoring the nanoscale materials' optical signal changes. Its spatial resolution is typically limited by the optical resolution of the system, and when a super resolution imaging technique may be applied, its resolution can be extended from microscale to nanometre scale. Luminescence thermometry has been applied for temperature measurements in live cells [103].

Motivated by the advance of material science and photonics, the field of intracellular thermometry has developed fast, achieving numerous discoveries in biology [2]. For example, Seiichi Uchiyama and his colleagues monitored the temperature change across the cell cycle and found the temperature gap between nucleus and cytoplasm was dependent on the cell cycle [104]. Moreover, this temperature gap became smaller in the S/G2-phased cells than in the G1 phase [104]. It is well-known that temperature is one of the most crucial biophysical parameters in any Biosystems. The dynamics and properties of the living organism are highly dependent on the temperature. The biomolecules, such as proteins, will suffer denature process when the temperature of the organisms is lower or higher than 37 °C [105]. Therefore, the development of intracellular thermometers is vital to elucidate the foundation of biological reactions by simultaneously monitoring the dynamics and temperature variation.

In the past decades, a myriad of luminescence intracellular thermometers, including Aggregation-Induced Emission (AIE) dots [106, 107], carbon-based fluorescent temperature probes [104, 108-111], organic dyes [112, 113], UCNPs [114, 115], quantum dots (QDs) [116, 117], fluorescent proteins (FPs) [118, 119], and hybrids complex [120, 121], has emerged to study the temperature variation in living cells. These non-contact luminescence thermometers show great potential in the temperature detection of fluidics [122], catalytic systems [123], microelectronic device [124], living cells [115, 118], and animals [125]. However, with the rapid development of intracellular luminescence thermometers, the reliability issue of thermometry techniques as well as the discrepancy between the experimental results and theoretical calculations has been raised by Baffou et al [126]. Baffou et al argued that a single cell could not substantially increase the temperature by endogenous thermogenesis and the

temperature variation measured by the thermometers came from the artefacts of the system [126]. Therefore, a large number of researchers put effort into making the temperature readouts reliable by improving the sensitivity and resolution of thermometers. In this part, I will illustrate the working principles of intracellular luminescent thermometers and further introduce recent progress in biomedical application. The physiological meaning of temperature detection in living organisms will be discussed at last.

1.2.1 Mechanism of intracellular luminescence thermometers

Luminescence is the emission of light from a given substance, occurring from electronically excited states that have been populated by an external excitation source (optical radiation, in the case of photoluminescence) [127]. The photon emission process of luminescence thermometers is strongly dependent on the temperature. Thus, the thermal imaging of materials is obtained by evaluating the relationship between local temperature and luminescence properties. Temperature readouts can be typically extracted from six physical parameters, including intensity, intensity ratio, lifetime, spectral position, optically detected magnetic resonance (ODMR), and polarization (**Figure 1-8**) [2].

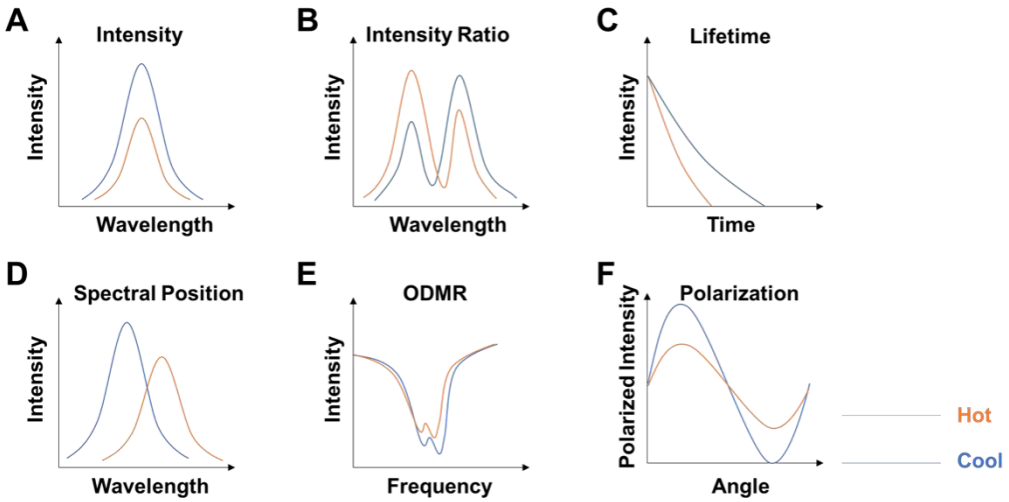

Figure 1-8 Schematic representation of the typical temperature-sensing strategies relying on A. Intensity, B. Intensity Ratio, C. Lifetime, D. Spectral position, E. ODMR, and F. Polarization. *Yellow lines correspond to the higher temperature and blue lines correspond to lower lines. Adapted with permission from reference [2].*

1.2.1.1 Intensity Luminescence Thermometry.

The readouts of temperature are obtained from the intensity of a specific band or wavelength (**Figure 1-8A**). For example, in some organic dyes, the fluorescence intensity will decrease when the local temperature elevates [128]. Some polymer-based luminescent thermometers show a distinct profile [129]. These temperature probes are composed of temperature-responsive dyes and nanogel. When the temperature increases, the nanogel will shrink and lose water molecules. Thus the dyes in the nanogel will be brighter [129]. However, the intensity-based luminescent thermometers is not very reliable because it can be affected by the heterogeneous distribution in the living cells or organisms, migration, bleaching, and excitation power [2].

1.2.1.2 Ratiometric Luminescence Thermometry.

In this case, the temperature readouts are according to the ratio of intensities from two emission wavelengths (**Figure 1-8B**). It is a powerful approach to mapping intracellular temperature variations because the ratio of two peaks is independent of the concentration of probe and focus drift [127]. Lanthanide ions are good candidates used for ratiometric thermometry, as they have abundant energy levels. Typically, the temperature is inferred by measuring the intensities from two energy levels in thermal equilibrium [130]. The temperature scale is based exclusively upon the validity of the Boltzmann distribution and this nonempirical procedure was documented initially for the $^2H_{11/2} \rightarrow {}^4I_{15/2}$ and $^4S_{3/2} \rightarrow {}^4I_{15/2}$ Er^{3+} transitions [131, 132] The energy gap between $^2H_{11/2}/^4S_{3/2}$ Er^{3+} is ~800 cm^{-1}, permitting the $^2H_{11/2}$ level to be populated from $^4S_{3/2}$ by thermal agitation [133]. Apart from Er^{3+}, other lanthanides can also work as a thermometer based on the luminescence intensity ratio, such as Nd^{3+} ($^4F_{7/2}$ and $^4F_{3/2}$ states), Sm^{3+} ($^4G_{7/2}$ and $^4G_{5/2}$ states), and so on [134]. In 2010, Vetrone *et al.* used $NaYF_4$:Er^{3+}, Yb^{3+} in intracellular temperature sensing [135]. Sedlmeier *et al.* investigated the temperature-dependent properties of $NaYF_4$ nanoparticles doped with Yb^{3+}, X^{3+} (X^{3+} = Er^{3+}, Ho^{3+}, and Tm^{3+}) and reported that nanoparticles UCNPs of $NaYF_4$: Yb^{3+}, Er^{3+} is a better choice for temperature measurements in physiological range from 293 K to 318 K [136]. The ratio of green luminescent intensities emitting from Er^{3+} doped in the $NaYF_4$ matrix is sensitive to the temperature and governed by the Boltzmann equation:

$$\frac{I_{525}}{I_{545}} = C\exp\left(-\frac{\Delta E}{kT}\right) \quad (1)$$

where I_{525} and I_{545} are the integrated intensities of around 525 nm and 545 nm emission peaks, respectively, C is a constant, ΔE is the $^4S_{3/2}$ to $^2H_{11/2}$ energy difference of the Er^{3+} ion, k is the Boltzmann constant, and T is the absolute temperature [135]. The NIR excitation of the upconversion process inhibits the autofluorescence from biological sample and reduces photodamage to cells, tissues, and animals. Hexagonal phase $NaYF_4$ has been considered as the most efficient upconversion host and been widely investigated with mature synthesis methods to control its morphologies and size as a nanoparticle. Therefore, in this thesis we will focus on using UCNPs (β-$NaYF_4$: Yb^{3+}, Er^{3+}) as the luminescent thermometer.

1.2.1.3 Lifetime Luminescence Thermometry.

Lifetime is also a reliable parameter in the temperature readouts as it is not affected by the concentration of sensors, environmental viscosity, or the excitation power (**Figure 1-8C**). Therefore, lifetime-based thermometers is widely used for intracellular temperature mapping. For example, with the temperature increased from 2 to 80 ºC, the photoluminescence lifetime of carbon dots decreased from 11 to 5.3 ns [137]. However, the polymeric luminescent thermometer showed an increase in a lifetime with the temperature increased [104].

1.2.1.4 Spectral-Position Luminescence Thermometry.

In this case, the temperature readouts are obtained from the position of emission spectral (**Figure 1-8D**). It is highly dependent on the material itself but independent of the probe concentration. Commonly, the spectral shift of QDs is responsive to the temperature. Yang *et al.* investigated the heat generation under the stimulations of Ca^{2+} stress and cold shock in living NIH/3T3 murine fibroblast cells by spectral shifts of QDs [138].

1.2.1.5 Optically detected magnetic resonance (ODMR)

Measuring the ODMR to provide a readout of the local temperature is commonly applied in the luminescent nanodiamonds (FNDs)-based thermometers. FNDs contains negatively charged nitrogen-vacancy (NV^-) centres. The zero-field splitting D_0 of the NV^- centre in FNDs is temperature-dependent. The ODMR spectra are fitted with a double Lorentzian function (**Figure 1-8E**), and the changes in temperature are

extracted according to the equation,

$$\Delta T = \frac{\Delta D}{\alpha} \qquad (2)$$

where ΔD is the shift in the transition frequency and α = dD/dT = −74 kHz/K is the temperature susceptibility [139, 140].

1.2.1.6 Fluorescence Polarization Anisotropy.

The temperature readouts are obtained from the polarization anisotropy. The polarization anisotropy is related to the molecular rotation caused by Brownian motion. The Brownian motion of the fluorophores accelerates with the temperature increasing. The more re-emitted photons will lose the memory of the incident light polarization. Therefore, high temperatures will lead to a decrease in polarization anisotropy (**Figure 1-8F**). Most importantly, polarization anisotropy is independent of the concentration of probes, migration, and photo-bleaching [118]. Many green fluorescent proteins and dyes-based thermometers achieve temperature sensing by polarization anisotropy [118].

1.2.2 Development of intracellular luminescence thermometers

To shed light on the thermal dynamics of intracellular activities, a collection of temperature-sensitive probes has been developed, benefiting from the advance physicochemical synthesis routes and state-of-the-art imaging techniques (**Figure 1-9**).

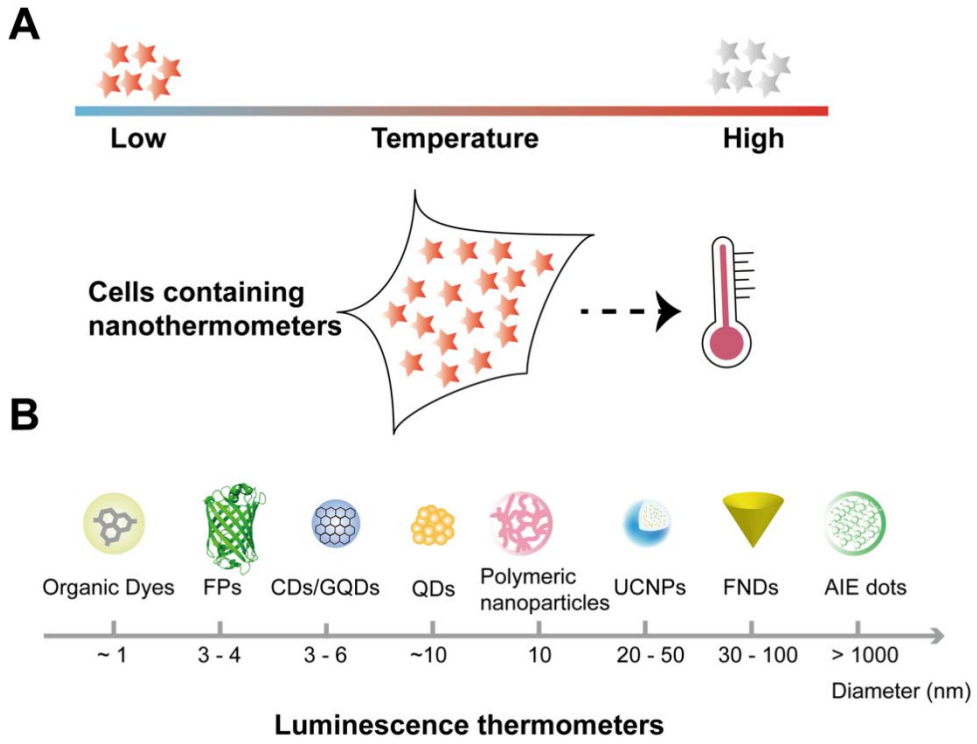

Figure 1-9 Schematic drawing of intracellular luminescence thermometers. *A. The representation of luminescence thermo-sensors in the cell. The thermometers can be introduced to the living cells by incubation or microinjection. The physical properties of luminescence thermometers will change with the temperature variation. B. Intracellular luminescence thermo-sensors with variable sizes, which are made by organic or inorganic materials.*

- **Dyes-based fluorescent thermometers**

Dyes are fluorescent chemical compounds with a small molecular weight, which emit light under excitation. It is commonly used to stain substructures in the cells and tissues and further be analyzed by fluorescent imaging or spectroscopy because dyes can disperse in the cell easily and achieve organelle targeting. The absorption and emission spectral of dyes are determined by the substituents of compounds [141]. Especially, there is a class of dyes, which of the spectral properties are sensitive to the temperature variation. The free rotation of substituents in the dyes leads to the temperature-dependent property. The quantum yield of dyes increases with temperature decreases. One of the most classical temperature-dependent dyes is Rhodamine B [128]. The fluorescent intensity of Rhodamine B reduces when the local temperature is elevated, indicating that Rhodamine B is a kind of intensity-based fluorescent thermo-sensors (**Figure 1-8A**) [128]. However, the intensity-based thermometers are easily affected by

the concentration of thermometers, thus it is difficult to repeat the results in separate experiments. Then the researchers developed dyes-based ratiometric fluorescent thermometers. It is composed of two units. One is the temperature-sensitive unit, and the other one is the temperature-insensitive unit. The temperature-independent unit works as a reference probe to eliminate the influence of concentration. Mitsumasa Homma *et al* report the first dyes-based ratiometric thermo-sensor by linking Rhodamine A and CS NIR dye and investigating the mitochondrial temperature variation under FCCP stimulation in living cells [142]. Nevertheless, there are still many problems related to the dyes-based thermometers as dyes are easy to be photo-bleached and can be affected by the autofluorescence from the biological sample. Most importantly, dye-based fluorescent thermo-sensors are less sensitive [143].

- **Polymeric nanoparticles-based fluorescent thermometers**

Polymeric nanoparticles-based fluorescent thermometers commonly consist of a temperature-sensitive unit and a water-sensitive fluorescent molecule. In 2009, Gota *et al.* developed the first intracellular thermometer using the fluorescent nanogel [129]. The water-sensitive fluorophores are packaged into the interior of temperature-sensitive nanogel. At low temperatures, the nanogel absorbs the water, and then the fluorophores are quenched by the water. At high temperatures, the nanogel shrinks, and the fluorophores inside become brighter [129]. The temperature is read out by lifetime with a good temperature resolution, which is better than 0.5 ºC [129]. However, the limitation of the fluorescent nanogel thermometer is low hydrophilicity, which makes it hard to disperse in the intracellular environment [129]. Therefore, more efforts are being made to improve the hydrophilicity of polymeric fluorescent thermometers. Okabe *et al.* designed a polymeric thermometer containing three functional units. One is a temperature-responsive unit. The second one is a fluorescent unit, and the third one is a hydrophilic unit to make the polymer nanoparticles have better distribution in the solution and the cells [104]. This hydrophilic thermometer has been used to do the intracellular temperature mapping and obtained a temperature resolution of 0.18 - 0.58 °C [104]. Moreover, Seiichi Uchiyama *et al.* developed a new polymeric fluorescent probe aiming to improve cell permeability [144]. This cell-permeable polymeric fluorescent thermometer contains the thermosensitive unit, the fluorescent unit, and the cation unit [144]. The cation unit enables to drive the polymer

nanoparticles into HeLa cells within 10 minutes [144]. This cell-permeable polymer-based fluorescent temperature probe also displays a high temperature resolution of 0.05°C to 0.54°C in the range from 28°C to 38°C in HeLa cells extract [144]. However, the fluorescent lifetime measurement requires a longer time (~ 1 minute) for imaging than that of fluorescent intensity imaging (~ 1 second) [145]. Thus, some research groups put efforts into developing ratiometric fluorescent polymeric thermometers as the ratiometric thermometers are capable of avoiding the effect of the environment [146] [113]. Qiao *et al.* demonstrated a ratiometric polymeric thermo-sensor based on transferrin protein-stabilized gold nanoclusters and temperature-sensitive polymer to improve the uptake of cells [146]. Although the polymer-based fluorescent thermometers have a high temperature resolution, the complex structures, tedious fabrication procedures, and poor permeability still limit the polymer-based fluorescent thermometers' development. Most importantly, the fluorophores conjugated with the polymers are easily quenched or weakened in the concentrated or aggregated state [107].

- **AIE-based fluorescent thermometers**

AIE, as a kind of abnormal phenomenon existing in some organic compounds, has attracted much attention in the field of imaging and biosensor [147]. The higher fluorescence efficiency of AIE is attributed to the restriction of intramolecular motion. They are inherently sensitive to the viscosity of the environment [106]. AIE-based fluorescent thermometers are commonly composed of AIE-dyes and polymers. Yang and his colleagues reported an AIE-based temperature sensor with a thermo-responsive polymer poly (N-isopropyl acrylamide) [148]. The phase transition changes with temperature and further induces the fluorescence intensity variation [148]. Interestingly, Gao *et al* utilized butter as a matrix, which of a phase temperature change was closed to the human temperature [106]. And these AIE dots is used as the reporter to reflect the temperature according to the viscosity change in the butter with a temperature sensitivity of 0.2%/ºC [106]. The hydrophilicity of this temperature probe is improved by the hydrophilic polymers. The AIE-active polymer-based fluorescent thermometers have compensated for the aggregation-caused effect, but the problem of water-solubility and cell-permeability are still existing. In 2021, Guan *et al.* designed AIE-active fluorescent thermometers with the size down to 5 nm based on self-assembled amphiphilic block copolymers [147].

- **Engineered Fluorescent Proteins-based fluorescent thermometers**

Engineered fluorescent proteins are popular in cell biology and molecular biology. The discovery and development of the green fluorescent protein (GFP) by Martin Chalfie and Roger Tsien won the Nobel Prize in 2008 [149]. The engineered proteins can be introduced to the living cells or organisms by transfection with no interference in the cellular activities. Moreover, the emission of GFP is dependent on the temperature. Jon S. Donner *et al.* reported a non-invasive method for intracellular temperature mapping [118]. They use GFP as a thermometer by measuring their fluorescence polarization anisotropy (**Figure 1-8F**). The cancer cells are transfected with GFP and heated by gold nanorods. Moreover, the temperature resolution and spatial resolution of this approach are 0.4°C and 300 nm, respectively [118]. However, the application of GFP in intracellular temperature mapping has a low signal-to-noise ratio because their fluorescent intensity cannot change with the temperature sensitively [150]. To overcome the above problem, Kiyonaka *et al.* developed genetically encoded GFP-based thermometers-tsGFPs [119]. In tsGFPs, the Salmonella thermos sensing protein tlpA and GFP form a coiled-coil structure. This coiled-coil structure transmits conformational changes of thermos sensing protein tlpA to GFP and then converts temperature changes into visible and quantifiable fluorescence changes [119]. tsGFPs selectively target to mitochondria and reveal mitochondrial heterogeneity in thermogenesis [119]. In 2017, Nakano *et al*. used two fluorescent temperature-sensitive proteins, enabling a fast-tracking of the temperature change with a time resolution of 50 ms [151].

- **Carbon-based luminescence thermometers**

Carbon nanoparticles were first discovered by Scrivens and co-workers in 2004 [152]. Then in 2006, Sun and his colleagues named these carbon nanoparticles with intense photoluminescence in both the solution and solid-state as “carbon dots” [153]. The good biocompatibility, simple synthesis steps, low cytotoxicity, and being environmentally friendly make the CDs popular in biomedicine [154]. Among these nanoparticles, there is a class of CDs that are sensitive to temperature. Their surface states or molecular states may change with the temperature and further affect the photoluminescence

intensity [155]. Kalytchuk *et al.* reported a nitrogen, sulfur-co-doped CDs, which of the photoluminescence lifetime was dependent on the temperature, but independent on the pH (5-12), concentrations, and environmental ions [137]. In 2021, Khan and co-authors developed blue-emitting CDs, exhibiting dual-mode thermal sensing (intensity/lifetime) in the temperature range from room temperature to 70 ºC [109]. The thermal average sensitivity of intensity and lifetime is ~1.3%/ ºC and ~1.09%/ ºC, respectively [109]. Moreover, Han *et al.* designed a ratiometric CDs-based thermal sensor with a high thermal sensitivity of ~0.082 / ºC. However, the emission of CDs is mainly in the visible region. The fluorescence can be interfered with by the autofluorescence of the biological samples.

Fluorescent nanodiamonds (FNDs) are a kind of nanocarbon material. Similar to CDs, nanodiamonds are biocompatible and easy to do the surface modification for following biological applications. The unique properties of no photo-bleaching or photo-blinking in the visible and near-infrared make them popular biomedication [154]. Most importantly, the emission of the nitrogen-vacancy centres within nanodiamonds is sensitive to the temperature [110]. Thus, nanodiamonds can work as a temperature probe in biological systems [110, 140]. Wu *et al.* reported the nanodiamonds coated with a nanogel shell and the photothermal agent to study the temperature photothermal effect *in situ* and living cells [140].

Graphene quantum dots (GQDs) are carbon-based nanoparticles with many advantages, such as biocompatibility, high dispersity, small size, and photostability [154, 156]. At present, the GQDs synthesis methods can be divided into top–down and bottom–up approaches. Top-down synthetic methods use graphene or carbon black to produce nano-quantum dots by chemical/electrochemical exfoliation, hydrothermal/solvothermal treatment, and microwave/ultrasonic treatment. Bottom–up synthetic methods utilize chemical reactions, such as step-by-step organic synthesis, to convert organic small molecules (such as citric acid, fullerenes, and polycyclic aromatic hydrocarbons) or organic precursors into high-quality quantum dots. Lee and co-workers developed two types of GQDs-based thermometers: nitrogen-doped graphene quantum dots (N-GQDs) and reduced graphene quantum dots (RGQDs). N-GQDs were synthesized from glucosamine precursors via bottom-up approaches and RGQDs were synthesized from reduced graphene oxide via top-down approach. Both RGQDs and N-GQDs are

sensitive to the temperature in the visible, while RGQDs also show emission in the NIR [156]. Moreover, both types of GQDs-based temperature probe showed more than 40% quenching response in HeLa cells in the temperature range from 25 ºC to 45 ºC [156].

- **Quantum dots (QDs)-based luminescence thermometers**

Quantum dots (QDs) are commonly wide used optical sensors because of their high brightness, excellent photostability, and broad excitation/emission spectra [127]. Its luminescence properties are dependent on the temperature. The luminescent intensity decreases or the spectral position shifts when the local temperature increases [150]. Yang *et al.* reported QDs-based spectral shift luminescence thermometer delivered into NIH/3T3 murine fibroblast cells and mapped the heat generation under Ca^{2+} stress and cold shock [138]. In 2016, Tanimoto *et al.* developed a QDs-based ratiometric luminescence thermal sensor by splitting the emission spectrum of a single quantum dot with a monochromator and by detecting them separately with a photomultiplier tube, and then studied inhomogeneous heat production in the living human-derived neuronal cell SH-SY5Y [116]. The relative temperature sensitivity is 6.3%/K, which is higher than that of conventional QDs-based thermal sensors [116]. Hui Zhang *et al.* synthesized $CuInS_2$/ZnS QDs micelles and achieved high thermal sensitivity of 2.0%/ ˚C in living cells [157]. However, compared with other luminescence thermometers, QDs are toxic to living cells. Thus, surface modification is crucial for QDs to reduce cytotoxicity.

- **Upconversion nanoparticles-based luminescence thermometers**

In recent years, UCNPs show the great potential of temperature sensing because of their superior luminescence performance and photochemical stability [158]. The excellent optical properties such as large anti-Stokes shifts, long luminescence lifetimes, non-auto fluorescence, and high photochemical stability make UCNPs attract tremendous interest in the biological application. In addition, UCNPs show excellent temperature-dependent luminescence. Zhu *et al.* used UCNPs ($NaLuF_4$:Yb,Er@$NaLuF_4$) combined with photothermal material to real-time monitor the temperature changes in photothermal therapy [159]. Shi *et al.* designed core-shell structure UCNPs doped with Er^{3+} and Nd^{3+} with the excitations of 808 nm and 980 nm lasers. It showed a method to monitor temperature change in a living cell [103]. Although many groups have made big

progress in UCNPs-based thermometers, obtaining UCNPs with an excellent dispersibility in the physiological buffer is still extremely challengeable. Di et al. developed a UCNPs ($NaYF_4$: Yb, Er)-based ratiometric thermal sensor coated with the cross-linked polymer network to improve the dispersion in the living cell and monitor temperature variations of mitochondria under chemical and nutrient stimulations [115]. The excellent luminescence properties of UCNPs make them suitable for biological detection and imaging. At present, the most important is to design biocompatible, targetable, and stable UCNPs in the physiological environment to avoid the aggregation and non-specific bindings.

1.2.3 Intracellular temperature dynamics

Most chemical reactions and biological processes within live cells are dependent on temperature. The temperature variation can reflect the cell is under the physiological status or in diseases. Hence, studying the temperature dynamics of organelles in the living cells is pivotal to understanding the mechanism and meaning of intracellular activities.

- **Mitochondria.**

As an energy factory, mitochondria are involved in cellular respiration. During the respiratory activity, mitochondria transform carbohydrates to ATP, releasing the heat simultaneously. Consequently, monitoring the temperature dynamics of mitochondria is key to understanding mitochondrial function through the cell. Many researchers investigate mitochondrial thermal dynamics [1, 112, 115, 150]. Di *et al.* observed the elevation of mitochondrial temperature was almost 2 degrees after adding FCCP by UCNPs ($NaYF_4$: 20%Yb^{3+}, 2%Er^{3+})-based temperature sensor [115]. Savchuk *et al.* used a GFP-based thermometer to directly monitor temperature changes induced by FCCP and observed a 3-degree increase compared with the mitochondrial temperature before adding FCCP [160]. These two researches illustrated that the temperature was capable of reflecting the dynamics or the function of mitochondria. Most importantly, no matter the nanoparticles introduced to the living cells or endogenesis expression by the living cells, they both showed an elevation in the mitochondrial temperature after adding FCCP, which illustrated the reliability of luminescence thermometers. It also demonstrated that the elevated temperature was not attributed to the artifacts of the

system. As mitochondrion is a highly dynamic organelle, it is essential to permanently fix the temperature sensors in the mitochondria. Huang and co-authors synthesized the first fixable and fluorescent thermo-sensor and monitored temperature changes of living cells under phorbol 12-myristate-13-acetate (PMA) stimulation (**Figure 1-10**)[112]. PMA can activate the protein kinase C system and further release heat. The author observed a 3-degree increase in the temperature of mitochondria in Michigan Cancer Foundation-7 (MCF-7) cells [112].

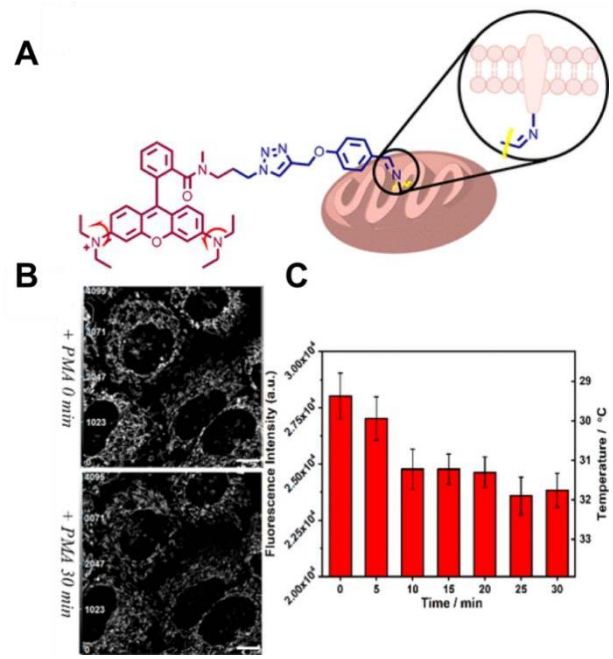

Figure 1- 10 Real-time monitoring of mitochondrial-temperature changes in PMA-stimulated MCF-7 cells. *A. Working principle of the fixable thermometer. B. Time-course image of PMA-stimulated MCF-7 cells (t = 0 and 30 min). C. Changes in the fluorescence intensity of Mito-TEM with stimulation time. MCF-7 cells were treated with Mito-TEM (3 μM). Scale bar: 10 μm. Adapted with permission from reference [112].*

- **Endoplasmic reticulum (ER)**

ER is responsible for the synthesis and exportation of proteins and membrane lipids with a closed and high-frequency contact with mitochondria. It has been reported that the sacro/ER Ca^{2+}-ATPase is related to the intracellular thermogenesis [161]. The sacro/ER Ca^{2+}-ATPase transport Ca^{2+} ion across the membrane using the chemical energy derived from ATP hydrolysis. The heat released during ATP hydrolysis by sacro/ER Ca^{2+}-ATPase may vary from 10 up to 30 kcal/mol [161]. To investigate the thermogenesis in ER, Kiyonaka *et al.* developed a GFP-based thermometer to study

the thermogenesis of ER during the reaction of ATP turnover by the sarco/ER Ca^{2+}-ATPase in the cultured myotubes differentiated from myogenic C2C12 (mouse myoblast) cells [119]. After adding cyclopiazonic acid, it showed a temperature reduction. Kriszt *et al.* reported the first thermosensitive fluorescent dye-ERthermAC, which could target to ER and monitor thermogenesis in WT-1 cells (**Figure 1-11**) [162]. ERtherm AC displayed a distinct change in the fluorescent intensity after FCCP stimulation (**Figure 1-11C**) [162].

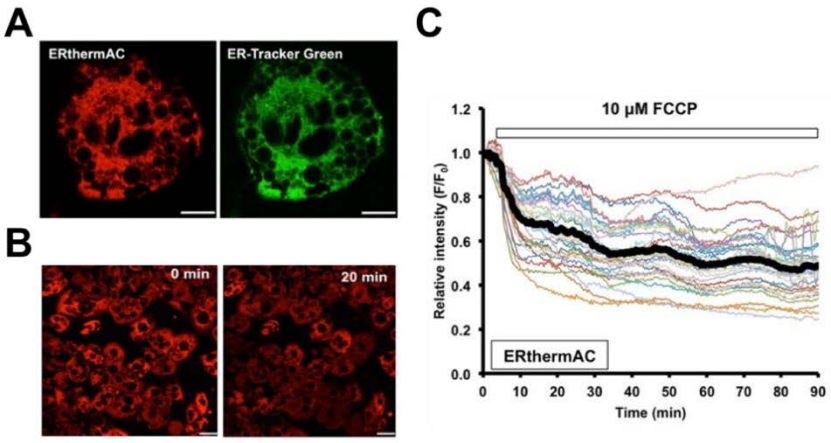

Figure 1-11 Real-time monitoring of ER-temperature changes in FCCP-stimulated WT-1 cells. *A. ERthermAC (red) co-localises with ER-Tracker Green (green) in WT-1 cells. Scale bar: 10 μm. B. Time-course image of FCCP-stimulated WT-1 cells (t = 0 and 20 min). Scale bar: 20 μm. C. ERthermAC intensity drastically decreases upon FCCP stimulation in all cells, without any lag phase, indicating increased intracellular temperature. The thick black curve corresponds to the mean relative intensity; n =35 cells from 2 cultures. Adapted with permission from reference [162].*

- **The other intracellular substructure**

The nucleus is a membrane-bound organelle and is responsible for many cellular activities, such as DNA replication, transcription, and RNA processing. It is separated from the cytoplasm because of the unique reactions. Seiichi Uchiyama research group studied the temperature gap of the nucleus and cytoplasm by polymeric fluorescent thermometers using fluorescence lifetime imaging microscopy (**Figure 1-12**) [104]. They found the average temperature difference between the nucleus and the cytoplasm was 0.96 ºC (**Figure 1-12B&C**) [104]. This temperature gap was dependent on the cell cycle and became smaller in S/G2-phased cells (**Figure 1-12D&E**) [104]. Moreover,

they also discovered that the temperature of the centrosome was 0.75 ºC higher than that of the cytoplasm [104]. In addition, Oyama *et al.* find that the transportation on the microtubule is accelerated when the local temperature is increasing [163].

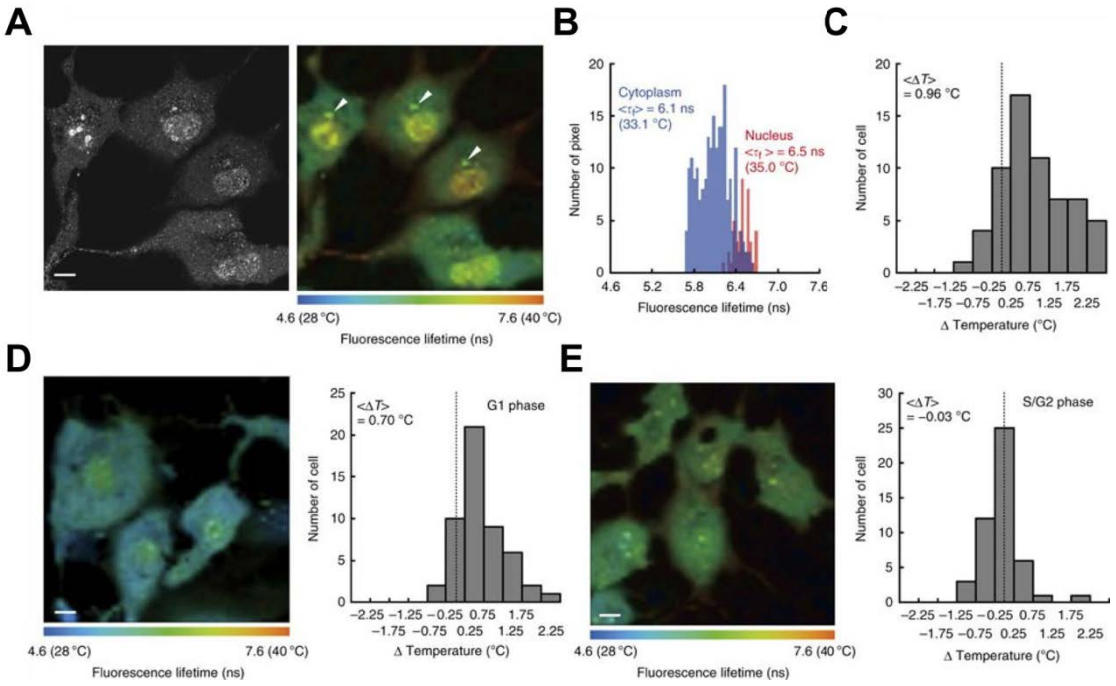

Figure 1-12 Temperature mapping of nucleus and cytoplasm in living COS7 cells. *A. Fluorescence intensity image (left) and lifetime image (right) of polymeric fluorescent thermometer. B. Histograms of the fluorescence lifetime in the nucleus and the cytoplasm in a COS7 cell. C. Histogram of the temperature differences between the nucleus and the cytoplasm (n = 62). < ΔT> represents an average of the histogram. D-E. Cell-cycle-dependent thermogenesis in the nucleus. Representative fluorescence lifetime images and histograms of ΔTemperature in living cells synchronized to G1 phase (n = 51) (D) and s/G2 phase (n = 48) (E). scale bar: 10 μm. Adapted with permission from reference [150].*

1.2.4 Validations of Intracellular Thermometry

With the rapid development of intracellular thermometry, a critique issue of the reliability is proposed by Baffou et al. He argued that the value of ΔT should be smaller than 10^{-5} K within a single cell according to the equation [126],

$$\Delta T = \frac{P}{\kappa L} \qquad (3)$$

where κ is the thermal conductivity, L is the size of a heat source, and P is the Power. The intracellular environment is complex and the cells have heterogeneity. It is hard to

use equations to mimic the cellular environment [150]. However, further advance is necessary to improve and assure the reliability of intracellular thermometry. An ideal intracellular thermometer is expected to meet the following properties,

- Be independent of the thermo-sensor's concentration.
- Be independent of the excitation power.
- Be independent of the intracellular environmental factors, such as pH, ion strength (K^+, Ca^{2+}, and Mg^{2+}), viscosity, oxygen species, proteins, and enzymatic activities.
- Be closer to the organelles. The organelles in a single living cell are highly dynamic. We need to design intracellular thermometry to be covalently linked to the specific organelle.
- Improve the imaging technology with fast speed and higher spatial and temporal resolution.

In the future, advance in material science and microscopy is essential to developing more accurate and reliable intracellular thermometers. Besides, we need to verify the intracellular thermogenesis by several various kinds of thermometers to enhance productivity. Most importantly, other biophysical parameters, such as mitochondrial depolarization, oxygen consumption, extracellular acidification rate, and lysosomal pH, should be recorded simultaneously with the intracellular temperature measurements.

1.2.5 Physiological Meaning of Intracellular Thermometry

Temperature is a significant biophysical parameter in multiple cellular activities. The variation of temperature is capable of reflecting the status of cells. Many intracellular chemical reactions, such as enzymatic activities, DNA replication, RNA transcription, cell division, and proliferation, are processed under a reasonable temperature. As everyone knows, the temperature of a human will elevate when the person has a fever. It is because the immune system is working to protect itself. The phenomenon of abnormal temperature commonly exists in the pathological status, e.g. tumor, inflammation, and cancer.

Intracellular activities need the energy to process the reactions. Mitochondria produce ATP for cellular activities and release heat. That's why the researchers focus on studies of mitochondrial temperature. Moreover, the mitochondrion is a highly dynamic

organelle and contacts with ER, lysosomes, peroxisomes, and the nucleus. The direct physical contacts between the organelles can be studied by the super-resolution microscope and the signalling pathways contacts can be studied by molecular biology, such as siRNA (small interfering RNA), CRISPR-Cas9, and SDS-PAGE [56, 164]. But we have no idea about the energy or heat propagation within the organelles coordination network. The exact temperature of the specific organelle may work as an indicator for disease detection. In addition, it will be necessary to simultaneously monitor the temperature variations between organelles, aiming to study the network of organelles from the view of temperature.

Apart from the networks between organelles, the activities of the enzyme are also associated with temperature. The higher or lower temperature will cause the denaturation of proteins. For example, lysosomes are the recycling factories in the cell, which are responsible for the digestion of large molecules and the transportation of fragments to the other organelles [4]. Several enzymes, such as hydrolytic enzymes, are involved in this reaction. If the enzymes in the lysosomes are denaturized by the temperature, the large molecules will accumulate and further kill the cell.

Therefore, the studies of intracellular temperature mapping in living cells will provide a better understanding of cellular events and develop novel diagnoses and therapies.

1.3 Surface Functionalization of Upconversion Nanoparticles

UCNPs are widely used in the bioanalytical applications because of excitation of NIR light and generation of visible light, which can suppress the autofluorescence and light scattering in biological samples.

Lanthanide-doped UCNPs (such as $NaLnF_4$, Ln is the Y, Gd, Yb etc) are typically synthesized in organic solvents, such as OA and 1-octadecene, which requires a subsequent phase transfer to aqueous solutions and modified with functional groups for further biomedical application. Hence, I will introduce the methods for generating a hydrophilic surface on UCNPs ($NaYF_4$: 20%Yb^{3+}, 2%Er^{3+}) and conjugating with biomolecules, followed by the approaches of targeting mitochondria.

1.3.1 Generating a hydrophilic surface on UCNPs

The UCNPs with the composition of $NaYF_4$: Yb^{3+}, Er^{3+} are typically synthesized in

high-boiling organic solvents, such as OA [165]. Usually, OA controls the growth of nanoparticles and forms a hydrophobic layer on the surface of UCNPs ($NaYF_4$: 20%Yb^{3+}, 2%Er^{3+}). To generate a hydrophilic surface on UCNPs ($NaYF_4$: Yb^{3+}, Er^{3+}), it is necessary to exchange or coat the OA layer with hydrophilic ligands. The most commonly used surface modification strategies are ligand exchange, coating with a silica shell, ligand interaction, layer by layer deposition, ligand oxidation, and ligand removal by acid treatment (**Figure 1-13**) [165].

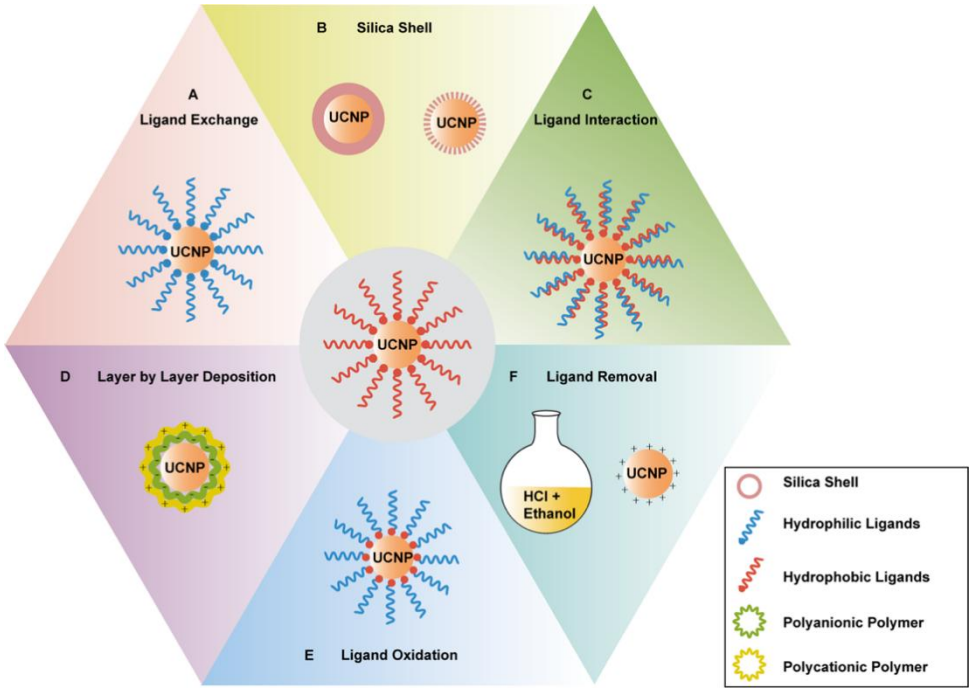

Figure 1-13 The diagram of common strategies for surface modification of UCNPs ($NaYF_4$: 20%Yb^{3+}, 2%Er^{3+}) coated with oleic acid. *Obtaining hydrophilic UCNPs ($NaYF_4$: 20%Yb^{3+}, 2%Er^{3+}) by (A)Ligand exchange, (B) silica shell, (C) Ligand interaction, (D) Layer by layer deposition, (E)Ligand oxidation, and (F)Ligand removal. Adapted from Reference [166].*

1.3.1.1 Ligand Exchange

The hydrophobic ligands (e.g. OA) on the surface of UCNPs ($NaYF_4$: 20%Yb^{3+}, 2%Er^{3+}) can be exchanged by the hydrophilic ligands, such as PDA, polymers, alendronate, and so on (**Figure 1-13A**). The exchange efficiency of these ligands is controlled by the temperature, the solvent, the number, chemical structure, and properties of hydrophilic ligands [165, 167]. The dispersity of hydrophobic ligands (e.g. OA) and hydrophilic ligands should be considered when choosing a suitable solvent. For example, Nsubuga *et al.* developed 'Stealth' (β-$NaYF_4$:1%Nd^{3+}, 20%Yb^{3+}, 2%Er^{3+} @$NaYF_4$: 25%Nd^{3+}) for

biomedical application by exchanging the OA with $NOBF_4$ in chloroform to obtain hydrophilic nanoparticles [168]. Hien *et al.* transformed the UCNPs ($NaYF_4$: 20%Yb^{3+}, 2%Er^{3+}) into the water by exchanging them with three di-block copolymers in THF [167]. Moreover, compared with di-block copolymers with carboxylic and sulphonyl acid groups, the exchange efficiency of the phosphate ligands was highest. The di-block copolymer with phosphate ligands can replace all the OA capped on the surface of UCNPs ($NaYF_4$: 20%Yb^{3+}, 2%Er^{3+}) [167].

1.3.1.2 Coating with a Silica Shell

The silica shell is one of the most commonly used strategies to transfer hydrophobic UCNPs into hydrophilic ones. It influences slightly on the luminescence intensities of UCNPs but provides a biocompatible and chemically inert shell, which is ideal for bioapplication [165].

The method of coating silica shells on the hydrophilic UCNPs is typically modified on the Stöber process [169]. Briefly, the UCNPs with the hydrophilic surfaces are mixed with tetraethyl orthosilicates (TEOS) in the alcoholic solvents containing ammonia to yield a silica shell (**Figure 1-13B left**). The thickness of the silica shell can be adjusted by varying amounts of TEOS and stirring time [170, 171]. The microemulsion method is usually used to coat a silica shell on hydrophobic UCNPs [172]. In a reverse micelle, the aqueous solution is enclosed in nanosized droplets, which is stabilized by detergents and distributed in nonpolar solvents. Then the reaction is started by adding ammonia. The ratio between the water and the detergent determines the size of these droplets [173]. The size of the droplets can be adjusted to form a uniform silica shell on the single UCNP [173]. In addition, UCNPs can be coated by a mesoporous silica shell to generate a hydrophilic surface (**Figure 1-13B right**)[174]. A mesoporous silica shell is achieved by adding detergents such as cationic cetyltrimethylammonium bromide (CTAB) during the synthesis of the silica shell. The detergent-formed micelles in the mesoporous silica shell can be removed by washing with ammonium nitrate or calcination. Compared with silica shells, the mesoporous silica shell provides UCNPs with more reaction sites to load drugs, dyes, or photosensitizers [175]. For example, Chen *et al.* designed a nucleus-based photodynamic therapy by loading rose bengal on the mesoporous silica-coated UCNPs to kill cancer cells [176]. Although coating a silica shell is widely used to get a hydrophilic UCNP, there are still some disadvantages. It

is difficult to control the morphology of silica shells. One to several UCNPs can be encapsulated into one silica shell. This superstructure leads to poor dispersity in an aqueous buffer. Moreover, UCNPs with silica shells are not stable in the physiological buffer and have non-specific binding with biomolecules, such as proteins, which affects detection sensitivity [177]. The most important is that it needs further silanization to generate amine, carboxylic, or silanol groups.

1.3.1.3 Ligand Interaction

The hydrophobic ligands of OA or oleylamine on UCNPs (e.g., $NaYF_4$) surface can also provide attachment sites for the second layer of amphiphilic molecules. Amphiphilic molecules are typically composed of hydrophobic and hydrophilic units. The hydrophobic units such as alkyl chains can react with OA or oleylamine on the UCNPs (β-$NaYF_4$: Yb^{3+}, Er^{3+}) by van-der-Waals interactions or hydrophobic interaction (**Figure 1-13C**) [165]. For example, hydrophilic poly(acrylic acid) (PAA) can be modified to be an amphiphilic polymer by reacting with octylamine [178]. Then nanoparticles covered with OA interact with the modified amphiphilic PAA polymer via hydrophobic interactions and form a stable dispersion in the water, ethanol, and buffer [178]. However, the modified PAA polymer quenches the upconversion luminescence by approximately 60% at 525 nm and 545 nm [178]. Hydrophobic polymers also react with hydrophilic molecules to form amphiphilic polymers. For example, poly (maleic anhydride-alt-1-octadecene) (PMHC18) reacts with polyethylene glycol functionalized with amine groups to form a new amphiphilic polymer. The modified PMHC18 polymer can attach to OA on the $NaYF_4$: Yb^{3+}, Er^{3+}/Tm^{3+} surface by hydrophobic interaction, forming stable dispersion in aqueous suspension [179].

Additionally, surfactants can improve the dispersity and stability of UCNPs ($NaYF_4$: Yb^{3+}, Er^{3+}/Tm^{3+}) in aqueous suspension. The commonly used surfactants include anionic sodium dodecyl sulfate (SDS), CTAB, and polyethylene glycol tert-octylphenyl ether [180]. The surfactants form the nanosized micelles to encapsulate UCNPs ($NaYF_4$: Yb^{3+}, Er^{3+}/Tm^{3+}) in microemulsion. The concentration of the surfactant is crucial in maintaining the dispersity of single UCNPs in each micelle, as the lower concentration will lead to large superstructures of UCNPs ($NaYF_4$: Yb^{3+}, Er^{3+}/Tm^{3+}) [180]. It has been reported that the luminescence intensity of UCNPs ($NaYF_4$: Yb^{3+}, Er^{3+}/Tm^{3+}) coated with surfactants may drop about 30% [180].

1.3.1.4 Layer by Layer Deposition

Layer by layer deposition is a process that which polyanions or polycations can be deposited on a charged surface by electrostatic interactions (**Figure 1-13D**) [181]. The surface charge of UCNPs ($NaYF_4$: 20%Yb^{3+}, 2%Er^{3+}) is positive after washing by hydrochloric acid. Then the polyanions can be deposited on the UCNPs ($NaYF_4$: 20%Yb^{3+}, 2%Er^{3+}) by stirring in the solution directly. The size of hydrophilic UCNPs is controlled by layers of deposition [182]. Liu *et al* coat UCNPs (NaYF4:18%Yb^{3+}, 2%Er^{3+}) with a silica shell and further attach poly-l-lysine on the UCNPs to generate amine groups [183]. It is extremely easy to modify the surface of UCNPs (e.g., $NaYF_4$) with functional groups, but the deposited polymer layers prefer to drop off from UCNPs.

1.3.1.5 Ligand Oxidation

The double bonds of OA on the surface of UCNPs ($NaYF_4$: 20%Yb^{3+}, 2%Er^{3+}) can be oxidized into carboxylic groups by Lemieux-von Rudloff reagent (**Figure 1-13E**), which transfers the hydrophobic layer into the hydrophilic surface [165]. Lemieux-von Rudloff reagent contains permanganate (MnO_4^-) and periodate (IO_4^-). Both reagents are needed for the three-step conversion of the double bond into two carboxylic groups, and the reaction time should be less than 2 hours to avoid the by-products of MnO_2, which may decrease the luminescence intensity of UCNPs (β-NaGdF4:Ho^{3+}/Yb^{3+}) [184]. These hydrophilic UCNPs (β-NaGdF4:Ho^{3+}/Yb^{3+}) obtained by oxidation can disperse stably in the water and polar solvents [184]. Another approach to oxidize the double bond of OA is by ozonolysis [185]. The surface of UCNPs ($NaYF_4$: 20%Yb^{3+}, 2%Er^{3+}) contains aldehydes after oxidation by ozonolysis [185]. There is no influence on the size, shape, and photonic properties after oxidation by ozonolysis [185]. Moreover, the biomolecules with amines can be conjugated to the UCNPs ($NaYF_4$: 20%Yb^{3+}, 2%Er^{3+}) directly by the reduction to aldehyde through dimethyl sulfide [185].

1.3.1.6 Ligand Removal by Acid Treatment

The OA ligands on the surface of UCNPs ($NaYF_4$: 20%Yb^{3+}, 2%Er^{3+}) can be removed by strong acid treatment (**Figure 1-13F**), such as hydrochloric acid and ethanol. With the appropriate hydrochloric acid treatment and duration (typically 10 mins), the oleate on the surface of UCNPs ($NaYF_4$: 20%Yb^{3+}, 2%Er^{3+}) are protonated and then detached. The stability of “naked” UCNPs in the solution depends on the surface charge and

can be adjusted by the pH [165]. The "naked" UCNPs show positive charge at low pH but change to negative at pH ≥ 7 [165]. As the strong electrostatic repulsion of nanoparticles with the same surface charge promotes the formation of stable colloidal systems, ''naked'' UCNPs show high dispersion stability at pH≤4 and ≥7, respectively [165]. For biomedical applications, ''naked'' UCNPs require a subsequent modification with functional groups.

1.3.2 Bioconjugation

The hydrophobic UCNPs ($NaYF_4$: 20%Yb^{3+}, 2%Er^{3+}) are transferred to be hydrophilic UCNPs ($NaYF_4$: 20%Yb^{3+}, 2%Er^{3+}), which are dissolvable and stable in the aqueous buffer. However, it still requires further bioconjugation for biomedical applications, such as conjugating with antibodies, glycans, single-stranded DNA, double-stranded DNA, aptamers, peptides, enzymes, and small molecules (**Figure 1-14A**).

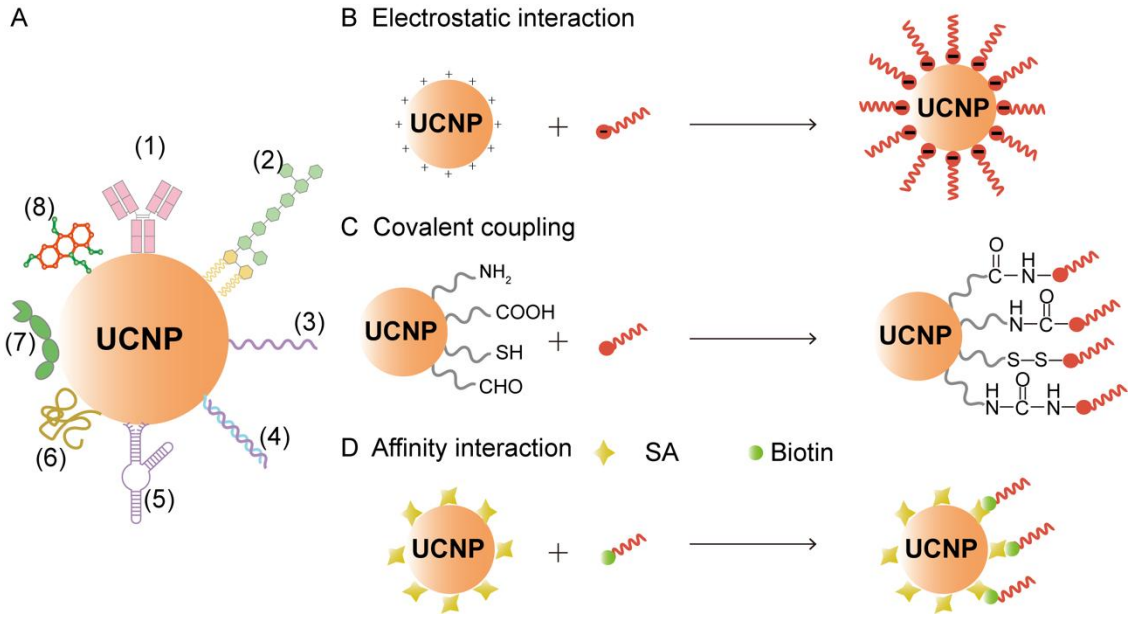

Figure 1-14 Schematic illustration of the bioconjugation of UCNPs. *A. UCNPs ($NaYF_4$: 20%Yb^{3+}, 2%Er^{3+}) are functionalized with different biomolecules, including (1) antibodies, (2) glycans, (3) single-stranded DNA, (4) double-stranded DNA, (5) aptamers, (6) peptides, (7) enzymes, and (8) small molecules. B. UCNPs ($NaYF_4$: 20%Yb^{3+}, 2%Er^{3+}) interact with biomolecules by electrostatic interaction. C. UCNPs ($NaYF_4$: 20%Yb^{3+}, 2%Er^{3+}) interact with biomolecules by covalent coupling. D. UCNPs ($NaYF_4$: 20%Yb^{3+}, 2%Er^{3+}) interact with biomolecules by affinity interaction.*

After surface modification, UCNPs ($NaYF_4$: 20%Yb^{3+}, 2%Er^{3+}) commonly contain amine, carboxylic, thiol, or aldehyde groups, which are used for conjugation with

biomolecules (**Figure 1-14C**). Antibodies or small biomolecules usually conjugate with UCNPs by EDC/NHS reaction [172, 186]. During EDC/NHS reaction, the reactant containing carboxylic groups are first activated by EDC/NHS and then conjugate with amine groups. The ideal reaction time is 8-12 hours, depending on the reaction sites of reactants. A small number of proteins with thiol groups can specifically react with maleimides. Moreover, Moreover, the amines on the UCNPs ($NaYF_4$: Yb^{3+}, Er^{3+}) surface can react with aldehydes groups to form imines [187]. The reaction between UCNPs and biomolecules is strong and stable, but the efficiency is a bit low as the protein structure may change in the buffer under various pH and ion strength, hiding specific reaction sites for conjugation. Also, proteins are possibly being denatured during the reaction.

Apart from conjugation by covalent bonds, UCNPs ($NaYF_4$: Yb^{3+}, Er^{3+}) can also be linked with biomolecules through affinity interaction (**Figure 1-14D**), such as the interaction between streptavidin and biotin [188]. One streptavidin conjugates with four biotins with high affinity. This interaction is fast and unaffected by pH, ion strength. Moreover, DNA has a strong interaction with histone through electrostatic interactions (**Figure 1-14B**). The bioconjugation between nanoparticles and biomolecules makes UCNPs practicable in biomedical applications.

1.3.3 Approaches to targeting mitochondria

Mitochondria are responsible for a wide range of cellular activities. The dysfunctions of mitochondria are related to the causes of many diseases, such as cancer. Specific targeting to mitochondria and localized modulations will help to understand the function and cellular activities. There are four approaches used for the specific targeting of molecules and nanoparticles to mitochondria, typically via triphenylphosphonium (TPP) cations, heterocyclic aromatic cations, mitochondria-targeted peptides and vesicles.

1.3.3.1 By triphenylphosphonium cations

The lipophilic TPP cations (**Figure 1-15 red**) can selectively accumulate within the mitochondria because of the large negative membrane potential of the mitochondrial inner membrane [189, 190]. The potential of the cell membrane is -30 to -60 mV and the potential of the inner membrane of mitochondria is -150 to -170 mV. The large membrane potential can drive these lipophilic molecules into the cell and accumulate

in the mitochondria [191]. TPP cations are commonly used to deliver some nanoparticles or bioactive molecules to the mitochondria [190]. Robin A. J. *et al.* developed a strategy that TPP conjugated with a coenzyme Q or Vitamin E derivative. When the drugs were taken orally, TPP enabled to lead the drugs to accumulate in those tissues with mitochondrial dysfunction [192]. Beibei Wang *et al.* designed a kind of two-photon carbon dots labelled with TPP to achieve mitochondria imaging in the living cells [193]. Yanyan Liu *et al.* demonstrated mitochondria-targeting UCNPs ($NaYF_4$:18%Yb, 2%Er) loaded with photosensitizer and TPP to achieve photodynamic therapy [183]. Under NIR laser, these mitochondria-targeting nanoparticles cause severe mitochondrial matrix swelling and then kill the cancer cells [183]. **Figure 1-15** illustrates a typical structure of a different functional group modified with TPP [190]. The functional moiety is shown in blue including bioactive molecules (antioxidants, drugs, and scavengers) or nanoparticles. The functional moiety (**Figure 1-15, blue**) and the targeting moiety (**Figure 1-15, red**) are linked by a linker ((**Figure 1-15, green**)). The length of the alkyl chain (linker) has a significant influence on the lipophilicity of probes, the efficiency of cellular uptake, and the localization of mitochondria (matrix or membrane) [190]. Additionally, the TPP-linked carboxylic acid and TPP-linked amines may undergo differential protonation in the cytoplasm and mitochondria. The pH of cytoplasm and mitochondria are 7.2 and 8.0, respectively. Compared with TPP-linked alkyl, deprotonation of TPP-linked carboxylic acid provides an additional driving force during the accumulation of nanoparticles in the mitochondria (**Figure 1-16**) [190]. However, deprotonation of TPP-linked amines has an inverse effect on the nanoparticles accumulation in mitochondria (**Figure 1-16**) [190].

TPP-based mitochondria targeting probes are highly stable and safe in biological systems with very low chemical reactivity to the components in the cell. Moreover, the targeting moiety-TPP has no influence on the emission in the range of visible or NIR light [190].

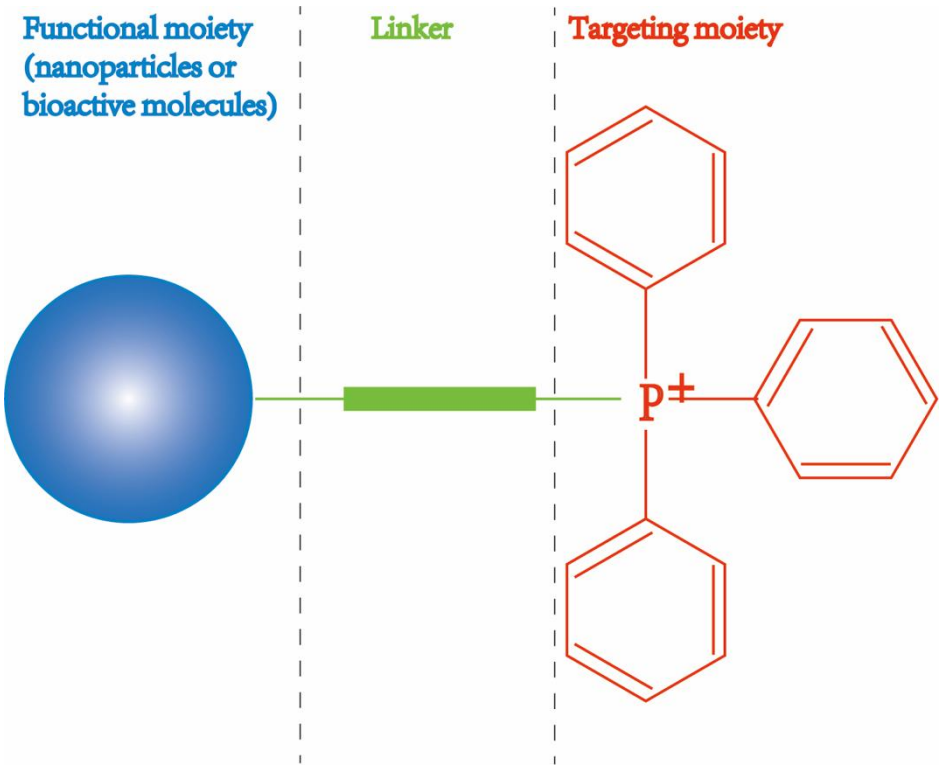

Figure 1-15 Structure of TPP-based mitochondria targeting molecules. *The red colour represents the mitochondria targeting unit-TPP$^+$, the blue color represents the functional unit, including nanoparticles or biomolecules, and the green color is the linker between the functional unit and TPP$^+$. Adapted from [190].*

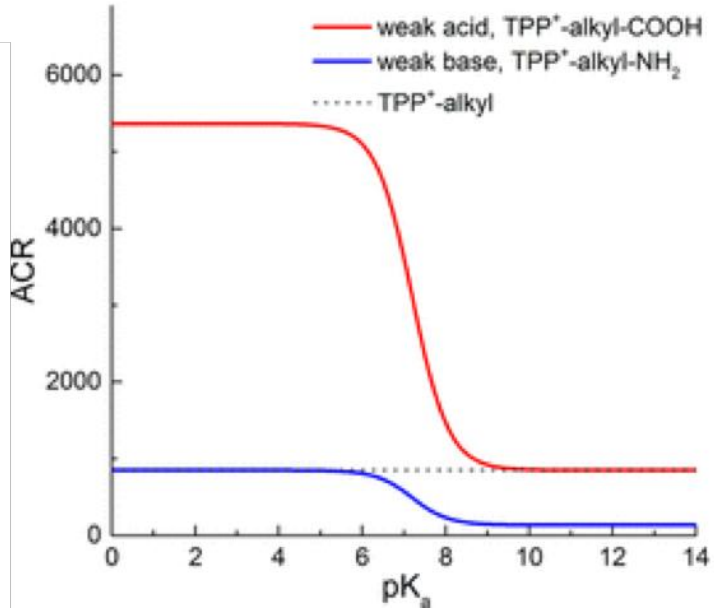

Figure 1-16 Comparison of the mitochondria to cytosol accumulation rate (ACR) for TPP$^+$-linked carboxylic acid and amines, calculated equilibrium ACR values as a function of pK$_a$ of acids and bases. *Adapted from [190].*

1.3.3.2 By heterocyclic aromatic cations

Small lipophilic cations such as rhodamine [194], pyridinium [195], and indolium derivatives have been extensively used to study mitochondrial dynamics[190] (**Figure 1-17**). Akos A. Gerencser *et al.* use a bis-oxonol-type indicator and tetramethylrhodamine methyl ester to analyze mitochondrial membrane potential quantitatively [196]. Small heterocyclic cations can also selectively accumulate within the mitochondria [197, 198]. Most importantly, the cellular uptake and localization in mitochondria can be improved when rhodamine-linked compounds are conjugated with tetraphenylborate anion [199].

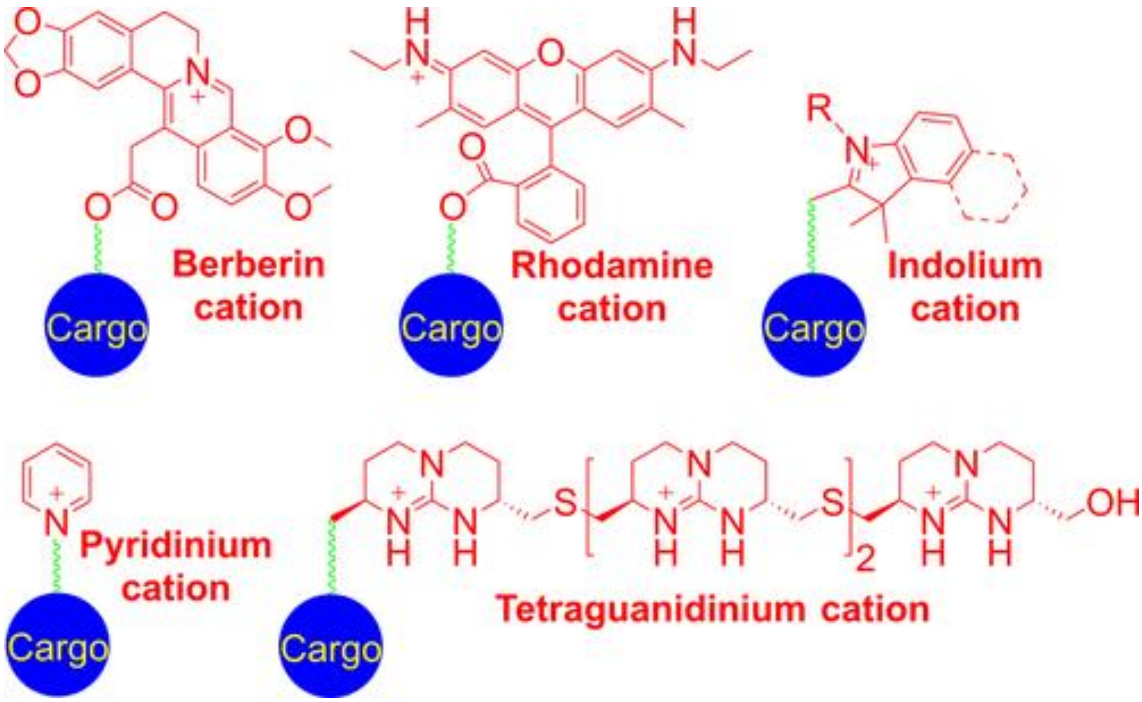

Figure 1-17 Examples of heterocyclic cations used as mitochondria-targeting Moieties. *The red color represents targeting moiety. The green color represents linker. The blue color represents functional moiety. All the targeting moieties have positive charge. Adapted from [190].*

1.3.3.3 By mitochondria-targeted peptides

Another method to deliver bioactive molecules to mitochondria is by mitochondria-targeted peptides. Both natural peptides and synthetic peptides can be used as the mitochondria targeting moiety. These peptides commonly carry hydrophobic (phenylalanine, tyrosine, isoleucine) and positively charged (arginine, lysine) amino acids [200, 201]. The positive charge on the amino acids (arginine, lysine) enables to lead the bioactive molecules into the mitochondria. The first mitochondria targeting

peptide is Szeto-Schiller peptides, which is discovered by Hazel H. zeto and Peter W [202]. Schiller. An antioxidant conjugated with the Szeto-Schiller peptides can specifically accumulate in the mitochondria [202]. Horton *et al.* engineered several mitochondria-targeted peptides that could efficiently deliver biomolecules into human cells and specifically localize to mitochondria [203]. Xiaoman Zhang *et al.* used an arginine-rich mitochondria-targeted peptide modified UCNPs ($NaYbF_4$:Nd@$NaGdF_4$:Yb/Er@$NaGdF_4$ core-shell-shell) for photodynamic therapy, improving the therapeutic efficiency [204].

1.3.3.4 By mitochondria-targeted vesicles

Due to the positive charges of liposomes, it can be used as an efficient carrier to cargo biomolecules to the mitochondria [190]. The liposomes are first designed to deliver DNA and paclitaxel into mitochondria [205]. Recently, it can also be used to deliver other bioactive compounds [206, 207]. Parul Benien *et al.* mixed TPP with several different commercial phospholipids to prepare liposomes, which preferentially accumulated within the mitochondria [206]. The major merit of mitochondriotropic liposomes is delivering a large number of different sizes and different hydrophobicities bioactive compounds into mitochondria, from small molecules to proteins. Another efficient strategy is that the bioactive molecules-loaded nanoparticle is first enveloped with mitochondrial membrane and then modified with an octaarginine peptide [190]. These mitochondrial membrane-coated nanoparticles can be internalized by cells and further taken by mitochondria via membrane fusion [190].

1.4 Aims and Outline

This thesis advances UCNPs ($NaYF_4$: 20%Yb^{3+}, 2%Er^{3+})-based luminescent thermometers to study intracellular temperature dynamics. Specifically, the thesis investigates the colloidal stability of hydrophilic UCNPs ($NaYF_4$: 20%Yb^{3+}, 2%Er^{3+}) when being coated with five different surface modifications, and identifies the copolymer-based strategy to enhance the conjugation efficiency of UCNPs ($NaYF_4$: 20%Yb^{3+}, 2%Er^{3+}) with biomolecules by EDC/NHS method (chapter 2). Then it focuses on the surface functionalization and conjugation strategies to specifically target intracellular mitochondria and lysosomes so that to map the intracellular temperature dynamics using the organelle-targeting UCNPs ($NaYF_4$: 20%Yb^{3+}, 2%Er^{3+}) (chapter

3 & 4). Preliminary data was also obtained to study the landscape of mtDNA replication across the cell cycle (chapter 5).

Chapter 2 investigates the colloidal stability of UCNPs ($NaYF_4$: 20%Yb^{3+}, 2%Er^{3+}) with five different surface modifications in water, aiming to obtain the hydrophilic and monodispersed UCNPs ($NaYF_4$: 20%Yb^{3+}, 2%Er^{3+}). The morphology, size, and dispersibility of UCNPs ($NaYF_4$: 20%Yb^{3+}, 2%Er^{3+}) using the five surface modification strategies were first compared, followed by incubating these nanoparticles with HeLa cells to check the stability and cytotoxicity, and finally, the hydrophilic UCNPs ($NaYF_4$: 20%Yb^{3+}, 2%Er^{3+}) were used to label microtubules. This chapter demonstrated that the ligand-$PEGMEMA_{80}$-*b*-$EGMP_3$ di-block copolymers provided the highest stability for UCNPs ($NaYF_4$: 20%Yb^{3+}, 2%Er^{3+}).

Chapter 3 reports the set of published results (Nano Letter, 2021) of using UCNPs ($NaYF_4$: 20%Yb^{3+}, 2%Er^{3+})-based thermometer to study the temperature changes of mitochondria in living Hela cells. By coating with a crosslinked network, the UCNPs ($NaYF_4$: 20%Yb^{3+}, 2%Er^{3+})-based thermometer with long-term stability is independent of probe concentration and medium conditions. By linking with lipophilic TPP cations, the UCNPs ($NaYF_4$: 20%Yb^{3+}, 2%Er^{3+}) can be delivered to and accumulate in mitochondria. The thermal dynamics of mitochondria were monitored by treating the cells with chemical and nutrient stimulation. The relative sensing sensitivity was 3.2% K^{-1} in HeLa cells and the cells displayed distinct response time and thermal dynamic profiles under the stimulation of high glucose, lipid, Ca^{2+} shock, and the inhibitor of oxidative phosphorylation.

Chapter 4 demonstrates two temperature-sensitive UCNPs ($NaYF_4$: 20%Yb^{3+}, 2%Er^{3+})-based temperature probes with high-density organelle-target modifications that can be used to monitor the thermal generation and transfer between lysosomes and mitochondria. By improving the surface modification, UCNPs ($NaYF_4$: 20%Yb^{3+}, 2%Er^{3+})-based thermometers can be localized to the specific organelles through cascade-targeting. The relative temperature sensing sensitivity was 2.7% K^{-1} and uncertainty was 0.8 K in HeLa cells. Under the chemical stimulation to the cells, I observed the opposite thermal dynamics of lysosomes and mitochondria.

Chapter 5 summarizes this thesis and provides future directions from this research. The surface modification with enriched conjugation sites suggests a new insight to get UCNPs ($NaYF_4$: 20%Yb^{3+}, 2%Er^{3+}) with excellent dispersibility in the physiological buffer and organelle's targeting specificity. The ability of intracellular temperature mapping suggests that UCNPs ($NaYF_4$: 20%Yb^{3+}, 2%Er^{3+}) work as a powerful platform for multifunctional imaging and sensing. Moreover, this chapter provides several new potential directions of using luminescence thermometers for future biomedical applications.

Chapter 2 **Investigation of Colloidal Stability of Hydrophilic Upconversion Nanoparticles**

2.1 Background

With the advance of materials science, nanoparticles have been widely applied in biomedical applications, such as QDs, metal nanoparticles, and UCNPs. However, these inorganic nanoparticles cannot be applied in biomedical applications directly. They require further surface modification to be dispersible and targetable in the living cells, tissues, and organs [165]. The improper nanoparticles surface modification leads to aggregations in the physiological buffer and poor reproducibility. Therefore, I started to investigate the stability of colloidal nanoparticles after different strategies of surface modification. According to the surface functionalization strategies, PDA, AEP, alendronate, 3,4-DHCA, and copolymer were chosen to modify the surface of UCNPs ($NaYF_4$: 20%Yb^{3+}, 2%Er^{3+}) (**Figure 2-1**). PDA, AEP, and alendronate provide nanoparticles surface with amine groups. 3,4-DHCA and copolymer provide nanoparticles surface with carboxyl groups.

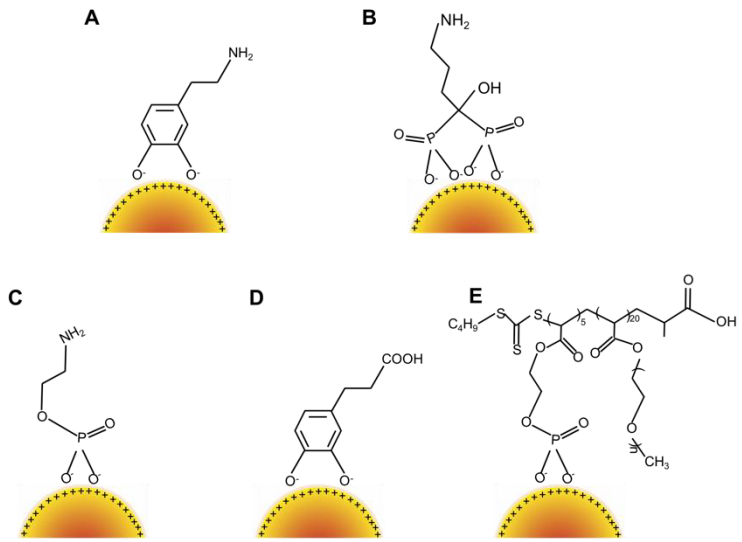

Figure 2-1 Schematic of UCNPs ($NaYF_4$: 20%Yb^{3+}, 2%Er^{3+}) with five different surface modifications. *A. UCNPs ($NaYF_4$: 20%Yb^{3+}, 2%Er^{3+}) coated with PDA. B. UCNPs ($NaYF_4$: 20%Yb^{3+}, 2%Er^{3+}) coated with alendronate. C. UCNPs ($NaYF_4$: 20%Yb^{3+}, 2%Er^{3+}) coated with AEP. D. UCNPs ($NaYF_4$: 20%Yb^{3+}, 2%Er^{3+}) coated with 3,4-DHCA. E. UCNPs ($NaYF_4$: 20%Yb^{3+}, 2%Er^{3+}) coated with copolymer.*

- **Polydopamine (UCNPs@PDA)**

Polydopamine (PDA) is a synthetic polymer, obtained by the oxidization of dopamine [208]. In 2007, Lee *et al.* developed a simple method by coating inorganic and organic nanoparticles with dopamine self-polymerization films, which were inspired by mussels [209]. Then nanoparticles coated with PDA can serve as a platform for further conjugation with bioactive molecules. A large number of amine groups provided by PDA on the surface of nanoparticles enhance the loading capability of specific biomedical moieties [208]. Li and co-workers synthesized dopamine-derived PDA nanoparticles, loading the anticancer drug doxorubicin to investigate the drug resistance [210]. Zhong *et al.* used PDA as a carrier for loading radionuclides and cancer drugs simultaneously, which achieved an excellent cancer treatment with a bit of toxicity in the animals' experiments [211]. In conclusion, the easy synthesis protocol, simple modification, good biocompatibility, and high drug loading efficiency make PDA popular in surface modification of nanoparticles [211].

- **Alendronate (UCNPs@Alendronate)**

Duong *et al.* proposed that polymers with multiple anchoring negatively charged phosphate provide excellent colloidal stability for UCNPs ($NaYF_4$: 20%Yb^{3+}, 2%Er^{3+}) [167]. Alendronate has two anchoring negatively charged phosphate, which can be attached to the surface of UCNPs tightly (**Figure 2-1B**). Nsubuga *et al.* studied the colloidal stability of UCNPs (β-$NaYF_4$:1%Nd^{3+}, 20%Yb^{3+}, 2%Er^{3+} @$NaYF_4$: 25%Nd^{3+}) capped with alendronate systematically [168]. UCNPs@Alendronate They display the long-term stability in the physiological buffer, and there is no formation of biomolecular corona after exposure to human serum [168]. The amine groups provided by alendronate enable further functionalization with biomolecules, such as DNA, enzymes, peptides, and antibodies [168].

- **2-aminoethyl dihydrogen phosphate (UCNPs@AEP)**

2-aminoethyl dihydrogen phosphate (AEP) is composed of one phosphate and one amine group. The negatively charged phosphate serves as an anchor on attaching to the UCNPs ($NaYF_4$: 20%Yb^{3+}, 2%Er^{3+}) surface, and the positive amine group works as a linker to conjugate with some functional biomolecules. Gu *et al.* investigated the effect of AEP surface modification on cellular uptake, demonstrating a low nonspecific

binding and cytotoxicity [212].

- **3,4-Dihydroxyhydrocinnamic acid (3,4-DHCA) (UCNPs@3,4-DHCA)**

3,4-DHCA contains two hydroxyl groups and one carboxyl group. The OA on the UCNPs ($NaYF_4$: 20%Yb^{3+}, 2%Er^{3+}) surface can be replaced by hydroxyl groups through the ligand exchange approach. UCNPs@3,4-DHCA disperses in the aqueous buffer and carboxyl groups on the UCNPs@3,4-DHCA surface are ready for subsequent bioconjugation [213].

- **$PEGMEMA_{80}$-*b*-$EGMP_3$ di-block copolymer (UCNPs@copolymer)**

$PEGMEMA_{80}$-*b*-$EGMP_3$ di-block copolymer was first reported by Hien *et al.* in 2018 [167]. In this research, three di-block copolymers bearing phosphate, carboxylic, or sulphonic acid were synthesized by reversible addition fragmentation chain transfer (RAFT) [167]. She investigated colloidal stability and found that di-block copolymer with phosphate acid could provide the highest long-term stability in the physiological buffer [167]. This copolymer contains five phosphate groups and one carboxyl group. The five phosphate acids can replace the oleic acid totally by ligand exchange [167].

I investigated the stability and dispersity of UCNPs ($NaYF_4$: 20%Yb^{3+}, 2%Er^{3+}) with the above five various surface modification before starting the measurements of intracellular temperature.

2.2 Methodology

2.2.1 Materials

For UCNPs synthesis, yttrium(III) chloride hexahydrate (YCl_3•$6H_2O$, 99.99%), ytterbium chloride hexahydrate ($YbCl_3$•$6H_2O$, 99.99%), erbium chloride hexahydrate ($ErCl_3$•$6H_2O$, 99.9%), ethanol, cyclohexane, 1-octadecane, and OA were purchased from Sigma-Aldrich. For surface modification of UCNPs, $PEGMEMA_{80}$-*b*-$EGMP_3$ was synthesized by Lin Zhang (PhD candidate in the University of New South Wales from Martina Stenzel group). TEOS, polydopamine (PDA), AEP, alendronate, 3,4-DHCA, copolymer, 1-Ethyl-3-(3-dimethylamino-propyl)-carbodiimide (EDC), N-Hydroxysuccinimide (NHS), MES buffer, HEPES buffer, Tetrahydrofuran (THF), N, N-Dimethylformamide (DMF), $NOBF_4$, hexane, chloroform, and NaOH were purchased from Sigma-Aldrich with reagent grade or higher. For cell experiments, Dulbecco's

Modified Eagle Medium (DMEM), fetal bovine serum (FBS), Phosphate-Buffered Saline (PBS), trypsin, T75 flasks, and T25 flasks were purchased from ThermoFisher. Penicillin-Streptomycin (PS), 4%PFA, Triton X-100, and bovine serum albumin (BSA) were purchased from Sigma-Aldrich with reagent grade or higher.

2.2.2 Synthesis of UCNPs ($NaYF_4$: 20%Yb^{3+}, 2%Er^{3+})

UCNPs ($NaYF_4$: 20%Yb^{3+}, 2%Er^{3+}) were synthesized following the previously reported protocols with some modification [214]. In a typical process, 6 mL of OA and 15 mL of 1-octadecane were added into a 50 mL round bottom flask with three necks, and then added 1.95 mL of YCl_3 stock solution (0.4 M in methanol), 1.0 mL of $YbCl_3$ stock solution (0.2 M in methanol), and 0.2 mL of $ErCl_3$ stock solution (0.1 M in methanol). The mixture was stirred under argon protection and then heated to 160 °C to get rid of methanol and H_2O. Second, 0.1 g of NaOH and 0.14815 g of NH_4F were dissolved in the 5 mL of methanol and then added into the mixture until it cooled down to 30 °C and stirred for 30 minutes. Subsequently, the mixture was heated to 100 °C for 30 minutes and then heated to 300 °C for 1.5 hours. Finally, 5 mL of ethanol was added into the mixture to precipitate UCNPs ($NaYF_4$: 20%Yb^{3+}, 2%Er^{3+}). UCNPs ($NaYF_4$: 20%Yb^{3+}, 2%Er^{3+}) were washed three times with ethanol and cyclohexane. After washing, the product UCNPs ($NaYF_4$: 20%Yb^{3+}, 2%Er^{3+}) were dispersed in cyclohexane.

2.2.3 Coating UCNPs ($NaYF_4$: 20%Yb^{3+}, 2%Er^{3+}) with PDA

UCNPs ($NaYF_4$: 20%Yb^{3+}, 2%Er^{3+}) coated with PDA were synthesized following the previously reported protocols with some modification [215]. PDA (100 mg) was first dissolved in 500 μL of deionized water, followed by adding 12 mL of THF. The above mixture was transferred to a 25 mL three-necked flask and heated to 50 °C under argon flow. Then 1 mL of UCNPs (1 mM) in cyclohexane was centrifuged at 9000 g for 10 minutes, and then the precipitation was dissolved in 2 mL of THF. UCNPs ($NaYF_4$: 20%Yb^{3+}, 2%Er^{3+}) dispersed in THF were added into the mixture, and the reaction was incubated at 50 °C for 4.5 hours. After incubation, 200 μL of HCl (1 M) was added to the mixtures to form a precipitate, which was collected by centrifugation and redispersed in 7 mL of ultrapure Millipore water (18.2 Ω) in a 25 mL bottle. UCNPs@PDA was washed with ethanol for three times and stored in ultrapure Millipore water at 4 ºC for further use.

2.2.4 Coating UCNPs ($NaYF_4$: 20%Yb^{3+}, 2%Er^{3+}) with Alendronate

UCNPs ($NaYF_4$: 20%Yb^{3+}, 2%Er^{3+}) coated with alendronate were synthesized following the previously reported protocols with some modification [168]. 30 mg of $NOBF_4$ in 3 mL of DMF and 3 mL UCNPs (1 mM) in cyclohexane were mixed and stirred vigorously for 10 minutes at room temperature. Then 20 mL of chloroform was added to the mixture before centrifugation at 23,830g for 15 minutes. The washing step with chloroform was repeated twice. Then the transparent pellet was dispersed in 5 mL of DMF by sonication and centrifuged at 1000 g for 3 minutes to remove large aggregates. The BF_4^--coated UCNPs ($NaYF_4$: 20%Yb^{3+}, 2%Er^{3+}) stock solution was mixed with alendronate in 3 mL of 1M $NaHCO_3$ solution and stirred vigorously for 2 hours. The final turbid dispersion was washed with water for three times and re-dispersed in ultrapure Millipore water.

2.2.5 Coating UCNPs ($NaYF_4$: 20%Yb^{3+}, 2%Er^{3+}) with AEP/ 3,4-DHCA/Copolymer

UCNPs ($NaYF_4$: 20%Yb^{3+}, 2%Er^{3+}) coated with AEP/ 3,4-DHCA/Copolymer were synthesized following the previously reported protocols with some modification [167]. 5 mg of UCNPs ($NaYF_4$: 20%Yb^{3+}, 2%Er^{3+}) and 5 mg of AEP/ 3,4-DHCA/Copolymer were dissolved in 1 mL of THF and then shaken at room temperature for 12 hours. Next, the mixtures were washed with THF twice and deionized water twice. Finally, the hydrophilic UCNPs ($NaYF_4$: 20%Yb^{3+}, 2%Er^{3+}) were dissolved in 0.5 mL of ultrapure Millipore water for further use.

2.2.6 Characterization

The morphology of UCNPs was characterized using the FEI Tecnai transmission electron microscopy (FEI, U.S.A.). The hydrodynamic size and zeta potential of UCNPs were determined by a zeta sizer nano (Malvern, U.K.).

2.2.7 Bioconjugation of streptavidin with UCNPs@copolymer

1 mg of UCNPs@copolymer, 2 mg of EDC, and 2 mg of NHS were dissolved in 0.5 mL of MES buffer (20 mM, pH 6.0) and shaken for 30 minutes for activation. After centrifugation, the activated products and 0.1 mg of streptavidin (SA) were dissolved in 1 mL of pH 7.02 HEPES buffer and reacted overnight. On the second day, reaction

products were washed 3 times with deionized water at 14680 rpm for 20 minutes. Then nanoparticles were centrifuged at 4400 rpm for 5 minutes to remove the large aggregates. Finally, UCNPs@copolymer conjugated with streptavidin (UCNPs@SA) was stocked in 0.5 mL of deionized water.

2.2.8 Cell Culture

HeLa cells stored in the liquid nitrogen were warmed in a 37 °C bath incubator. Then HeLa cells were mixed with 15 mL of DMEM containing 10%FBS in the T75. After 48 hours, the culture medium was removed and 3 mL of pre-warmed trypsin was added. Five minutes later, 9 mL of DMEM containing 10%FBS was added into the flask to neutralize the trypsin. Finally, 1 mL of cell suspension was transferred to T25 flask and added 4 mL of DMEM containing 10%FBS, then cultured in a 37 °C incubator.

2.2.9 Immunostaining of microtubules with UCNPs

The HeLa cells were seeded on the fluoro-dish (35 mm) at 10^5 cell density and incubated in DMEM medium containing 10% v/v FBS for 12 hours. Then the cells were washed 3 times with PBS and fixed with 200 μL of 4% PFA for 15 minutes at room temperature. Next, the cells were permeabilized with 500 μL of 0.5% Triton X-100 for 5 minutes and further blocked with a blocking buffer containing 5% BSA and 0.5% Triton X-100 for 30 minutes at room temperature. Then the cells were incubated with 200 μL of anti-α-tubulin(biotin) at 4 °C overnight. The second day, UCNPs@SA solution containing 0.5% BSA, 0.5% Triton X-100 and 2 mM NaF were incubated with HeLa cells for 1 hour. The cells were ready for imaging after washing three times with PBS.

2.3 Results and Discussion

2.3.1 Synthesis and Characterization of UCNPs@OA

The temperature in the synthesis of UCNPs ($NaYF_4$: 20%Yb^{3+}, 2%Er^{3+}) is crucial to determine the size and morphology. As shown in **Figure 2-2A**, the morphology of UCNPs was not uniform, and the size was in the range of 10 to 30 nm. This was because unstable temperature control at 300 °C during the growth. The lower or higher temperature during the crystal growth might lead to the UCNPs in large size variations. Then, the temperature was kept at 300 °C carefully in the second synthesis. However,

the morphologies were hexagonal and rectangle (**Figure 2-2B**). The size was larger than 100 nm, which was too big for cell experiments. This might be attributed to the over-adding of NaOH-NH_4F methanol solution. The excessive amount of NaOH-NH_4F methanol solution would lead to the larger size of UCNPs.

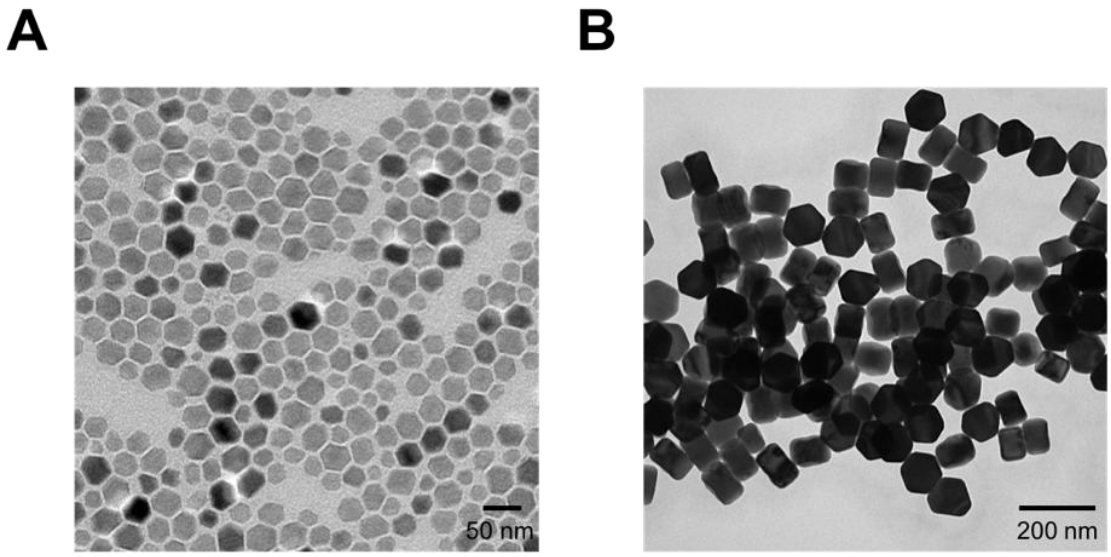

Figure 2-2 TEM images of as-synthesized UCNPs ($NaYF_4$: 20%Yb^{3+}, 2%Er^{3+}) capped with OA. *A. TEM image of UCNPs ($NaYF_4$: 20%Yb^{3+}, 2%Er^{3+}) synthesized under temperature over 300 °C. B. TEM image of UCNPs ($NaYF_4$: 20%Yb^{3+}, 2%Er^{3+}) synthesized with excessive amount of NaOH-NH_4F methanol solution.*

Taking care of the amount of NaOH-NH_4F methanol solution, the growth temperature and heating time, uniform UCNPs ($NaYF_4$: 20%Yb^{3+}, 2%Er^{3+}) with good morphology were obtained (**Figure 2-3A**). The size was around 25-30 nm. Then I repeated the experiment of UCNPs ($NaYF_4$: 20%Yb^{3+}, 2%Er^{3+}) synthesis three times. All the three batches of UCNPs ($NaYF_4$: 20%Yb^{3+}, 2%Er^{3+}) showed good morphology and uniform size (**Figure 2-3B-D**). While the monodispersity of them were improved gradually, which is dependent on the coverage of surface ligand (OA) on these UCNPs ($NaYF_4$: 20%Yb^{3+}, 2%Er^{3+}). The coverage degree is highly affected by the adding amount of washing solvents and washing times.

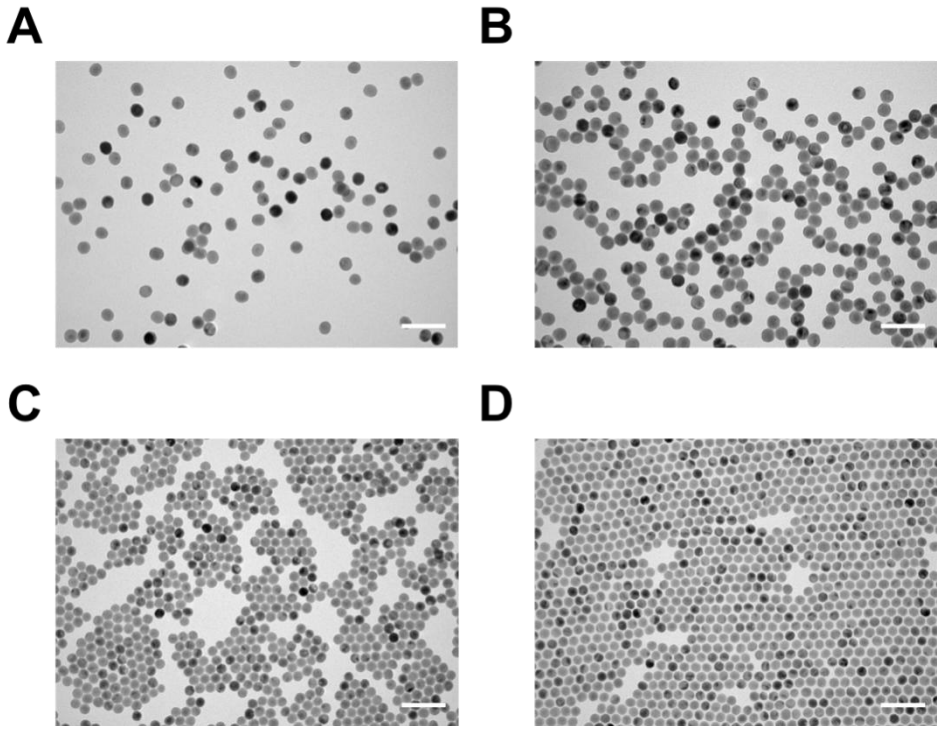

Figure 2-3 TEM images of as-synthesized UCNPs (NaYF$_4$: 20%Yb^{3+}, 2%Er^{3+}). *A-D represents four batches of UCNPs (NaYF$_4$: 20%Yb^{3+}, 2%Er^{3+}) synthesized under the same condition . Scale bar: 100 nm.*

The size and molarity of UCNPs@OA were summarized in **Table 2-1**. Mackenzie *et al* presented a theory to estimate the molecular weight of UCNPs with hexagonal crystal structure [216]. The molecular weights of UCNPs in 25 nm and 30 nm were 25 MDa and 40 MDa from this theory, and the volume of UCNPs(V_{UCNPl}) was calculated by [216]

$$V_{UCNP} = \frac{4}{3}\pi r^3 \qquad (2)$$

where r is the radius of the UCNP [216]. Thus, the molarity of UCNPs can be calculated and summarized in Table 2-1.

Table 2-1 Quantitative analysis of as-synthesized UCNPs@OA.

UCNPs@OA	Diameter (nm)	Concentration (mg/mL)	Molecular Weight (MDa)	Molarity (pmol/μL)
No.3	~ 30	6.8	40	0.17
No.4	~ 30	14.8	40	0.37
No.5	~ 25	14.4	25	0.576
No.6	~ 25	15	25	0.6

2.3.2 Characterization of Hydrophilic UCNPs ($NaYF_4$: 20%Yb^{3+}, 2%Er^{3+})

2.3.2.1 Coating UCNPs ($NaYF_4$: 20%Yb^{3+}, 2%Er^{3+}) with PDA/ Alendronate/AEP

Then UCNPs ($NaYF_4$: 20%Yb^{3+}, 2%Er^{3+}) modified with PDA, alendronate, and AEP were explored. TEM images showed that the morphology and the size were uniform with no obvious variation between UCNPs@OA and UCNPs@PDA (**Figure 2-4A-B**). DLS results proved that the UCNPs@PDA had a good distribution in the PBS buffer (pH~7.4) with the hydrodynamic size of 36.17±4.55 nm. The UCNPs@PDA dispersed well in the PBS buffer when prepared (**Figure 2-5A)**, but significantly aggregated after 24 hours (**Figure 2-5B)**. The average zeta potential was +29.7 ± 2.62 mV, which was beneficial to delivering nanoparticles into living cells (**Table 2-2**). Then I further explored the stability of newly prepared UCNPs@PDA by incubation with HeLa cells for 6 hours. As shown in **Figure 2-6**, there are only several UCNPs@PDA spots in the living HeLa cell. The four big green dots indicate the aggregation of UCNPs@PDA in the living HeLa cell. The FBS in the culture medium and the metabolite of cells might have an effect on the stability of UCNPs@PDA.

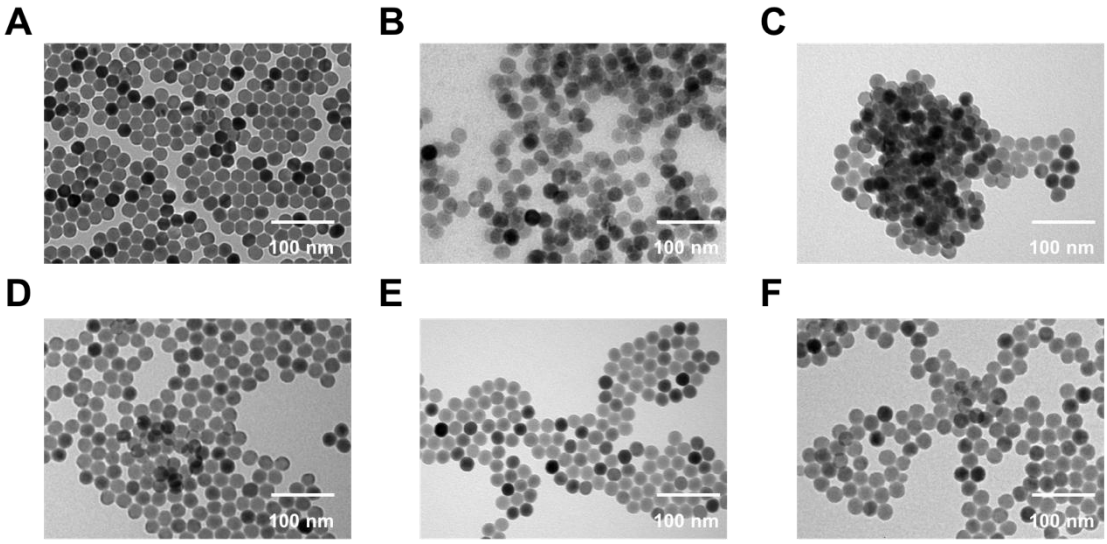

Figure 2-4 TEM images of five ligands capped UCNPs ($NaYF_4$: 20%Yb^{3+}, 2%Er^{3+}). *A. TEM image of UCNPs@OA. B. TEM image of UCNPs@PDA. C. TEM image of UCNPs@Alendronate. D. TEM image of UCNPs@AEP. E. TEM image of UCNPs@3,4-DHCA. F. TEM image of UCNPs@copolymer.*

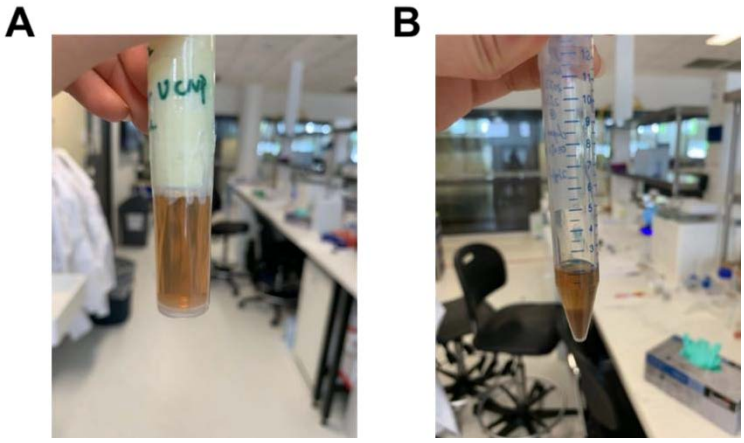

Figure 2-5 Images of UCNPs@PDA prepared after 1 hour (A) and 24 hours (B). The precipitant was observed at the bottom of the tube after 24 hours.

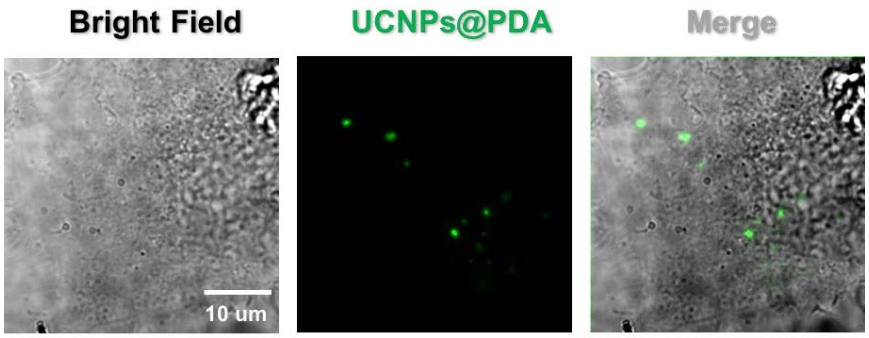

Figure 2-6 Images of UCNPs@PDA incubated with HeLa cells for 6 hours. *The left image is bright field of a HeLa cell under TIRF microscope. The middle is the luminescent image of UCNPs@PDA in HeLa cells under 980 nm NIR excitation. The right is the merged image of HeLa cells under bright filed (left) and luminescent image of UCNPs@PDA (middle). Scale bar: 10 μm.*

Another ligand providing amine groups on the UCNPs ($NaYF_4$: 20%Yb^{3+}, 2%Er^{3+}) surface is alendronate. UCNPs ($NaYF_4$: 20%Yb^{3+}, 2%Er^{3+}) modified with alendronate aggregated under TEM (**Figure 2-5C**). DLS result presented that the average size was over 200 nm and the average zeta potential was +36.4 ± 0.95 mV (**Table 2-2**). Although it showed a higher positive zeta potential, the distribution of UCNPs@Alendronate in the physiological buffer (PBS buffer, pH~7.4) was too poor to work as a probe in the living cells.

AEP also provides UCNPs ($NaYF_4$: 20%Yb^{3+}, 2%Er^{3+}) surface with amine groups by ligand exchange. UCNPs@AEP had a similar performance to UCNPs@Alendronate (**Figure 2-5D**). The nanoparticles showed a high aggregation in the PBS buffer (pH~7.4) with more than 200 nm in size, which could not satisfy the requirement of biomedical application (**Table 2-2**).

In conclusion, UCNPs ($NaYF_4$: 20%Yb^{3+}, 2%Er^{3+}) caped with ligands providing amine groups, e.g. PDA, alendronate, and AEP, gave a higher positive surface zeta potential (**Table 2-2**). The potential of the cell membrane is -30 to -60 mV [190]. The large membrane potential can drive nanoparticles into the cell. However, the poor distribution and low long-term colloidal stability limit their application in the living cell. Compared with UCNPs@Alendronate and UCNPs@AEP, UCNPs@PDA showed a good colloidal stability in the water. However, UCNPs@PDA preferred to aggregate when incubating with living Hela cells.

2.3.2.2 Coating UCNPs ($NaYF_4$: 20%Yb^{3+}, 2%Er^{3+}) with 3,4-DHCA/Copolymer

3,4-DHCA and copolymer were chosen as the representatives of ligands with carboxyl groups. UCNPs ($NaYF_4$: 20%Yb^{3+}, 2%Er^{3+}) capped with these two ligands were uniform in the size (**Figure 2-5E-F**). For UCNPs@3,4-DHCA, the average size and zeta potential were 65.35 ± 0.82 nm and -10.85 ± 3.27 mV, respectively. For UCNPs@copolymer, the average size and zeta potential were 59.72 ± 0.16 nm and -18.37 ± 1.65 mV, respectively. The surface zeta potential of UCNPs@copolymer was lower than that of UCNPs@3,4-DHCA, indicating the surface of UCNPs@copolymer had more carboxyl groups. The higher carboxyl groups would enhance the efficiency of conjugation with biomolecules.

Apart from the characterization by TEM, DLS, and zeta potential, the long-term stability of nanoparticles was checked by incubation with living cells. UCNPs@3,4-DHCA and UCNPs@copolymer were incubated with HeLa cells for 6 hours, respectively. In the merged image of HeLa cells under bright field and luminescent UCNPs@3,4-DHCA (**Figure 2-7)**, it was obvious that some UCNPs@3,4-DHCA were not swallowed by the living HeLa cells. The red frame in **Figure 2-7** showed the aggregation of UCNPs@3,4-DHCA in the living HeLa cell. In the merged image of HeLa cells under bright field and luminescent UCNPs@copolymer (**Figure 2-7)**, UCNPs@copolymer exhibited a good distribution in the culture medium. Lots of UCNPs@copolymer were swallowed by the living HeLa cells. Thus, the copolymer was used for subsequent cell experiments.

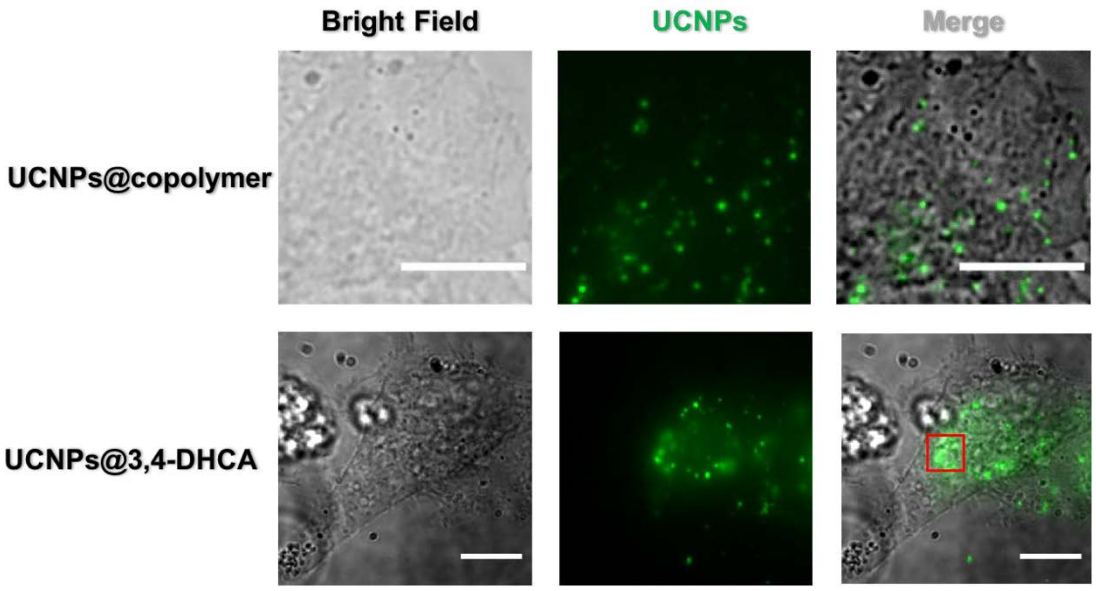

Figure 2-7 Images of UCNPs@copolymer (up) and UCNPs@3,4-DHCA (bottom) incubated with HeLa cells for 6 hours. *The left images are bright field of HeLa cells under TIRF microscope. The middle is the luminescent images of UCNPs@copolymer (up) and UCNPs@3,4-DHCA (bottom) in HeLa cells under 980 nm NIR excitation. The right is the merged image of HeLa cells under bright filed (left) and luminescent images (middle) of UCNPs@copolymer (up) and UCNPs@3,4-DHCA (bottom). Scale bar: 10 μm.*

Table 2- 2 The size and Zeta potential of five ligands capped UCNPs.

Ligand	Surface Functional Group	Hydrodynamic Size (nm)	Zeta Potential (mV)
UCNPs@PDA	$-NH_2$	36.17±4.55	+29.7±2.62
UCNPs@Alendronate	$-NH_2$	>200 nm	+36.4±0.95
UCNPs@AEP	$-NH_2$	>200 nm	+30.3±1.34
UCNPs@3,4-DHCA	-COOH	65.35±0.82	-10.85±3.27
UCNPs@copolymer	-COOH	59.72±0.16	-18.37±1.65

2.3.3 Microtubules Labelling

Microtubule plays a crucial role in cellular activities, such as intracellular transportation and cell division [217]. It is the major constituent of the cytoskeleton, which is involved

in the maintaining of cell structure. Microtubules are hollow tubes that are composed of alpha- and beta- tubulin [218]. They are the largest structures in the cytoskeleton at about 24 nm in thickness [219].

With the advance in super-resolution microscope and materials science, a wide range of ultrastructure of organelles has been observed [220]. Stephan *et al.* visualized the dynamics of mitochondrial cristae in live cells by stimulated emission depletion (STED) nanoscopy in 2019 [221]. In addition, some luminescent nano-materials have been used to label the intracellular ultrastructures [222]. Compared with traditional fluorescent dyes, they are optical stable and chemical stable with no bleaching or blinking [222]. Among these luminescent nano-materials, UCNPs have attracted much attention because of their excellent optical characteristics [222-225]. For example, excitation by NIR light hardly induces cellular autofluorescence and photo damage. To further explore the ability of hydrophilic UCNPs@copolymer in biomedical application, I tried to label microtubules in the fixed HeLa cells by using UCNPs@copolymer.

I synthesized UCNPs doped with 20% Yb and 8% Tm. UCNPs doped with Tm are ideal for super-resolution imaging [225, 226]. Then the hydrophobic UCNPs capped with OA were first modified with copolymer by ligand exchange, and then conjugated with SA (**Figure 2-8**). TEM results showed the morphology uniformity of the UCNPs before and after the surface functionalization of copolymer (**Figure 2-9A-B**). However, the UCNPs@copolymer aggregated after the conjugation with SA (**Figure 2-9C)**. The peak values of hydrodynamic size increased from 25 ± 5.87 nm to 42.57 ± 2.98 nm and 107.32 ± 7.42 nm after each step of surface modifications, suggesting the aggregation of UCNPs@SA (**Table 2-3**).

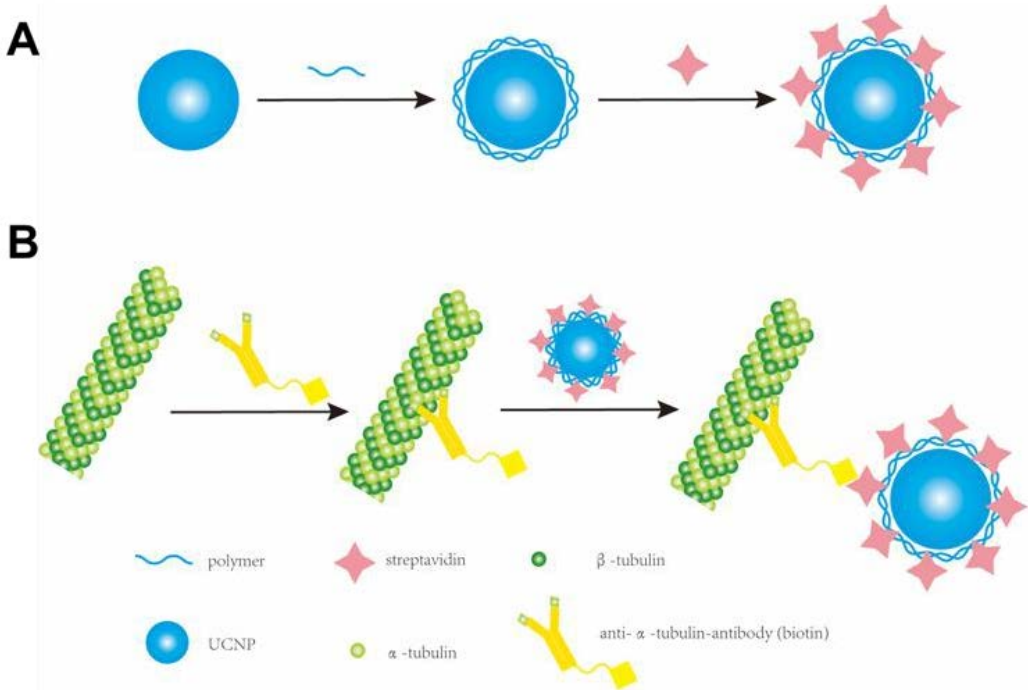

Figure 2-8 Schematic of microtubules labelling. *A. The surface functionalization of UCNPs ($NaYF_4$: 20%Yb^{3+}, 8%Tm^{3+}). UCNPs ($NaYF_4$: 20%Yb^{3+}, 8%Tm^{3+}) are first modified with copolymer and then conjugated with streptavidin. B. Immunostaining of microtubules by UCNPs@SA. Microtubules are incubated with primary antibody (anti- α -tubulin-antibody-biotin), and then incubated with UCNPs@SA.*

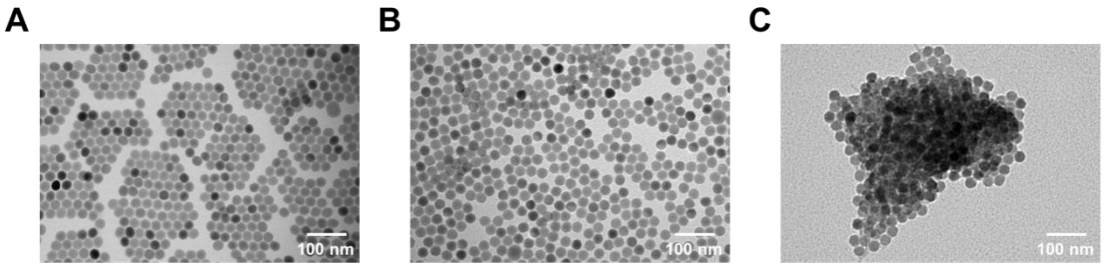

Figure 2-9 TEM images of UCNPs@OA (left), UCNPs@copolymer (middle), and UCNPs@SA (right).

Table 2-3 The DLS results for UCNPs with different modification.

Ligand	Hydrodynamic size (nm)
Bare UCNPs	25±5.87
UCNPs@copolymer	42.57±2.98
UCNPs@SA	107.32±7.42

The fixed HeLa cells were first permeabilized by Triton X-100 and then incubated with anti-α-tubulin (biotion). One SA can specifically bind to four biotins stably [227]. Then, UCNPs functionalized with SA were added to the fixed cells for 1 hour. Finally, the cells were imaged by a custom-made STED microscope [225]. As shown in **Figure 2-10**, it is hard to observe the structure of microtubules. Then I optimised the concentrations of anti-α-tubulin (biotion) and UCNPs@SA, the incubation time, and the permeabilization time. However, there was no significant improvement in the labelling efficiency. It was caused by low conjugation efficiency between UCNPs@copolymer and SA. From the chemical structure of copolymer, there was only one carboxyl group, which might limit the loading efficiency of SA.

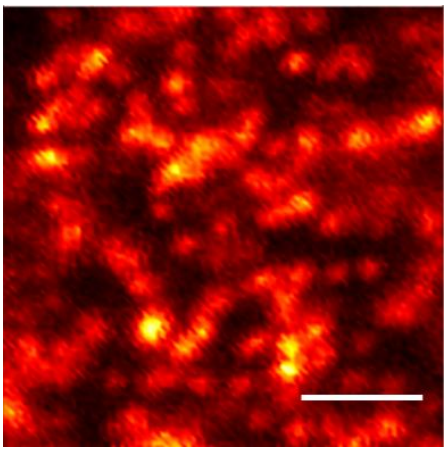

Figure 2-10 Images of microtubules labelled by UCNPs@SA. *Imaging conditions: 980 nm excitation beam with the power density of 10 mw; the emissive optical signal was collected after an 800 nm shortpass filter. Scale bar: 100 nm.*

2.4 Conclusion and Discussion

By optimization of the method for nanoparticles surface modification and colloidal stability investigation of the five surface modifications (PDA, AEP, alendronate, 3,4-DHCA, and copolymer), I found that the copolymer had a good distribution in the aqueous solution. The other five ligands dispersed well in the buffer when just prepared, but preferred to aggregate after a long time or incubation with cells.

By labelling microtubules with UCNPs ($NaYF_4$: 20% Yb, 8% Tm), I learned that not only the colloidal stability in the buffer of nanoparticles was important, the conjugation

efficiency with antibodies also played a crucial role in the biomedical application. Enhancing the loading efficiency of antibody were able to improve the microtubule labelling density. The perfect surface modification ligands are anticipated to have several phosphate groups to strongly bind with the surface exposed lanthanide ions on a UCNP ($NaYF_4$: 20% Yb, 8% Tm) and have many functional groups such as amine or carboxyl groups to link with antibodies or biomolecules. Moreover, it is easier for hydrophilic UCNPs to conjugate with small biomolecules than antibodies. The antibody is a kind of protein with a 3D conformation structure. Protein conformation changes in the buffer with different pH, which results in the functional group inward [228]. And the size of UCNPs (>30 nm) was too big to closely attach to the antigen during the microtubule labelling because of the steric hindrance. Nanoparticles with the diameter less than 10 nm will be ideal to label microtubules.

Chapter 3 Quantitatively Monitoring in situ Mitochondrial Temperature Dynamics by Upconversion Nanoparticles

The contents of this chapter adapted with permission from:

Xiangjun Di, et al., "Quantitatively Monitoring in situ Mitochondrial Thermal Dynamics by Upconversion Nanoparticles." *Nano Letters*. 2021, 21, 4, 1651–1658.

3.1 Abstract

Temperature dynamics reflect the physiological conditions of cells and organisms. Mitochondria regulate temperature dynamics in living cells, as they oxidize the respiratory substrates and synthesize ATP, with heat being released as a by-product of active metabolism.

Here, we report an UCNPs ($NaYF_4$: 20%Yb^{3+}, 2%Er^{3+})-based thermometer that allows *in situ* thermal dynamics monitoring of mitochondria in living cells. We demonstrate that the upconversion thermometers can efficiently target mitochondria and the temperature-responsive feature is independent of probe concentration and medium conditions. The relative sensing sensitivity of 3.2% K^{-1} in HeLa cells allows us to measure the mitochondrial temperature difference through the stimulations of high glucose, lipid, Ca^{2+} shock, and the inhibitor of oxidative phosphorylation. Moreover, cells display distinct response time and thermal dynamics profiles under different stimulations, which highlights the potential applications of this thermometer to study *in situ* vital processes related to mitochondrial metabolism pathways and interactions between organelles.

3.2 Background

Intracellular temperature is a crucial parameter to assess the status of living cells and organisms [229]. The activations of a wide range of chemical reactions in the living cell, especially in the mitochondria, produce a large amount of energy and cause the change of temperature. Mitochondria provide energy to the living cell through the oxidative phosphorylation process [230]. During this chemical reaction, about 67% of the

energy is used to synthesize ATP and the other ~33% dissipates in the form of heat [231]. Failure

to produce ATP will cause a change of mitochondria temperature so that the variation of mitochondria temperature indicates the cellular metabolism status [232]. Given its importance to fundamental studies, disease diagnosis, and therapy, accurate and specific temperature sensing at subcellular scale remains as a challenge due to the lack of noninvasive sensing probes [233-236].

Luminescence thermometry has emerged to noninvasively reveal the localized intracellular temperature in living cells [237]. Temperature responsive luminescent materials [238-240], including small molecules [241], fluorescent polymers [229], fluorescent proteins [118], and inorganic particles [138, 242], have been extensively explored. For example, Homma *et al*. developed a ratiometric thermo-sensor by using thermo-sensitive rhodamine B and thermo-insensitive CS NIR dye that enable the temperature monitoring of mitochondria under chemical stimulation [241]. Yang *et al*. designed photoluminescence spectral shifts quantum dots (QDots) to monitor temperature change in NIH/3T3 cells under Ca^{2+} stress and cold shock [138]. However, due to the concerns of photo-bleaching and photo-blinking issues, these luminescent thermometers are limited in the area of long-term tracking and sensing.

UCNPs ($NaYF_4$: 20%Yb^{3+}, 2%Er^{3+}) with unique nanophotonic characteristics are suitable for long-term bio-sensing, bio-imaging [226, 243], and photothermal therapy [244], as UCNPs are optically stable [245] and biologically compatible [246]. The anti-Stokes emission process, upon NIR light excitation, avoids cellular autofluorescence and can minimize the potential photo-damage to cells, as well as allowing deep tissue penetration [246]. UCNPs ($NaYF_4$: 20%Yb^{3+}, 2%Er^{3+})-based thermometers have been first demonstrated to monitor the temperature change of living cells upon external heating [135]. UCNPs doped with erbium ions display a temperature-dependent luminescence following the Boltzmann distribution [247],

$$\frac{I_{525}}{I_{545}} = C exp\left(-\frac{\Delta E}{kT}\right) \qquad (1)$$

where I_{525} and I_{545} are the integrated luminescent intensities around 525 nm and 545 nm emission peak, respectively; C is a constant; ΔE is the $^4S_{3/2}$ to $^2H_{11/2}$ energy difference of the Er^{3+} ion; k is the Boltzmann constant and T is the absolute temperature. Recently, UCNPs-based thermometers have been further applied for *in vivo* temperature monitoring in small animal imaging [243, 248]. Several other remarkable works

include the Nd^{3+} doped UCNPs to sense temperature changes in NIH/3T3 cells [243] and a hybrid structure composed of PbS QDs and Tm-doped UCNPs to realize intratumoral monitor *in vivo* [248].

Though clear advances have been made, there remains a big gap to enable UCNPs-based thermometers with *in situ* organelle targeting capability for localized intracellular temperature sensing. The key is to functionalize UCNPs to become biocompatible and specific to target organelle otherwise, the relatively large UCNPs (e.g., 20 nm) with positive charges from the trivalent lanthanide ions exposed on the surface tend to be aggregated, less stable in the physiological environment, and cause the issue of non-specific bindings [249].

In this study, by using mitochondria-targeting, temperature-dependent, and non-photobleaching UCNPs ($NaYF_4$: 20%Yb^{3+}, 2%Er^{3+}), I monitored the *in situ* mitochondrial temperature dynamics under different nutrient conditions and chemical stimulations. A crosslinked polymer network was applied to avoid the aggregation of UCNPs ($NaYF_4$: 20%Yb^{3+}, 2%Er^{3+}) in the cell culture medium [250]. Copolymers were further modified with 4Arm-PEG-NH_2 to allow the mitochondria targeting moiety of TPP to be covalently functionalized onto UCNPs ($NaYF_4$: 20%Yb^{3+}, 2%Er^{3+}). This strategy leads to UCNPs ($NaYF_4$: 20%Yb^{3+}, 2%Er^{3+}) capable of targeting mitochondria [251, 252], as the large membrane potential gradient from cell plasma to mitochondria allows the stepwise accumulation of TPP from initially in cell plasma to mitochondria [252]. The practicality of the intracellular temperature-sensing strategy was validated by real-time monitoring of the mitochondrial temperature variations induced by external nutrient conditions and chemical stimulations, including glucose, lipid, Ca^{2+}, and the inhibitor of oxidative phosphorylation. Interestingly, mitochondria respond faster and stay longer at a relatively high-temperature level in high OA versus high glucose culture medium, which indicates different pathways of glycometabolism and lipid metabolism. The difference in distinct thermal dynamics highlights the extensive applications of the mitochondria-targeting thermometer to study vital biological processes related to mitochondrial metabolism pathways and interactions between mitochondria and other organelles, like lysosome, ER [96] Golgi [253], lipid droplet, and peroxisome [254].

3.3 Materials and Methods

3.3.1 Reagents

For UCNPs synthesis, yttrium(III) chloride hexahydrate (YCl_3•$6H_2O$, 99.99%), ytterbium chloride hexahydrate ($YbCl_3$•$6H_2O$, 99.99%), erbium chloride hexahydrate ($ErCl_3$•$6H_2O$, 99.9%), ethanol, cyclohexane, 1-octadecane, and oleic acid were purchased from Sigma-Aldrich. For surface modification of UCNPs, $PEGMEMA_{80}$-*b*-$EGMP_3$ was synthesized by Lin Zhang (PhD candidate in the University of New South Wales from Martina Stenzel group). 4 Arm-PEG-NH2 was purchased from Laysan Bio, Inc. TPP, EDC, NHS, MES buffer, HEPES buffer, Tetrahydrofuran (THF), N, N-Dimethylformamide (DMF) were purchased from Sigma-Aldrich with reagent grade or higher. For cell experiments, DMEM, FBS, PBS, Penicillin-Streptomycin (PS), MTT (3-(4,5-Dimethylthiazol-2-yl)-2,5-Diphenyltetrazolium Bromide), MitoTracker (MitoTracker™ Deep Red FM, Invitrogen™ M22426), LysoTracker (LysoTracker™ Deep Red FM, Invitrogen™ L12492), and Mitochondria Isolation Kit were purchased from Life Technologies. Bovine Serum Albumin (BSA), dimethyl sulfoxide (DMSO), glucose, oleic acid-albumin from bovine serum liquid, carbonyl cyanide-4-(trifluoromethoxy)phenylhydrazone (FCCP) and ionomycin calcium salt were purchased from Sigma-Aldrich with reagent grade or higher.

3.3.2 Methods

3.3.2.1 Synthesis of hydrophobic UCNPs ($NaYF_4$: 20%Yb^{3+}, 2%Er^{3+}).

UCNPs ($NaYF_4$: 20%Yb^{3+}, 2%Er^{3+}) nanoparticles were synthesized following the previously reported protocols with some modification [214]. OA and 15 mL of 1-octadecane were added into a 50 mL round bottom flask with three necks, and then added 1.95 mL of YCl_3 stock solution (0.4 M in methanol), 1.0 mL of $YbCl_3$ stock solution (0.2 M in methanol), and 0.2 mL of $ErCl_3$ stock solution (0.1 M in methanol). The mixture was stirred under argon protection and then heated to 160 °C to get rid of methanol and H_2O. Second, 5 mL of NaOH-NH_4F methanol solution was added into the mixture until it cooled down to 30 °C and stirred for 30 minutes. Subsequently, the mixture was heated to 100 °C for 30 minutes and then heated to 300 °C for 1.5 hours.

Finally, 5 mL of ethanol was added into the mixture to precipitate UCNPs. UCNPs were washed three times with ethanol and cyclohexane before using.

3.3.2.2 Modification of UCNPs.

(1) The first step was to modify the UCNPs' surface with Copolymers [167]. 5 mg of UCNPs and 5 mg of Copolymers were dissolved in 1 mL of THF and then shaken at room temperature for 12 hours. Next, the UCNPs coated with di-block copolymers (UCNPs@copolymer) were washed with THF and DI water. Finally, the UCNPs@copolymer was dissolved in 0.5 mL of DI water for further use.

(2) The second step was to conjugate UCNPs@copolymer with 4Arm-PEG-NH_2 [250]. 5 mg of UCNPs@copolymer, 10 mg of EDC, and 10 mg of NHS were dissolved in 1 mL of MES buffer (20 mM, pH 6.0) and shaken for 30 minutes for activation. After centrifugation, the activated products and 10 mg of 4Arm-PEG-NH_2 were dissolved in 1 mL of pH 7.02 HEPES buffer and reacted overnight. On the second day, reaction products were washed three times with DI water. Then nanoparticles were centrifuged at 4400 rpm for 5 minutes to remove the large aggregates. Finally, UCNPs@copolymer conjugated with 4Arm-PEG-NH_2 (UCNPs@PEG) were stocked in 0.5 mL of DI water.

(3) The third step was to conjugate UCNPs@PEG with TPP. 30 mg of TPP, 10 mg of EDC, and 10 mg of NHS were first dissolved into 1mL of DMF by ultrasound. After 1 hour, 10 mg of UCNPs@PEG were added to the mixture. The reaction was stirred at room temperature for 12 hours and then washed with DMF and DI water. Finally, the product UCNPs@PEG conjugated with TPP (UCNPs@PEG @TPP) was stored in 0.5 mL of DI water.

3.3.2.3 Characterization.

The morphology of UCNPs was characterized using the FEI Tecnai transmission electron microscopy (FEI, U.S.A.). The hydrodynamic size and zeta potential of UCNPs were determined by a zeta sizer nano (Malvern, U.K.).

3.3.2.4 Luminescence stability of UCNPs@PEG@TPP against environmental parameters.

The spectrometer was used to measure the emission spectrum of UCNPs@PEG@TPP under different pH, ionic strength (Mg^{2+}, Ca^{2+}, and K^{+}), and refractive index (*n*). The

PBS with gradient pH values (4 – 10) were tuned by adding different amounts of HCl or KOH. Ionic strength (0 – 500 mM KCl) was controlled by adding different amounts of KOH. 0 – 2.0 mM $CaCl_2$, and 0 – 1.2 mM $MgCl_2$ were obtained by adding different amounts of $CaCl_2$ and $MgCl_2$. The solutions with different refractive indexes were achieved by glucose. 30% glucose (n = 1.3805), 36% (n = 1.3912) glucose and 52% (n = 1.4222) glucose. 1 mg of UCNPs@PEG@TPP were dissolved in the PBS with different pH, different concentrations of ionic strength, or different refractive indexes and transferred to the cuvette. UCNPs@PEG@TPP were excited at 980 nm and the spectrum was captured from 480 nm to 600 nm.

3.3.2.5 Long-term bio-stability of UCNPs@PEG@TPP.

0.5 mg of UCNPs@PEG@TPP were added into 1 mL of DMEM containing 10% FBS or DMEM containing 2% FBS and 0.5% BSA. The hydrodynamic size was applied to monitor the stability of UCNPs@PEG@TPP for seven days.

3.3.2.6 Cytotoxicity Assay.

HeLa cells were purchased from ATCC. First of all, 5 mg of MTT was dissolved into 1 mL of sterile PBS buffer. Then 10,000 cells were seeded in the 96-well plate. UCNPs@PEG@TPP (0, 1, 10, 50, 250, 500, 1000 μg/mL) were added to each well. Then fresh culture medium was added into the plate after 24 hours. 10 μL of MTT stock solution was added to each well. This 96-well plate was kept in a 37 °C incubator for another 4 hours. Finally, 50 μL of DMSO was added into each well. The microplate reader (Infinite M200 PRO) was applied to read absorbance at 540 nm.

3.3.2.7 Colocalization of UCNPs with MitoTracker or LysoTracker.

The HeLa cells were seeded on the fluoro-dish (35 mm) at 10^5 cell density and incubated in the DMEM medium containing 10% v/v FBS for 12 hours. Then the cells were washed three times with PBS and incubated with UCNPs (50 μg/mL, 1 mL) for 12 hours (mitochondria colocalization experiment) or 4 hours (lysosomes colocalization experiment) at 37 °C with 5% CO_2. Next, the cells were washed with PBS and incubated with 200 nM MitoTracker or 200 nM LysoTracker for 0.5 hours. Finally, the cells were washed with PBS and waiting for imaging in DMEM. The colocalization results were analysed by image J. The result is +1 for perfect correlation, 0 for no correlation, and -1 for perfect anti-correlation. Usually, we consider a Pearson's

correlation coefficient higher than 0.6 as credible colocalizations [255].

3.3.2.8 Mitochondria isolation and Fluorescence Intensity Analysis.

Mitochondria from HeLa cells were isolated by a kit bought from Thermo Fisher. Briefly, following the manufacturer's manual. The protease inhibitors were added into Reagent A and Reagent C before starting the experiment. 2×10^7 cells were cultured in two flask T175 and treated with 50 μg/mL UCNPs@copolymer, UCNPs@PEG, and UCNPs@PEG@TPP for 12 hours. Then 2×10^7 cells were collected by centrifugation. 800 μL of Reagent A was added into the cell pellet and vortexed at medium speed for 5 seconds. The cell suspension was put on the ice for exactly 2 minutes. Next, 10 μL of Reagent B was added to the cell suspension and vortexed at maximum speed for 5 seconds. The mixture was incubated on the ice for another 5 minutes. After 800 μL of Reagent C were added into the cell suspension, the mixture was centrifuged at 700*g for 10 minutes at 4°C. Then the supernatant was transferred to a new tube and centrifuged at 12,000×g for 15 minutes at 4°C. The cell pellet was dissolved in 500 μL of Reagent C and centrifuged at 12,000×g for 5 minutes. Finally, the pellet was re-suspended in the 50 μL PBS buffer and transferred to a 96-well plate. The luminescence intensity was recorded by a homemade Total Internal Reflection Fluorescence (TIRF) Microscopy with an excitation wavelength at 980 nm.

3.3.2.9 Relative temperature sensing sensitivity and uncertainty.

The relative temperature sensing sensitivity (S_R) indicates the relative change of Δ per degree of temperature change and was calculated using [130]:

$$S_r = \frac{1}{\Delta}\left|\frac{\partial \Delta}{\partial T}\right| \qquad (1)$$

The temperature uncertainty δT is the smallest temperature change that can be detected in given measurement and was defined by [130]:

$$\delta T = \frac{\delta \Delta}{S_r \bullet \Delta} \qquad (2)$$

3.3.2.10 Temperature mapping and temperature sensing of mitochondria.

The HeLa cells were cultured in DMEM containing 10% v/v FBS and 1% v/v PS at 37 °C with 5% CO_2. Cells were transferred into the fluoro-dish (35 mm in diameter with No.1 coverglass bottom). Then the cells were incubated in the 1 mL culture medium containing 50 μg/mL UCNPs@PEG@TPP at 37 °C for 12 hours. The UCNPs@PEG@TPP labelled cells were imaged on a home-build total internal reflected luminescent TIRF microscope by a 980 nm laser excitation under different temperatures (from 32 °C to 42 °C). The homemade TIRF microscopy was installed with an external temperature controller.

For the glucose, oleic acid, FCCP, and Ca^{2+}-induced temperature changes, first, the UCNPs@PEG@TPP were incubated with HeLa cells for 12 hours. Then, the HeLa cells were stained with MitoTracker. Next, glucose (5 mg/mL), oleic acid (5 μM), FCCP (10 μM), or ionomycin calcium salt (1 μM) was incubated with HeLa cells. The luminescence intensity ratio (I_{525}/I_{545}) of UCNPs@PEG@TPP was determined for the green upconversion emission under 980 nm laser excitation.

3.3.2.11 Statistical Analysis.

Student's t-test was applied to examine the differences among variables. Data were shown as mean ± SD. *p values ≤ 0.05 are considered to be statistically significant.

3.4 Results and Discussion

3.4.1 Design of UCNPs@PEG@TPP

To construct the stable mitochondria targeting thermometer, a crosslinked polymer network was applied to functionalize UCNPs ($NaYF_4$: 20%Yb^{3+}, 2%Er^{3+}) surface (**Figure 3-1, Figure 3-2A**). The ligands OA on the UCNPs ($NaYF_4$: 20%Yb^{3+}, 2%Er^{3+}) surface were first replaced by copolymer by the ligand exchange method. Then UCNPs@copolymer were further conjugated with 4 Arm-PEG-NH_2 to form polymer layers on the UCNPs ($NaYF_4$: 20%Yb^{3+}, 2%Er^{3+}) surface with free amine groups.

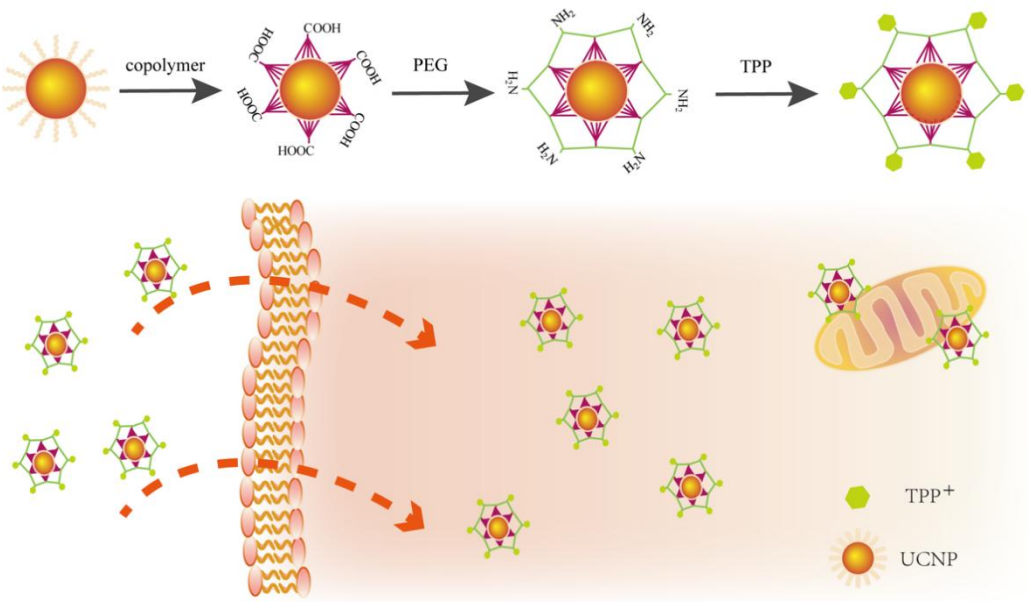

Figure 3-1 The conjugation steps and selective accumulation of UCNPs@PEG@TPP to the mitochondria through incubation. *Copolymers, 4Arm-PEG-NH_2 and TPP were sequentially conjugated to the UCNPs ($NaYF_4$: 20%Yb^{3+}, 2%Er^{3+}) to make them dispersible in cell culture medium and able to specifically target mitochondria as an in situ thermometers in HeLa cells.*

These hydrophilic, crosslinked coating layers can firmly anchor onto the surface of positively charged UCNPs and keep UCNPs stable in the cell culture medium and the intracellular environment. The TEM images (**Figure 3-2B-E**) showed the morphology uniformity and monodispersity of the UCNPs ($NaYF_4$: 20%Yb^{3+}, 2%Er^{3+}) before and after the surface functionalization. The size of UCNPs increased from 31.09 ± 2.76 nm of the as-synthesized UCNPs ($NaYF_4$: 20%Yb^{3+}, 2%Er^{3+}) to 39.43 ±1.64, 42.34 ± 2.54, and 45.13 ± 2.55 nm (measured by TEM in **Figure 3-2B-E**). The DLS results (**Figure 3-2F**) confirmed the high uniformity with the peak values of hydrodynamic size increasing from 51.77 nm to 72.08 nm and 103.10 nm after each step of surface modifications. For TPP conjugation, the amine groups of 4Arm-PEG-NH_2 on the crosslinked polymer network provide the anchoring groups for TPP. The Zeta potential results (**Figure 3-2G**) indicated the successful modification of each step, as the surface charge turns from negative 13 mV to positive 18 mV with the exposure of 4Arm-PEG-NH_2 and a further positive value of 32 mV with TPP by a carbodiimide reaction [256, 257]. The strong positive charge on the UCNPs' surface facilitates the nanoparticles to locate into cell cytoplasm and mitochondria [252]. By using ATR-FTIR, compared with

the spectra of UCNPs@OA, as shown in **Figure 3-3A**, the characteristic absorption of P=O stretches at 1102 cm^{-1} confirmed the copolymer grafted on the surface of UCNPs ($NaYF_4$: 20%Yb^{3+}, 2%Er^{3+}), and the appearance of =C-H stretching vibration bands from aromatic ring located in the range of 3100 to 3000 cm^{-1} and 752 to 636 cm^{-1} confirmed the presence of TPP on the UCNPs' surface. Furthermore, the long-term stability of UCNPs@PEG@TPP was tested by DLS (**Figure 3-3B**). These UCNPs@PEG@TPP bioconjugates exhibited excellent stability in the incubation medium (DMEM containing 2% v/v fetal bovine serum (FBS) and 0.5% v/v BSA) and the complete medium (DMEM containing 10% FBS and 1% v/v PS), as shown in **Figure 3-3C**.

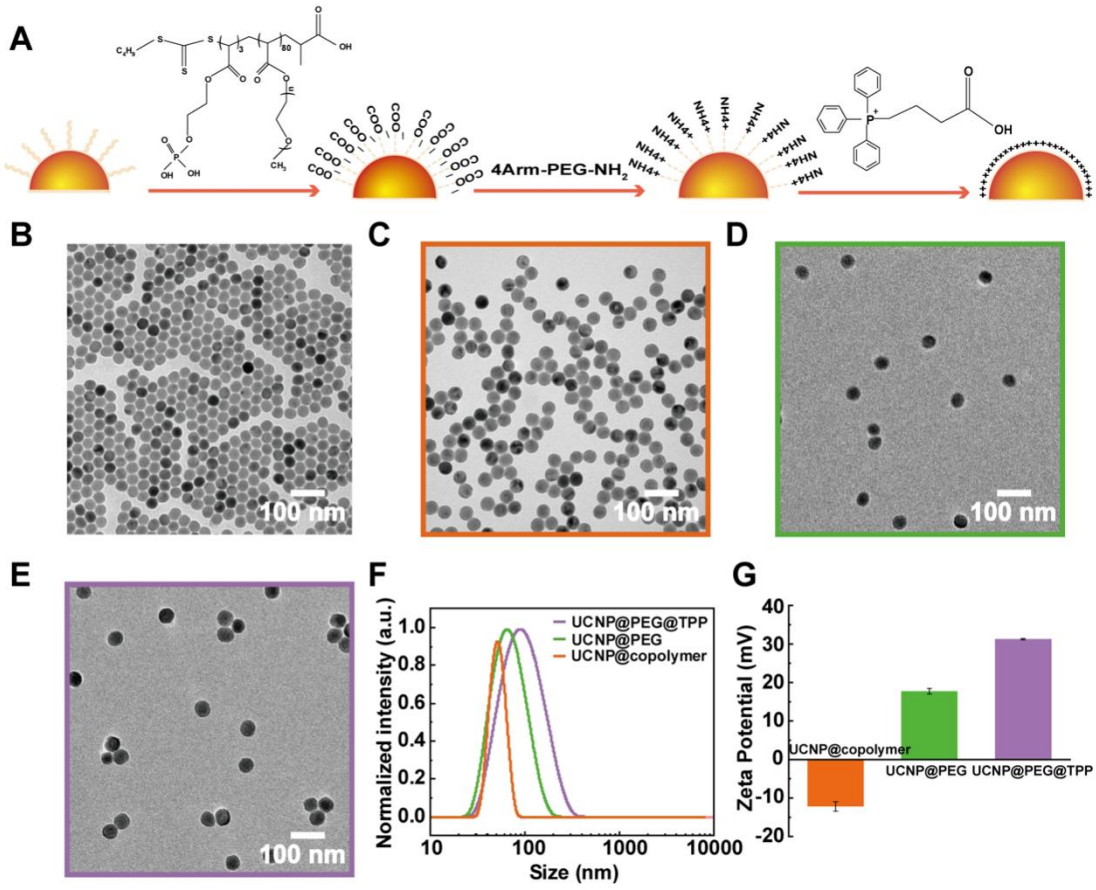

Figure 3-2 Characterization of UCNPs ($NaYF_4$: 20%Yb^{3+}, 2%Er^{3+})-based thermo-sensors. A. *Schematic illustration of the mitochondria-targeted probes with crosslinked polymer layers and TPP.* ***B-E.*** *Representative TEM images of UCNPs@OA, UCNPs@copolymer, UCNPs@PEG, and UCNPs@PEG@TPP.* ***F.*** *DLS for UCNPs ($NaYF_4$: 20%Yb^{3+}, 2%Er^{3+}) with different surface modifications.* ***G.*** *Zeta potential of UCNPs ($NaYF_4$: 20%Yb^{3+}, 2%Er^{3+}) with different surface modifications.*

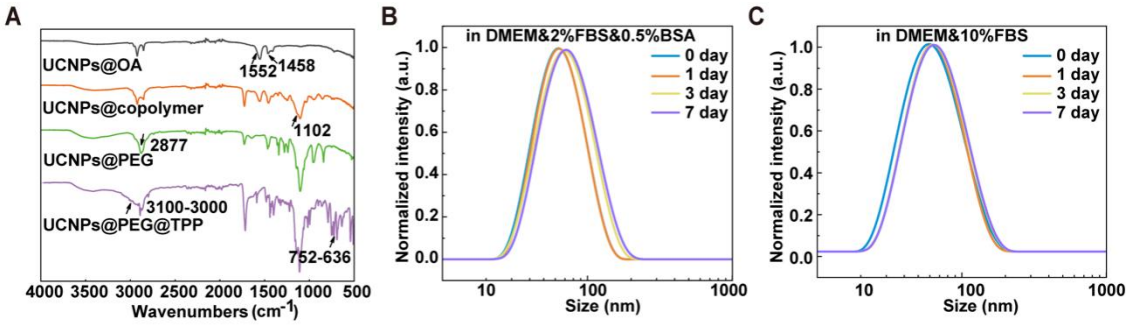

Figure 3-3 Characterization of UCNPs ($NaYF_4$: 20%Yb^{3+}, 2%Er^{3+}) thermo-sensors by ATR-FTIR and DLS. A. *The ATR-FTIR spectra of prepared UCNPs@OA, UCNPs@copolymer, UCNPs@PEG and UCNPs@PEG@TPP.* ***B.*** *Bio-stability of UCNPs@PEG@TPP in DMEM containing 2%FBS and 0.5%BSA.* ***C.*** *Bio-stability of UCNPs@PEG@TPP in DMEM containing 10%FBS. The sizes of UCNPs@PEG@TPP in different physiological buffer keep stable within 7 days.*

3.4.2 Thermal responsive properties of UCNPs@PEG@TPP *in vitro*

Under the 980 nm excitation, UCNPs@PEG@TPP emitted green emission consists of two distinct bands between 515-535 nm (centred at 525 nm) and 535-570 nm (centred at 545 nm) (**Figure 3-4A**), attributing to the $^2H_{11/2}$ and $^4S_{3/2}$ transitions of Er^{3+}, respectively. While the emitted intensities at both 525 nm and 545 nm peaks decreased when the temperature elevated from 30 °C to 60 °C due to thermal quenching, the ratio of 525 nm and 545 nm peaks increased following Boltzmann distribution (**Figure 3-4B**).

An accurate calibration curve is crucial to quantitatively analyze temperature dynamics in the intracellular environment [237]. Ideal luminescence thermo-sensors should be independent of the concentration as it's difficult to control and measure the concentration of luminescence thermo-sensors in living cells. As shown in **Figure 3-4B**, by calibrating two solutions containing different concentrations of UCNPs@PEG@TPP (5 and 10 mg/mL) using a purpose-built spectrometer, the Residual Sum of Squares (RSS) of these two linear fittings was measured as 0.013159, which indicated that UCNPs@PEG@TPP as a luminescence thermo-sensor was concentration-independent. To confirm this result, the calibration curves at the single-particle level were performed with a purpose-built total internal reflected luminescent (TIRF) microscopy system. Although the calibration results obtained by microscope were distinct from those by the spectrometer, due to the different sensitivities of the spectrometer with photomultiplier tube (PMT) detector and microscope with Electron-multiplying CCD (EMCCD) camera,

the RSS of these two linear fittings was measured as 0.00482. Notably, the thermal responsiveness of UCNPs@PEG@TPP was essentially unchanged under different concentrations, no matter whether from the single-particle level or in the solution.

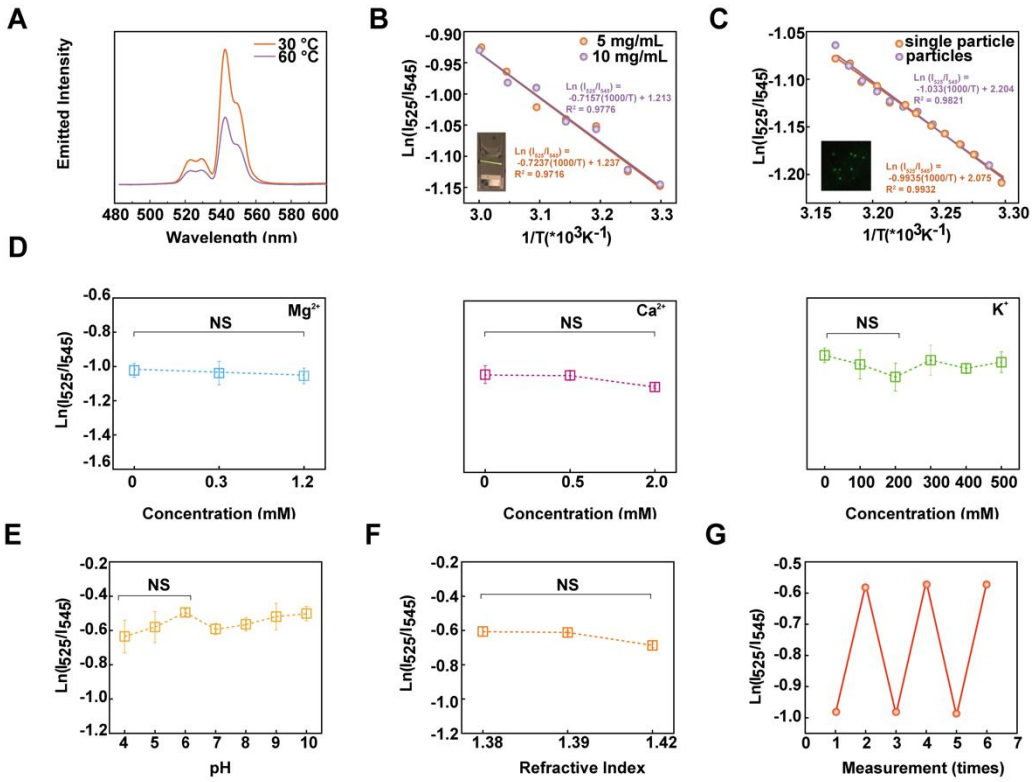

Figure 3-4 Thermal responsive properties of UCNPs@PEG@TPP in vitro. ***A.*** *Upconversion emission spectra obtained at two different cuvette temperatures (30 and 60 °C, λexc = 980 nm).* ***B.*** *Plots of ln(I_{525}/I_{545}) vs 1000/T to calibrate the thermometric scale in the solution with different concentrations(5 mg/ml: The 95% confidence interval for slope, Y-intercept, and X-intercept are -0.8660 to -0.5813, 0.7885 to 1.685, and 1.356 to 1.946, respectively. 10 mg/ml: The 95% confidence interval for slope, Y-intercept, and X-intercept are -0.8404 to -0.5910, 0.8206 to 1.605, and 1.388 to 1.911, respectively.)* ***C.*** *Plots of ln(I_{525}/I_{545}) vs 1000/T to calibrate the thermometric scale at the single-particle level versus multiple particle level. (Single particle: The 95% confidence interval for slope, Y-intercept, and X-intercept are -1.048 to -0.9391, 1.899 to 2.251, and 2.022 to 2.148, respectively. Particles: The 95% confidence interval for slope, Y-intercept, and X-intercept are -1.126 to -0.9409, 1.905 to 2.504, and 2.025 to 2.224, respectively.)* ***D.*** *Thermal sensitivity of UCNPs@PEG@TPP in response to Mg^{2+}(left), Ca^{2+}(middle) or K^{+}(right) (n = 3 independent experiments).* ***E.*** *Changes in the ln(I_{525}/I_{545}) ratio of UCNPs@PEG@TPP in response to pH (n = 3 independent experiments).* ***F.*** *Changes in the ln(I_{525}/I_{545}) ratio of UCNPs@PEG@TPP in response to refractive index (n = 3 independent experiments).* ***G.*** *Reversibility of the temperature-dependent*

changes of UCNPs@PEG@TPP luminescence. The solution temperature was changed from 30 ℃ to 45 ℃. Data points represent mean ± s.d.

The micro-environment conditions in living cells, like the ionic strength, pH value, and refractive index vary as time and locations change, also vary from one organelle to another [237]. For example, the refractive indexes of the cell cytoplasm, nucleus, and mitochondria are 1.38, 1.39, and 1.42, respectively [258]. The performance of luminescence thermo-sensors should keep stable in the living cell. **Figure 3-4D-F** illustrated that temperature-dependent luminescence of UCNPs@PEG@TPP was not affected by Mg^{2+} or Ca^{2+} at different physiological intracellular concentrations, ionic strength (0-500 mM), pH (4-10), and refractive indexes (1.38-1.42). Furthermore, the I_{525}/I_{545} ratios of UCNPs@PEG@TPP can be reproduced by heating and cooling between 30 °C and 45 °C for multiple cycles, demonstrating the reversibility of UCNPs@PEG@TPP without thermal denaturation (**Figure 3-4G**). Since the absorption spectrum of water is in the range of 680-1000 nm with the peak at 980 nm, we monitored the temperature variations of UCNPs@PEG@TPP excited by a 980 nm laser at an intensity of 0.5 kW/cm^2 for 30 minutes. As shown in **Figure 3-5**, an illumination of 0.5 kW/cm^2 980 nm laser did not lead to temperature elevation of the water within 30 minutes.

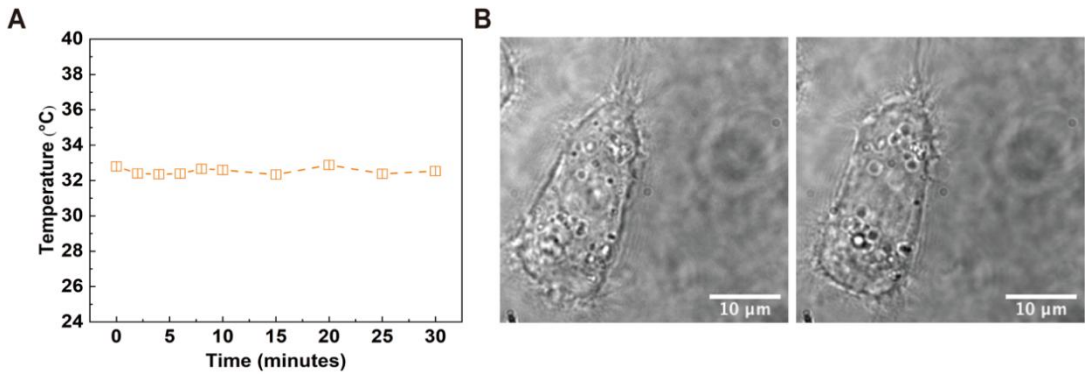

Figure 3-5 The phototoxicity of 980 nm laser. A. *The temperature changes of UCNPs@PEG@TPP in the water under 0.5 KW/cm^2 power density and 0.5 seconds exposure time within 30 minutes.* ***B.*** *The shape of the HeLa cell in the 0 and 30 minutes. The power of 0.5 kW/cm^2 is hardly to elevate the temperature of the water or particles, and has no damage to the living cells.*

3.4.3 UCNPs@PEG@TPP work as subcellular thermosensors in HeLa cells

To apply UCNPs@PEG@TPP in live cells, we first checked the cytotoxicity of UCNPs@PEG@TPP in live cells with short-time treatment at different concentrations measured by MTT test experiments. **Figure 3-6A** showed that the cell viability in the experimental groups was similar to that of the control group, indicating that UCNPs@PEG@TPP had negligible cytotoxicity to HeLa cells. Considering the labelling efficiency, 50 μg/mL was chosen in the following live-cell experiments.

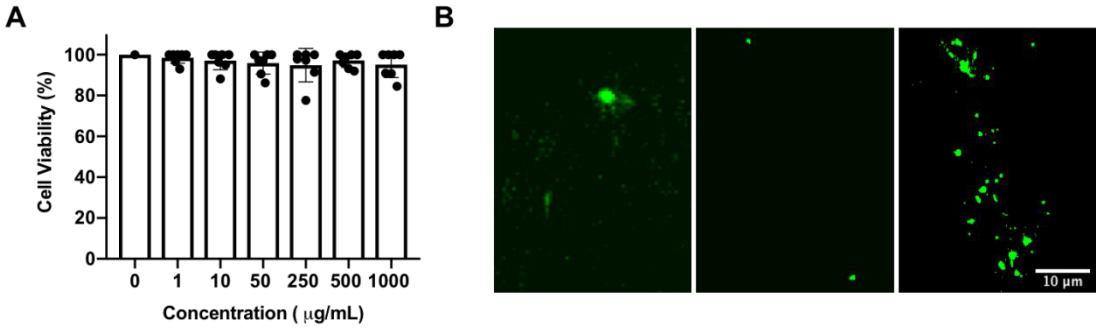

Figure 3-6 The cytotoxicity of UCNPs. A. *The cell toxicity of UCNPs@PEG@TPP achieved by the MTT experiment. The concentration of UCNPs@PEG@TPP is 0, 1, 10, 50, 250, 500, and 1000 μg/mL. These nanoparticles are low toxicity.* ***B.*** *The luminescent images of UCNPs@copolymer (left), UCNPs@PEG(middle) and UCNPs@PEG@TPP (right) in the isolated mitochondria.*

Next, the exact locations of nanoparticles in the live cell were tested. Colocalizations of UCNPs@PEG@TPP and MitoTracker Deep Red were conducted by a purpose-built TIRF microscope with 980 nm and 647 nm lasers as the light sources. As shown in **Figure 3-7A**, the green channel illustrated that these three kinds of nanoparticles dispersed into HeLa cells after 12 hours' incubation. UCNPs@copolymer and UCNPs@PEG preferred to form aggregates (**Figure 3-7A**, **red frame**), while UCNPs@PEG@TPP dispersed well within the cell. The merged images showed UCNPs@PEG@TPP had a better colocalization than those of control groups. Pearson's correlation coefficient for the experimental group was 0.70. In contrast, Pearson's correlation coefficient for the UCNPs@PEG and UCNPs@copolymer treatment groups were 0.40 and 0.27, respectively. Usually, we consider a Pearson's correlation coefficient higher than 0.6 as credible colocalizations [255]. These results indicated that UCNPs@PEG@TPP preferred to target mitochondria. Since the temporal and spatial

resolutions in microscopy imaging may affect the accuracy of colocalization results, we further confirmed the locations of UCNPs@PEG@TPP by isolating mitochondria from HeLa cells using a mitochondria isolation kit (Thermo Fisher), dispersed in 50 μL of PBS buffer. The mitochondria suspension was transferred to a 96-well plate and dried at room temperature, and the luminescence intensity of the isolated mitochondria was measured (**Figure 3-6B and 3-7B**). In the control groups with UCNPs@PEG and UCNPs@copolymer, the luminescence intensities of nanoparticles were barely seen (**Figure 3-6B)**, while the intensity of the UCNPs@PEG@TPP treated group was ~3 times higher than those of the other two control groups, indicating the successful mitochondria targeting (**Figure 3-7B)**.

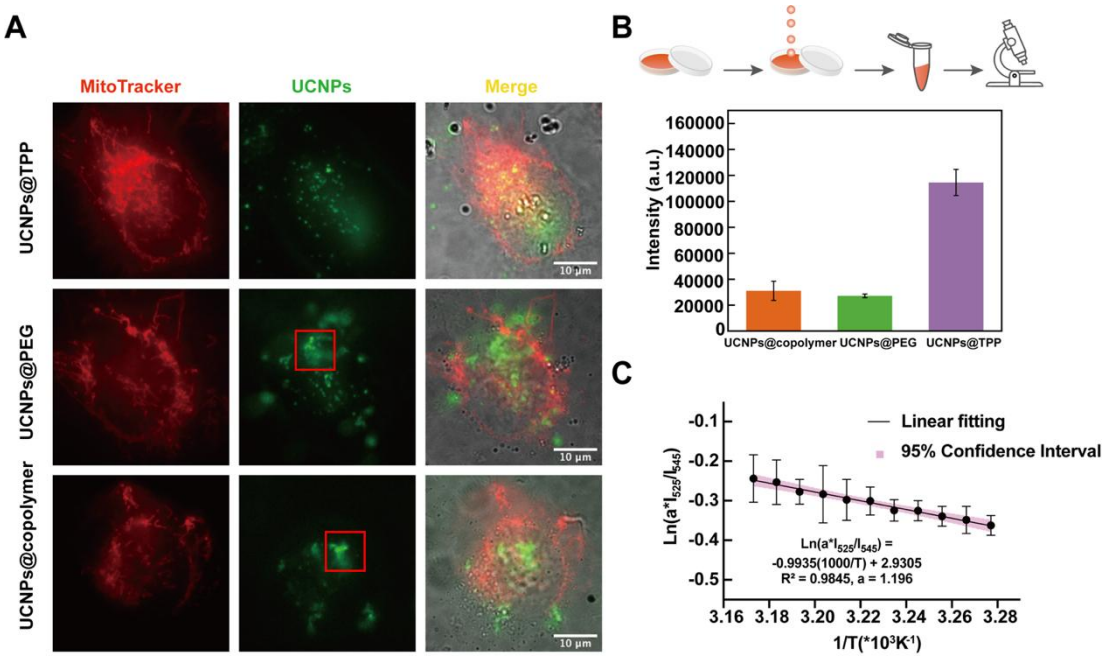

Figure 3-7 Temperature-dependent luminescence characteristics of UCNPs@PEG@TPP targeted to in situ mitochondria in HeLa cells. A. *Intracellular co-localization of UCNPs with MitoTracker (red channel is MitoTracker Deep Red excited by 647 nm laser; the green channel is UCNPs excited by 980 nm laser; the grey channel is the bright-field images).* ***B.*** *The luminescence intensity of isolated mitochondria treated with UCNPs (n = 10 fields of view from 3 independent repeats).* ***C.*** *Plot of $ln(a*I_{525}/I_{545})$ vs 1000/T to calibrate the thermometric scale in HeLa cells (n = 10 cells). Data points represent mean ± s.d. The error bars in Figure 3-12C represent the standard deviations of the mean values (95% confidence interval, n=10 cells). The 95% confidence interval for slope, Y-intercept, and X-intercept are -1.340 to -0.8790, 2.529 to 4.016, and 2.877 to 2.997, respectively. Scale bar: 10 μm.*

Furthermore, to rule out the possible interactions between UCNPs@PEG@TPP and

lysosomes, HeLa cells were stained with LysoTracker. After 4 hours' incubation, HeLa cells were washed with PBS. UCNPs@PEG@TPP dispersed into HeLa cells with a speed faster than those in control groups because more nanoparticles were delivered to the cells (**Figure 3-8**). Pearson's correlation coefficient for the UCNPs@PEG@TPP, UCNPs@PEG, and UCNPs@copolymer were 0.05, 0.12, and 0.29, respectively. The Pearson's correlation coefficient in the group of UCNPs@PEG@TPP was 0.05, indicating that UCNPs@PEG@TPP had no colocalization with lysosomes. The merged images in **Figure 3-8** also showed that UCNPs@PEG@TPP already escaped from lysosomes, as a result of the good lipophilicity of TPP.

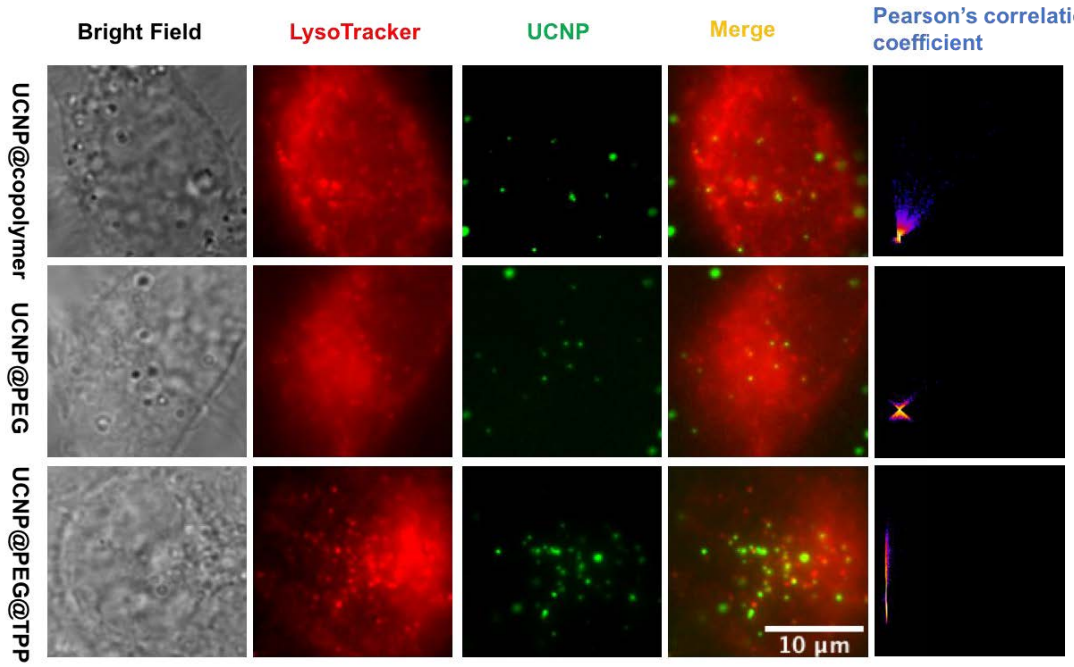

Figure 3-8 Intracellular co-localization of UCNPs with LysoTracker. *Red channel is LysoTracker Deep Red excited by 647 nm laser. Green channel was UCNPs excited by 980 nm laser. The Pearson's correlation coefficients for UCNPs@copolymer, UCNPs@PEG, and UCNPs@PEG@TPP are 0.29, 0.12 and 0.05, respectively.*

The above results allowed us to plot the calibration curves in HeLa cells. By changing the extracellular temperature of cell culture using a temperature controllable incubator on top of the microscope system, the logarithmic value of the I_{525}/I_{545} ratio showed much more gradual and linear luminescence changed in the range of 32 to 42 °C relative to the reciprocal temperature (**Figure 3-7C**), suggesting UCNPs@PEG@TPP as a quantitative thermo-sensor in living cells. The data analysis process was illustrated in

Figure 3-9. The equation of calibration curve was ln ($a*I_{525}/I_{545}$)=-0.9935(1000/T)+2.9305 (a=1.196). The relative sensing sensitivity in HeLa cells at 32 ºC was 3.2% K^{-1} and the temperature resolution was ~2.3 K.

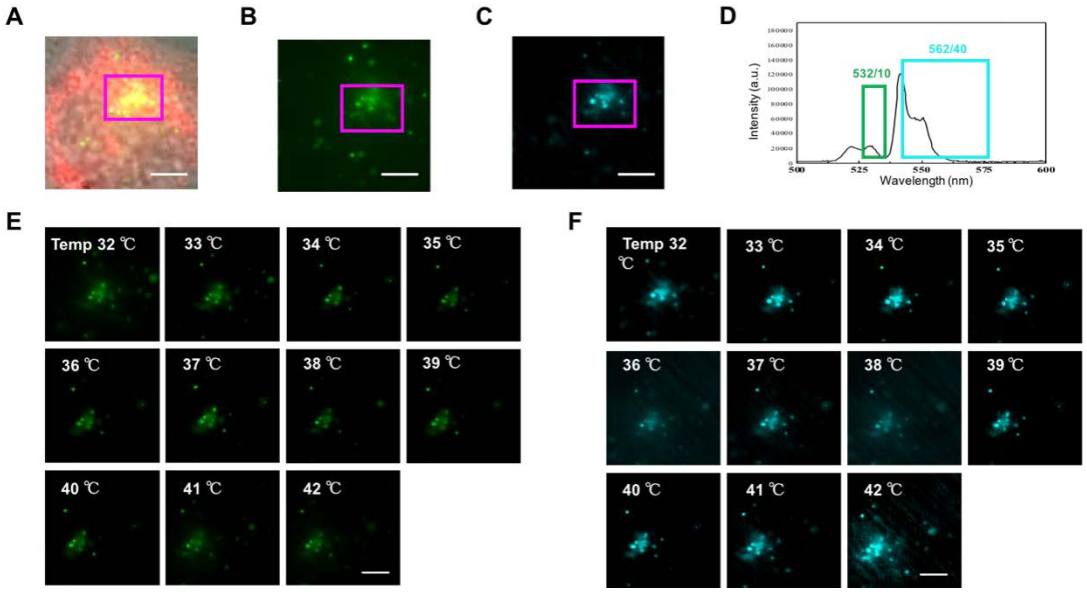

Figure 3-1 Data analysis of peak intensity calculation. ***A.*** *Merged images of Bright field, UCNPs and MitoTracker.* ***B.*** *Green channel was the emission of UCNPs in the range from 527 nm to 537 nm.* ***C.*** *Blue channel was the emission of UCNPs in the range from 542 nm to 582 nm.* ***D.*** *The spectra of UCNPs doped with erbium were excited by 980 nm laser. The green frame represented the intensity of peak 525 nm and the blue frame represented the intensity of peak 545 nm.* ***E.*** *Images represented the UCNPs emission in the range from 527 nm to 537 nm under various temperature (from 32 °C to 42 °C).* ***F.*** *Images represented the UCNPs emission in the range from 542 nm to 582 nm under various temperature (from 32 °C to 42 °C). Scale bar: 10 μm.*

3.4.4 Visualization of mitochondrial thermal dynamics in HeLa cells

We then applied UCNPs@PEG@TPP to monitor the mitochondrial temperature variations induced by external nutrient conditions and chemical stimulations. First, we tested a high glucose medium to HeLa cells. Glucose produces pyruvate in the cytosol and then participates in the Krebs Cycle in mitochondria, which generates heat. In the HeLa cells incubated with UCNPs@PEG@TPP, the mitochondria temperature increased significantly by 2.25 ℃ in the first 10 minutes by addition of 5 mg/mL glucose ($P < 0.0001$ by Students' t-test) (**Figure 3-10A**, right), before recovering to the original level after 20 minutes of treatment. As the control group with adding the same amount of PBS, the mitochondrial temperature remained stable within 30 minutes

(**Figure 3-10A**).

As an alternative nutrient source, oleic acid was then tested. Columns in **Figure 3-10B** demonstrated that the mitochondrial temperature increased by 2.74 ℃ only 5 minutes after adding 5 μM oleic acid in the culture medium, but the mitochondrial temperature didn't recover to the original level even after 30 minutes of treatment. Compared with glucose treatment, oleic acid treatment takes mitochondrial temperature to a higher peak value with a faster speed and a longer plateau time, which indicates the different metabolic pathways and energy efficiency for glucose and oleic acid.

The mitochondrial temperature in living cells can be elevated by Ca^{2+} shock as it can promote the pumping of ions and accelerate the respiration reactions [259]. Ionomycin calcium salt is an ionophore making cell membrane highly permeable of Ca^{2+} [117]. Here, **Figure 3-10C** showed that the temperature of mitochondria increased sharply after adding 1 μM ionomycin calcium salt within 6 minutes before dropping back in another 2 minutes (**Figure 3-10C**). Ionomycin calcium salt induces intracellular stress, possibly causing damage to mitochondria in HeLa cells [259].

Furthermore, FCCP was tested as a chemical stimulation in HeLa cells. FCCP is an inhibitor of oxidative phosphorylation, which disrupts ATP synthesis by transporting protons across the mitochondrial inner membrane [260]. During this process, mitochondria release a large amount of heat. In the HeLa cells incubated with UCNPs@PEG@TPP, the mitochondrial temperature elevated by almost 2 degrees in the first 10 minutes after adding 10 μM FCCP ($P < 0.0001$ by Students' t-test) (**Figure 3-10D**). In the following 20 minutes, the mitochondrial temperature kept increasing by ~1 ℃. Mitochondria eventually recovered to the original temperature after 30 minutes of FCCP treatment. In comparison, the temperature in the control group remained at a similar level after DMSO treatment. These results provide evidence that UCNPs@PEG@TPP works as a precise subcellular thermosensor for monitoring mitochondrial thermodynamics.

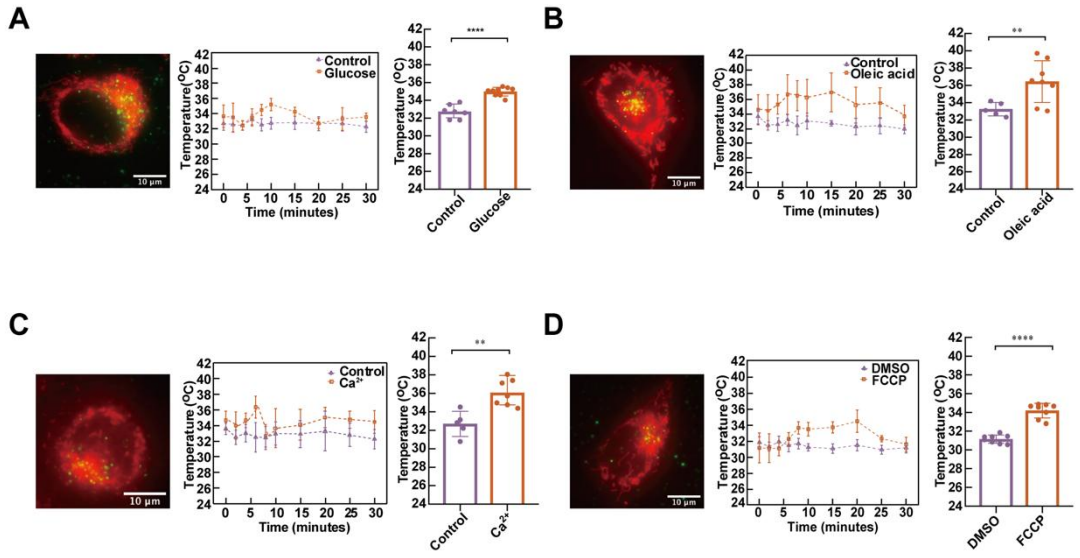

Figure 3-2 Visualization of mitochondrial temperature dynamics in HeLa cells response to nutrient and chemical stimulations. ***A.*** *UCNP@PEG@TPP images (left) and mitochondrial temperature dynamics (middle) in the presence of 5 mg/mL glucose within 30 minutes and Student's t-test of no glucose and glucose at 10 minutes ($p < 0.0001$, right).* ***B.*** *UCNP@PEG@TPP images (left) and mitochondrial temperature variations (middle) in the presence of 5 μM oleic acid within 30 minutes and Student's t-test of no oleic acid and oleic acid at 15 minutes ($p < 0.05$, right).* ***C.*** *UCNP@PEG@TPP images (left) and mitochondrial temperature changes (middle) in the presence of 1 μM ionomycin calcium salt within 30 minutes and Student's t-test of no calcium and calcium at 6 minutes ($p < 0.05$, right).* ***D.*** *UCNP@PEG@TPP images (left) and mitochondrial temperature fluctuations (middle) in the presence of 10 μM FCCP within 30 minutes and Student's t-test of DMSO and FCCP at 10 minutes ($p < 0.0001$, right). The temperature in A-D are calculated by the calibration plot in* ***Figure 3-12C****. n = 5~8 cells for* ***A-D****, data points represent mean ± s.d. The merged cell images in A-D are MitoTracker (red) and UCNPs@PEG@TPP (green) from different treatment.*

3.5 Conclusion

Intracellular temperature, especially mitochondrial thermodynamics, is one of the most crucial biophysical parameters to assess the status of living cells and organisms, which is related to homeostasis and energy balance [261]. Towards the development of a precise thermosensor both *in vitro* and in living cells, we have synthesized a series of UCNPs@copolymer, UCNPs@PEG, and UCNPs@PEG@TPP nanosensors. We applied the non-photobleaching ratiometric thermosensor for monitoring the *in situ* mitochondrial thermodynamics under different physiological and chemical stimuli.

UCNPs@PEG@TPP conjugate enables us to monitor the glucose-, lipid-, Ca^{2+}-, and FCCP-dependent thermodynamics in the mitochondria within living HeLa cells. UCNPs@PEG@TPP is a powerful tool for analyzing how mitochondria metabolism activates and maintains cellular homeostasis in living cells. The distinct thermodynamics highlight the extensive applications of thermometers to study vital biological processes related to mitochondrial metabolism and interactions between mitochondria and other organelles, like lysosome, ER [96], Golgi [253], lipid droplet, and peroxisome [254].

Chretien *et al.* recently reported that mitochondrial temperature reached >323K (50 ℃) using MitoThermo Yellow (MTY) in HEK293T cells treated with an oxygen-rich buffer to fully functionalize the respiration [262]. Intracellular temperature measurement using organic dyes is not suitable for long-term monitoring purposes. Hu *et al.* reported another large increase in temperature by using plasmonic nanostructures with Au nanoparticles in the cytoplasm of CaSki cells during active Ca^{2+} transportation [263]. Intracellular temperature measurement using inorganic probes requires precise calibration both in the extracellular environment and accurate colocalization of organelles with specific targeting organelle. A fluorescent protein (FP) based thermometer was also reported in HeLa cells by Nakano *et al.* with a 6-9 ℃ temperature increase, which is consistent with our results [151]. A comparison of different thermometers will be meaningful, including fluorescent proteins [151], organic dyes [241, 262], plasmonic materials [263], UCNPs-based [248] thermometer for living cells, etc.

The unique optical properties of UCNPs allow us to track long-term thermodynamics in mitochondria across cell cycles or even in live deep tissues with the NIR excitation wavelength in the future [238, 239, 264]. The bio-conjugation system we developed will allow us to establish a library of different organelle-targetted thermometers, like lysosome, ER, and Golgi. Combined with other mitochondria evaluation methods, like live-cell super-resolution imaging [265, 266], *in vitro* reconstitution assay [230, 267, 268], and near-infrared deep tissue imaging [244], the UCNPs-based mitochondrial thermometer will be a powerful platform for multifunctional imaging, sensing [269], therapy [244] and even tracking the pace of life [270].

Chapter 4 Spatiotemporally Mapping Temperature dynamics of Lysosomes and Mitochondria using Cascade Organelle-targeting Upconversion Nanoparticles

4.1 Motivation

In chapter 3, mitochondrial temperature dynamics under different nutrient conditions and chemical stimulations were studied using mitochondria-targeting, temperature-dependent, and non-photobleaching UCNPs ($NaYF_4$: 20%Yb^{3+}, 2%Er^{3+}). However, the conjugation efficiency with TPP was not very high. There were still some non-specific binding. Therefore, the surface functionalization should be optimised to enhance the targeting efficiency.

UCNPs ($NaYF_4$: 20%Yb^{3+}, 2%Er^{3+}) modified with copolymer showed an excellent stability and dispersity in the aqueous buffer, but sometimes the carboxyl groups might be folded into the polymer. If the functional group cannot be exposed outside, the carboxyl groups will not react with amine groups, leading to the low loading efficiency of mitochondrial targeting ligand TPP. To solve this problem, I used copolymer as a stable unit to obtain hydrophilic UCNPs ($NaYF_4$: 20%Yb^{3+}, 2%Er^{3+}). As the surface zeta potential of UCNPs@copolymer is negative in PBS buffer (pH~7.4), poly-l-lysine (PLL) is chosen as a second layer to provide amine groups. UCNPs@copolymer can be packed up by PLL through electrostatic interaction. The amine groups provided by PLL largely increase the conjugation efficiency with TPP.

4.2 Abstract

The intracellular metabolism of organelles, like lysosomes and mitochondria, is highly coordinated spatiotemporally and functionally. The activities of lysosomal enzymes significantly rely on the cytoplasmic temperature, and heat is constantly released by mitochondria as the byproduct of ATP generation during active metabolism. Here, we developed temperature-sensitive LysoDots and MitoDots to monitor the *in situ* thermal dynamics of lysosomes and mitochondria. The design is based on UCNPs ($NaYF_4$: 20%Yb^{3+}, 2%Er^{3+}) with high-density surface modifications to achieve the

exceptionally high sensitivity of 2.7% K^{-1} and low uncertainty of 0.8 K for thermometry to be used in living cells. We show the measurement is independent of the ion concentrations and pH values. With Ca^{2+} ion shock, the temperatures of both lysosomes and mitochondria increased by 2~4 °C. Intriguingly, with Chloroquine treatment, the lysosomal temperature was observed to decrease by up to ~3 °C, while mitochondria remained relatively stable. Lastly, with oxidative phosphorylation inhibitor treatment, we observed a 3~7 °C temperature increase and a thermal transition from mitochondria to lysosomes. These observations indicate different metabolic pathways and thermal transitions between lysosomes and mitochondria inside HeLa cells. The thermometry probes provide a powerful tool for multi-modality functional imaging of subcellular organelles and interactions with high spatial, temporal and thermal dynamics resolutions.

4.3 Background

The intracellular temperature and its dynamics are vital to maintaining the homeostasis of organelles as well as their biochemical reactions and metabolic processes. Thermal variations indicate whether cells are under their healthy physiological or disease status [1, 2]. The coordination of different organelles is required to maintain intracellular homeostasis and normal cellular functions. The intracellular organelles not only possess their specific functions but also communicate with each other through membrane contacts or membrane fusion, which together contribute to the survival, growth and division of the cells. Lysosomes and mitochondria, as the two major contributors to enzyme activity and energy production, are essential to cellular metabolism participating in many key biological processes such as autophagy, proliferation, cell death [4, 271], etc. Dysfunction of lysosomes and mitochondria has been found in several diseases [272].

The maintenance of both lysosomal and mitochondrial physiological functions and cellular homeostasis relies on intracellular temperature dynamics [273, 274]. Lysosomes are highly dynamic organelles responsible for the turnover of some proteins and lipids through digestive enzymes [275]. The enzymatic activities are highly dependent on a healthy pH and temperature environment. During the process of heatstroke, the pH values of lysosomes were observed to increase, which leads to cell death. A higher or lower temperature may reduce enzymatic activities and further disturb cellular

homeostasis [276]. Mitochondria are involved in the cellular respiratory and function as the energy factory [3]. During the respiratory activity, mitochondria transform energy from carbohydrates to ATP, simultaneously releasing heat as a byproduct.

Due to the lack of enabling techniques and tools, the functions of lysosomes and mitochondria have been independently studied in the past, though there must be intense crosstalks between the two organelles [4]: The dysfunctional mitochondria lead to the elevation of lysosomal pH [67]; and in some lysosomal storage diseases, the defects in the lysosomes also contribute to the dysfunction of mitochondria because the abnormal mitochondria cannot be cleared by lysosomes, leading to the pathological signalling [277]. At present, the interactions of lysosomes and mitochondria are usually studied from either their direct physical membrane contacts using super-resolution microscopy [254] or signalling pathways using molecular biology tools [4]. It is unclear how the spatiotemporal thermal dynamics of lysosomes and mitochondria contribute to maintaining homeostasis during pathological processes within a living cell.

Up to now, a series of thermometers based on fluorescence or luminescence imaging have been reported, including small organic dyes [112, 162], green fluorescent proteins (GFPs) [151, 160], polymeric nanoparticles [278], nanodiamonds [110, 140], quantum dots [117], and lanthanide-doped nanoparticles [279, 280]. The applications of intracellular thermometry in living cells have uncovered spontaneous thermogenesis and temperature variation [281-283]. Rationally designed luminescent Ln^{3+}-bearing polymeric micellar probes (Ln = Sm, Eu) have been used to measure the thermogenesis in individual cells, revealing the inhomogeneous intracellular temperature progressions [284]. Moreover, lysosome-targeting luminescent lanthanide complexes have been developed to simultaneously image the pH and temperature in the lysosomes [285, 286]. Additionally, several thermometers have been proposed for *in vivo* temperature sensing. For example, Ag_2S nanodots have been used to monitor brain thermoregulation [287] and UCNPs have been used for subcutaneous thermal sensing [279]. The unique photophysical properties, such as high brightness, superior photochemical stability, excellent temperature-responsive optical properties with large anti-Stokes shifts and long luminescence lifetimes, make UCNPs favourable to temperature sensing [158]. Though many advances have been made in using UCNPs-based thermometers to monitor the temperature variations in living cells, tissues, or animals [103, 125],

organelle-specific temperature sensing remains challenging in the physiological environment.

Here, we report surface modifications of high-density polymer linkers that can assist UCNPs ($NaYF_4$: 20%Yb^{3+}, 2%Er^{3+}) to be specifically guided and accumulated into lysosomes and mitochondria in living cells. We established a novel cascade targeting strategy in this work. We first introduce $PEGMEMA_{80}$-*b*-$EGMP_3$ di-block copolymers to transfer the hydrophobic UCNPs ($NaYF_4$: 20%Yb^{3+}, 2%Er^{3+}) to hydrophilic ones that can be internalized through the endocytosis process and ended in the lysosomes [288]. We name the structure of UCNPs@copolymer as **LysoDots**. To facilitate the escape of UCNPs ($NaYF_4$: 20%Yb^{3+}, 2%Er^{3+}) from lysosomes and relocation to pass through the potential barrier of the mitochondrial membrane, we then introduce Poly-L-Lysine (PLL) to further functionalize UCNPs ($NaYF_4$: 20%Yb^{3+}, 2%Er^{3+}) with a mitochondrial targeting moiety with high lipophilicity, (3-carboxypropyl)triphenylphosphonium bromide (TPP) [288]. We then name the structure of UCNP@PLL@TPP as **MitoDots**. This strategy allows two sets of thermometers with organelle-targeted properties to simultaneously and quantitatively sense the *in situ* temperature dynamics of lysosomes and mitochondria. The series of LysoDots and MitoDots demonstrate a relative temperature sensitivity at 32 °C of 2.7% K^{-1} and a temperature uncertainty of 0.8 K in HeLa cells, and more importantly, their performances are independent of the ion concentrations or pH conditions. We have observed intriguing spatiotemporal temperature dynamics in HeLa cells: i) with organelle non-specific Ca^{2+} ion shock, both lysosomal and mitochondrial temperature increase 2-4 °C; ii) with lysosome-specific drug treatment, the lysosomal temperature drops ~3 °C while the mitochondrial temperature remains 37 °C; iii) with mitochondria-specific drug treatment, we observed an interesting temperature increment (3-7 °C) and spatiotemporal thermal transition (1-2 min delay) from mitochondria to lysosomes. These observations indicate different metabolic pathways and thermal transitions between lysosomes and mitochondria. The live-cell thermal probes provide a powerful toolbox with multi-modality and multi-functional imaging capacities.

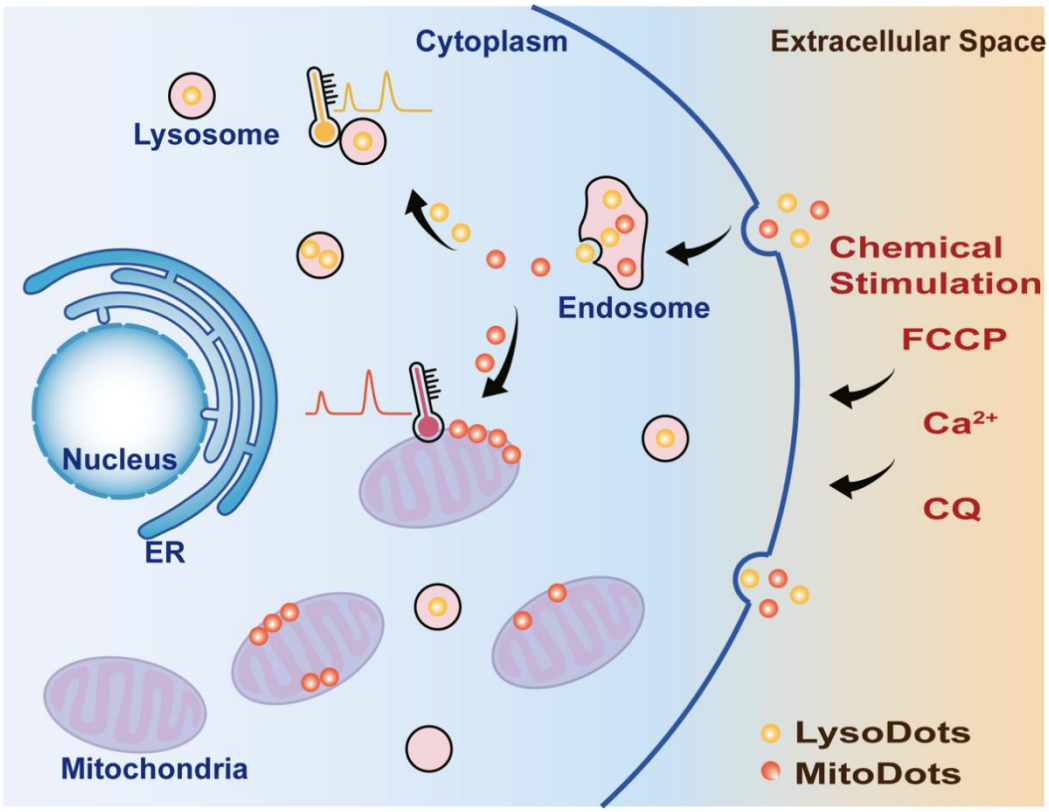

Figure 4-1 Schematic diagram of cascade organelle-targeted thermometers platform based on upconversion nanoparticles (UCNPs) *– UCNPs@copolymer (LysoDots) and UCNPs@PLL@TPP (MitoDots). LysoDots and MitoDots can be internalized by cells and accumulated in the lysosomes. The mitochondrial targeting moiety-TPP help MitoDots escape from the lysosomes and further accumulated into the mitochondria.*

4.4 Materials and Methods

4.4.1 Materials.

Yttrium(III) chloride hexahydrate (YCl_3•$6H_2O$, 99.99%), ytterbium chloride hexahydrate ($YbCl_3$•$6H_2O$, 99.99%), erbium chloride hexahydrate ($ErCl_3$•$6H_2O$, 99.9%), ethanol, cyclohexane, 1-octadecane (ODE), and oleic acid （OA） were purchased from Sigma-Aldrich. $PEGMEMA_{80}$-*b*-$EGMP_3$ di-block copolymer (copolymer) was a gift from Prof Martina Stenzel group in the University of New South Wales. Poly-l-lysine (PLL), (3-carboxypropyl) triphenylphosphonium bromide (TPP), 1-Ethyl-3-(3-dimethylamino-propyl)-carbodiimide (EDC), N-Hydroxysuccinimide (NHS), MES buffer, HEPES buffer, Tetrahydrofuran (THF), N, N-Dimethylformamide (DMF) were purchased from Sigma-Aldrich with reagent grade or higher. Dulbecco's Modified

Eagle Medium (DMEM), fetal bovine serum (FBS), Phosphate-Buffered Saline (PBS), Penicillin-Streptomycin (PS), MitoTracker (MitoTracker™ Deep Red FM, Invitrogen™ M22426), LysoTracker (LysoTracker™ Deep Red FM, Invitrogen™ L12492) were purchased from Life Technologies. Bovine Serum Albumin (BSA), dimethyl sulfoxide (DMSO), carbonyl cyanide-4-(trifluoromethoxy)phenylhydrazone (FCCP), ionomycin calcium salt were purchased from Sigma-Aldrich with reagent grade or higher. Chloroquine (CQ, 14774S) was purchased from Cell Signaling Technology.

4.4.2 Synthesis of hydrophilic upconversion nanoparticles

UCNPs ($NaYF_4$: 20%Yb^{3+}, 2%Er^{3+}) nanoparticles were synthesized following the previously reported protocols with some modification [214]. In a typical process, prepare stock solution of YCl_3 (0.4 M in methanol), $YbCl_3$ (0.2 M in methanol) and $ErCl_3$ (0.1 M in methanol). Then, 6 mL of OA and 15 mL of 1-octadecane were added into a 50 mL round-bottom flask with three necks, and then added 1.95 mL of YCl_3 stock solution (0.4 M in methanol), 1.0 mL of $YbCl_3$ stock solution (0.2 M in methanol), and 0.2 mL of $ErCl_3$ stock solution (0.1 M in methanol). The mixture was stirred under argon protection and then heated to 100 °C for 10 minutes and 160 °C for 30 minutes to get rid of methanol and H_2O. Second, 5 mL of NaOH (0.1 g) -NH_4F (0.14815 g) methanol solution was added into the mixture when it cooled down to 30 °C and stirred for 30 minutes. Subsequently, the mixture was heated to 100 °C for 30 minutes and then heated to 300 °C for 1.0 hours. Finally, 5 mL of ethanol was added into the mixture to precipitate UCNPs ($NaYF_4$: 20%Yb^{3+}, 2%Er^{3+}). UCNPs ($NaYF_4$: 20%Yb^{3+}, 2%Er^{3+}) were washed 3 times with ethanol and cyclohexane before using. Finally, the UCNPs ($NaYF_4$: 20%Yb^{3+}, 2%Er^{3+}) were dissolved in the 10 mL of cyclohexane and stored in the fridge.

To obtain hydrophilic UCNPs ($NaYF_4$: 20%Yb^{3+}, 2%Er^{3+}), the nanoparticles were first modified with copolymer [167]. 5 mg of UCNPs ($NaYF_4$: 20%Yb^{3+}, 2%Er^{3+}) and 5 mg polymer were dissolved in 1 mL of THF and then shaken at room temperature for 12 hours. Next, the UCNPs ($NaYF_4$: 20%Yb^{3+}, 2%Er^{3+}) coated with a polymer (UCNPs@copolymer) were washed with THF three times and pure water three times. Finally, the UCNPs@copolymer was dissolved in 0.5 mL of PBS buffer and stored at 4 °C for further use.

4.4.3 Bioconjugation of upconversion nanoparticles with (3-carboxypropyl)triphenylphosphonium bromide (TPP)

To function hydrophilic nanoparticles with amine groups, 0.5 mL of UCNPs@copolymer were dissolved in the 0.5 mL of PLL solution and stirred at room temperature for 40 minutes. The reaction was stopped by centrifugation and washed three times with pure water. Finally, the UCNPs nanoparticles functionalized with amine groups (UCNPs@PLL) were stored in the fridge.

For the bioconjugation of UCNPs@PLL with TPP, 30 mg of TPP, 10 mg of EDC, and 10 mg of NHS were first dissolved into 1mL of DMF by ultrasound. After 1h, 10 mg of UCNPs@PLL were added to the mixture. The reaction was stirred at room temperature for 12 hours and then washed with DMF and pure water. Finally, the product UCNPs@PLL conjugated with TPP (UCNPs@PLL@TPP) was stored in 0.5 mL of PBS buffer for further use.

4.4.4 Characterization

The morphology of UCNPs was characterized using the FEI Tecnai transmission electron microscopy (FEI, U.S.A.). The hydrodynamic size and zeta potential of UCNPs were determined by a zeta sizer nano (Malvern, U.K.). The spectra were measured by a custom-built spectrometer. The intensity of single UCNP has been measured by a purpose-built scanning confocal system, which is shown in **Figure 4-2**. The excitation wavelength is a 980 nm laser, which is focused onto the sample through a 100x objective lens (NA 1.4). The emission of UCNPs ($NaYF_4$: 20%Yb^{3+}, 2%Er^{3+}) is collected by the same objective lens, then focused by a tube lens to an optical fibre. A Single Photon Counting Avalanche Diode detector is connected to the collection optical fibre to detect the emission intensity. The scanning is achieved by the x-y movement of the 3D piezo stage. After the point-by-point scanning process, each single UCNP ($NaYF_4$: 20%Yb^{3+}, 2%Er^{3+}) will present a Gaussian spot in the confocal scanning microscope image. The maximum brightness value (photon count) of each Gaussian spot can be used to represent the intensity of a single particle.

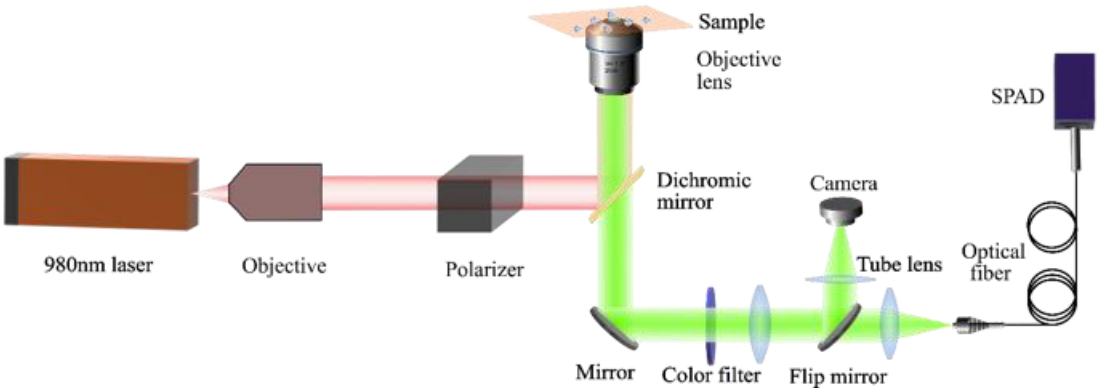

Figure 4-2 Scanning confocal system for single UCNP ($NaYF_4$: 20%Yb^{3+}, 2%Er^{3+}) emission measurements.

4.4.5 Luminescence Stability of UCNPs@TPP Against Environmental Parameters

The spectrometer was used to measure the emission spectrum of LysoDots or MitoDots under different pH, ionic strength (Mg^{2+}, Ca^{2+} and K^{+}) and drugs (CQ and FCCP). The PBS with gradient pH values (4 - 10) were tuned by adding different amounts of HCl or KOH. Ionic strength (0 - 500 mM KCl) was controlled by adding different amounts of KOH. 0 - 2.0 mM $CaCl_2$, and 0 - 1.2 mM $MgCl_2$ were obtained by adding different amounts of $CaCl_2$ and $MgCl_2$. 1 mg of LysoDots or MitoDots were dissolved in the PBS with different pH, different concentrations of ionic strength, or drugs and transferred to the cuvette. The samples were excited at 980 nm and the spectrum was captured from 480 nm to 600 nm.

4.4.6 Colocalization of UCNPs with MitoTracker or/and LysoTracker.

The HeLa cells were seeded on the fluoro-dish (35 mm) at 10^5 cell density and incubated in DMEM medium containing 10% v/v FBS for 12 hours. Then the cells were washed 3 times with PBS and incubated with UCNPs ($NaYF_4$: 20%Yb^{3+}, 2%Er^{3+}) (50 μg/mL, 1 mL) for 12 hours at 37 °C with 5% CO_2. Next, the cells were washed with PBS and incubated with 200 nM MitoTracker or/and 200 nM LysoTracker for 0.5 hours. Finally, the cells were washed with PBS and waiting for imaging in DMEM.

4.4.7 Time-dependent Localization/Accumulation of LysoDots and MitoDots

To track the intracellular fate of the LysoDots and MitoDots after being internalized by the cells, the time-dependent location/accumulation of LysoDots and MitoDots were characterized, respectively. HeLa cells were cultured in the glass-bottomed dish and incubated cells with LysoDots or MitoDots for 2, 4, 6, and 8 hours. Then the cells were stained with LysoTracker DeepRed or MitoTracker DeepRed for 30 min right before the TIRF imaging. The cell samples were imaged with dual-colour TIRF microscopy at the wavelength of 980 nm and 647 nm.

4.4.8 Relative temperature sensing sensitivity and uncertainty.

The relative temperature sensing sensitivity (S_R) indicates the relative change of Δ per degree of temperature change and was calculated using [130]:

$$S_r = \frac{1}{\Delta}\left|\frac{\partial \Delta}{\partial T}\right| \qquad (1)$$

The temperature uncertainty δT is the smallest temperature change that can be detected in given measurement and was defined by [130]:

$$\delta T = \frac{\delta \Delta}{S_r \bullet \Delta} \qquad (2)$$

4.4.9 *In situ* Calibration Curves and Temperature Sensing of Lysosomes and Mitochondria

The HeLa cells were cultured in DMEM containing 10% v/v FBS and 1% v/v PS at 37 °C with 5% CO_2. Cells were transferred into the fluoro-dish (35 mm in diameter with No.1 coverglass bottom). Then the cells were incubated in the dish with 1 mL culture medium containing 50 μg/mL UCNPs@TPP or/and UCNPs@copolymer at 37 °C for 12 hours.

To obtain the *in situ* calibration curves for temperature sensing inside HeLa cells, the UCNPs ($NaYF_4$: 20%Yb^{3+}, 2%Er^{3+})-labeled cells were fixed by 4% PFA and imaged immediately afterwards on a custom-built TIRF microscope with an external temperature controller. The calibration curves were obtained by a 980 nm laser

excitation and 525/545 nm emission under different temperatures (from 31 °C to 40 °C with 1 °C as the interval).

For the CQ-, FCCP-, and Ca^{2+}-induced lysosomal and mitochondrial temperature changes in **Figure 4-11**, firstly, the LysoDots and MitoDots were incubated with HeLa cells for 12 hours (overnight). Then, the HeLa cells were stained with LysoTracker Red and MitoTracker Deep Red following the manufacturer's instructions. Next, PBS (as solvent control), DMSO (1:1000 as solvent control), CQ (200 nM), FCCP (10 μM) or ionomycin calcium salt (1 μM) was incubated with HeLa cells before and during the TIRF imaging. The fluorescence intensities of LysoTracker Red and MitoTracker Deep Red were excited with 561 nm and 647 nm lasers (MPB Communication, Canada) and the emissions were detected with 593/40 and 680/42 emission filters (Semrock, USA), respectively. The luminescent intensities and ratio (I_{525} / I_{545}) of LysoDots and MitoDots were excited with a 980 nm laser (Thorlabs, USA) and detected by 525/15 and 545/30 emission filters (Semrock, USA), respectively. All the fluorescent and luminescent signals were detected by an EMCCD (DU897, Andor, UK).

For data analysis, the raw images were input into ImageJ (Fiji) and luminescent intensities of single particles were analysed with measurement tools. For lysosomal and mitochondrial temperature monitoring, $\ln(I_{525}/I_{545})$ was calculated for those UCNPs only colocalized with LysoTracker and MitoTracker, respectively. Then the *in situ* temperature of lysosomes and mitochondria was determined according to the calibration curve in **Figure 4-9F** and then plotted in **Figures 4-11 C, E** and **G**.

4.4.10 Statistical Analysis.

Student's t-test was applied to examine the differences among variables. Data were shown as mean ± SD. *p values ≤ 0.05 are considered to be statistically significant.

4.5 Results and Discussion

4.5.1 Design, Synthesis and Characterization of Organelle-Targeted Thermometers

To construct a stable and biocompatible UCNPs ($NaYF_4$: 20%Yb^{3+}, 2%Er^{3+}) based thermometer, the copolymer was used to transfer the hydrophobic UCNPs ($NaYF_4$: 20%Yb^{3+}, 2%Er^{3+}) into hydrophilic ones [167, 289]. The UCNPs ($NaYF_4$: 20%Yb^{3+},

2%Er^{3+}) modified with copolymers (UCNPs@copolymer) showed long-term colloidal stability in the culture medium (**Figure 4-3A**). This copolymer contains phosphate acid anchoring groups, which have greater absorption energy with lanthanide ions than that of OA [167]. Moreover, the carboxylic acid group at the terminal of the copolymer provides the potential for further conjugation in biological applications [290]. To improve the efficiency of the bio-conjugation and provide high-density amine groups on the UCNPs ($NaYF_4$: 20%Yb^{3+}, 2%Er^{3+}) surface, PLL was used to further modify the surface of UCNPs@copolymer through electrostatic interactions. Then UCNPs@PLL were further crosslinked with a mitochondria-targeted molecule (TPP) through the carbodiimide reaction (UCNPs@PLL@TPP) (**Figure 4-4A**). The TPP modification will guide and accumulate the particles to mitochondria for organelle-specific delivery [288]. Similarly, UCNPs@PLL@TPP exhibited chemical stability in the culture medium (**Figure 4-3B**). The three kinds of modified UCNPs (UCNPs@copolymer, UCNPs@PLL, and UCNPs@PLL@TPP) showed good morphology uniformity and monodispersity. The size of UCNPs ($NaYF_4$: 20%Yb^{3+}, 2%Er^{3+}) increased from 29.97 ± 0.98 nm of the as-synthesized UCNPs to 30.23 ±1.48, 30.54 ± 1.17, and 31.57 ± 1.23 nm (measured by TEM in **Figure 4-4B**). The DLS results confirmed the high uniformity with the average values of hydrodynamic size increasing from 55.67 ± 0.62 nm to 59.80 ± 0.25 nm and 66.51 ± 1.49 nm after each step of surface modifications (**Figure 4-4C**). The Zeta potential results (**Figure 4-4D**) indicated the successful modification of each step, as the surface charge turned from negative 14.28 ± 0.59 mV to positive 20.77 ± 0.30 mV with the exposure of PLL and 12.18 ± 0.47 mV with TPP. The presence of copolymers, PLL, and TPP on the surface of UCNPs was further confirmed by ATR-FTIR. As shown in **Figure 4-5**, after grafting the copolymers on the surface of the nanoparticles, the asymmetric COO- stretching at 1547 cm^{-1} of oleic acid molecules completely disappeared, with both the characteristic ATR-FTIR spectral peak at 1100 cm^{-1} (C−O−C stretching) and the new Ph-P band at 1440 cm^{-1} confirming the success in copolymers and TPP ligands modifications.

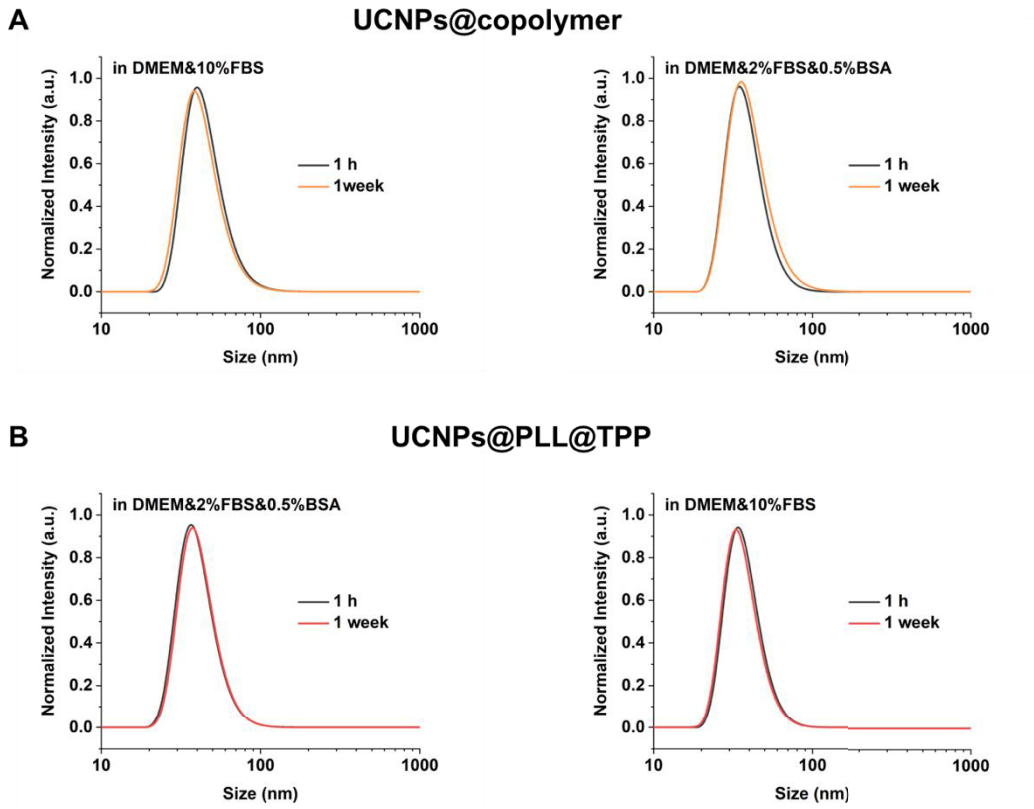

Figure 4-3 The long-term bio-stability of UCNPs in aqueous solution. *(A) DLS CONTIN plots of UCNPs@copolymer in culture medium before and after 1 week. (B) DLS CONTIN plots of UCNPs@PLL@TPP in culture medium before and after 1 week.*

In chapter 3, the crosslinked polymer networks composed of copolymers and 4Arm-PEG-NH_2 on the surface of UCNPs (UCNPs@PEG) demonstrated good stability but relatively low emission intensity. As shown in **Figure 4-4E & F, Figure 4-6**, the intensity measurements indicated that the luminescent intensity of UCNPs@PLL was 1.8 times higher than that of UCNPs@PEG compared with the method in chapter 3. Molecules close to the UCNP surface can also reduce the intensity, since the vibrational states of chemical bonds like O–H, C–H or N–H match the phonon states of the host material resulting in non-radiative relaxation of the excited lanthanide ions [291]. Moreover, PLL provides much more free amine groups than 4Arm-PEG-NH_2 on the UCNPs ($NaYF_4$: 20%Yb^{3+}, 2%Er^{3+}) surface because PLL is an amino acid chain, and it decorates the UCNPs ($NaYF_4$: 20%Yb^{3+}, 2%Er^{3+}) surface by electrostatic interactions. To verify UCNPs@PLL provide more amine groups on the surface than that of UCNPs@PEG, the conjugation efficiency of TPP was measured. 10 mg of TPP and 5 mg of nanoparticles were conjugated overnight through EDC-NHS reaction. After the

reaction, unreacted TPP was completely removed by centrifugal ultrafiltration and the supernatant was retained so that, according to the UV−vis absorptions at 268 nm of various concentrations of TPP in the supernatant (**Figure 4-7**), the conjugation efficiency of TPP has been enhanced from 0.332 mg to 1.545 mg for 5 mg of UCNPs@PEG and UCNPs@PLL, respectively.

In our cascade organelle-targeting strategy, after being internalized by the cells [288], UCNPs@copolymer nanoparticles translocate from the early endosomes to the late endosomes that ferry the nanoparticles into lysosomes, and therefore as a thermometer to naturally target lysosome (**LysoDots**); UCNPs@PLL@TPP nanoparticles first being accumulated in the lysosomes, and due to the lipophilic and positive TPP moieties, can escape from endo-lysosomes to specifically target mitochondria (**MitoDots**).

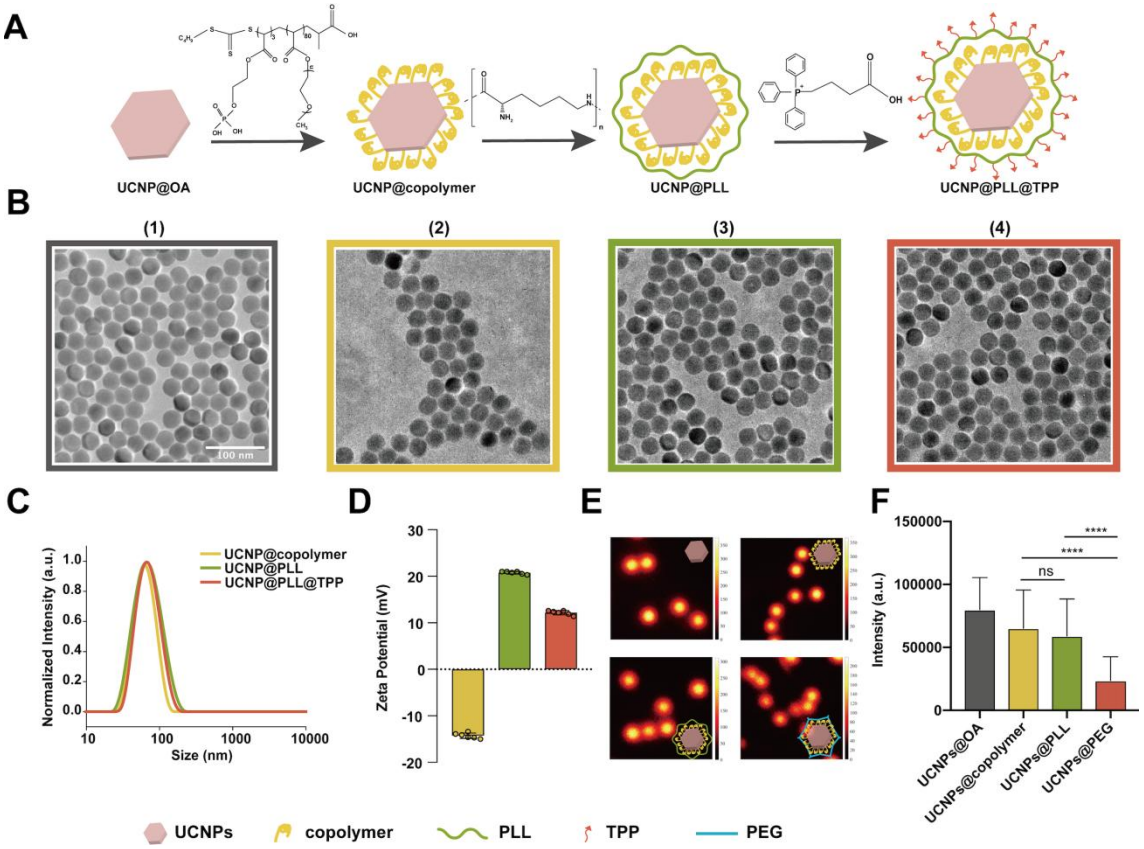

Figure 4-4 Surface modification strategy and characterization of UCNPs (NaYF$_4$: 20%Yb^{3+}, 2%Er^{3+}) to produce efficient organelle-targeting thermometers. *A. Schematic illustration of the cascade modification steps based on UCNPs with the surface modified from oleic acid (OA, pink), to PEGMEMA$_{80}$-b-EGMP$_3$ di-block copolymers (yellow), poly-l-lysine (PLL, green) and (3-carboxypropyl)triphenylphosphonium bromide (TPP, red), respectively. B. Representative transmission electron microscopy (TEM) images of 1) UCNPs-OA (grey), 2) UCNPs@copolymer*

*(LysoDots, yellow), 3) UCNPs@PLL (green), and 4) UCNPs@PLL@TPP (MitoDots, red), respectively. Scale bar, 100 nm. C. Dynamic light scattering (DLS) size analysis of UCNPs after different surface modifications (colour-codes same as in Fig1B). D. ζ-Potentials of UCNPs after different surface modifications (colour-codes same as in Fig1B). E. Luminescence emission images from single UCNPs coated with OA, copolymer, PLL, and 4Arm-PEG-NH_2 (PEG) under 980 nm excitation. F. Statistics of the emission intensity of single individual UCNPs in Fig.1E. Data points represent mean ± SD. N = 160 single particles. Significance label ****, p<0.0001.*

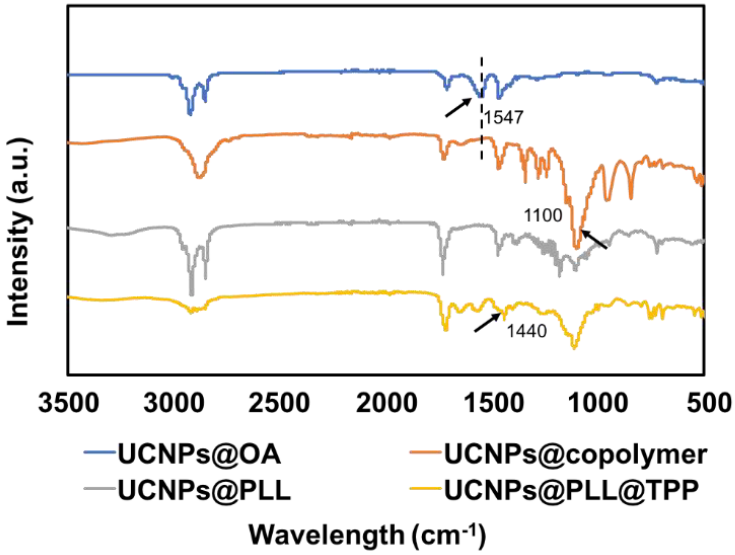

Figure 4-5 The ATR-FTIR spectra of prepared UCNPs@OA, UCNPs@copolymer, UCNPs@PLL and UCNPs@PLL@TPP.

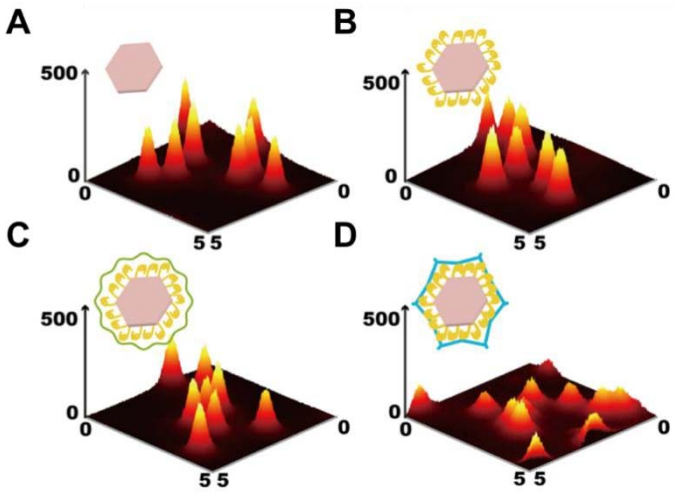

Figure 4-6 Luminescence emission images from individual UCNP coated with OA, copolymer, PLL, and PEG under 980 nm excitation.

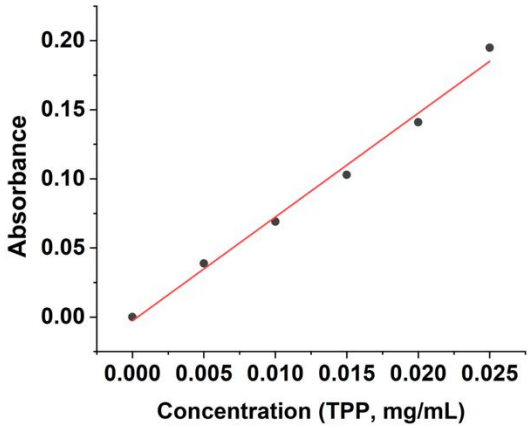

Figure 4-7 UV-Vis absorption standard curve of TPP (268 nm) at various concentrations. *It should be noted that for the TPP standard curve, as the EDC and NHS mixture in the sample solution showed obvious UV-Vis absorption, corresponding EDC and NHS need to be added as background into the standard TPP solution.*

4.5.2 *in vitro* Thermo-responsive Properties of LysoDots and MitoDots

The luminescence of UCNPs doped with Yb^{3+} ions and Er^{3+} ions strongly depend on the temperature (**Figure 4-8A(1)**) [135]. Within a single nanoparticle, Yb^{3+} ions transfer the energy to the Er^{3+} ions under the 980 nm excitation, and the Er^{3+} ions emit two distinct green emissions between 515-535 nm (centred at 525 nm) and 535-570 nm (centred at 545 nm) (**Figure 4-8(2)**). The intensity ratio of 525 nm and 545 nm peaks following the Boltzmann distribution and cannot be affected by the concentration of nanoparticles [115],

$$\frac{I_{525}}{I_{545}} = C exp\left(-\frac{\Delta E}{kT}\right) \qquad (4)$$

where I_{525} and I_{545} are the integrated luminescent intensities around 525 nm and 545 nm emission peak, respectively; C is a constant; ΔE is the $^4S_{3/2}$ to $^2H_{11/2}$ energy difference of the Er^{3+} ion; k is the Boltzmann constant, and T is the absolute temperature. Then the calibration curve of nanoparticles in the water was plotted, and it showed a great linear fitting (**Figure 4-8A(3)**).

Living cells are complex systems with the environment changing in both spatial and temporal domains. For example, the pH value is much lower in lysosomes than that in other organelles. The concentrations of Ca^{2+} in mitochondria and lysosomes also vary across the different phases of the cell cycle. To validate the thermal detection stability

of LysoDots and MitoDots, we measured the temperature-dependent spectrum in different pH (4-10) and ion concentration conditions, including Ca^{2+} (0-2 mM), Mg^{2+} (0-1.2 mM) and K^{+} (0-500 mM). **Figure 4-8B** confirms that the luminescence responding to the temperature of LysoDots (**Figure 4-8B left panel**) and MitoDots (**Figure 4-8B right panel**) are independent of either ion concentration or pH conditions.

To demonstrate the advance of the cascade modification strategy in enhancing the mitochondrial targeting efficiency, both MitoDots, based on UCNPs@PLL@TPP (**Figure 4-8C top panel**) and UCNPs@PEG@TPP used in chapter 3 (**Figure 4-8C bottom panel**) were incubated with HeLa cells for 12 hours. As shown in (**Figure 4-8D**), the average intensity of individual foci from UCNPs@PLL@TPP (MitoDots) was almost 10-times higher than that of UCNPs@PEG@TPP. The results suggest that the more TPP on the surface of UCNPs@PLL enabled the more efficient mitochondria-targeting ability of thermometer-MitoDots.

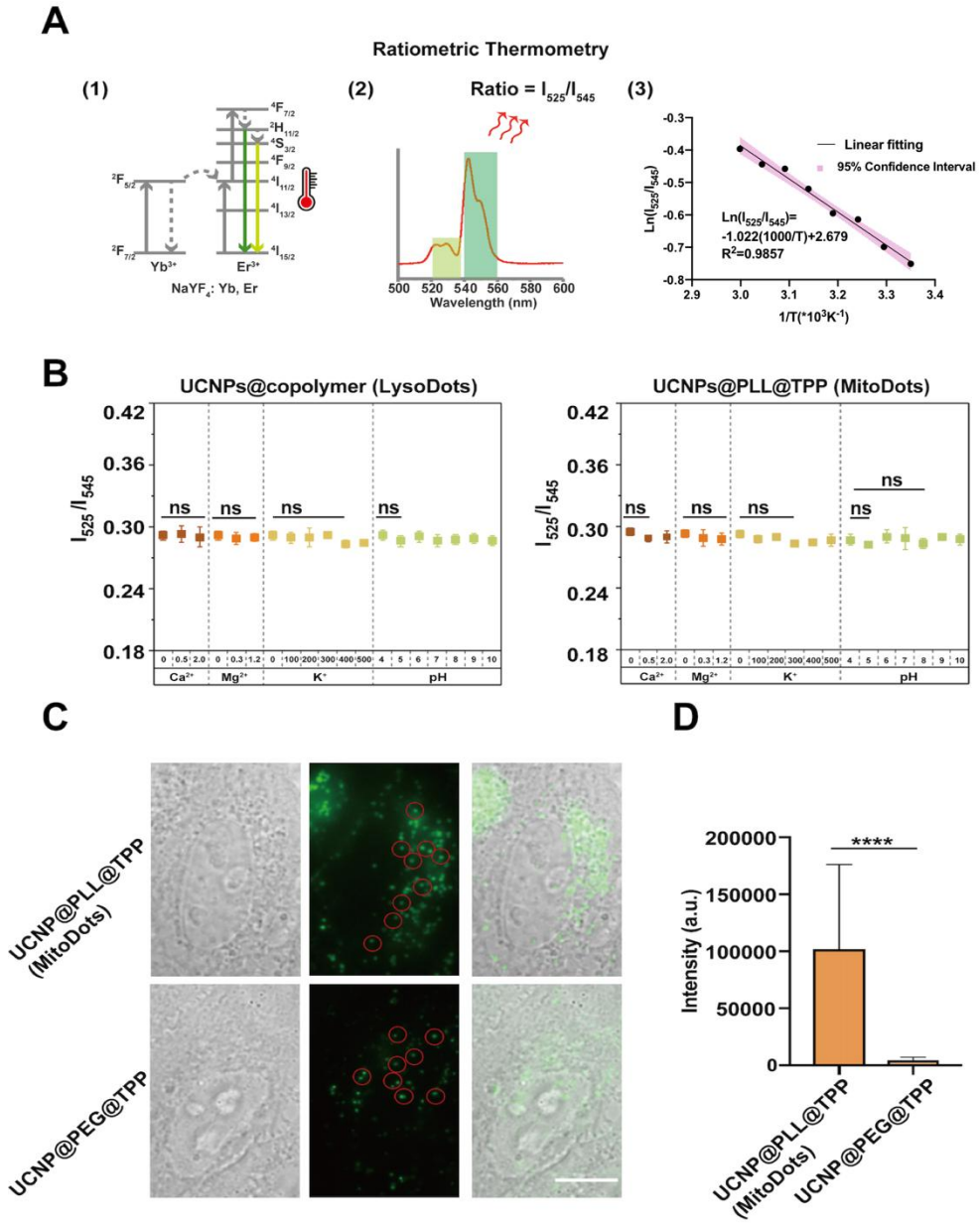

Figure 4-8 **Stable and efficient LysoDots and MitoDots.** ***A.*** *Energy level (1) and ratiometric thermomeer (2) of temperature-sensitive UCNPs. Standard temperature sensing curve (3) by plotting* $ln(I_{525}/I_{545})$ *vs 1000/T to calibrate the thermometric scale in the water. The equation is* $ln(I_{525}/I_{545}) = -1.022(1000/T) + 2.679$ ($R^2 = 0.9857$). *The 95% confidence interval for slope, Y-intercept, and X-intercept are -1.145 to -0.8989, 2.288 to 3.069, and 2.545 to 2.682, respectively.* ***B.*** *Stability tests of ratiometric thermometers at different* Ca^{2+} *ion concentrations (0-2 mM),* Mg^{2+} *ion concentrations (0~1.2 mM),* K^+ *ion concentrations (0~500 mM) and pH values (4~10). N = 3 independent repeats.* ***C.*** *Bright Field, luminescence, and merge images of UCNPs@PLL@TPP (MitoDots) and UCNPs@PEG@TPP in HeLa cells. Scale bar = 10 μm.* ***D.*** *Quantification of enhanced emission intensities from UCNPs@PEG@TPP to UCNPs@PLL@TPP (MitoDots) used in HeLa cells. Data points represent mean ± SD. N = 200 regions of interest (ROIs). Significance label ****,*

$p<0.0001$.

4.5.3 Specificities of the Cascade Organelle-targeting and Accumulation of LysoDots and MitoDots

Using LysoTracker and MitoTracker as controls, we further performed both the independent and the simultaneous colocalization assays in HeLa cells to evaluate the intracellular specific localizations and organelle accumulation efficiencies of LysoDots and MitoDots. It is based on a purpose-built TIRF microscopy system with 561 nm, 647 nm and 980 nm excitation lasers and a live cell incubator.

We first checked the targeting specificity of LysoDots by incubating HeLa cells with LysoDots alone for 12 hours, followed by LysoTracker Red and MitoTracker DeepRed staining for 30 minutes before TIRF imaging. As shown in **Figure 4-9A top panel**, LysoDots (cyan) colocalized cohesively with LysoTracker (magenta) with similar dotted morphology. The Pearson's correlation coefficient between LysoDots and LysoTracker (**Figure 4-9B**) was as high as 0.95, almost twice higher than that between LysoDots and MitoTracker (0.54). Usually, we consider a Pearson's correlation coefficient higher than 0.6 as credible colocalizations [255].

Similarly, we then checked the specificity of MitoDots by incubating HeLa cells with MitoDots (cyan) alone for 12 hours, followed by LysoTracker and MitoTracker staining. As shown in **Figure 4-9A bottom panel**, we found that MitoDots also colocalized cohesively with MitoTracker (yellow) with similar linear and network morphologies. The Pearson's correlation coefficients (**Figure 4-9B**) between MitoDots and LysoTracker and between MitoDots and MitoTracker were 0.82 and 0.77, respectively, revealing the process of MitoDots' escape from lysosomes to mitochondria. The significantly higher Pearson's correlation coefficient between MitoDots and MitoTracker (0.77), compared with that between LysoDots and MitoTracker (0.54, $p < 0.001$, **Figure 4-9C**), confirmed that the sufficient amount of TPP moieties on the surface of MitoDots has efficiently facilitated thermometers to anchor onto mitochondria. The internalization and specific accumulation process have been further revealed by time-dependent imaging and an increment in Pearson's correlation coefficient values in **Figure 4-10**. As a result, in our cascade organelle-targeting strategy, after being internalized by the cells [288], UCNPs@copolymer nanoparticles

(LysoDots) translocate from the early endosomes to the late endosomes that ferry the nanoparticles into lysosomes, and therefore as a thermometer to naturally target lysosome; UCNPs@TPP nanoparticles (MitoDots) first being accumulated in the lysosomes, and due to the lipophilic and positive TPP moieties, can escape from endo-lysosomes to specifically target mitochondria.

To get an *in situ* calibration curve for temperature sensing, we plotted the temperature value versus the $\ln(I_{525}/I_{545})$ of LysoDots and MitoDots in paraformaldehyde (PFA) fixed HeLa cells by changing the temperature using an external temperature-controllable incubator. As shown in **Figure 4-9D**, both LysoDots and MitoDots were incubated with HeLa cells for 12 hours, then cells were stained with LysoTracker and MitoTracker for 30 min and followed by PFA fixation before TIRF imaging when the temperature increased from 31 °C to 40 °C (**Figure 4-9E**). Both the logarithmic values of the I_{525}/I_{545} ratio for LysoDots and MitoDots showed gradual and linear luminescence relative to the reciprocal temperature, i.e. $\ln(a \cdot I_{525}/I_{545}) = -0.9935(1000/T) + 2.6608$ ($R^2 = 0.9921$) and $\ln(a \cdot I_{525}/I_{545}) = -1.0204(1000/T) + 2.7492$ ($R^2 = 0.9957$), respectively. As shown in **Figure 4-9F**, the root-mean-square deviation (RMSD) of these two linear fittings was measured as 0.007025, indicating no difference between LysoDots and MitoDots. The relative sensing sensitivity at 32 ºC is 2.7% K^{-1} and the temperature resolution (uncertainty) is ~0.8 K.

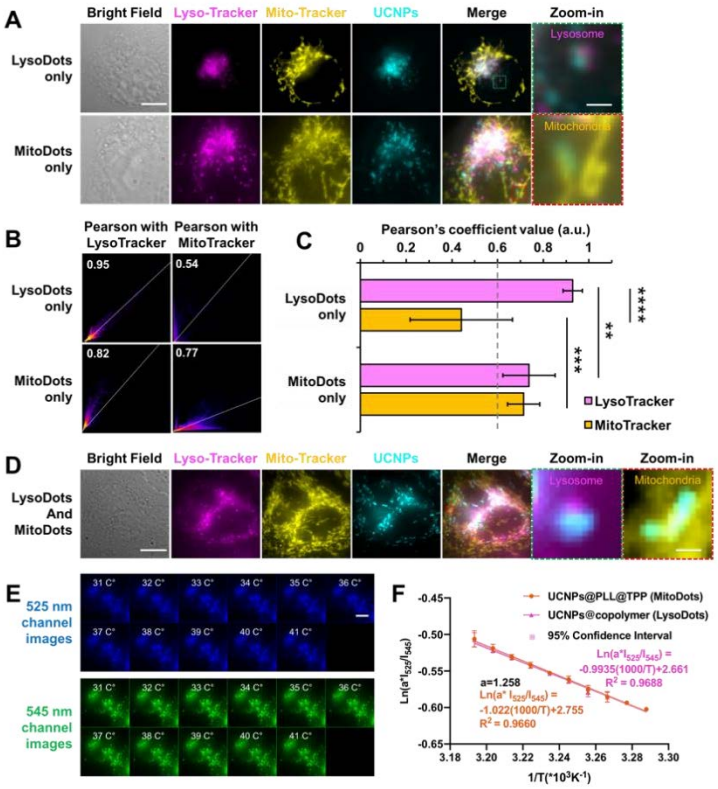

Figure 4-9 Organelle-specific accumulations of LysoDots and MitoDots. ***A.*** *Images of representative cells were incubated with LysoDots (cyan, top panel) or MitoDots only (cyan, bottom panel) for 12 hrs followed by LysoTracker (magenta) and MitoTracker (yellow) staining for 30 min before TIRF imaging. The zoom-in areas show colocalizations and morphologies. The line profiles demonstrate colocalization across the three channels. Scale bar = 10 μm for the whole-cell images and 1 μm for the zoom-in images.* ***B.*** *Pearson's correlation coefficient value of LysoDots with LysoTracker and MitoTracker (top panel) and MitoDots with LysoTracker and MitoTracker (bottom panel).* ***C.*** *Statistics of Pearson's coefficient values in Fig.3B. Data points represent mean ± SD. N = 30 ROIs from 3 independent biological experiments. Significance label **, p<0.01; ***, p<0.001.* ***D.*** *Images of a representative cell incubated with both LysoDots and MitoDots (cyan) for 12 hrs and stained with LysoTracker (magenta) and MitoTracker (yellow) 30 min before fixation and TIRF imaging, and the zoom-in areas to show the colocalization and morphology.* ***E.*** *Snapshot images of 525 nm emission (blue, top panel) and 545 nm emission (green, bottom panel) from UCNPs when external temperature increased from 31 to 41 C° (1 C° as interval).* ***F.*** *Plot of $\ln(a \cdot I_{525}/I_{545})$ vs 1000/T to calibrate the thermometric scale of LysoDots (magenta line, the 95% confidence interval for slope, Y-intercept, and X-intercept are -1.016 to -0.9712, 2.588 to 2.733, and 2.665 to 2.691, respectively.) and MitoDots (orange line, the 95% confidence interval for slope, Y-intercept, and X-intercept are -1.046 to -0.9982, 2.677 to 2.833, and 2.682 to 2.708, respectively.) in HeLa cells. Data represent mean ± SD (n = 25 cells from 3 independent biological experiments.). The error bars represent the standard deviations of the mean values (95% confidence interval, n=25 cells).*

Scale bar = 10 μm.

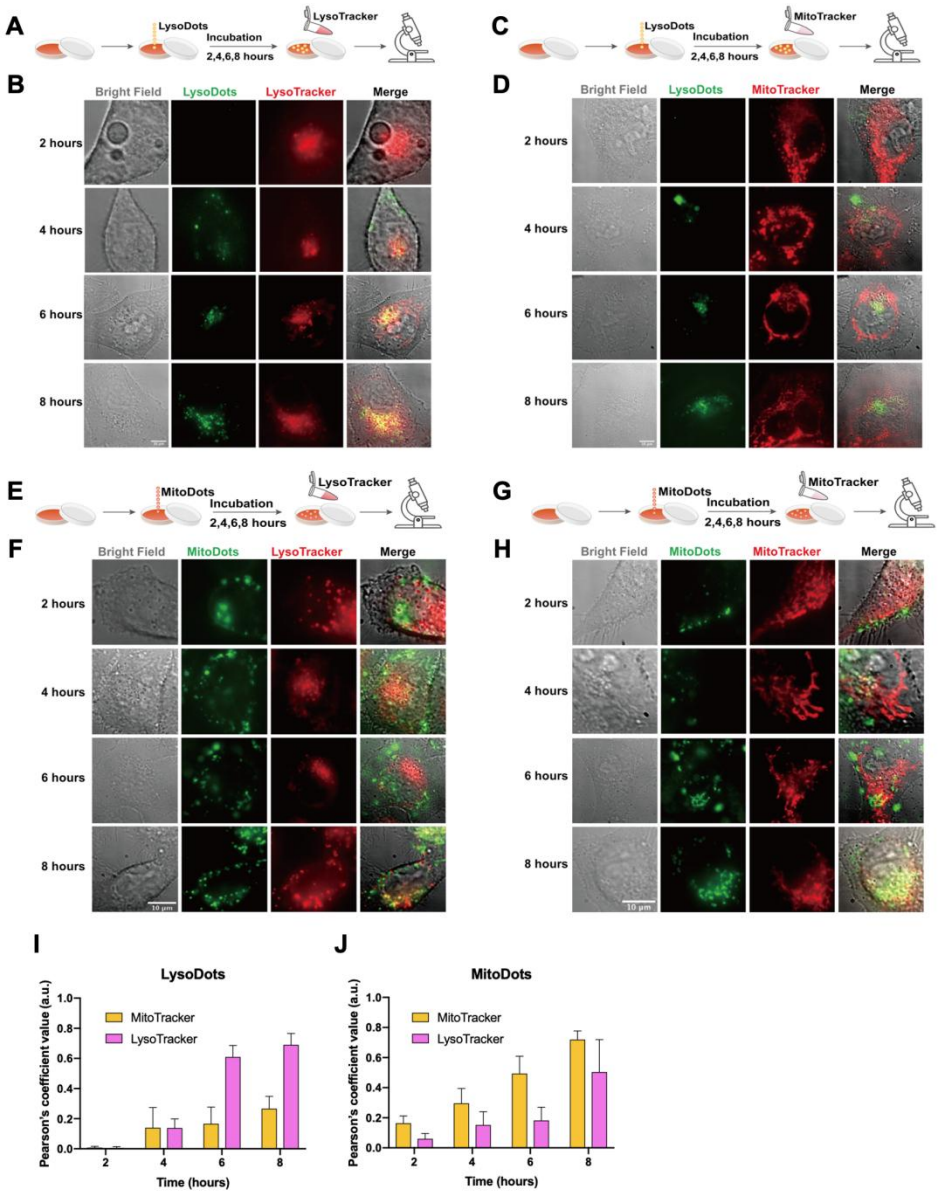

Figure 4-10 Cascade-targeting evaluations and time-dependent accumulation of LysoDots and MitoDots in living HeLa cells. *A. The schematic of the experimental design for time-dependent accumulation of LysoDots with LysoTracker in living HeLa cells. B. The representative bright field (grey) and TIRF images of HeLa cells that were incubated with LysoDots (green) for 2, 4, 6, and 8 hours, and then stained with Lysotracker DeepRed (red) for an additional 30 minutes. Scale bars, 10 μm. C. The schematic of the experimental design for time-dependent accumulation of LysoDots with MitoTracker in living HeLa cells. D. The representative bright field (grey) and TIRF images of HeLa cells that were incubated with LysoDots (green) for 2, 4, 6, and 8 hours, and then stained with MitoTracker DeepRed (red) for an additional 30 minutes. Scale bars, 10 μm. E. The schematic of the experimental design for time-dependent accumulation of MitoDots with LysoTracker in living HeLa*

cells. F. The representative bright field (grey) and TIRF images of HeLa cells that were incubated with MitoDots (green) for 2, 4, 6, and 8 hours, and then stained with Lysotracker DeepRed (red) for an additional 30 minutes. Scale bars, 10 μm. G. The schematic of the experimental design for time-dependent accumulation of MitoDots with MitoTracker in living HeLa cells. H. The representative bright field (grey) and TIRF images of HeLa cells that were incubated with MitoDots (green) for 2, 4, 6, and 8 hours, and then stained with MitoTracker DeepRed (red) for an additional 30 minutes. Scale bars, 10 μm. I. Statistics of Pearson's correlation coefficient values of LysoDots with LysoTracker (purple) and Mitotracker (yellow) in Fig. 4-10 B and D. Data points represent mean ± SD. N = 5 cells. J. Statistics of Pearson's correlation coefficient values of MitoDots with LysoTracker (purple) and Mitotracker (yellow) in Fig. 4-10 F and H. Data points represent mean ± SD. N = 30 ROIs from 10 cells.

4.5.4 Mapping the Thermodynamics of Lysosomes and Mitochondria Under Chemical Stimulations

By incubating HeLa cells with both LysoDots and MitoDots for 12 hours and with LysoTracker and MitoTracker for 30 min, we simultaneously mapped the temperature dynamics of both lysosomes and mitochondria under external chemical stimulations.

We first treated HeLa cells with Ca^{2+} ion shock, which is an organelle non-specific treatment. The Ca^{2+} ion shock can promote the pumping of ions and accelerate respiration reactions [292]. Ionomycin calcium salt is an ionophore that makes the cell membrane highly permeable for Ca^{2+} ions [117], which induces intracellular stress, possibly causing damage to both lysosomes and mitochondria in HeLa cells [292]. As shown in **Figure 4-11A-C**, upon a 1 μM ionomycin calcium salt treatment, the lysosomal and mitochondrial temperatures first sharply increased by 2~3°C within 6 minutes before dropping back together in the next 20 minutes (**Figure 4-11B**). As a solvent control, the temperature remained at a relatively stable level regardless of the addition of 1:1000 DMSO into the culture media (**Figure 4-11C**).

Next, we treated live cells with a lysosome-specific Chloroquine (CQ) stimulation (**Figure 4-11D**). CQ has originally been used to treat malaria and is now a sensitizing agent to treat certain cancers [293]. CQ is a lysosomotropic weak base, which increases the pH of lysosomes and therefore inhibits autophagic degradation in the lysosomes [294]. Intriguingly, the thermometry measurements by LysoDots and MitoDots revealed a significant decrease in lysosomal temperature by ~3 °C after 10 min treatment of 200

nM CQ, while the mitochondrial temperature remains relatively stable as the basal level in HeLa cells (**Figure 4-11E**). In comparison, the temperature in the solvent treatment groups remained at a relatively stable level after adding PBS to the culture media (**Figure 4-11E**).

We then treated HeLa cells with a mitochondria-specific drug, carbonyl cyanide-4-(trifluoromethoxy)phenylhydrazone (FCCP, **Figure 4-11F**). FCCP is an inhibitor of mitochondrial oxidative phosphorylation, as it disrupts ATP synthesis by transporting protons across the mitochondrial inner membrane [260]. LysoDots and MitoDots not only revealed a significant increase of both the lysosomal and mitochondrial temperature by almost 3~7 °C in the first 10 min after adding 10 μM FCCP ($P < 0.0001$ by Students' t-test, **Figure 4-11G**), but also mitochondria release a large amount of heat, which is consistent with the previous observation [280], but with better uncertainty using MitoDots. Here, a clear delay by approximately 1~2 min in the time domain during the process of both temperature increase (0-6 min) and decrease (10-14 min) between lysosomes and mitochondria has been demonstrated (**Figure 4-11G**). The significant temperature increase reflects a large amount of heat released by mitochondria, with the trend being consistent with the previous observation [280]. The new ability of MitoDots suggests better temperature-sensing uncertainty, and the observation of time delays further indicates a thermal transition from mitochondria to the lysosomes. In the following 20 min, the lysosomal and mitochondrial temperature eventually recovered to the original temperature, but the cellular morphology significantly changed, indicating cell death after mitochondrial dysfunction.

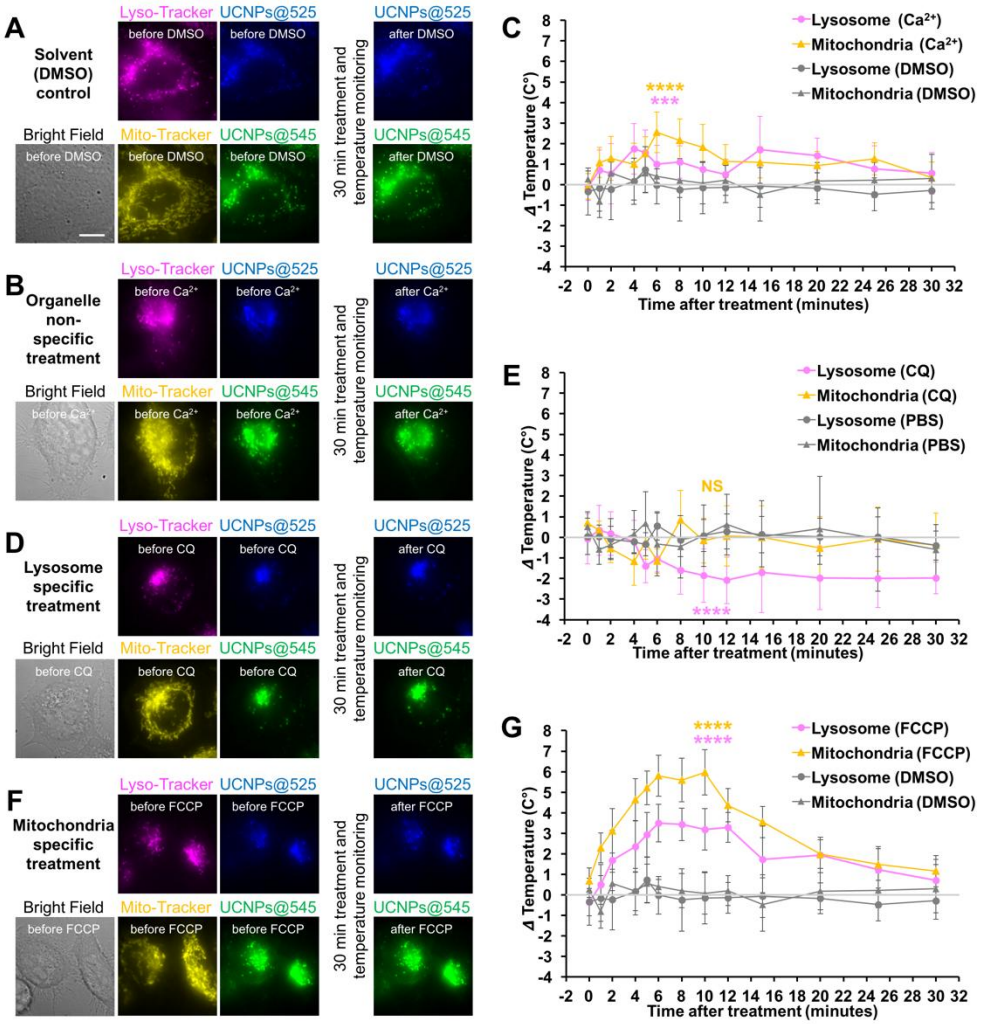

Figure 4-11 Distinct lysosomal and mitochondrial temperature dynamics in response to chemical stimulations in living HeLa cells. *A-B. Bright-field (grey), LysoTracker (magenta), MitoTracker (yellow), 525 nm (blue) and 545 nm (green) emission of UCNPs images of a representative live HeLa cell before and after the treatment with 1:1000 DMSO as the solvent control (A) and Ca^{2+} ion shock (B). Scale bar = 10 μm. C. The temperature dynamic curves of lysosomes with Ca^{2+} ion shock (magenta circles), mitochondria with Ca^{2+} ion shock (orange triangles), lysosomes with DMSO (control, grey circles) and mitochondria with DMSO (control, grey triangles) within 30 min after treatment. Data represent mean ± SD (n = 15 ROIs from 5 cells) and Student's t-test at 6 min (***, p < 0.001; ****, p < 0.0001). D. Bright-field (grey), LysoTracker (magenta), MitoTracker (yellow), 525 nm (blue) and 545 nm (green) emission of UCNPs images of a representative live HeLa cell before and after the treatment with 200 nM Chloroquine (CQ). E. The temperature dynamic curves of lysosomes with CQ (magenta circles), mitochondria with CQ (orange triangles), lysosomes with PBS (control, grey circles) and mitochondria with PBS (control, grey triangles) within 30 min after treatment. Data represent mean ± SD (n = 15 ROIs from 5 cells) and Student's t-test at 10 min (NS, no significance; ****, p < 0.0001). F. Bright-field (grey), LysoTracker (magenta), MitoTracker*

*(yellow), 525 nm (blue) and 545 nm (green) emission of UCNPs images of a representative live HeLa cell before and after the treatment with 10 μM FCCP. (G) The temperature dynamic curves of lysosomes with FCCP (magenta circles), mitochondria with FCCP (orange triangles), lysosomes with DMSO (control, grey circles) and mitochondria with DMSO (control, grey triangles) within 30 min after treatment. Data represent mean ± SD (n = 15 ROIs from 5 cells) and Student's t-test at 10 min (****, p < 0.0001).*

4.6 Conclusion

The intracellular thermal dynamics, as one of the most pivotal biophysical parameters, plays a critical role in maintaining the cells' homeostasis or driving the cells into dysfunction status. With the advances made in non-contact luminescent thermometers, a wide variety of intracellular thermometers have been developed and applied to monitor organelle temperature variations [282]. Previous literature reports have been briefly summarized in **Table 4-1**, indicating that the mitochondrial temperature increases in the range from 2 to 10 °C under biochemical stimulations. The advantages of LysoDots and MitoDots are their simultaneous non-photobleaching property, better uncertainty, and multiple organelles targeting strategy. In our work, the temperature of mitochondria increases 3-7 °C after adding FCCP, which agrees with previous observations but disagrees with the physical model of heat transfer. The theory calculations suggest that heat gradients across cells could not be greater than 10^{-5} K [295, 296]. The physical models also assume that mitochondria are membrane-bound spheres and heat is produced across the surface of the spheres [295, 297]. However, mitochondria are tubular and networking morphologies with double bi-layered membranes [230]. The heat production occurs across the cristae membranes, which typically lie in parallel, potentially retaining heat within the matrix [298]. Moreover, mitochondria are highly dynamic with fission and fusion. The components of the mitochondrial inner membrane are full of cardiolipin, which is different from the cell membrane [230]. This is probably another reason that mitochondria can retain heat better than smaller individual compartments [298]. Additionally, the exact locations of thermal probes in living cells also affect the validity of temperature measurements. Following the typical endocytosis internalizations of nanoparticles [288], both types of thermometers are first accumulated into endosomes and translocated to lysosomes (**Figure 4-9** and **Figure 4-10**). The large amount of TPP on the surface of MitoDots would facilitate themselves to escape from

lysosomes and attach to mitochondrial outer membrane surfaces or penetrate the potential barrier of the mitochondrial intermembrane [190]. Thus, the generated heat from the lysosomes or mitochondria is transferred from the organelles' membrane to the temperature probes directly, which bypasses the cytosol. It can also be speculated that the temperature of the mitochondrial membrane is higher than that of cytosol and changes discontinuously at the interface. A such discontinuity may explain the controversy between experimental results and physical calculations.

Table 4-1Mitochondrial temperature variation summary by the intracellular thermometer

	Thermo-meters	Speci-ficity	Relative sensitivity (%/ºC)	Uncer-tainty (ºC)	Photo-bleaching	Stimu-lations	ΔT	Ref.
Fluorescent Proteins	tsGFP1-mito	YES	N/A	N/A	Yes	FCCP	~ 6 ºC	[119]
						Rotenone	decrease	
	gTEMP	YES	2.6	0.4	Yes	FCCP	6 ~ 9 ºC	[151]
	emGFP-mito	YES	2.5	0.26	Yes	FCCP	3 ~ 5 ºC	[160]
Organic Dyes	Mito-RTP	YES	2.72	0.6	Yes	FCCP	~ 3 ºC	[142]
	MTY	YES	N/A	N/A	Yes	respiration activation	~ 10 ºC	[299]
	Mito-TEM	YES	6.65	N/A	Yes	PMA	~ 3 ºC	[112]
Polymeric nanoparticle		YES	N/A	<0.98 ± 0.08	Yes	FCCP	~ 2.4 ºC	[113]
						Ca^{2+}	~ 2 ºC	
		NO	N/A	0.18 ~ 0.58	Yes	FCCP	1.02 ± 0.17	[104]
		NO	N/A	0.05 ~ 0.54	Yes	CCCP	1.57 ± 1.41	[144]
Inorganic nanoparticles	Quantum dots	NO	6.2	0.098	blinking	CCCP	0.94	[116]
	UCNPs	YES	3.2	2.3	No	FCCP	~ 2 ºC	[280]
						Ca^{2+}	~ 3.3 ºC	
	LysoDots MitoDots	YES (multiple)	2.7	0.8	No	FCCP	3 ~ 7 ºC	this study
						CQ	~ 0 ºC	
						Ca^{2+}	2 ~ 4 ºC	

In living cells, the energy is utilized to maintain the high-dimensional structures, such as membranes, proteins, and nucleic acids, and also to control chemical reactions [300]. For example, the heat generated by enzymatic reactions is commonly used for the diffusion of the enzymes themselves [301]. Besides, the temperature-sensitive heat shock proteins within a living cell will initially respond to the environmental temperature changes. With a 5-20 ºC increase in temperature, Richter et al observed the overexpression of heat shock proteins [302]. At present, researchers start to identify the molecular mechanism in intracellular temperature regulation, but it is still unknown

about the generated heat is dissipated as other types of energy or through heat conduction. Therefore, more efforts have to be put to study the dissipation of energy converted from heat as well as the heat conduction in living cells.

The ability in mapping the distinct temperature dynamics highlights the extensive range of applications using the organelle-targeting strategy to study the vital biological processes, among lysosome [271], mitochondria [280], endoplasmic reticulum [96], Golgi apparatus [253], lipid droplet, peroxisome [254], etc. The unique properties of UCNPs, which have also been used to sense the *in situ* pH values [303], make it feasible to develop "all-in-one" nanoscale sensors to simultaneously monitor the pH dynamics. The time-dependent colocalization analysis in **Figure 4-9** and **Figure 4-10** suggests the amount of MitoDots being stuck in the lysosome after 8 hours incubation was not negligible, additional rational design strategies, e.g. introducing alternative small molecules, are needed to further improve the escape efficiency of MitoDots, besides enriching the density of TPP demonstrated in this work. At least, this work suggests the cascade modification and bioconjugation strategy can target other organelles and establish a library of organelle-targetted thermometers.

In summary, we observed for the first time the temperature decrease in lysosomes under CQ treatment, and the thermal transition from mitochondria to lysosomes under FCCP stimulation. To better reveal the thermal transmission across multiple organelles, it becomes critical to further increase the spatial and temporal resolutions of our imaging system [304], so that the new series of thermometers can be used to map the long-term thermal dynamics of individual organelles across cell cycles or even in deep tissues [239] with single-particle sensitivity and resolution. Introducing the state-of-the-art *in situ* organelle imaging and assay approaches, including live-cell super-resolution imaging [265, 266], *in vitro* reconstitution assay [230, 267] and near-infrared deep tissue imaging [244, 305], and adoptions of the new developments of live-cell thermometry, membrane potential sensors and pH probes will together form a powerful platform for multifunctional imaging, sensing [306], therapy [244] and even tracking the pace of life [270] in living cells and organisms.

Chapter 5 Conclusions and Future works

5.1 Conclusions

To develop tools to monitor the function of mitochondria, this thesis focuses on the development of a UCNPs-based mitochondrial thermometry platform. First of all, I have systematically investigated the long-term colloidal stability and cytotoxicity of UCNPs ($NaYF_4$: 20%Yb^{3+}, 2%Er^{3+}) capped with five different hydrophilic ligands (PDA, AEP, alendronate, 3,4-DHCA, and copolymer). The copolymer was chosen as the first modification layer of UCNPs ($NaYF_4$: 20%Yb^{3+}, 2%Er^{3+}), which can enhance the stability, dispersity, hydrophilicity, and uniformity of UCNP ($NaYF_4$: 20%Yb^{3+}, 2%Er^{3+}). Then I have developed a mitochondria targeted UCNPs-based temperature probe to monitor mitochondrial thermal dynamics under different physiological or pathological status. Moreover, to improve the mitochondria-targeting UCNPs thermometry, I have further optimised the surface functionalization of UCNPs ($NaYF_4$: 20%Yb^{3+}, 2%Er^{3+}) and successfully designed two kinds of UCNPs-based thermometers, which could target lysosomes and mitochondria, respectively, and achieved the relative temperature sensing sensitivity of 2.7% K^{-1} and uncertainty of 0.8 K in living HeLa cells. An opposite temperature reaction behaviour of lysosomes and mitochondria has been observed under the treatment of CQ. To our best knowledge, this is the first time to monitor in situ thermal dynamics of lysosomes and mitochondria simultaneously, specifically, and quantitatively. The live-cell thermal probes provide a powerful tool with multi-modality and multi-functional imaging capacities, including spatial, temporal, and thermal dynamics of selective organelles.

Chapter 1 was the literature review with three main sections. The first section introduces the basic knowledge about mitochondrial function, including mitochondrial metabolism, mitochondrial dynamics, the contacts with other organelles, and mitochondrial DNA. The second section provides a detailed review of luminescent thermometry, including the working principles, the recent developments of fluorescence-based temperature probes, and their intracellular applications. The physiological meaning has been discussed in this section. The third section focuses on the knowledge of UCNPs' surface functionalization, including the methods for obtaining hydrophilic UCNPs ($NaYF_4$: 20%Yb^{3+}, 2%Er^{3+}), functioning UCNPs with chemical groups, and conjugating with

biomolecules. The surface functionalization of UCNPs is fundamentally important for the subsequent biological application. A perfect surface modification makes the nanoparticles stealth in the living cells without interfering with intracellular activities.

In Chapter 2, I systematically studied the stability and dispersibility of ligands, including PDA, alendronate, AEP, 3,4-DHCA, and copolymer. Ligands of PDA, alendronate, and AEP provide amine groups on the surface of UCNPs ($NaYF_4$: 20%Yb^{3+}, 2%Er^{3+}) for subsequent bioconjugation, but they tend to aggregate in the physiological buffer. Ligands of 3,4-DHCA and copolymer provide carboxyl groups on the surface of UCNPs ($NaYF_4$: 20%Yb^{3+}, 2%Er^{3+}) for subsequent bioconjugation. Compared with PDA, alendronate, AEP, and 3,4-DHCA, UCNPs ($NaYF_4$: 20%Yb^{3+}, 2%Er^{3+}) coated with copolymer resulted in the highest stability in the aqueous buffer. Then the experiment of labelling microtubules by UCNPs was used to evaluate the functionalized UCNPs and revealed the steric hindrance effect on the surface proteins and the limited conjugation sites on the surface of UCNPs@copolymer made the nanoparticles hard to access to the antigen sites on the microtubules. This problem may be solved by increasing the density of functional groups (e.g. carboxyl groups) on the UCNPs surface towards the enhanced conjugation efficiency.

With the experience acquired during the process of functioning the nanoparticle surface, I developed mitochondrial targeting UCNPs ($NaYF_4$: 20%Yb^{3+}, 2%Er^{3+})-based temperature probes to monitor the thermal dynamics of mitochondria in Chapter 3. TPP is a mitochondria targeted moiety that can drive nanoparticles to be accumulated into mitochondria. To conjugate with TPP, the crosslinked polymer network has been applied. UCNPs ($NaYF_4$: 20%Yb^{3+}, 2%Er^{3+}) were modified with copolymer first to obtain UCNPs@copolymer with the long-term stability and further conjugated with 4Arm-PEG-NH_2 to obtain amine groups. With the mitochondria-targeting UCNP-based thermometer, I observed that the cells displayed distinct thermal dynamics profiles under the different chemical stimulations.

Based on the outcomes from Chapter 3, I continued to optimize the UCNPs surface, as I realized that the labelling density of mitochondria by UCNPs@PEG@TPP was insufficient. In Chapter 4, I tried to increase the conjugation efficiency to load more TPP onto UCNPs. The first layer was still based on the copolymer because of the excellent colloidal stability. PLL was introduced as the second layer, instead of

4Arm-PEG-NH_2. PLL is a polymer containing many amine groups with a positive charge and can be strongly adsorbed on the surface. UCNPs can react with PLL by electrostatic interaction, which avoids the conjugation with UCNPs@copolymer through EDC-NHS reaction. The large number of amine groups on the surface of UCNPs@PLL provide a higher loading efficiency of TPP. Finally, the design using UCNPs@copolymer (LysoDots) and UCNPs@PLL@TPP (MitoDots) by cascade-targeting allowed simultaneous monitoring the temperature variations of lysosomes and mitochondria. The relative temperature sensing sensitivity was 2.7% K^{-1} and uncertainty was 0.8 K in HeLa cells. Lysosomes and mitochondria demonstrated 3~6 °C heat up with the treatment of oxidative phosphorylation inhibitor treatment and Ca^{2+} ion shock. Interestingly, the lysosomal temperature decreased ~3 °C with CQ treatment, while mitochondria remained relatively stable, indicating different metabolic pathways.

5.2 Future works

This thesis suggests new scopes of future developments in at least three disciplines: (1) continuous improvements of thermometry materials (2) requirements of developing imaging instrumentation with high spatial and temporal resolutions. (3) explorations of new biomedical applications using fluorescence thermometry platform technologies.

5.2.1 Materials design and challenges

To improve the labelling density of thermometers on a specific organelle, UCNPs with a small size (less than 10 nm, ideally less than 5 nm) and high brightness will be desirable. In this thesis, the size of UCNPs was around 30 nm, which caused a steric hindrance effect when being conjugated with antibodies. Large sized UCNPs are hard to access to intracellular organelles, as well as interfering with the physiological cellular activities. Moreover, from this thesis, we observed that surface ligands with a multiple number of anchor groups and functional groups benefit the specific targeting and high-density labeling. The high number of anchor groups can improve the efficiency in replacing the hydrophobic ligands on the UCNPs surface with stronger adsorption onto the UCNPs' surface, and a large number of functional groups can increase the loading capability of biomolecules. In addition, the hybrid complex of different types of nanoparticles can be an excellent approach to improving the temperature sensing sensitivity. Qiu *et al.* developed a hybrid complex composed of QDs and UCNPs and

achieved a sensitivity of ~5.6% K^{-1} with dual emissions at the same wavelength to minimize the impacts of the absorption and scattering through the complex biological samples [125].

5.2.2 Instrumentation development

The advancement in fluorescence microscopy has uncovered a wide range of biological discoveries [220]. Integrating the state-of-the-art modalities of microscopy, like live-cell super-resolution imaging [221] and near-infrared deep tissue imaging [244], and combined use of thermometers enable multifunctional imaging, sensing [269], therapy [244] and even tracking the pace of life [270].

5.2.3 Biomedical applications

To shed light on the intracellular activities, UCNPs-based luminescent thermometry can work together with other intracellular sensors and probes to diagnose the physiological conditions and dynamics, including the localized pH, lipid membrane's depolarization, oxygen consumption, and extracellular acidification rate. The convergence and correlative data of these multiple indicators will provide a comprehensive and insightful understanding of the physiological activities as well as validating the accuracies among the multiple channels of readouts. Moreover, a series of specific organelle-targeting UCNPs are desirably required to study the network activities and communications of mitochondria, lysosomes, ER, Golgi, lipid droplet, peroxisome, and so on, as well as correlating the molecular signaling pathways, including mtDNA. Simultaneously mapping the thermal dynamics of the coordinated organelles within a single cell is a potential approach to studying the vital biological processes, including metabolism and dysfunctions.

At the closing of my PhD program, for a particular interest, I conducted an imaging experiment on mtDNA to further explore the functions of mitochondria, which experiment may be correlated with UCNPs-based thermal dynamics imaging in the near future.

5.2.3.1 Motivation

mtDNA encodes a variety of rRNAs (Ribosomal RNA), tRNAs (Transfer RNA), and respiratory chain complex proteins [83]. The integrity of mtDNA supports

mitochondrial functions and plays an essential role in numerous physiological and pathological processes. Mutations in mtDNA cause metabolic diseases and aging. The mtDNA within the human cells are packaged into hundreds of nucleoids within the mitochondrial matrix. Knowledge of how the nucleoids are dynamically distributed and organized within mitochondria is the key to understanding mtDNA's signalling and functions. Therefore, visualizing the distribution and dynamics of mtDNA within mitochondria is a powerful approach to understating the regulation of mtDNA replication and transcription.

The advances made in microscopy have enabled researchers to gain an in-depth understanding of mtDNA. By using in vivo time-lapse imaging, Nuria *et al.* found the mitochondrial nucleoids were highly dynamic and often redistributed in the mitochondrial network [307]. Lewis *et al.* discovered a subset of ER-mitochondria contacts were related to the mitochondrial division and its mtDNA synthesis [58]. McArthur and the co-workers illustrated the activation of BAK/BAX (Bcl-2 homologous antagonist/killer/Bcl-2-associated X protein) led to the release of mtDNA into the cytoplasm, which could trigger the innate immune cGAS/STING pathway, causing mitochondrial apoptosis [308]. Although the behaviour, function, and distribution of mitochondrial nucleoids have been described, the organization and the replication pattern within a single nucleoid are elusive. Here, the preliminary data of the mtDNA replication pattern were presented.

Here, sequential labelling of mtDNA by EdU and BrdU was used to explore the function of mitochondria. Interestingly, I found that the replication pattern of mtDNA correlated with the cell cycle.

5.2.3.2 Methodology

5.2.3.2.1 Materials

BrdU (5-bromo-2'-deoxyuridine), Tween 20, Triton X-100, DMSO, and PBS were purchased from Sigma-Aldrich. EdU (5-ethynyl-dU) and Click-iT™ Cell Reaction Buffer Kit were purchased from Thermo Fisher. Anti-BrdU antibody was purchased from BD Biosciences. All solutions and buffers used in this study should be prepared using analytical grade reagents and dissolved in ddH_2O, followed by filtration with 0.2 μm syringe filters to remove impurities, which may contain auto-fluorescence

during fluorescence imaging. Prepare and store all reagents, solutions and buffers at room temperature (unless indicated otherwise). Diligently follow all waste disposal regulations when disposing of waste materials.

5.2.3.2.2 Incorporation of BrdU and EdU

HeLa cells were cultured in culture medium at 37 ℃ and in the presence of 5% CO_2. 10 mM stock solution of BrdU was prepared by dissolving 3 mg of BrdU in 1 mL of ddH2O and 10 mM stock solution of EdU was prepared by dissolving 2.52 mg of EdU in 1 mL of DMSO. Then 10 mM BrdU/EdU stock solution was diluted in cell culture medium to make a 10~100 μM BrdU/EdU labelling solution. The next day, the culture medium was removed from the cells and replaced with the labelling solution. The HeLa cells were incubated with the EdU labelling solution for 0.5 hour at 37 ℃ and in the presence of 5% CO_2. Then the EdU labelling solution was removed from the cells and washed twice in PBS for about 5 seconds per wash. The HeLa cells were further incubated with the EdU labelling solution for 0.5 hour at 37 ℃ and in the presence of 5% CO_2. Next, the BrdU labelling solution was removed from the cells and washed twice in PBS for about 5 seconds per wash. The cells were fixed with 4%PFA solution for 15 minutes and washed three more times with PBS. Finally, the sample was ready for immunostaining.

5.2.3.2.3 BrdU labelling

The fixed cells were treated with 2 M HCL in 0.1% PBS-Tween for 30 minutes at room temperature to denature the double-strand DNA and expose the BrdU epitope. Then the cells were incubated with the blocking buffer at room temperature. After 30 minutes, the cells were incubated with primary antibody anti-BrdU antibody in blocking buffer overnight at 4 ℃. The cells were washed with PBS buffer three times for 5 minutes and further incubated with dye-labelled secondary antibody (1:50~1:200) for 1 hour at room temperature. Next, the sample was washed with PBS buffer three times for 5 min each wash. Finally, the cells were post-fixed with 4% PFA in PBS buffer for 10 min at room temperature and imaged by a fluorescence microscope.

5.2.3.2.4 EdU labelling

HeLa cells were fixed by 4% PFA in PBS pH 7.4 for 15 min at room temperature and washed the cells twice with 1 mL of 3% BSA in PBS. Then the cells were incubated with 1 mL of 0.5% Triton X-100 in PBS (permeabilization buffer) for 20 minutes. The permeabilization buffer was removed and washed twice in 3% BSA in PBS. 500 μL of Click-iT® reaction cocktail was added to the dish and incubated for 30 minutes at room temperature, avoiding light. Then wash the cells twice with 3% BSA in PBS and post-fixed with 4% PFA in PBS for 10 min at room temperature. Finally, mtDNA's distribution was imaged using a fluorescence microscope.

5.2.3.2.4 Dual BrdU and EdU labelling

HeLa cells were treated with 1 mL of 0.5% Triton X-100 in PBS for 10 min at room temperature. The sample was labelled with EdU first, following the protocol described above, as the HCl treatment does not compromise the EdU signal. Then 2 M HCl was added to the dish for 30 min at 37 °C to recover the BrdU epitope. The cells were washed three times in PBS and labelled with BrdU following the protocol described above. After post-fixed the samples with 4% PFA in PBS for 10 min at room temperature, the cells were imaged by a fluorescent microscope.

5.2.3.3 Results and Discussion

5.2.3.3.1 mtDNA synthesis labelled by EdU

EdU and BrdU are thymidine analogues that can be incorporated into the DNA structure during the DNA replication, as the fluorescence markers to study the mtDNA synthesis. Firstly, EdU was used to label the newly synthesized DNA. As shown in **Figure 5-1**, with Tom 20 used to stain the outer membrane of mitochondria and EdU indicating the newly synthesized DNA, though the signal intensity of mtDNA was lower compared with that of the nucleus, it showed mtDNA replication was along with nucleus, as most of the cells with mtDNA positive signals can be correlated with the ones with positive nucleus. However, there are also some cells with only mtDNA (**Figure 5-2**). It is still a question if the mtDNA replication is synchronized with the nucleus. It is believed that the mtDNA replication is active through the entire cell cycle and the peaks of mtDNA replication are synchronized with nuclear DNA synthesis [309]. As our result (**Figure 5-2**) suggest some cells only with mtDNA, the question remains if the mtDNA replication is synchronized with the nucleus.

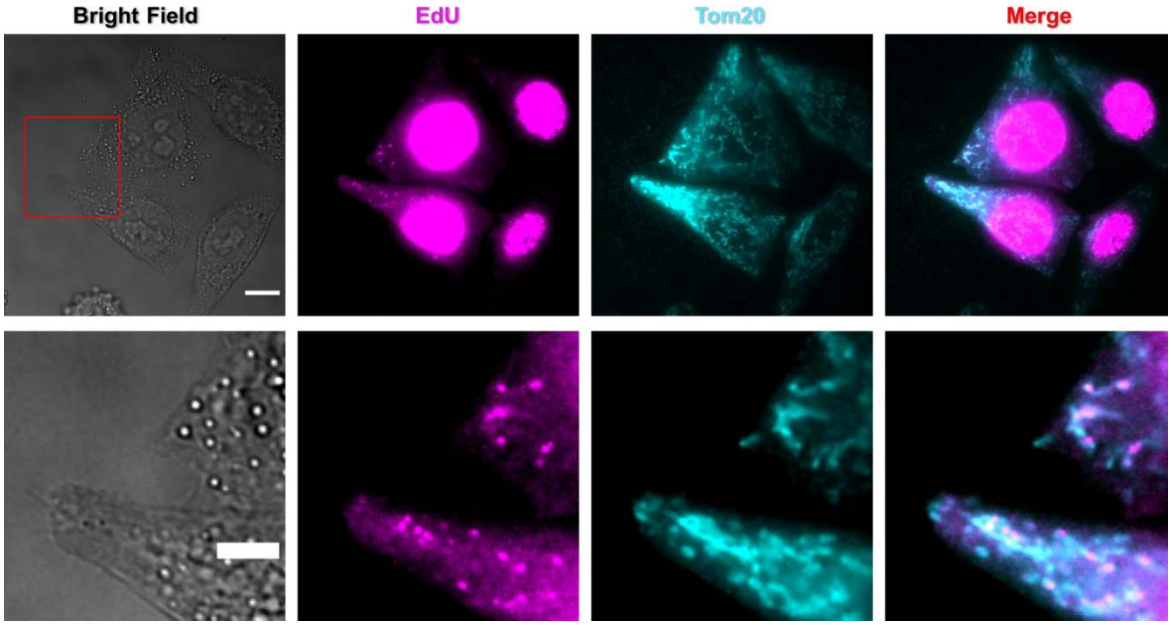

Figure 5-1 DNA synthesis labelled by EdU. *The Gray channel is Bright Field, the Magenta channel is EdU, the Cyan channel is Tom20, the Red channel is the colocalization of EdU and Tom20. The bottom is the enlarge of the red frame. Scale bar: 5* μm.

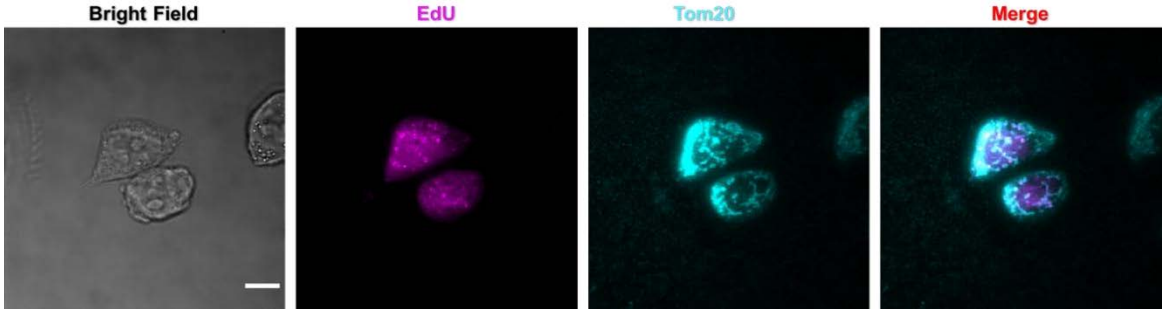

Figure 5- 2 mtDNA synthesis labelled by EdU. *The Gray channel is Bright Field, the Magenta channel is EdU, the Cyan channel is Tom20, the Red channel is the colocalization of BrdU and Tom20. Scale bar: 5* μm.

5.2.3.3.2 mtDNA synthesis labelled by BrdU

Then, BrdU was used to label the mtDNA synthesis. The principle of BrdU labelled mtDNA synthesis was a bit different from that of EdU. EdU stain experiment was achieved by click-chemistry, but BrdU labelling was an immunostaining experiment. It took me more than 30 experiments before I could master the labelling protocol and label the mtDNA synthesis successfully.

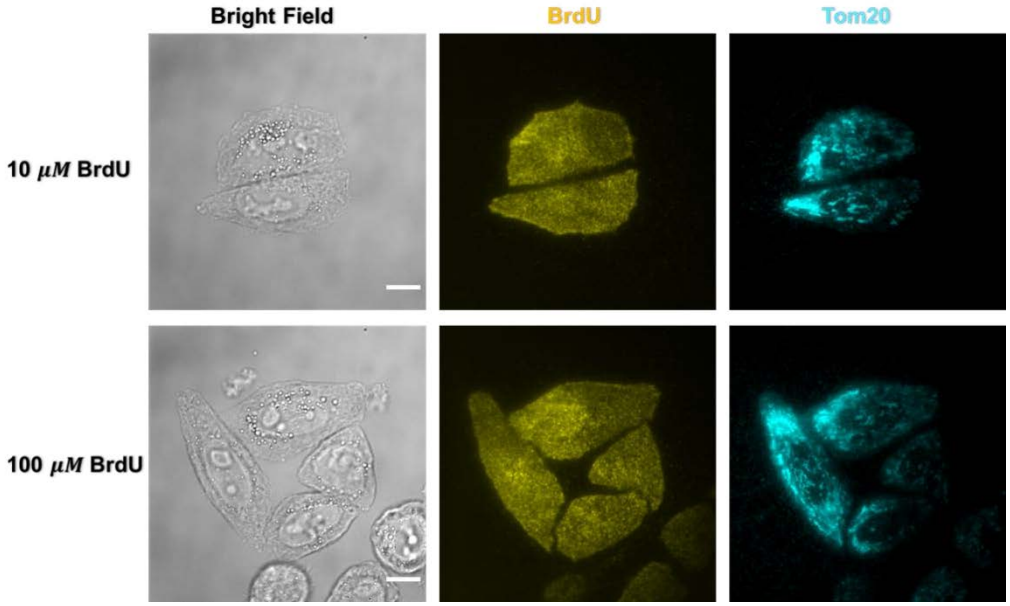

Figure 5-3 A typical result from a failure experiment suing BrdU to label the mtDNA synthesis. *The Gray channel is Bright Field, the Yellow channel is BrdU, the Cyan channel is Tom20. Scale bar: 5 μm.*

The protocol includes staining microtubules to check if the cell was under normal physiological status. I found HCl treatment as an essential step in the protocol, as HCl treatment can denature the double-strand DNA and expose the BrdU epitope, otherwise, no signal (**Figure 5-4**) of DNA synthesis can be observed. **Figure 5-5** shows the results of BrdU labelling were similar to that of the EdU, and in particular, only mtDNA was stained by BrdU in some cells (**Figure 5-6**), confirming the result of EdU labelled mtDNA (**Figure 5-2**).

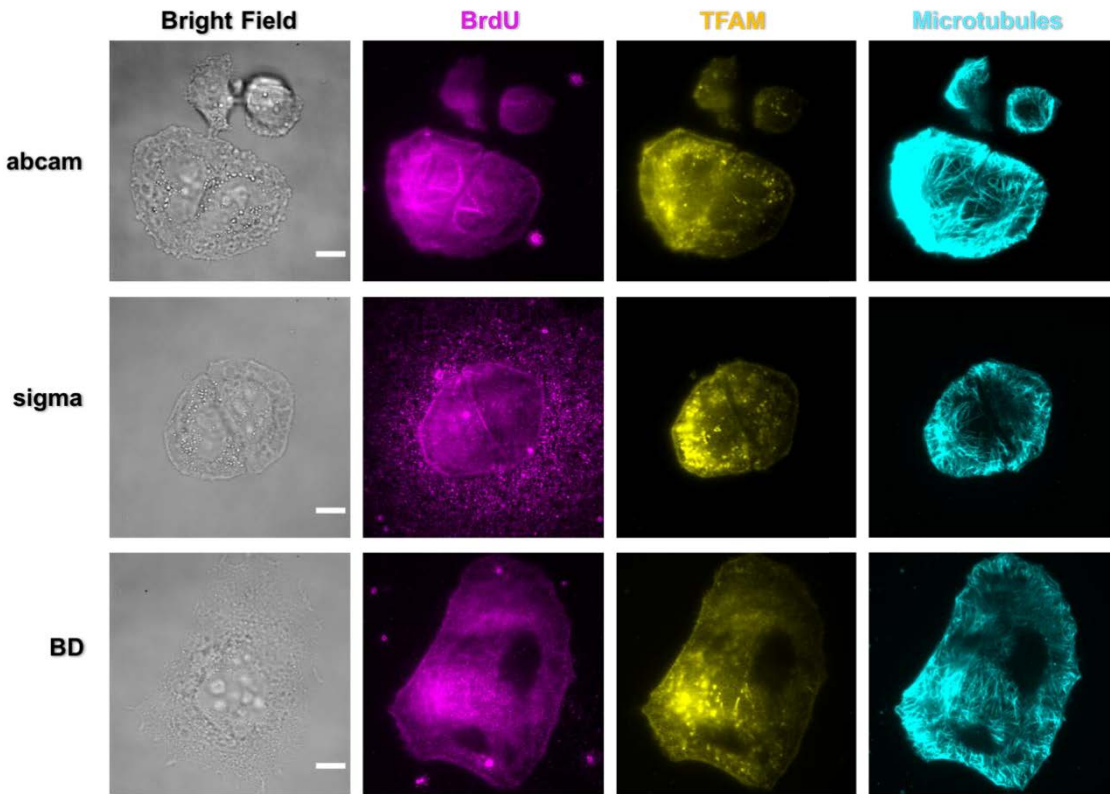

Figure 5-4 DNA synthesis labelled by BrdU with different antibodies. *The Gray channel is Bright Field, the Magenta channel is BrdU, the Yellow channel is TFAM, the Cyan channel is Microtubules. TFAM was used to labelled newly synthesis mtDNA, microtubules were used to check the status of Hela cells. BrdU incorporated DNA were stained by antibody from abcam (upper), sigma (middle), and BD (bottom), respectively. Scale bar: 5* μm.

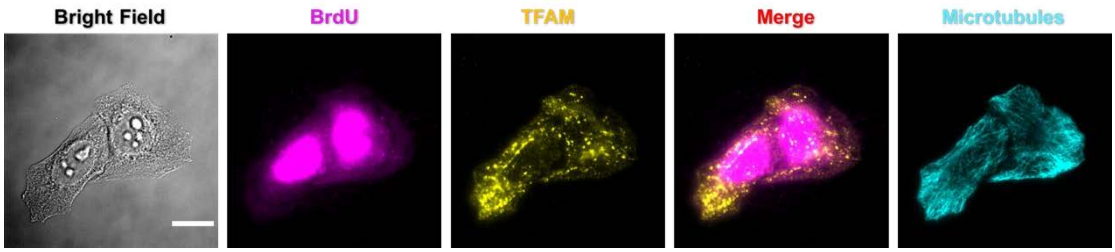

Figure 5-5 A typical successful labelling result of the mtDNA synthesis by BrdU. *The Gray channel is Bright Field, the Magenta channel is BrdU, the Yellow channel is TFAM, the Cyan channel is Microtubules. TFAM was used to labelled newly synthesized mtDNA, microtubules were used to check the status of Hela cells. Scale bar: 5* μm.

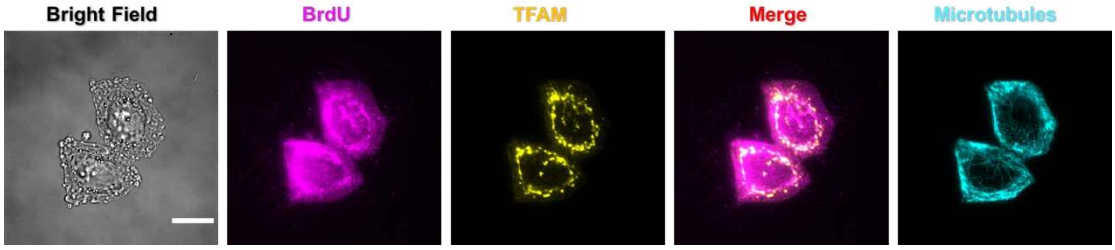

Figure 5-6 mtDNA synthesis labelled by BrdU. *The Gray channel is Bright Field, the Magenta channel is BrdU, the Yellow channel is TFAM, the Cyan channel is Microtubules. TFAM was used to labelled newly synthesis mtDNA, microtubules were used to check the status of Hela cells. Scale bar: 5* μm.

5.2.3.3.3 Dual label of mtDNA synthesis by EdU and BrdU across the cell cycle

To shed light on the mtDNA replication pattern, both EdU and BrdU were used to label the mtDNA. The HeLa cells were treated with Nocodazole for 16 hours. After washing with PBS, Hela cells were cultured in the medium and released for 6, 8, 10, and 12 hours. The cells were first labelled by EdU for the first 30 minutes and BrdU for the next 30 minutes. Finally, the cells were fixed for the subsequent immunostaining experiments and click-chemistry experiments.

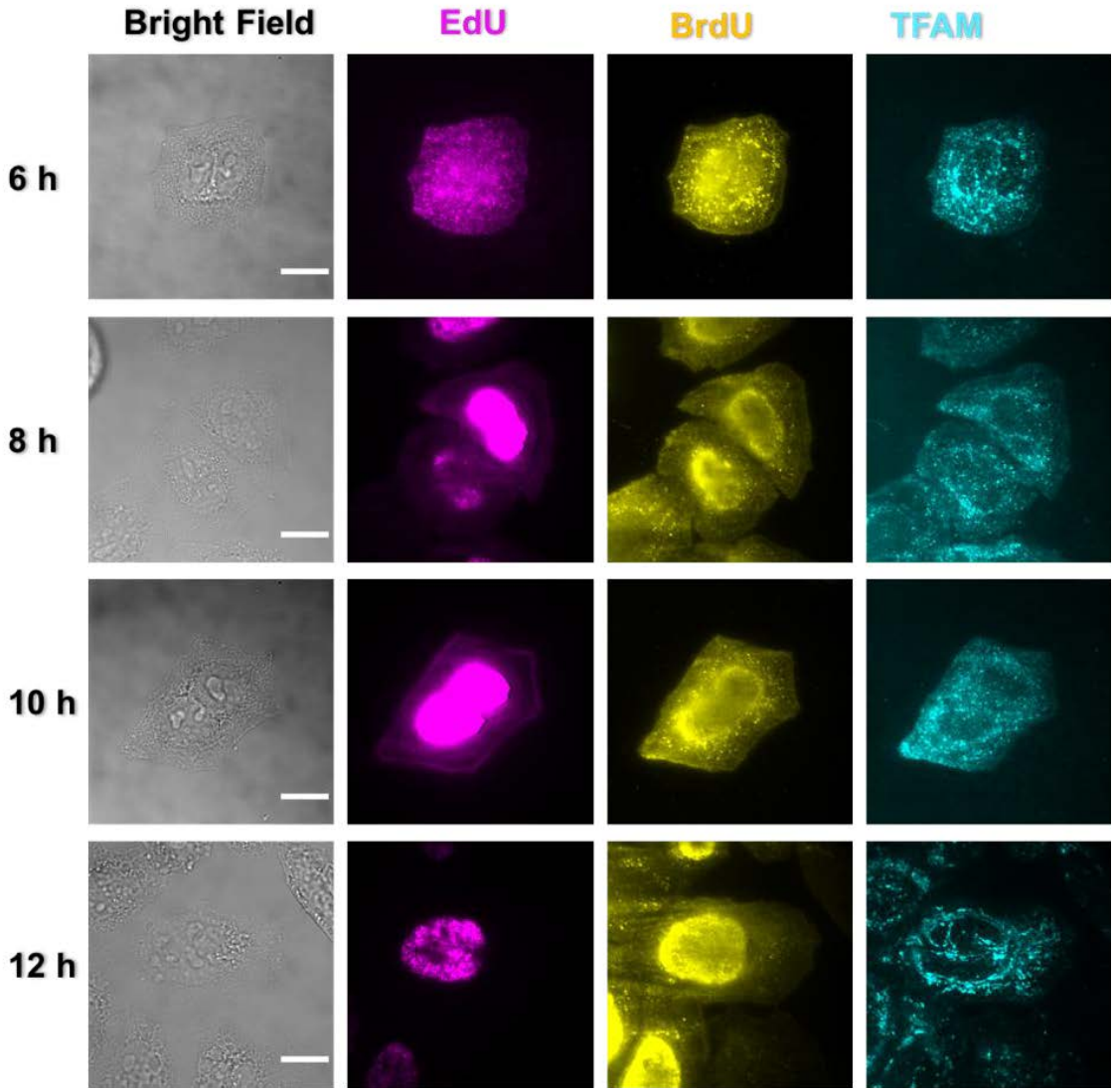

Figure 5-7 Dual labelling results of DNA synthesis by EdU and BrdU across the different phases of cell cycle. *The Gray channel is Bright Field, the Magenta channel is BrdU, the Yellow channel is TFAM, and the Cyan channel is Microtubules. TFAM was used to label the newly synthesis mtDNA, microtubules were used to check the status of Hela cells. Scale bar: 5 μm.*

After releasing for 6 hours, most DNA replication exist in the mitochondria. It was hard to observe nucleus DNA replication. With increasing the releasing time, the intensity of nucleus DNA was stronger while the intensity of mtDNA was weaker. However, the intensity of BrdU labelled cells after the second 30 minutes was higher than that of EdU labelling results after the first 30 minutes for the releasing times of 6 and 8 hours (**Figure 5-7**). The ratio of I_{BrdU} (the intensity of BrdU) and I_{EdU} (the intensity of EdU) was defined to describe the pattern of mtDNA replication. According to the mtDNA replication mechanism of strand-displacement mode, mtDNA synthesis starts from

the origin O_H/O_L (**Figure 1-6**, **Figure 5-8A**), there are three modes of EdU-BrdU labelled mtDNA: (1) when the EdU labelling time equals to the mtDNA replication origin, then the ratio of I_{BrdU}/ I_{EdU} is around 1 (**Figure 5-8B(1)**). (2) When the EdU labelling time is earlier than the mtDNA replication orgiin, then the labelling time of EdU is shorter than 30 minutes, but the labelling time of BrdU is 30 minutes. Thus, the ratio of I_{BrdU}/ I_{EdU} is bigger than 1 (**Figure 5-8B(2)**). (3) When the EdU labelling time is later the mtDNA replication origin, then the labelling time of EdU is 30 minutes, but the labelling time of BrdU is shorter than 30 minutes. Then the ratio of I_{BrdU}/ I_{EdU} is smaller than 1 (**Figure 5-8B(3)**). The results in **Figure 5-9** show that the ratio was more than 1 between 8 and 10 hours releasing time after being treated with Nocodazole. The ratio was around to 1 in the 12-hour releasing time. The HeLa cells start to enter the S phase after releasing for 12 hours. This suggests that mtDNA replication is synchronized with the nuclear DNA replication, but this finding needs to be further verified by further experiments. Though there might be two extreme cases, e.g. I_{BrdU} is zero or I_{EdU} is zero, I haven't observed either case in my experiments. Maybe I need to extend the releasing time to 16, 20, and 24 hours.

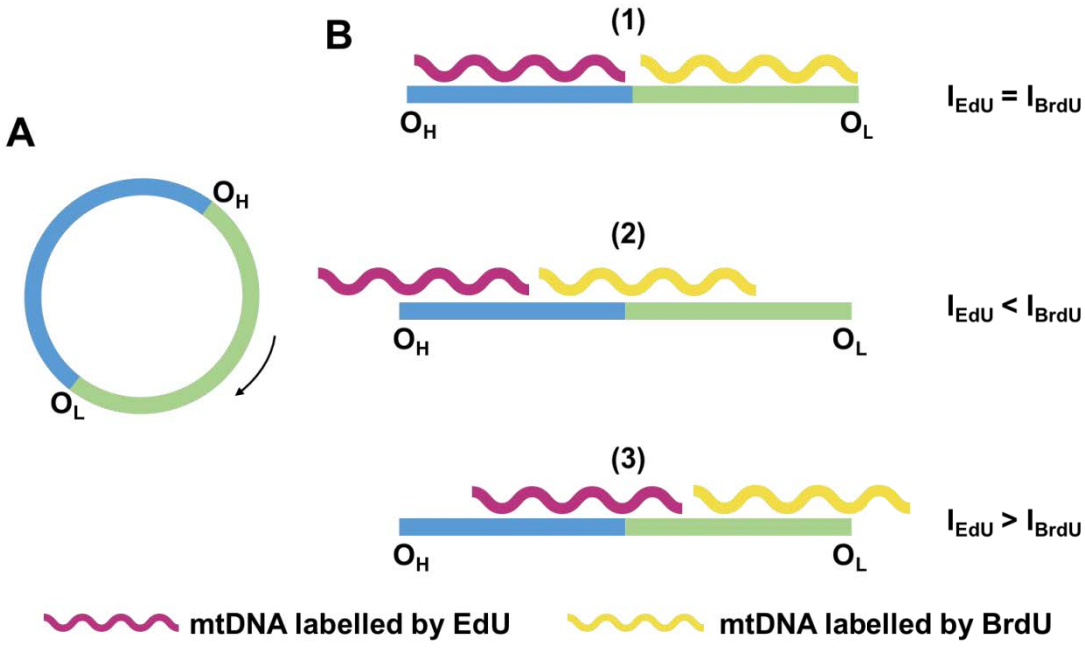

Figure 5-8 Illustration of human mtDNA replication patterns. *A. Human mtDNA replication starts from O_H to O_L. B. (1) The time of adding EdU is same with the mtDNA replication origin O_H. (2) The time of adding EdU is early than the mtDNA replication origin O_H. (3) The time of adding EdU is late than the mtDNA replication origin O_H.*

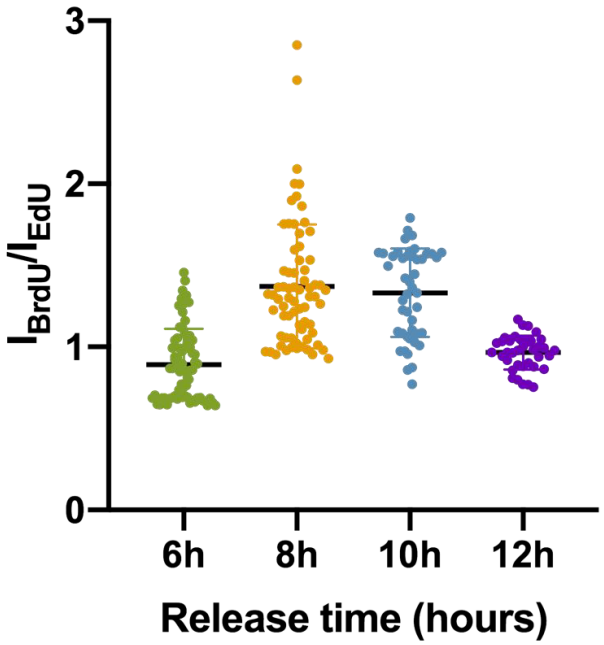

Figure 5-9 The ratio of I_{BrdU} to I_{EdU} at different releasing time after 16-hour Nocodazole treatment.
n = 40 ROI from 5 cells.

5.2.3.4 Conclusion

The obtained preliminary data show that the pattern (I_{BrdU}/I_{EdU}) of mtDNA replication varies according to the different phases of the cell cycle. It would be highly interesting if the thermal dynamics of mitochondria across the cell cycle can be monitored and correlated to this result and study the relationship between the temperature variation and the mtDNA replication pattern. Simultaneously monitoring the thermal dynamic and mtDNA replication pattern across the cell cycle will help us to understand mitochondrial function with new insights.

References

[1] Z. Huang, N. Li, X. Zhang, and Y. Xiao, "Mitochondria-Anchored Molecular Thermometer Quantitatively Monitoring Cellular Inflammations," *Anal Chem,* vol. 93, no. 12, pp. 5081-5088, Mar 30 2021.

[2] J. Zhou, B. Del Rosal, D. Jaque, S. Uchiyama, and D. Jin, "Advances and challenges for fluorescence nanothermometry," *Nat Methods,* vol. 17, no. 10, pp. 967-980, Oct 2020.

[3] J. R. Friedman and J. Nunnari, "Mitochondrial form and function," *Nature,* vol. 505, no. 7483, pp. 335-343, 2014/01/01 2014.

[4] C. M. Deus, K. F. Yambire, P. J. Oliveira, and N. Raimundo, "Mitochondria-Lysosome Crosstalk: From Physiology to Neurodegeneration," *Trends Mol Med,* vol. 26, no. 1, pp. 71-88, Jan 2020.

[5] Y. Wang *et al.*, "Sensitive and Stable Thermometer Based on the Long Fluorescence Lifetime of Au Nanoclusters for Mitochondria," *Anal Chem,* Oct 7 2021.

[6] J. Nunnari and A. Suomalainen, "Mitochondria: in sickness and in health," *Cell,* vol. 148, no. 6, pp. 1145-59, Mar 16 2012.

[7] J. R. Friedman and J. Nunnari, "Mitochondrial form and function," *Nature,* vol. 505, no. 7483, pp. 335-43, Jan 16 2014.

[8] A. J. Roger, S. A. Muñoz-Gómez, and R. Kamikawa, "The Origin and Diversification of Mitochondria," *Current Biology,* vol. 27, no. 21, pp. R1177-R1192, 2017/11/06/ 2017.

[9] T. Gabaldón and M. A. Huynen, "Shaping the mitochondrial proteome," (in eng), no. 0006-3002 (Print).

[10] C. M. Gustafsson, M. Falkenberg, and N.-G. Larsson, "Maintenance and Expression of Mammalian Mitochondrial DNA," *Annual Review of Biochemistry,* vol. 85, no. 1, pp. 133-160, 2016/06/02 2016.

[11] S. Fung, T. Nishimura, F. Sasarman, and E. A. Shoubridge, "The conserved interaction of C7orf30 with MRPL14 promotes biogenesis of the mitochondrial large ribosomal subunit and mitochondrial translation," (in eng), *Molecular biology of the cell,* vol. 24, no. 3, pp. 184-193, 2013.

[12] M. R. Sharma, P. P. Koc Ec Fau - Datta, T. M. Datta Pp Fau - Booth, L. L. Booth Tm Fau - Spremulli, R. K. Spremulli Ll Fau - Agrawal, and R. K. Agrawal, "Structure of the mammalian mitochondrial ribosome reveals an expanded functional role for its component proteins," (in eng), no. 0092-8674 (Print).

[13] W. Neupert and J. M. Herrmann, "Translocation of proteins into mitochondria," (in eng), no. 0066-4154 (Print).

[14] O. Schmidt, N. Pfanner, and C. Meisinger, "Mitochondrial protein import: from proteomics to functional mechanisms," *Nature Reviews Molecular Cell Biology,* vol. 11, no. 9, pp. 655-667, 2010/09/01 2010.

[15] R. C. Scarpulla, D. P. Vega Rb Fau - Kelly, and D. P. Kelly, "Transcriptional integration of mitochondrial biogenesis," (in eng), no. 1879-3061 (Electronic).

[16] J. Nunnari and A. Suomalainen, "Mitochondria: in sickness and in health," (in eng), *Cell,* vol. 148, no. 6, pp. 1145-1159, 2012.

[17] W. Kühlbrandt, "Structure and function of mitochondrial membrane protein complexes," *BMC Biology,* vol. 13, no. 1, p. 89, 2015/10/29 2015.

[18] E. Blachly-Dyson and M. Forte, "VDAC Channels," *IUBMB Life,* https://doi.org/10.1080/15216540152845902 vol. 52, no. 3-5, pp. 113-118, 2001/09/01 2001.

[19] J. M. Herrmann and W. Neupert, "Protein transport into mitochondria," *Current Opinion in Microbiology,* vol. 3, no. 2, pp. 210-214, 2000/04/01/ 2000.

[20] J. E. Chipuk, L. Bouchier-Hayes, and D. R. Green, "Mitochondrial outer membrane permeabilization during apoptosis: the innocent bystander scenario," *Cell Death & Differentiation,* vol. 13, no. 8, pp. 1396-1402, 2006/08/01 2006.

[21] S. Orrenius and B. Zhivotovsky, "Cardiolipin oxidation sets cytochrome c free," *Nature Chemical Biology,* vol. 1, no. 4, pp. 188-189, 2005/09/01 2005.

[22] C. Garrido, L. Galluzzi, M. Brunet, P. E. Puig, C. Didelot, and G. Kroemer, "Mechanisms of cytochrome c release from mitochondria," *Cell Death & Differentiation,* vol. 13, no. 9, pp. 1423-1433, 2006/09/01 2006.

[23] C. Han *et al.*, "Cytochrome c light-up graphene oxide nanosensor for the targeted self-monitoring of mitochondria-mediated tumor cell death," *Biosensors and Bioelectronics,* vol. 173, p. 112791, 2021/02/01/ 2021.

[24] P. Manickam, A. Kaushik, C. Karunakaran, and S. Bhansali, "Recent advances in cytochrome c biosensing technologies," *Biosensors and Bioelectronics,* vol. 87, pp. 654-668, 2017/01/15/ 2017.

[25] J. B. McMillin and W. Dowhan, "Cardiolipin and apoptosis," *Biochimica et Biophysica Acta (BBA) - Molecular and Cell Biology of Lipids,* vol. 1585, no. 2, pp. 97-107, 2002/12/30/ 2002.

[26] L. C. Schenkel and M. Bakovic, "Formation and Regulation of Mitochondrial Membranes," *International Journal of Cell Biology,* vol. 2014, p. 709828, 2014/01/22 2014.

[27] L. K. Sharma, J. Lu, and Y. Bai, "Mitochondrial respiratory complex I: structure, function and implication in human diseases," (in eng), *Current medicinal chemistry,* vol. 16, no. 10, pp. 1266-1277, 2009.

[28] K. S. Oyedotun and B. D. Lemire, "The quaternary structure of the Saccharomyces cerevisiae succinate dehydrogenase. Homology modeling, cofactor docking, and molecular dynamics simulation studies," (in eng), no. 0021-9258 (Print).

[29] S. Dröse and U. Brandt, "The Mechanism of Mitochondrial Superoxide Production by the Cytochrome bc1 Complex*," *Journal of Biological Chemistry,* vol. 283, no. 31, pp. 21649-21654, 2008/08/01/ 2008.

[30] B. Kadenbach, L. Kuhn-Nentwig, and U. BÜGe, "Evolution of a Regulatory Enzyme: Cytochrome-c Oxidase (Complex IV)," in *Current Topics in Bioenergetics*, vol. 15, C. P. Lee, Ed.: Elsevier, 1987, pp. 113-161.

[31] A. I. Jonckheere, J. A. M. Smeitink, and R. J. T. Rodenburg, "Mitochondrial ATP synthase: architecture, function and pathology," *Journal of Inherited Metabolic Disease,* https://doi.org/10.1007/s10545-011-9382-9 vol. 35, no. 2, pp. 211-225, 2012/03/01 2012.

[32] P. Mitchell and J. Moyle, "Chemiosmotic Hypothesis of Oxidative Phosphorylation," *Nature,* vol. 213, no. 5072, pp. 137-139, 1967/01/01 1967.

[33] D. C. Chan, "Mitochondrial Fusion and Fission in Mammals," *Annual Review of Cell and Developmental Biology,* vol. 22, no. 1, pp. 79-99, 2006/11/01 2006.

[34] A. R. Fenton, T. A. Jongens, and E. L. F. Holzbaur, "Mitochondrial dynamics: Shaping and remodeling an organelle network," *Current Opinion in Cell Biology,* vol. 68, pp. 28-36, 2021/02/01/ 2021.

[35] S. A. Detmer and D. C. Chan, "Functions and dysfunctions of mitochondrial dynamics," *Nature Reviews Molecular Cell Biology,* vol. 8, no. 11, pp. 870-879, 2007/11/01 2007.

[36] T. Kleele *et al.*, "Distinct fission signatures predict mitochondrial degradation or biogenesis," *Nature,* vol. 593, no. 7859, pp. 435-439, 2021/05/01 2021.

[37] K. Okamoto and J. M. Shaw, "Mitochondrial morphology and dynamics in yeast and multicellular eukaryotes," (in eng), no. 0066-4197 (Print).

[38] P. Mishra and D. C. Chan, "Mitochondrial dynamics and inheritance during cell division, development and disease," *Nature Reviews Molecular Cell Biology,* vol. 15, no. 10, pp. 634-646, 2014/10/01 2014.

[39] T. S. Fung, W.-K. Ji, H. N. Higgs, and R. Chakrabarti, "Two distinct actin filament populations have effects on mitochondria, with differences in stimuli and assembly factors," *Journal of Cell Science,* vol. 132, no. 18, 2019.

[40] T. Wai and T. Langer, "Mitochondrial Dynamics and Metabolic Regulation," *Trends in Endocrinology & Metabolism,* vol. 27, no. 2, pp. 105-117, 2016/02/01/ 2016.

[41] W.-K. Ji, R. Chakrabarti, X. Fan, L. Schoenfeld, S. Strack, and H. N. Higgs, "Receptor-mediated Drp1 oligomerization on endoplasmic reticulum," *Journal of Cell Biology,* vol. 216, no. 12, pp. 4123-4139, 2017.

[42] E. Smirnova, L. Griparic, D.-L. Shurland, and A. M. van der Bliek, "Dynamin-related Protein Drp1 Is Required for Mitochondrial Division in Mammalian Cells," *Molecular Biology of the Cell,* vol. 12, no. 8, pp. 2245-2256, 2001/08/01 2001.

[43] C. Fröhlich *et al.*, "Structural insights into oligomerization and mitochondrial remodelling of dynamin 1-like protein," *The EMBO Journal,* https://doi.org/10.1038/emboj.2013.74 vol. 32, no. 9, pp. 1280-1292, 2013/05/02 2013.

[44] E. Ingerman *et al.*, "Dnm1 forms spirals that are structurally tailored to fit mitochondria," *Journal of Cell Biology,* vol. 170, no. 7, pp. 1021-1027, 2005.

[45] J. E. Lee, L. M. Westrate, H. Wu, C. Page, and G. K. Voeltz, "Multiple dynamin family members collaborate to drive mitochondrial division," *Nature,* vol. 540, no. 7631, pp. 139-143, 2016/12/01 2016.

[46] L. Tilokani, S. Nagashima, V. Paupe, and J. Prudent, "Mitochondrial dynamics: overview of molecular mechanisms," *Essays in Biochemistry,* vol. 62, no. 3, pp. 341-360, 2018.

[47] N. Ishihara, Y. Eura, and K. Mihara, "Mitofusin 1 and 2 play distinct roles in mitochondrial fusion reactions via GTPase activity," *Journal of Cell Science,* vol. 117, no. 26, pp. 6535-6546, 2004.

[48] S. Cipolat, O. M. de Brito, B. Dal Zilio, and L. Scorrano, "OPA1 requires mitofusin 1 to promote mitochondrial fusion," *Proceedings of the National Academy of Sciences of the United States of America,* vol. 101, no. 45, p. 15927, 2004.

[49] Y. Ge, X. Shi, S. Boopathy, J. McDonald, A. W. Smith, and L. H. Chao, "Two forms of Opa1 cooperate to complete fusion of the mitochondrial inner-membrane," *eLife,* vol. 9, p. e50973, 2020/01/10 2020.

[50] O. M. de Brito and L. Scorrano, "Mitofusin 2 tethers endoplasmic reticulum to mitochondria," *Nature,* vol. 456, no. 7222, pp. 605-610, 2008/12/01 2008.

[51] T. Misgeld and T. L. Schwarz, "Mitostasis in Neurons: Maintaining Mitochondria in an Extended Cellular Architecture," *Neuron,* vol. 96, no. 3, pp. 651-666, 2017/11/01/ 2017.

[52] A. D. Pilling, D. Horiuchi, C. M. Lively, and W. M. Saxton, "Kinesin-1 and Dynein Are the Primary Motors for Fast Transport of Mitochondria in Drosophila Motor Axons," *Molecular Biology of the Cell,* vol. 17, no. 4, pp. 2057-2068, 2006/04/01 2006.

[53] Z.-H. Sheng and Q. Cai, "Mitochondrial transport in neurons: impact on synaptic homeostasis and neurodegeneration," (in eng), *Nature reviews. Neuroscience,* vol. 13, no. 2, pp. 77-93, 2012.

[54] A. Gutnick, M. R. Banghart, E. R. West, and T. L. Schwarz, "The light-sensitive dimerizer zapalog reveals distinct modes of immobilization for axonal mitochondria," *Nature Cell Biology,* vol. 21, no. 6, pp. 768-777, 2019/06/01 2019.

[55] S. R. Chada and P. J. Hollenbeck, "Nerve Growth Factor Signaling Regulates Motility and Docking of Axonal Mitochondria," *Current Biology,* vol. 14, no. 14, pp. 1272-1276, 2004/07/27/ 2004.

[56] A. Murley and J. Nunnari, "The Emerging Network of Mitochondria-Organelle Contacts," *Molecular Cell,* vol. 61, no. 5, pp. 648-653, 2016/03/03/ 2016.

[57] L. L. Lackner, "The Expanding and Unexpected Functions of Mitochondria Contact Sites," *Trends in Cell Biology,* vol. 29, no. 7, pp. 580-590, 2019/07/01/ 2019.

[58] S. C. Lewis, L. F. Uchiyama, and J. Nunnari, "ER-mitochondria contacts couple mtDNA synthesis with mitochondrial division in human cells," *Science,* vol. 353, no. 6296, p. aaf5549, Jul 15 2016.

[59] A. A. Rowland and G. K. Voeltz, "Endoplasmic reticulum-mitochondria contacts: function of the junction," (in eng), *Nature reviews. Molecular cell biology,* vol. 13, no. 10, pp. 607-625, 2012.

[60] M. Xia, Y. Zhang, K. Jin, Z. Lu, Z. Zeng, and W. Xiong, "Communication between mitochondria and other organelles: a brand-new perspective on mitochondria in cancer," *Cell & Bioscience,* vol. 9, no. 1, p. 27, 2019/03/19 2019.

[61] A. Raturi and T. Simmen, "Where the endoplasmic reticulum and the mitochondrion tie the knot: the mitochondria-associated membrane (MAM)," (in eng), no. 0006-3002 (Print).

[62] S. Marchi, S. Patergnani, and P. Pinton, "The endoplasmic reticulum-mitochondria connection: one touch, multiple functions," (in eng), no. 0006-3002 (Print).

[63] U. Schlattner *et al.*, "Mitochondrial cardiolipin/phospholipid trafficking: the role of membrane contact site complexes and lipid transfer proteins," (in eng), no. 1873-2941 (Electronic).

[64] N. Raimundo, L. Fernández-Mosquera, K. F. Yambire, and C. V. Diogo, "Mechanisms of communication between mitochondria and lysosomes," *The International Journal of Biochemistry & Cell Biology,* vol. 79, pp. 345-349, 2016/10/01/ 2016.

[65] Y. Elbaz-Alon *et al.*, "Lam6 Regulates the Extent of Contacts between Organelles," *Cell Reports,* vol. 12, no. 1, pp. 7-14, 2015/07/07/ 2015.

[66] N.-G. Larsson *et al.*, "Mitochondrial transcription factor A is necessary for mtDNA maintance and embryogenesis in mice," *Nature Genetics,* vol. 18, no. 3, pp. 231-236, 1998/03/01 1998.

[67] F. Baixauli *et al.*, "Mitochondrial Respiration Controls Lysosomal Function during Inflammatory T Cell Responses," *Cell Metabolism,* vol. 22, no. 3, pp. 485-498, 2015/09/01/ 2015.

[68] C. L. Nezich, C. Wang, A. I. Fogel, and R. J. Youle, "MiT/TFE transcription factors are activated during mitophagy downstream of Parkin and Atg5," *Journal of Cell Biology,* vol. 210, no. 3, pp. 435-450, 2015.

[69] J. Demers-Lamarche *et al.*, "Loss of Mitochondrial Function Impairs Lysosomes*," *Journal of Biological Chemistry,* vol. 291, no. 19, pp. 10263-10276, 2016/05/06/ 2016.

[70] J.-A. Lim, L. Li, O. Kakhlon, R. Myerowitz, and N. Raben, "Defects in calcium homeostasis and mitochondria can be reversed in Pompe disease," *Autophagy,* vol. 11, no. 2, pp. 385-402, 2015/02/01 2015.

[71] A. Raffaello, C. Mammucari, G. Gherardi, and R. Rizzuto, "Calcium at the Center of Cell Signaling: Interplay between Endoplasmic Reticulum, Mitochondria, and Lysosomes," *Trends in Biochemical Sciences,* vol. 41, no. 12, pp. 1035-1049, 2016/12/01/ 2016.

[72] R. M. Denton, "Regulation of mitochondrial dehydrogenases by calcium ions," *Biochimica et Biophysica Acta (BBA) - Bioenergetics,* vol. 1787, no. 11, pp. 1309-1316, 2009/11/01/ 2009.

[73] R. G. Hansford and J. B. Chappell, "The effect of Ca2+ on the oxidation of glycerol phosphate by blowfly flight-muscle mitochondria," *Biochemical and Biophysical Research Communications,* vol. 27, no. 6, pp. 686-692, 1967/06/23/ 1967.

[74] R. Rizzuto, D. De Stefani, A. Raffaello, and C. Mammucari, "Mitochondria as sensors and regulators of calcium signalling," *Nature Reviews Molecular Cell Biology,* vol. 13, no. 9, pp. 566-578, 2012/09/01 2012.

[75] D. L. Medina *et al.*, "Lysosomal calcium signalling regulates autophagy through calcineurin and TFEB," *Nature Cell Biology,* vol. 17, no. 3, pp. 288-299, 2015/03/01 2015.

[76] Q. Cao, X. Z. Zhong, Y. Zou, R. Murrell-Lagnado, M. X. Zhu, and X.-P. Dong, "Calcium release through P2X4 activates calmodulin to promote endolysosomal membrane fusion," *Journal of Cell Biology,* vol. 209, no. 6, pp. 879-894, 2015.

[77] B. Mirnikjoo, K. Balasubramanian, and A. J. Schroit, "Mobilization of Lysosomal Calcium Regulates the Externalization of Phosphatidylserine during Apoptosis*," *Journal of Biological Chemistry,* vol. 284, no. 11, pp. 6918-6923, 2009/03/13/ 2009.

[78] B. Vega Rick, M. Huss Janice, and P. Kelly Daniel, "The Coactivator PGC-1 Cooperates with Peroxisome Proliferator-Activated Receptor α in Transcriptional Control of Nuclear Genes Encoding Mitochondrial Fatty Acid Oxidation Enzymes," *Molecular and Cellular Biology,* vol. 20, no. 5, pp. 1868-1876, 2000/03/01 2000.

[79] C. Settembre *et al.*, "TFEB controls cellular lipid metabolism through a starvation-induced autoregulatory loop," *Nature Cell Biology,* vol. 15, no. 6, pp. 647-658, 2013/06/01 2013.

[80] G. Mansueto *et al.*, "Transcription Factor EB Controls Metabolic Flexibility during Exercise," *Cell Metabolism,* vol. 25, no. 1, pp. 182-196, 2017/01/10/ 2017.

[81] M. Schrader, L. F. Costello J Fau - Godinho, M. Godinho Lf Fau - Islinger, and M. Islinger, "Peroxisome-mitochondria interplay and disease," (in eng), no. 1573-2665 (Electronic).

[82] Y. Cohen *et al.*, "Peroxisomes are juxtaposed to strategic sites on mitochondria," (in eng), no. 1742-2051 (Electronic).

[83] M. Falkenberg, "Mitochondrial DNA replication in mammalian cells: overview of the pathway," *Essays in Biochemistry,* vol. 62, no. 3, pp. 287-296, 2018.

[84] E. Yakubovskaya, Z. Chen, J. A. Carrodeguas, C. Kisker, and D. F. Bogenhagen, "Functional Human Mitochondrial DNA Polymerase γ Forms a Heterotrimer*," *Journal of Biological Chemistry,* vol. 281, no. 1, pp. 374-382, 2006/01/06/ 2006.

[85] M. J. Longley, D. Nguyen, T. A. Kunkel, and W. C. Copeland, "The Fidelity of Human DNA Polymerase γ with and without Exonucleolytic Proofreading and the p55 Accessory Subunit*," *Journal of Biological Chemistry,* vol. 276, no. 42, pp. 38555-38562, 2001/10/19/ 2001.

[86] J. A. Korhonen, M. Gaspari, and M. Falkenberg, "TWINKLE Has 5′ → 3′ DNA Helicase Activity and Is Specifically Stimulated by Mitochondrial Single-stranded DNA-binding Protein*," *Journal of Biological Chemistry,* vol. 278, no. 49, pp. 48627-48632, 2003/12/05/ 2003.

[87] B. Mignotte, M. Barat, and J.-C. Mounolou, "Characterization of a mitochondrial protein binding to single-stranded DNA," *Nucleic Acids Research,* vol. 13, no. 5, pp. 1703-1716, 1985.

[88] D. L. Robberson, H. Kasamatsu, and J. Vinograd, "Replication of Mitochondrial DNA. Circular Replicative Intermediates in Mouse L Cells," *Proceedings of the National Academy of Sciences,* vol. 69, no. 3, p. 737, 1972.

[89] S. Wanrooij, J. M. Fusté, G. Farge, Y. Shi, C. M. Gustafsson, and M. Falkenberg, "Human mitochondrial RNA polymerase primes lagging-strand DNA synthesis in vitro," *Proceedings of the National Academy of Sciences,* vol. 105, no. 32, p. 11122, 2008.

[90] J. Miralles Fusté *et al.*, "In Vivo Occupancy of Mitochondrial Single-Stranded DNA Binding Protein Supports the Strand Displacement Mode of DNA Replication," *PLOS Genetics,* vol. 10, no. 12, p. e1004832, 2014.

[91] J. M. Fusté *et al.*, "Mitochondrial RNA Polymerase Is Needed for Activation of the Origin of Light-Strand DNA Replication," *Molecular Cell,* vol. 37, no. 1, pp. 67-78, 2010/01/15/ 2010.

[92] P. A. Martens and D. A. Clayton, "Mechanism of mitochondrial DNA replication in mouse L-cells: Localization and sequence of the light-strand origin of replication," *Journal of Molecular Biology,* vol. 135, no. 2, pp. 327-351, 1979/12/05/ 1979.

[93] D. A. Clayton, "Replication and Transcription of Vertebrate Mitochondrial DNA," *Annual Review of Cell Biology,* vol. 7, no. 1, pp. 453-478, 1991/11/01 1991.

[94] C. Kukat *et al.*, "Cross-strand binding of TFAM to a single mtDNA molecule forms the mitochondrial nucleoid," *Proceedings of the National Academy of Sciences,* vol. 112, no. 36, p. 11288, 2015.

[95] Y. Shi *et al.*, "Mammalian transcription factor A is a core component of the mitochondrial transcription machinery," *Proceedings of the National Academy of Sciences,* vol. 109, no. 41, p. 16510, 2012.

[96] J. Qin *et al.*, "ER-mitochondria contacts promote mtDNA nucleoids active transportation via mitochondrial dynamic tubulation," *Nat Commun,* vol. 11, no. 1, p. 4471, Sep 8 2020.

[97] G. A. Fontana and H. L. Gahlon, "Mechanisms of replication and repair in mitochondrial DNA deletion formation," *Nucleic Acids Research,* vol. 48, no. 20, pp. 11244-11258, 2020.

[98] R. R. Alencar, C. M. P. F. Batalha, T. S. Freire, and N. C. de Souza-Pinto, "Chapter Eight - Enzymology of mitochondrial DNA repair," in *The Enzymes*, vol. 45, L. Zhao and L. S. Kaguni, Eds.: Academic Press, 2019, pp. 257-287.

[99] W. Zhu, W. Qin, and E. R. Sauter, "Large-scale mitochondrial DNA deletion mutations and nuclear genome instability in human breast cancer," *Cancer Detection and Prevention,* vol. 28, no. 2, pp. 119-126, 2004/01/01/ 2004.

[100] E. Bua *et al.*, "Mitochondrial DNA–Deletion Mutations Accumulate Intracellularly to Detrimental Levels in Aged Human Skeletal Muscle Fibers," *The American Journal of Human Genetics,* vol. 79, no. 3, pp. 469-480, 2006/09/01/ 2006.

[101] S. D. Taylor *et al.*, "Targeted enrichment and high-resolution digital profiling of mitochondrial DNA deletions in human brain," (in eng), no. 1474-9726 (Electronic).

[102] D. Wang *et al.*, "Analysis of serum β-amyloid peptides, α2-macroglobulin, complement factor H, and clusterin levels in APP/PS1 transgenic mice during progression of Alzheimer's disease," *NeuroReport,* vol. 27, no. 15, 2016.

[103] Z. Shi *et al.*, "Dual functional NaYF4:Yb3+, Er3+@NaYF4:Yb3+, Nd3+core–shell nanoparticles for cell temperature sensing and imaging," *Nanotechnology,* vol. 29, no. 9, p. 094001, 2018/01/25 2018.

[104] K. Okabe, N. Inada, C. Gota, Y. Harada, T. Funatsu, and S. Uchiyama, "Intracellular temperature mapping with a fluorescent polymeric thermometer and fluorescence lifetime imaging microscopy," *Nat Commun,* vol. 3, p. 705, Feb 28 2012.

[105] G. N. Somero, "Proteins and Temperature," *Annual Review of Physiology,* vol. 57, no. 1, pp. 43-68, 1995/10/01 1995.

[106] H. Gao, C. Kam, T. Y. Chou, M.-Y. Wu, X. Zhao, and S. Chen, "A simple yet effective AIE-based fluorescent nano-thermometer for temperature mapping in living cells using fluorescence lifetime imaging microscopy," *Nanoscale Horizons,* 10.1039/C9NH00693A vol. 5, no. 3, pp. 488-494, 2020.

[107] B. Saha, B. Ruidas, S. Mete, C. D. Mukhopadhyay, K. Bauri, and P. De, "AIE-active non-conjugated poly(N-vinylcaprolactam) as a fluorescent thermometer for intracellular temperature imaging," *Chemical Science,* 10.1039/C9SC04338A vol. 11, no. 1, pp. 141-147, 2020.

[108] Y. Han, Y. Liu, H. Zhao, A. Vomiero, and R. Li, "Highly efficient ratiometric nanothermometers based on colloidal carbon quantum dots," *Journal of*

Materials Chemistry B, 10.1039/D1TB00224D vol. 9, no. 20, pp. 4111-4119, 2021.

[109] W. U. Khan, L. Qin, A. Alam, P. Zhou, Y. Peng, and Y. Wang, "Fluorescent Carbon Dots an Effective Nano-Thermometer in Vitro Applications," *ACS Applied Bio Materials,* vol. 4, no. 7, pp. 5786-5796, 2021/07/19 2021.

[110] F. Pedroza-Montero *et al.*, "Thermometric Characterization of Fluorescent Nanodiamonds Suitable for Biomedical Applications," *Applied Sciences,* vol. 11, no. 9, 2021.

[111] B. H. Lee, R. L. McKinney, M. T. Hasan, and A. V. Naumov, "Graphene Quantum Dots as Intracellular Imaging-Based Temperature Sensors," (in eng), *Materials (Basel, Switzerland),* vol. 14, no. 3, p. 616, 2021.

[112] Z. Huang, N. Li, X. Zhang, C. Wang, and Y. Xiao, "Fixable Molecular Thermometer for Real-Time Visualization and Quantification of Mitochondrial Temperature," *Analytical Chemistry,* vol. 90, no. 23, pp. 13953-13959, 2018/12/04 2018.

[113] J. Qiao *et al.*, "Simultaneous Monitoring of Mitochondrial Temperature and ATP Fluctuation Using Fluorescent Probes in Living Cells," *Analytical Chemistry,* vol. 90, no. 21, pp. 12553-12558, 2018/11/06 2018.

[114] H. Zhou *et al.*, "Upconversion NIR-II fluorophores for mitochondria-targeted cancer imaging and photothermal therapy," *Nature Communications,* vol. 11, no. 1, p. 6183, 2020/12/03 2020.

[115] X. Di *et al.*, "Quantitatively Monitoring In Situ Mitochondrial Thermal Dynamics by Upconversion Nanoparticles," *Nano Letters,* vol. 21, no. 4, pp. 1651-1658, 2021/02/24 2021.

[116] R. Tanimoto *et al.*, "Detection of Temperature Difference in Neuronal Cells," *Scientific Reports,* vol. 6, no. 1, p. 22071, 2016/03/01 2016.

[117] J.-M. Yang, H. Yang, and L. Lin, "Quantum Dot Nano Thermometers Reveal Heterogeneous Local Thermogenesis in Living Cells," *ACS Nano,* vol. 5, no. 6, pp. 5067-5071, 2011/06/28 2011.

[118] J. S. Donner, S. A. Thompson, M. P. Kreuzer, G. Baffou, and R. Quidant, "Mapping Intracellular Temperature Using Green Fluorescent Protein," *Nano Letters,* vol. 12, no. 4, pp. 2107-2111, 2012/04/11 2012.

[119] S. Kiyonaka *et al.*, "Genetically encoded fluorescent thermosensors visualize subcellular thermoregulation in living cells," *Nature Methods,* vol. 10, no. 12, pp. 1232-1238, 2013/12/01 2013.

[120] W. Cao, Y. Cui, Y. Yang, and G. Qian, "Dyes Encapsulated Nanoscale Metal–Organic Frameworks for Multimode Temperature Sensing with High Spatial Resolution," *ACS Materials Letters,* vol. 3, no. 9, pp. 1426-1432, 2021/09/06 2021.

[121] S. Sotoma *et al.*, "In situ measurements of intracellular thermal conductivity using heater-thermometer hybrid diamond nanosensors," *Science Advances,* vol. 7, no. 3, p. eabd7888.

[122] C. D. S. Brites *et al.*, "Instantaneous ballistic velocity of suspended Brownian nanocrystals measured by upconversion nanothermometry," *Nature Nanotechnology,* vol. 11, no. 10, pp. 851-856, 2016/10/01 2016.

[123] R. G. Geitenbeek *et al.*, "In Situ Luminescence Thermometry To Locally Measure Temperature Gradients during Catalytic Reactions," *ACS Catalysis,* vol. 8, no. 3, pp. 2397-2401, 2018/03/02 2018.

[124] C. Mi, J. Zhou, F. Wang, G. Lin, and D. Jin, "Ultrasensitive Ratiometric Nanothermometer with Large Dynamic Range and Photostability," *Chemistry of Materials,* vol. 31, no. 22, pp. 9480-9487, 2019/11/26 2019.

[125] X. Qiu, Q. Zhou, X. Zhu, Z. Wu, W. Feng, and F. Li, "Ratiometric upconversion nanothermometry with dual emission at the same wavelength decoded via a time-resolved technique," *Nature Communications,* vol. 11, no. 1, p. 4, 2020/01/07 2020.

[126] G. Baffou, H. Rigneault, D. Marguet, and L. Jullien, "A critique of methods for temperature imaging in single cells," (in eng), no. 1548-7105 (Electronic).

[127] D. Jaque and F. Vetrone, "Luminescence nanothermometry," *Nanoscale,* 10.1039/C2NR30764B vol. 4, no. 15, pp. 4301-4326, 2012.

[128] M. J. Snare, F. E. Treloar, K. P. Ghiggino, and P. J. Thistlethwaite, "The photophysics of rhodamine B," *Journal of Photochemistry,* vol. 18, no. 4, pp. 335-346, 1982/01/01/ 1982.

[129] C. Gota, K. Okabe, T. Funatsu, Y. Harada, and S. Uchiyama, "Hydrophilic Fluorescent Nanogel Thermometer for Intracellular Thermometry," *Journal of the American Chemical Society,* vol. 131, no. 8, pp. 2766-2767, 2009/03/04 2009.

[130] C. D. S. Brites, A. Millán, and L. D. Carlos, "Chapter 281 - Lanthanides in Luminescent Thermometry," in *Handbook on the Physics and Chemistry of Rare Earths*, vol. 49, B. Jean-Claude and P. Vitalij K, Eds.: Elsevier, 2016, pp. 339-427.

[131] M. D. Shinn, W. A. Sibley, M. G. Drexhage, and R. N. Brown, "Optical transitions of ${\mathrm{Er}}^{3+}$ ions in fluorozirconate glass," *Physical Review B,* vol. 27, no. 11, pp. 6635-6648, 06/01/ 1983.

[132] M. J. Weber, "Probabilities for Radiative and Nonradiative Decay of ${\mathrm{Er}}^{3+}$ in La${\mathrm{F}}_{3}$," *Physical Review,* vol. 157, no. 2, pp. 262-272, 05/10/ 1967.

[133] W. T. Carnall, H. Crosswhite, and H. M. Crosswhite, "Energy level structure and transition probabilities in the spectra of the trivalent lanthanides in LaF_3," United States1978-01-01 1978, Available: https://www.osti.gov/biblio/6417825 https://www.osti.gov/servlets/purl/6417825.

[134] M. D. Dramićanin, "Trends in luminescence thermometry," *Journal of Applied Physics,* vol. 128, no. 4, p. 040902, 2020/07/28 2020.

[135] F. Vetrone *et al.*, "Temperature Sensing Using Fluorescent Nanothermometers," *ACS Nano,* vol. 4, no. 6, pp. 3254-3258, 2010/06/22 2010.

[136] A. Sedlmeier, D. E. Achatz, L. H. Fischer, H. H. Gorris, and O. S. Wolfbeis, "Photon upconverting nanoparticles for luminescent sensing of temperature," *Nanoscale,* 10.1039/C2NR32314A vol. 4, no. 22, pp. 7090-7096, 2012.

[137] S. Kalytchuk *et al.*, "Carbon Dot Nanothermometry: Intracellular Photoluminescence Lifetime Thermal Sensing," *ACS Nano,* vol. 11, no. 2, pp. 1432-1442, 2017/02/28 2017.

[138] J. M. Yang, H. Yang, and L. Lin, "Quantum dot nano thermometers reveal heterogeneous local thermogenesis in living cells," *ACS Nano,* vol. 5, no. 6, pp. 5067-71, Jun 28 2011.

[139] Y. Wu *et al.*, "Fluorescent Nanodiamond–Nanogels for Nanoscale Sensing and Photodynamic Applications," *Advanced NanoBiomed Research,* https://doi.org/10.1002/anbr.202000101 vol. 1, no. 7, p. 2000101,

2021/07/01 2021.
[140] Y. Wu *et al.*, "Nanodiamond Theranostic for Light-Controlled Intracellular Heating and Nanoscale Temperature Sensing," *Nano Letters,* vol. 21, no. 9, pp. 3780-3788, 2021/05/12 2021.
[141] S. Arai *et al.*, "Mitochondria-targeted fluorescent thermometer monitors intracellular temperature gradient," *Chemical Communications,* 10.1039/C5CC01088H vol. 51, no. 38, pp. 8044-8047, 2015.
[142] M. Homma, Y. Takei, A. Murata, T. Inoue, and S. Takeoka, "A ratiometric fluorescent molecular probe for visualization of mitochondrial temperature in living cells," *Chemical Communications,* 10.1039/C4CC10349A vol. 51, no. 28, pp. 6194-6197, 2015.
[143] H. Gao, C. Kam, T. Y. Chou, M. Y. Wu, X. Zhao, and S. Chen, "A simple yet effective AIE-based fluorescent nano-thermometer for temperature mapping in living cells using fluorescence lifetime imaging microscopy," *Nanoscale Horiz,* vol. 5, no. 3, pp. 488-494, Mar 2 2020.
[144] T. Hayashi, N. Fukuda, S. Uchiyama, and N. Inada, "A cell-permeable fluorescent polymeric thermometer for intracellular temperature mapping in mammalian cell lines," (in eng), no. 1932-6203 (Electronic).
[145] J. Qiao, X. Mu, and L. Qi, "Construction of fluorescent polymeric nano-thermometers for intracellular temperature imaging: A review," *Biosensors and Bioelectronics,* vol. 85, pp. 403-413, 2016/11/15/ 2016.
[146] J. Qiao *et al.*, "Ratiometric Fluorescent Polymeric Thermometer for Thermogenesis Investigation in Living Cells," *Analytical Chemistry,* vol. 87, no. 20, pp. 10535-10541, 2015/10/20 2015.
[147] X. Guan *et al.*, "A versatile synthetic approach to tunable dual-emissive Pdots with very small-size based on amphiphilic block copolymers for cell imaging," *Materials Chemistry Frontiers,* 10.1039/D0QM00497A vol. 5, no. 1, pp. 355-367, 2021.
[148] J. Yang, K. Gu, C. Shi, M. Li, P. Zhao, and W.-H. Zhu, "Fluorescent thermometer based on a quinolinemalononitrile copolymer with aggregation-induced emission characteristics," *Materials Chemistry Frontiers,* 10.1039/C9QM00147F vol. 3, no. 8, pp. 1503-1509, 2019.
[149] M. Zimmer, "GFP: from jellyfish to the Nobel prize and beyond," (in eng), no. 1460-4744 (Electronic).
[150] K. Okabe, R. Sakaguchi, B. Shi, and S. Kiyonaka, "Intracellular thermometry with fluorescent sensors for thermal biology," *Pflügers Archiv - European Journal of Physiology,* vol. 470, no. 5, pp. 717-731, 2018/05/01 2018.
[151] M. Nakano, Y. Arai, I. Kotera, K. Okabe, Y. Kamei, and T. Nagai, "Genetically encoded ratiometric fluorescent thermometer with wide range and rapid response," *PLoS One,* vol. 12, no. 2, p. e0172344, 2017.
[152] X. Xu *et al.*, "Electrophoretic Analysis and Purification of Fluorescent Single-Walled Carbon Nanotube Fragments," *Journal of the American Chemical Society,* vol. 126, no. 40, pp. 12736-12737, 2004/10/01 2004.
[153] Y. P. Sun *et al.*, "Quantum-sized carbon dots for bright and colorful photoluminescence," (in eng), no. 0002-7863 (Print).
[154] T. Sun, Y. Zhang, R. Yan, Y. Jiang, and Y. Zhao, "Preparation and Applications of Carbon-Based Fluorescent Nanothermometers," *Particle & Particle Systems Characterization,* vol. 38, no. 3, p. 2000261, 2021.

[155] W. Su *et al.*, "Carbon dots: a booming material for biomedical applications," *Materials Chemistry Frontiers,* 10.1039/C9QM00658C vol. 4, no. 3, pp. 821-836, 2020.
[156] B. H. Lee, R. L. McKinney, M. T. Hasan, and A. V. Naumov, "Graphene Quantum Dots as Intracellular Imaging-Based Temperature Sensors," *Materials,* vol. 14, no. 3, 2021.
[157] H. Zhang *et al.*, "Accurate intracellular and in vivo temperature sensing based on CuInS2/ZnS QD micelles," *J Mater Chem B,* vol. 7, no. 17, pp. 2835-2844, May 7 2019.
[158] A. Gupta *et al.*, "Up-conversion hybrid nanomaterials for light- and heat-driven applications," *Progress in Materials Science,* vol. 121, p. 100838, 2021/08/01/ 2021.
[159] X. Zhu *et al.*, "Temperature-feedback upconversion nanocomposite for accurate photothermal therapy at facile temperature," *Nature Communications,* vol. 7, no. 1, p. 10437, 2016/02/04 2016.
[160] O. A. Savchuk, O. F. Silvestre, R. M. R. Adão, and J. B. Nieder, "GFP fluorescence peak fraction analysis based nanothermometer for the assessment of exothermal mitochondria activity in live cells," *Scientific Reports,* vol. 9, no. 1, p. 7535, 2019/05/17 2019.
[161] L. de Meis, A. P. Arruda, and D. P. Carvalho, "Role of Sarco/Endoplasmic Reticulum Ca2+-ATPase in Thermogenesis," *Bioscience Reports,* vol. 25, no. 3-4, pp. 181-190, 2005.
[162] R. Kriszt *et al.*, "Optical visualisation of thermogenesis in stimulated single-cell brown adipocytes," *Scientific Reports,* vol. 7, no. 1, p. 1383, 2017/05/03 2017.
[163] K. Oyama *et al.*, "Walking nanothermometers: spatiotemporal temperature measurement of transported acidic organelles in single living cells," *Lab on a Chip,* 10.1039/C2LC00014H vol. 12, no. 9, pp. 1591-1593, 2012.
[164] D. Wang *et al.*, "Increased Formation of Follicular Antrum in Aquaporin-8-Deficient Mice Is Due to Defective Proliferation and Migration, and Not Steroidogenesis of Granulosa Cells," *Frontiers in Physiology,* vol. 9, 2018.
[165] A. Sedlmeier and H. H. Gorris, "Surface modification and characterization of photon-upconverting nanoparticles for bioanalytical applications," *Chemical Society Reviews,* 10.1039/C4CS00186A vol. 44, no. 6, pp. 1526-1560, 2015.
[166] B. P. Chhetri, A. Karmakar, and A. Ghosh, "Recent Advancements in Ln-Ion-Based Upconverting Nanomaterials and Their Biological Applications," *Particle & Particle Systems Characterization,* https://doi.org/10.1002/ppsc.201900153 vol. 36, no. 8, p. 1900153, 2019/08/01 2019.
[167] H. T. T. Duong *et al.*, "Systematic investigation of functional ligands for colloidal stable upconversion nanoparticles," *RSC Advances,* vol. 8, no. 9, pp. 4842-4849, 2018.
[168] A. Nsubuga *et al.*, "Facile preparation of multifunctionalisable 'stealth' upconverting nanoparticles for biomedical applications," *Dalton Transactions,* 10.1039/C8DT00241J vol. 47, no. 26, pp. 8595-8604, 2018.
[169] W. Stöber, A. Fink, and E. Bohn, "Controlled growth of monodisperse silica spheres in the micron size range," *Journal of Colloid and Interface Science,* vol. 26, no. 1, pp. 62-69, 1968/01/01/ 1968.

[170] A.-L. Morel *et al.*, "Sonochemical Approach to the Synthesis of Fe3O4@SiO2 Core−Shell Nanoparticles with Tunable Properties," *ACS Nano,* vol. 2, no. 5, pp. 847-856, 2008/05/01 2008.
[171] C. Graf, D. L. J. Vossen, A. Imhof, and A. van Blaaderen, "A General Method To Coat Colloidal Particles with Silica," *Langmuir,* vol. 19, no. 17, pp. 6693-6700, 2003/08/01 2003.
[172] P. Zhang, W. Steelant, M. Kumar, and M. Scholfield, "Versatile Photosensitizers for Photodynamic Therapy at Infrared Excitation," *Journal of the American Chemical Society,* vol. 129, no. 15, pp. 4526-4527, 2007/04/01 2007.
[173] F. J. Arriagada and K. Osseo-Asare, "Synthesis of Nanosize Silica in a Nonionic Water-in-Oil Microemulsion: Effects of the Water/Surfactant Molar Ratio and Ammonia Concentration," *Journal of Colloid and Interface Science,* vol. 211, no. 2, pp. 210-220, 1999/03/15/ 1999.
[174] S. Gai *et al.*, "Synthesis of Magnetic, Up-Conversion Luminescent, and Mesoporous Core–Shell-Structured Nanocomposites as Drug Carriers," *Advanced Functional Materials,* https://doi.org/10.1002/adfm.200902274 vol. 20, no. 7, pp. 1166-1172, 2010/04/09 2010.
[175] H. S. Qian, H. C. Guo, P. C.-L. Ho, R. Mahendran, and Y. Zhang, "Mesoporous-Silica-Coated Up-Conversion Fluorescent Nanoparticles for Photodynamic Therapy," *Small,* https://doi.org/10.1002/smll.200900692 vol. 5, no. 20, pp. 2285-2290, 2009/10/16 2009.
[176] X. Chen, Y. Zhang, X. Zhang, Z. Zhang, and Y. Zhang, "Rationally designed upconversion nanoparticles for NIR light-controlled lysosomal escape and nucleus-based photodynamic therapy," *Microchimica Acta,* vol. 188, no. 10, p. 349, 2021/09/22 2021.
[177] R. P. Bagwe, L. R. Hilliard, and W. Tan, "Surface Modification of Silica Nanoparticles to Reduce Aggregation and Nonspecific Binding," *Langmuir,* vol. 22, no. 9, pp. 4357-4362, 2006/04/01 2006.
[178] G.-S. Yi and G.-M. Chow, "Water-Soluble NaYF4:Yb,Er(Tm)/NaYF4/Polymer Core/Shell/Shell Nanoparticles with Significant Enhancement of Upconversion Fluorescence," *Chemistry of Materials,* vol. 19, no. 3, pp. 341-343, 2007/02/01 2007.
[179] L. Cheng, K. Yang, M. Shao, S.-T. Lee, and Z. Liu, "Multicolor In Vivo Imaging of Upconversion Nanoparticles with Emissions Tuned by Luminescence Resonance Energy Transfer," *The Journal of Physical Chemistry C,* vol. 115, no. 6, pp. 2686-2692, 2011/02/17 2011.
[180] S. Liang *et al.*, "Decoration of up-converting NaYF4:Yb,Er(Tm) nanoparticles with surfactant bilayer. A versatile strategy to perform oil-to-water phase transfer and subsequently surface silication," *CrystEngComm,* 10.1039/C2CE06578A vol. 14, no. 10, pp. 3484-3489, 2012.
[181] G. Decher, "Fuzzy Nanoassemblies: Toward Layered Polymeric Multicomposites," *Science,* vol. 277, no. 5330, pp. 1232-1237, 1997/08/29 1997.
[182] L. Wang *et al.*, "Fluorescence Resonant Energy Transfer Biosensor Based on Upconversion-Luminescent Nanoparticles," *Angewandte Chemie International Edition,* https://doi.org/10.1002/anie.200501907 vol. 44, no. 37, pp. 6054-6057, 2005/09/19 2005.

[183] Y. Liu *et al.*, "Upconversion nano-photosensitizer targeting into mitochondria for cancer apoptosis induction and cyt c fluorescence monitoring," *Nano Research,* vol. 9, no. 11, pp. 3257-3266, 2016/11/01 2016.

[184] R. Naccache, F. Vetrone, V. Mahalingam, L. A. Cuccia, and J. A. Capobianco, "Controlled Synthesis and Water Dispersibility of Hexagonal Phase NaGdF4:Ho3+/Yb3+ Nanoparticles," *Chemistry of Materials,* vol. 21, no. 4, pp. 717-723, 2009/02/24 2009.

[185] H.-P. Zhou, C.-H. Xu, W. Sun, and C.-H. Yan, "Clean and Flexible Modification Strategy for Carboxyl/Aldehyde-Functionalized Upconversion Nanoparticles and Their Optical Applications," *Advanced Functional Materials,* https://doi.org/10.1002/adfm.200901458 vol. 19, no. 24, pp. 3892-3900, 2009/12/23 2009.

[186] M. Wang *et al.*, "NIR-Responsive Silica-Coated NaYbF4:Er/Tm/Ho Upconversion Fluorescent Nanoparticles with Tunable Emission Colors and Their Applications in Immunolabeling and Fluorescent Imaging of Cancer Cells," *The Journal of Physical Chemistry C,* vol. 113, no. 44, pp. 19021-19027, 2009/11/05 2009.

[187] M. Wang *et al.*, "Immunoassay of Goat Antihuman Immunoglobulin G Antibody Based on Luminescence Resonance Energy Transfer between Near-Infrared Responsive NaYF4:Yb, Er Upconversion Fluorescent Nanoparticles and Gold Nanoparticles," *Analytical Chemistry,* vol. 81, no. 21, pp. 8783-8789, 2009/11/01 2009.

[188] F. van de Rijke *et al.*, "Up-converting phosphor reporters for nucleic acid microarrays," *Nature Biotechnology,* vol. 19, no. 3, pp. 273-276, 2001/03/01 2001.

[189] P. Lu, B. J. Bruno, M. Rabenau, and C. S. Lim, "Delivery of drugs and macromolecules to the mitochondria for cancer therapy," (in eng), no. 1873-4995 (Electronic).

[190] J. Zielonka *et al.*, "Mitochondria-Targeted Triphenylphosphonium-Based Compounds: Syntheses, Mechanisms of Action, and Therapeutic and Diagnostic Applications," *Chemical Reviews,* vol. 117, no. 15, pp. 10043-10120, 2017/08/09 2017.

[191] R. J. Burns and M. P. Murphy, "Labeling of mitochondrial proteins in living cells by the thiol probe thiobutyltriphenylphosphonium bromide," (in eng), no. 0003-9861 (Print).

[192] R. A. J. Smith, C. M. Porteous, A. M. Gane, and M. P. Murphy, "Delivery of bioactive molecules to mitochondria in vivo," (in eng), *Proceedings of the National Academy of Sciences of the United States of America,* vol. 100, no. 9, pp. 5407-5412, 2003.

[193] B. Wang *et al.*, "A mitochondria-targeted fluorescent probe based on TPP-conjugated carbon dots for both one- and two-photon fluorescence cell imaging," *RSC Advances,* 10.1039/C4RA07467J vol. 4, no. 91, pp. 49960-49963, 2014.

[194] M. L. Johnson Lv Fau - Walsh, L. B. Walsh Ml Fau - Chen, and L. B. Chen, "Localization of mitochondria in living cells with rhodamine 123," (in eng), no. 0027-8424 (Print).

[195] G. Dodin, P. Averbeck D Fau - Demerseman, S. Demerseman P Fau - Nocentini, J. Nocentini S Fau - Dupont, and J. Dupont, "Mitochondrial uptake of bridged

bis-methylpyridinium aldoximes and induction of the "petite" phenotype in yeast," (in eng), no. 0006-291X (Print).

[196] A. A. Gerencser *et al.*, "Quantitative measurement of mitochondrial membrane potential in cultured cells: calcium-induced de- and hyperpolarization of neuronal mitochondria," (in eng), *The Journal of physiology,* vol. 590, no. 12, pp. 2845-2871, 2012.

[197] E. J. Ngen, Y. Rajaputra P Fau - You, and Y. You, "Evaluation of delocalized lipophilic cationic dyes as delivery vehicles for photosensitizers to mitochondria," (in eng), no. 1464-3391 (Electronic).

[198] Y. N. Antonenko *et al.*, "Mitochondria-targeted plastoquinone derivatives as tools to interrupt execution of the aging program. 1. Cationic plastoquinone derivatives: synthesis and in vitro studies," (in eng), no. 1608-3040 (Electronic).

[199] Y. N. Antonenko *et al.*, "Intramitochondrial accumulation of cationic Atto520-biotin proceeds via voltage-dependent slow permeation through lipid membrane," (in eng), no. 0006-3002 (Print).

[200] S. R. Jean, M. Ahmed, E. K. Lei, S. P. Wisnovsky, and S. O. Kelley, "Peptide-Mediated Delivery of Chemical Probes and Therapeutics to Mitochondria," *Accounts of Chemical Research,* vol. 49, no. 9, pp. 1893-1902, 2016/09/20 2016.

[201] C. P. Cerrato, M. Pirisinu, E. N. Vlachos, and Ü. Langel, "Novel cell-penetrating peptide targeting mitochondria," (in eng), no. 1530-6860 (Electronic).

[202] H. H. Szeto and P. W. Schiller, "Novel therapies targeting inner mitochondrial membrane--from discovery to clinical development," (in eng), no. 1573-904X (Electronic).

[203] K. L. Horton, S. B. Stewart Km Fau - Fonseca, Q. Fonseca Sb Fau - Guo, S. O. Guo Q Fau - Kelley, and S. O. Kelley, "Mitochondria-penetrating peptides," (in eng), no. 1074-5521 (Print).

[204] X. Zhang, F. Ai, T. Sun, F. Wang, and G. Zhu, "Multimodal Upconversion Nanoplatform with a Mitochondria-Targeted Property for Improved Photodynamic Therapy of Cancer Cells," *Inorganic Chemistry,* vol. 55, no. 8, pp. 3872-3880, 2016/04/18 2016.

[205] V. Weissig, S.-M. Boddapati Sv Fau - Cheng, G. G. M. Cheng Sm Fau - D'Souza, and G. G. D'Souza, "Liposomes and liposome-like vesicles for drug and DNA delivery to mitochondria," (in eng), no. 0898-2104 (Print).

[206] M. A. Benien P Fau - Almuteri, A. S. Almuteri Ma Fau - Mehanna, G. G. M. Mehanna As Fau - D'Souza, and G. G. D'Souza, "Synthesis of triphenylphosphonium phospholipid conjugates for the preparation of mitochondriotropic liposomes," (in eng), no. 1940-6029 (Electronic).

[207] P. Benien, M. A. Solomon, P. Nguyen, E. M. Sheehan, A. S. Mehanna, and G. G. D'Souza, "Hydrophobized triphenyl phosphonium derivatives for the preparation of mitochondriotropic liposomes: choice of hydrophobic anchor influences cytotoxicity but not mitochondriotropic effect," (in eng), no. 1532-2394 (Electronic).

[208] M. E. Lynge, R. van der Westen, A. Postma, and B. Städler, "Polydopamine—a nature-inspired polymer coating for biomedical science," *Nanoscale,* 10.1039/C1NR10969C vol. 3, no. 12, pp. 4916-4928, 2011.

[209] H. Lee, M. Dellatore Shara, M. Miller William, and B. Messersmith Phillip, "Mussel-Inspired Surface Chemistry for Multifunctional Coatings," *Science,* vol. 318, no. 5849, pp. 426-430, 2007/10/19 2007.

[210] W.-Q. Li *et al.*, "Mitochondria-Targeting Polydopamine Nanoparticles To Deliver Doxorubicin for Overcoming Drug Resistance," *ACS Applied Materials & Interfaces,* vol. 9, no. 20, pp. 16793-16802, 2017/05/24 2017.

[211] X. Zhong *et al.*, "Polydopamine as a Biocompatible Multifunctional Nanocarrier for Combined Radioisotope Therapy and Chemotherapy of Cancer," *Advanced Functional Materials,* https://doi.org/10.1002/adfm.201503587 vol. 25, no. 47, pp. 7327-7336, 2015/12/01 2015.

[212] Y. Gu, X. Qiao, J. Zhang, Y. Sun, Y. Tao, and S. Qiao, "Effects of surface modification of upconversion nanoparticles on cellular uptake and cytotoxicity," *Chemical Research in Chinese Universities,* vol. 32, no. 3, pp. 474-479, 2016/06/01 2016.

[213] Y. Chen, C. D'Amario, A. Gee, H. T. T. Duong, O. Shimoni, and S. M. Valenzuela, "Dispersion stability and biocompatibility of four ligand-exchanged NaYF4: Yb, Er upconversion nanoparticles," *Acta Biomaterialia,* vol. 102, pp. 384-393, 2020/01/15/ 2020.

[214] M. Wang, G. Abbineni, A. Clevenger, C. Mao, and S. Xu, "Upconversion nanoparticles: synthesis, surface modification and biological applications," *Nanomedicine,* vol. 7, no. 6, pp. 710-29, Dec 2011.

[215] Y. Liu *et al.*, "Ionic Functionalization of Hydrophobic Colloidal Nanoparticles To Form Ionic Nanoparticles with Enzymelike Properties," *Journal of the American Chemical Society,* vol. 137, no. 47, pp. 14952-14958, 2015/12/02 2015.

[216] L. E. Mackenzie *et al.*, "The theoretical molecular weight of NaYF4:RE upconversion nanoparticles," *Scientific Reports,* vol. 8, no. 1, p. 1106, 2018/01/18 2018.

[217] E. Nogales, "Structural Insights into Microtubule Function," *Annual Review of Biophysics and Biomolecular Structure,* vol. 30, no. 1, pp. 397-420, 2001/06/01 2001.

[218] C. Weisenberg Richard, "Microtubule Formation in vitro in Solutions Containing Low Calcium Concentrations," *Science,* vol. 177, no. 4054, pp. 1104-1105, 1972/09/22 1972.

[219] M. C. Ledbetter and K. R. Porter, "A "MICROTUBULE" IN PLANT CELL FINE STRUCTURE," (in eng), *The Journal of cell biology,* vol. 19, no. 1, pp. 239-250, 1963.

[220] S. Jakobs, T. Stephan, P. Ilgen, and C. Brüser, "Light Microscopy of Mitochondria at the Nanoscale," *Annual Review of Biophysics,* vol. 49, no. 1, pp. 289-308, 2020/05/06 2020.

[221] T. Stephan, A. Roesch, D. Riedel, and S. Jakobs, "Live-cell STED nanoscopy of mitochondrial cristae," *Scientific Reports,* vol. 9, no. 1, p. 12419, 2019/08/27 2019.

[222] D. Jin, P. Xi, B. Wang, L. Zhang, J. Enderlein, and A. M. van Oijen, "Nanoparticles for super-resolution microscopy and single-molecule tracking," *Nature Methods,* vol. 15, no. 6, pp. 415-423, 2018/06/01 2018.

[223] G. Lin and D. Jin, "Responsive Sensors of Upconversion Nanoparticles," *ACS Sensors,* vol. 6, no. 12, pp. 4272-4282, 2021/12/24 2021.

[224] C. Chen *et al.*, "Multi-photon near-infrared emission saturation nanoscopy using upconversion nanoparticles," *Nature Communications,* vol. 9, no. 1, p. 3290, 2018/08/17 2018.

[225] C. Chen *et al.*, "Upconversion Nanoparticles: Heterochromatic Nonlinear Optical Responses in Upconversion Nanoparticles for Super-Resolution Nanoscopy (Adv. Mater. 23/2021)," *Advanced Materials,* https://doi.org/10.1002/adma.202170182 vol. 33, no. 23, p. 2170182, 2021/06/01 2021.
[226] S. Wen, J. Zhou, K. Zheng, A. Bednarkiewicz, X. Liu, and D. Jin, "Advances in highly doped upconversion nanoparticles," *Nature Communications,* vol. 9, no. 1, p. 2415, 2018/06/20 2018.
[227] M. Wilchek and E. A. Bayer, "The avidin-biotin complex in bioanalytical applications," *Analytical Biochemistry,* vol. 171, no. 1, pp. 1-32, 1988/05/15/ 1988.
[228] T. J. Zbacnik *et al.*, "Role of Buffers in Protein Formulations," (in eng), no. 1520-6017 (Electronic).
[229] N. Inada, N. Fukuda, T. Hayashi, and S. Uchiyama, "Temperature imaging using a cationic linear fluorescent polymeric thermometer and fluorescence lifetime imaging microscopy," *Nat Protoc,* vol. 14, no. 4, pp. 1293-1321, Apr 2019.
[230] C. Wang *et al.*, "Dynamic tubulation of mitochondria drives mitochondrial network formation," *Cell Res,* vol. 25, no. 10, pp. 1108-20, Oct 2015.
[231] Z. Huang, N. Li, X. Zhang, C. Wang, and Y. Xiao, "Fixable Molecular Thermometer for Real-Time Visualization and Quantification of Mitochondrial Temperature," *Anal Chem,* vol. 90, no. 23, pp. 13953-13959, Dec 4 2018.
[232] M. Rango, A. Arighi, C. Bonifati, R. Del Bo, G. Comi, and N. Bresolin, "The brain is hypothermic in patients with mitochondrial diseases," *J Cereb Blood Flow Metab,* vol. 34, no. 5, pp. 915-20, May 2014.
[233] B. del Rosal, E. Ximendes, U. Rocha, and D. Jaque, "In Vivo Luminescence Nanothermometry: from Materials to Applications," *Advanced Optical Materials,* vol. 5, no. 1, 2017.
[234] D. Jaque and F. Vetrone, "Luminescence nanothermometry," *Nanoscale,* vol. 4, no. 15, pp. 4301-26, Aug 7 2012.
[235] D. Ruiz *et al.*, "Ag/Ag2S Nanocrystals for High Sensitivity Near-Infrared Luminescence Nanothermometry," *Advanced Functional Materials,* vol. 27, no. 6, 2017.
[236] M. Suzuki, V. Tseeb, K. Oyama, and S. Ishiwata, "Microscopic detection of thermogenesis in a single HeLa cell," *Biophys J,* vol. 92, no. 6, pp. L46-8, Mar 15 2007.
[237] J. Zhou, B. del Rosal, D. Jaque, S. Uchiyama, and D. Jin, "Advances and challenges for fluorescence nanothermometry," *Nature Methods,* vol. 17, no. 10, pp. 967-980, 2020/10/01 2020.
[238] K. Green, K. Huang, H. Pan, G. Han, and S. F. Lim, "Optical Temperature Sensing With Infrared Excited Upconversion Nanoparticles," *Front Chem,* vol. 6, p. 416, 2018.
[239] J. Zhou, A. I. Chizhik, S. Chu, and D. Jin, "Single-particle spectroscopy for functional nanomaterials," *Nature,* vol. 579, no. 7797, pp. 41-50, Mar 2020.
[240] C. D. S. Brites *et al.*, "Thermometry at the nanoscale," *Nanoscale,* 10.1039/C2NR30663H vol. 4, no. 16, pp. 4799-4829, 2012.
[241] M. Homma, Y. Takei, A. Murata, T. Inoue, and S. Takeoka, "A ratiometric fluorescent molecular probe for visualization of mitochondrial temperature in living cells," *Chem Commun (Camb),* vol. 51, no. 28, pp. 6194-7, Apr 11 2015.

[242] K. Okabe, R. Sakaguchi, B. Shi, and S. Kiyonaka, "Intracellular thermometry with fluorescent sensors for thermal biology," *Pflugers Arch,* vol. 470, no. 5, pp. 717-731, May 2018.
[243] Z. Shi *et al.*, "Dual functional NaYF4:Yb(3+), Er(3+)@NaYF4:Yb(3+), Nd(3+) core-shell nanoparticles for cell temperature sensing and imaging," *Nanotechnology,* vol. 29, no. 9, p. 094001, Mar 2 2018.
[244] X. Zhu *et al.*, "Temperature-feedback upconversion nanocomposite for accurate photothermal therapy at facile temperature," *Nat Commun,* vol. 7, p. 10437, Feb 4 2016.
[245] S. Wu *et al.*, "Non-blinking and photostable upconverted luminescence from single lanthanide-doped nanocrystals," *Proc Natl Acad Sci U S A,* vol. 106, no. 27, pp. 10917-21, Jul 7 2009.
[246] S. H. Nam *et al.*, "Long-term real-time tracking of lanthanide ion doped upconverting nanoparticles in living cells," *Angew Chem Int Ed Engl,* vol. 50, no. 27, pp. 6093-7, Jun 27 2011.
[247] F. Vetrone *et al.*, "Temperature sensing using fluorescent nanothermometers," *ACS Nano,* vol. 4, no. 6, pp. 3254-8, Jun 22 2010.
[248] X. Qiu, Q. Zhou, X. Zhu, Z. Wu, W. Feng, and F. Li, "Ratiometric upconversion nanothermometry with dual emission at the same wavelength decoded via a time-resolved technique," *Nat Commun,* vol. 11, no. 1, p. 4, Jan 7 2020.
[249] V. Muhr, S. Wilhelm, T. Hirsch, and O. S. Wolfbeis, "Upconversion Nanoparticles: From Hydrophobic to Hydrophilic Surfaces," *Accounts of Chemical Research,* vol. 47, no. 12, pp. 3481-3493, 2014/12/16 2014.
[250] Y. Zhong *et al.*, "In vivo molecular imaging for immunotherapy using ultra-bright near-infrared-IIb rare-earth nanoparticles," *Nat Biotechnol,* vol. 37, no. 11, pp. 1322-1331, Nov 2019.
[251] X. H. Wang *et al.*, "Targetable phosphorescent oxygen nanosensors for the assessment of tumor mitochondrial dysfunction by monitoring the respiratory activity," *Angew Chem Int Ed Engl,* vol. 53, no. 46, pp. 12471-5, Nov 10 2014.
[252] J. Zielonka *et al.*, "Mitochondria-Targeted Triphenylphosphonium-Based Compounds: Syntheses, Mechanisms of Action, and Therapeutic and Diagnostic Applications," *Chem Rev,* vol. 117, no. 15, pp. 10043-10120, Aug 9 2017.
[253] H. Hao *et al.*, "Golgi-associated microtubules are fast cargo tracks and required for persistent cell migration," *EMBO Rep,* vol. 21, no. 3, p. e48385, Mar 4 2020.
[254] A. M. Valm *et al.*, "Applying systems-level spectral imaging and analysis to reveal the organelle interactome," *Nature,* vol. 546, no. 7656, pp. 162-167, Jun 01 2017.
[255] J. Adler and I. Parmryd, "Quantifying colocalization by correlation: the Pearson correlation coefficient is superior to the Mander's overlap coefficient," (in eng), *Cytometry A,* vol. 77, no. 8, pp. 733-42, Aug 2010.
[256] X. H. Wang *et al.*, "Poly-l-lysine assisted synthesis of core-shell nanoparticles and conjugation with triphenylphosphonium to target mitochondria," *J Mater Chem B,* vol. 1, no. 38, pp. 5143-5152, Oct 14 2013.
[257] H. He *et al.*, "Quantitative Lateral Flow Strip Sensor Using Highly Doped Upconversion Nanoparticles," *Anal Chem,* vol. 90, no. 21, pp. 12356-12360, Nov 6 2018.
[258] P. Y. Liu *et al.*, "Cell refractive index for cell biology and disease diagnosis: past, present and future," *Lab Chip,* vol. 16, no. 4, pp. 634-44, Feb 21 2016.

[259] Y. Takei *et al.*, "A Nanoparticle-Based Ratiometric and Self-Calibrated Fluorescent Thermometer for Single Living Cells," *ACS Nano,* vol. 8, no. 1, pp. 198-206, 2014/01/28 2014.
[260] A. C. Cutro, G. G. Montich, and O. A. Roveri, "Effect of carbonylcyanide-4-(trifluoromethoxy)phenylhydrazone (FCCP) on the interaction of 1-anilino-8-naphthalene sulfonate (ANS) with phosphatidylcholine liposomes," *J Bioenerg Biomembr,* vol. 46, no. 2, pp. 119-25, Apr 2014.
[261] X.-H. Wang *et al.*, "Targetable Phosphorescent Oxygen Nanosensors for the Assessment of Tumor Mitochondrial Dysfunction By Monitoring the Respiratory Activity," *Angewandte Chemie,* vol. 126, no. 46, pp. 12679-12683, 2014.
[262] D. Chretien *et al.*, "Mitochondria are physiologically maintained at close to 50 degrees C," *PLoS Biol,* vol. 16, no. 1, p. e2003992, Jan 2018.
[263] S. Hu *et al.*, "Quantifying Surface Temperature of Thermoplasmonic Nanostructures," *J Am Chem Soc,* vol. 140, no. 42, pp. 13680-13686, Oct 24 2018.
[264] R. Chen, V. D. Ta, F. Xiao, Q. Zhang, and H. Sun, "Multicolor hybrid upconversion nanoparticles and their improved performance as luminescence temperature sensors due to energy transfer," *Small,* vol. 9, no. 7, pp. 1052-7, Apr 8 2013.
[265] X. Yang *et al.*, "Mitochondrial dynamics quantitatively revealed by STED nanoscopy with an enhanced squaraine variant probe," *Nat Commun,* vol. 11, no. 1, p. 3699, Jul 24 2020.
[266] Q. P. Su *et al.*, "Superresolution imaging reveals spatiotemporal propagation of human replication foci mediated by CTCF-organized chromatin structures," *Proc Natl Acad Sci U S A,* vol. 117, no. 26, pp. 15036-15046, Jun 30 2020.
[267] Y. Chen, Q. P. Su, Y. Sun, and L. Yu, "Visualizing Autophagic Lysosome Reformation in Cells Using In Vitro Reconstitution Systems," *Current Protocols in Cell Biology,* vol. 78, no. 1, pp. 11.24.1-11.24.15, 2018.
[268] W. Du, X. Di, and Q. P. Su, "Studying Mitochondrial Network Formation by In Vivo and In Vitro Reconstitution Assay," *Methods in molecular biology,* vol. 2276, pp. 333-341, 2021.
[269] M. Xu *et al.*, "Ratiometric nanothermometer in vivo based on triplet sensitized upconversion," *Nat Commun,* vol. 9, no. 1, p. 2698, Jul 12 2018.
[270] D. J. Chung, T. M. Healy, J. L. McKenzie, A. J. Chicco, G. C. Sparagna, and P. M. Schulte, "Mitochondria, Temperature, and the Pace of Life," *Integrative and Comparative Biology,* vol. 58, no. 3, pp. 578-590, 2018.
[271] W. Du *et al.*, "Kinesin 1 Drives Autolysosome Tubulation," *Dev Cell,* vol. 37, no. 4, pp. 326-36, May 23 2016.
[272] M. Audano, A. Schneider, and N. Mitro, "Mitochondria, lysosomes, and dysfunction: their meaning in neurodegeneration," *J Neurochem,* vol. 147, no. 3, pp. 291-309, Nov 2018.
[273] L. F. Burbulla *et al.*, "Dopamine oxidation mediates mitochondrial and lysosomal dysfunction in Parkinson’s disease," *Science,* vol. 357, no. 6357, pp. 1255-1261, 2017.
[274] J. M. M. Donald and D. Krainc, "Lysosomal Proteins as a Therapeutic Target in Neurodegeneration," *Annual Review of Medicine,* vol. 68, no. 1, pp. 445-458, 2017.

[275] Q. P. Su *et al.*, "Vesicle Size Regulates Nanotube Formation in the Cell," *Sci Rep,* vol. 6, p. 24002, Apr 7 2016.
[276] Q. Wan, S. Chen, W. Shi, L. Li, and H. Ma, "Lysosomal pH rise during heat shock monitored by a lysosome-targeting near-infrared ratiometric fluorescent probe," *Angew Chem Int Ed Engl,* vol. 53, no. 41, pp. 10916-20, Oct 6 2014.
[277] N. Plotegher and M. R. Duchen, "Mitochondrial Dysfunction and Neurodegeneration in Lysosomal Storage Disorders," *Trends in Molecular Medicine,* vol. 23, no. 2, pp. 116-134, 2017/02/01/ 2017.
[278] S. Uchiyama, C. Gota, T. Tsuji, and N. Inada, "Intracellular temperature measurements with fluorescent polymeric thermometers," *Chemical Communications,* 10.1039/C7CC06203F vol. 53, no. 80, pp. 10976-10992, 2017.
[279] C. A.-O. Brites *et al.*, "Instantaneous ballistic velocity of suspended Brownian nanocrystals measured by upconversion nanothermometry," (in eng), no. 1748-3395 (Electronic).
[280] X. Di *et al.*, "Quantitatively Monitoring In Situ Mitochondrial Thermal Dynamics by Upconversion Nanoparticles," (in eng), *Nano Lett,* vol. 21, no. 4, pp. 1651-1658, Feb 24 2021.
[281] K. Okabe and S. Uchiyama, "Intracellular thermometry uncovers spontaneous thermogenesis and associated thermal signaling," *Communications Biology,* vol. 4, no. 1, p. 1377, 2021/12/09 2021.
[282] T. Bai and N. Gu, "Micro/Nanoscale Thermometry for Cellular Thermal Sensing," (in eng), no. 1613-6829 (Electronic).
[283] M. Suzuki and T. Plakhotnik, "The challenge of intracellular temperature," *Biophysical Reviews,* vol. 12, no. 2, pp. 593-600, 2020/04/01 2020.
[284] R. Piñol *et al.*, "Real-Time Intracellular Temperature Imaging Using Lanthanide-Bearing Polymeric Micelles," *Nano Letters,* vol. 20, no. 9, pp. 6466-6472, 2020/09/09 2020.
[285] D. B. Ambiliraj, B. Francis, and M. L. P. Reddy, "Lysosome-targeting luminescent lanthanide complexes: from molecular design to bioimaging," *Dalton Transactions,* 10.1039/D2DT00128D vol. 51, no. 20, pp. 7748-7762, 2022.
[286] W. Zhang *et al.*, "A lysosome-targeting nanosensor for simultaneous fluorometric imaging of intracellular pH values and temperature," *Microchimica Acta,* vol. 185, no. 12, p. 533, 2018/11/06 2018.
[287] B. del Rosal *et al.*, "In Vivo Contactless Brain Nanothermometry," *Advanced Functional Materials,* https://doi.org/10.1002/adfm.201806088 vol. 28, no. 52, p. 1806088, 2018/12/01 2018.
[288] Y. He *et al.*, "A combinational chemo-immune therapy using an enzyme-sensitive nanoplatform for dual-drug delivery to specific sites by cascade targeting," *Sci Adv,* vol. 7, no. 6, Feb 2021.
[289] L. Zhang *et al.*, "Optimizing the Polymer Cloak for Upconverting Nanoparticles: An Evaluation of Bioactivity and Optical Performance," *ACS Applied Materials & Interfaces,* vol. 13, no. 14, pp. 16142-16154, 2021/04/14 2021.
[290] M. Maddahfar *et al.*, "Stable and Highly Efficient Antibody–Nanoparticles Conjugation," *Bioconjugate Chemistry,* vol. 32, no. 6, pp. 1146-1155, 2021/06/16 2021.

[291] L. Zhang *et al.*, "Optimizing the Polymer Cloak for Upconverting Nanoparticles: An Evaluation of Bioactivity and Optical Performance," *ACS Appl Mater Interfaces,* vol. 13, no. 14, pp. 16142-16154, Apr 14 2021.
[292] Y. Takei *et al.*, "A nanoparticle-based ratiometric and self-calibrated fluorescent thermometer for single living cells," *ACS Nano,* vol. 8, no. 1, pp. 198-206, Jan 28 2014.
[293] A. F. Slater and A. Cerami, "Inhibition by chloroquine of a novel haem polymerase enzyme activity in malaria trophozoites," (in eng), no. 0028-0836 (Print).
[294] C. A. Homewood, D. C. Warhurst, W. Peters, and V. C. Baggaley, "Lysosomes, pH and the Anti-malarial Action of Chloroquine," *Nature,* vol. 235, no. 5332, pp. 50-52, 1972/01/01 1972.
[295] G. Baffou, H. Rigneault, D. Marguet, and L. Jullien, "A critique of methods for temperature imaging in single cells," *Nature Methods,* vol. 11, no. 9, pp. 899-901, 2014/09/01 2014.
[296] D. Macherel, F. Haraux, H. Guillou, and O. Bourgeois, "The conundrum of hot mitochondria," (in eng), *Biochim Biophys Acta Bioenerg,* vol. 1862, no. 2, p. 148348, Feb 1 2021.
[297] G. Baffou, H. Rigneault, D. Marguet, and L. Jullien, "Reply to: "Validating subcellular thermal changes revealed by fluorescent thermosensors" and "The 105 gap issue between calculation and measurement in single-cell thermometry"," *Nature Methods,* vol. 12, no. 9, pp. 803-803, 2015/09/01 2015.
[298] N. Lane, "Hot mitochondria?," *PLOS Biology,* vol. 16, no. 1, p. e2005113, 2018.
[299] D. Chrétien *et al.*, "Mitochondria are physiologically maintained at close to 50 °C," *PLOS Biology,* vol. 16, no. 1, p. e2003992, 2018.
[300] D. F. Rolfe and G. C. Brown, "Cellular energy utilization and molecular origin of standard metabolic rate in mammals," (in eng), no. 0031-9333 (Print).
[301] C. Riedel *et al.*, "The heat released during catalytic turnover enhances the diffusion of an enzyme," *Nature,* vol. 517, no. 7533, pp. 227-230, 2015/01/01 2015.
[302] K. Richter, J. Haslbeck M Fau - Buchner, and J. Buchner, "The heat shock response: life on the verge of death," (in eng), no. 1097-4164 (Electronic).
[303] Y. Liu *et al.*, "Stratified Disk Microrobots with Dynamic Maneuverability and Proton-Activatable Luminescence for in Vivo Imaging," *ACS Nano,* vol. 15, no. 12, pp. 19924-19937, 2021/12/28 2021.
[304] C. Chen *et al.*, "Multi-photon near-infrared emission saturation nanoscopy using upconversion nanoparticles," (in eng), *Nat Commun,* vol. 9, no. 1, p. 3290, Aug 17 2018.
[305] B. Liu *et al.*, "Upconversion Nonlinear Structured Illumination Microscopy," *Nano Lett,* vol. 20, no. 7, pp. 4775-4781, Jul 8 2020.
[306] Q. P. Su and L. A. Ju, "Biophysical nanotools for single-molecule dynamics," (in eng), *Biophys Rev,* Aug 18 2018.
[307] N. Garrido, L. Griparic, E. Jokitalo, J. Wartiovaara, A. M. van der Bliek, and J. N. Spelbrink, "Composition and Dynamics of Human Mitochondrial Nucleoids," *Molecular Biology of the Cell,* vol. 14, no. 4, pp. 1583-1596, 2003/04/01 2002.
[308] K. McArthur *et al.*, "BAK/BAX macropores facilitate mitochondrial herniation and mtDNA efflux during apoptosis," *Science,* vol. 359, no. 6378, Feb 23 2018.

[309] L. Chatre and M. Ricchetti, "Prevalent coordination of mitochondrial DNA transcription and initiation of replication with the cell cycle," *Nucleic Acids Research,* vol. 41, no. 5, pp. 3068-3078, 2013.